Ministero dell'Istruzione,
dell'Università e della Ricerca

UNIVERSITY OF SALERNO

Department of Civil Engineering

PhD course in

Risk and Sustainability in Civil, Architectural and Environmental Engineering Systems

XXXIII Cycle (2017-2020)

(a.y. 2019-2020)

Theoretical and Experimental Investigation on Conventional and Innovative Reinforced Concrete Beam-to-Column Joints with and without Floor Deck

Simona Streppone

Simona Streppone

Tutor

Prof. Rosario Montuori

Rosario Montuori

Coordinator

Prof. Fernando Fraternali

Fernando Fraternali

Co-tutor

Prof. Elide Nastri

Prof. Vincenzo Piluso

Abstract

Results of experimental tests carried out on Reinforced Concrete (RC) frames and connections equipped with integrated slab pointed out that the presence of the slab increases the flexural capacity of the connection, by acting as a flange for the beam. Consequently, the lateral resistance and stiffness of the structure are enhanced, and the capacity design weak beam-strong column failure can be altered. This thesis work focused on the effect of the floor deck on the flexural capacity of RC beam-to-column connections designed in compliance with the seismic European code, Eurocode 8 (EC8). Specifically, the effect of the floor deck made up of RC joists and upper slab, with interlaid hollow tile blocks, is investigated. Concerning this floor-system, indeed, few in-depth studies are available and EC8 does not specify how to account for the floor joists contribution in the resistance of RC connections.

The goals of this thesis were two. Firstly, the over-resistance due to the deck presence in conventional beam-to-column connection was experimentally evaluated and compared to the "equivalent beam" theoretical model prediction, to verify the model accuracy. The "equivalent beam" model provides a proper formula to evaluate the number of joists enhancing the beam resistance. Secondly, an innovative constructional detail for RC beams was proposed, aiming at reducing the joint resistance, by computing the existence of the deck contribution. According to the basic concept of the Reduced Beam Section (RBS) design, typical of the steel connections, the flexural capacity of the beam was reduced to create a localized plastic zone far from the column, able to avoid undesired partial collapse mechanisms.

The work is divided into three parts, the theoretical study, the experimental study, and the numerical modelling. The theoretical study consisted in modifying the formula of the "equivalent beam" model with reference to the test layout boundary conditions. The experimental campaign was conducted at the STRENGTH laboratory of the University of Salerno. In total, 12 full-scale specimens were tested in quasi-static loading, 6 of them are conventional beam-to-column joints with and without the floor deck, while the other 6 are innovative beam-to-column joints with and without the floor deck. The 3D Finite Element Model (FEM) of the RC joints, developed in the Abaqus software, reproduced the actual geometry of the experiments, as well as the same boundary conditions and loading as in the experimental program.

The results of the experimental tests confirm that the floor deck enhances the resistance of the connection, greatly in hogging rather than in sagging bending. Moreover, the accuracy of the "equivalent beam" theoretical model is proved. The resistance of specimens equipped with the deck is predicted fairly in positive loading direction, while it is slightly overrated in the negative one. The cracking evolution confirms the actual interaction between the elements assumed in the theoretical model. The innovative detail effectively reduces the flexural strength of the connection. In particular, the resistance of innovative specimens with the floor deck is in perfect agreement with the resistance of simple conventional specimens, especially in the positive loading direction. The plastic hinge develops in the RBS and smaller damage on the beam supporting the joists is observed. The FE-Models of the tested specimens show good agreements with the experimental results. However, further analyses have to be carried out.

Acknowledgements

The unique experience I had the chance to live during these years enriched me from both a human and professional perspective. This is why I wish to express my deepest gratitude to the people I met.

To my research team, Prof.R.Montuori, Prof.V.Piluso and Prof.E.Nastri, for allowing me to face the research world.

To the technician of the STRENGTH Laboratory, Eng.F.Perri, for his highly professional support and courtesy and to Eng.G.Califano and Eng.C.Esposito, who worked with me on this project providing me with excellent assistance during the tests.

To my dear friends, Alessandro and Bonaventura, thanks to whom I daily extended my knowledge.

To the colleagues of the PhD students room, Adamo, Luigi, and Sabatino, since their kindness and competence made the working days really pleasant.

To Prof.G.Rizzano, Prof.M.Latour and Eng.A.B.Francavilla, for teaching me cooperation and collaboration values, typical of a real team.

To Prof.M.Titirla, who was for me a mentor and also a special friend.

To my big little family, for their endless love and help.

Finally, thanks to Luca, who is every day by my side, always trusting in me, thus proving that our feelings are the best thing I have ever built in my life.

Contents

List of Figures

List of Tables

Chapter 1

Background and Motivation of the Work

1.1 Introduction

Reinforced Concrete (RC) is a widespread civil constructions material. The RC three-dimensional frame system, with his advantages, got so successful since its first employment as the great part of the current building heritage, in Italy as well as in other seismic prone countries, belongs to this technology. Over the years, the design methodology and the construction details concerning RC structures changed, thus currently the buildings may be divided in those dating back to before seismic codes and those complying with current regulations. Many issues affecting the oldest edifices are now overcome by the design concepts of modern provisions; many others still need to be examined in depth. Particularly of concern is the influence that the so-called secondary elements, like RC slab monolithically cast with the beam, can have on the response of the structure in terms of strength, stiffness and inelastic deformation of members. Many experimental tests, indeed, proved the slab contribution whereas many codes, like the European code Eurocode 8 (EC8) [1], still neglects or partially consider it in the design.

In the past, many researchers faced the topic of the seismic performance in RC structures, by performing several experimental tests on full-scale and reduced-scale frames and sub-assemblies. Most specimens were spatial beam-to-column joints with and without floor slab, intended to understand and quantify the amount of the slab participation in the frame overall response and beam behaviour. It turned out that the presence of the slab impacts on both the capacity and the demand of the elements, by enhancing the flexural strength of the beam, the overall resistance and the lateral stiffness of the structure, but also the local demand of critical regions, i.e. the joints. In the light of the capacity design conception, indeed, the beam flexural strength controls the beam shear, joint design and column flexural strength. Hence, whereas neglecting the slab can be conservative in the gravity load design approach since the slab favourably enhances the resistance of the beam, on the contrary, it may be detrimental in the current seismic design implementation as, especially when the hogging moment occurs, the "weak beam-strong column" criteria can easily switch to a “strong beam-weak column” failure mechanism.

1.2 State of the Art

Interest in investigating the slab effects on the response of RC beam-to-column joints starts in the 1980s, when the test carried out on a full-scale seven-storey building at the Building Research Institute (BRI) in Tsukuba, Japan, [2] exhibited a base shear 70% more than expected. The expected shear capacity of the structure, indeed, had been evaluated neglecting the contribution of the floor slab. In the context of US-Japan cooperative experimental program [3], different tests [3–8] were led up on slab-beam-column sub-assemblies, by simulating lateral loads and earthquake excitation. It was confirmed that the slab is the main element modifying the three-dimensional response of the structure under horizontal loads and it was demonstrated as well that the amount of slab participating increases if subjected to tensile stress since the slab reinforcement acts as additional reinforcement to the beam. The typologies of specimens widely tested over the years are shown in Figure 1.1. The floor deck consisted of an integrated slab monolithically cast with the beams. In this chapter, for the sake of consistency with the examined bibliography, the direction in which the load is applied will be referred to as longitudinal direction, while the orthogonal one will be referred to as transverse direction.

In order to describe the way the slab takes part in the behaviour of the connection, a common RC structure made up of rectangular beams and monolithically cast slab has to be considered. When the hogging moment, such as the negative moment, occurs at one end of the beam, the top fibres result in tension while the bottom ones are in compression, being the neutral axis located beyond the mid-height of the section. The upper part of the beam is then subjected to elongation and, for sake of kinematic congruence, the adjacent slab must undergo the same deformation, with the occurrence of tensile stresses in the slab reinforcement. The beam section, therefore, has to be considered not as rectangular anymore, but as T-beam or L-beam [7], in internal and corner connections respectively, with the flanges constituting by the slab getting mobilised by the beam.

On the contrary, under sagging or positive moments, the neutral axis is located in the upper part of the beam section, often in the concrete cover thickness, thus resulting in the top fibres in compression and the bottom fibres in tension. The slab reinforcement undergoes small levels of strain as compared to the hogging bending case when, as a consequence, the greatest enhancement in the flexural resistance is achieved. This was confirmed by several experimental studies [7, 8, 13], showing also a moderate increase in the flexural strength of the beam subjected to sagging moment [14]. In the model by [7], the slab was assumed to act as a tensile membrane element reinforcing the tension part of the beam once the cracking spreads in the concrete, concept well supported by [8] also. This assumption was justified by

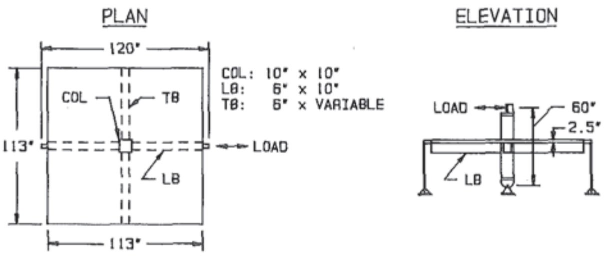

(a) MINNESOTA (EW1-3)

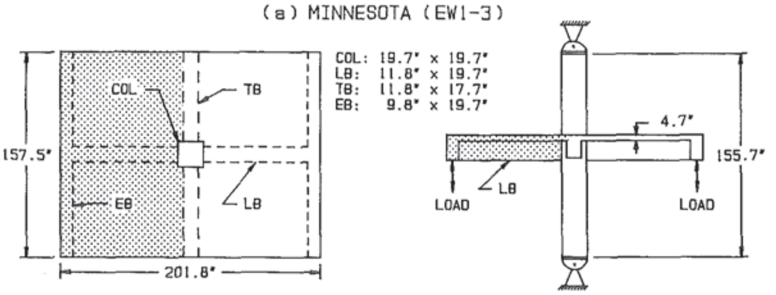

(b) TEXAS (TIP, TEP, TIM, TEM)

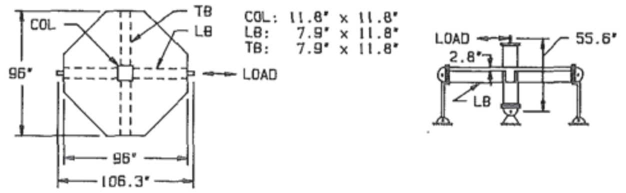

(c) JAPAN (UTa)

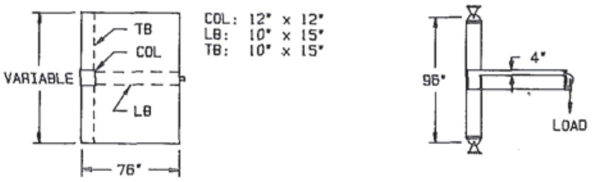

(d) RICE (J4-J7)

FIGURE 1.1: Layout of four test series conducted at the University of Minnesota [9], the University of Texas at Austin [10], the University of Tokyo [4], and Rice University [11]. Picture from [12]

the small depth of the slab as compared to that of the beam. By virtue of this evidence, the variation of the strain over the slab thickness may be considered negligible. Stated that the slab undergoes tensile strains due to the elongation of the beam, it becomes clear that the effect is stronger near the beam while it goes fading as the transverse distance from the beam increases [2, 7, 8, 15], thus causing a shear lag in the slab diaphragm. Crack patterns in tested specimens [16] testify this phenomenon which was also proved by the qualitative model in [17]. In [12], the non-uniformity of the strain in the slab rebars along the transverse direction is moreover attributed to deformations due to the slab in-plane shear forces. To summarise, not the entire slab in the bay span is responsible for the so-called slab contribution but only a part, depending on the factors previously presented and many others too.

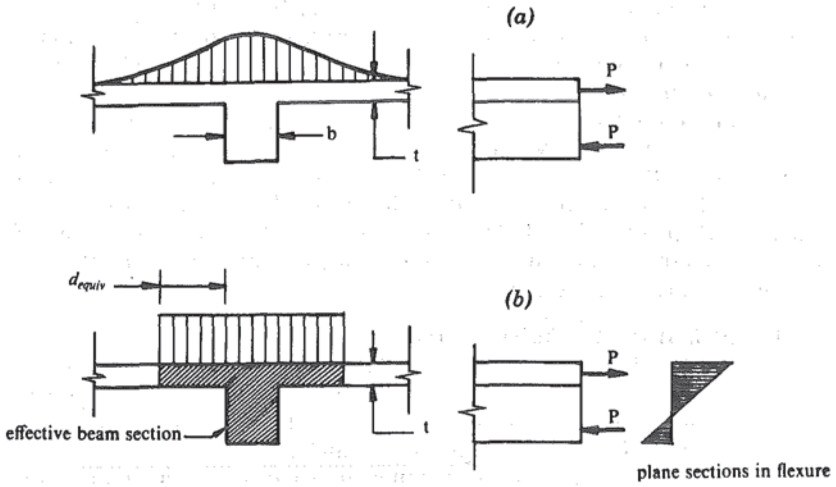

FIGURE 1.2: Original strain distribution (a) and uniform strain distribution (b) of the T-beam section in bending. Picture from [7]

1.2.1 Factors Affecting the Slab Participation Phenomenon

The slab contribution varies under sagging and hogging condition, inducing an asymmetrical flexural response [14] of the connection, with a greater resistance when the slab is in tension, due to the membrane action of the slab. Under tensile stresses, the strain in the slab reinforcement is responsible for defining the effective width of the slab, which depends also on other parameters, i.e. the lateral drift of the structure, the presence of the transverse beam and the presence of damage due to previously applied loads or bidirectional loads.

1.2.1.1 Lateral Drift

As the beam and the slab are tied by kinematic constraints, the extent of the slab contributing in the frame connection depends on the lateral drift the structure undergoes [3, 7, 8, 17, 18]. Increasing the inter-storey drift means to increase the beam rotation and the longitudinal strain in the beam and the adjacent slab as well [3]. When the beam is subjected to hogging bending, the larger is the lateral drift, the greater is the slab reinforcement brought into play far from the beam (in transverse direction). The slab reinforcement becomes fully effective once a large level of drift is imposed [3, 15, 19–22], like 3.8-7.2% [12].

In [23], the effective width of the slab under negative bending was 1.5 times the beam depth on both side of the web before the yielding, 2.0 in moderate post-yielding and 2.5 under very large drifts.

In [19], the flange width was 2 times the beam depth under hogging moment at interior connection and 1 beam depth under sagging moment in both internal and external connections.

In [14], experimental curves of slab-beam-column assemblies, subjected to increasing levels of inter-storey drift, showed, in terms of moment versus curvature

(Figure 1.3), that the resistance in negative bending does not stop growing as larger drift is imposed and, hence, more slab is activated. Moreover, in that case, is not possible to easily distinguish the yield point since the strain in the steel rebars decreases farther away from the connection. However, it turned out that at an inter-storey drift of 2%, which can be assumed as a compatible design target for RC structures, the increase in flexural strength of the connection is limited; hence not the entire width of the slab is mobilised [3, 8, 12].

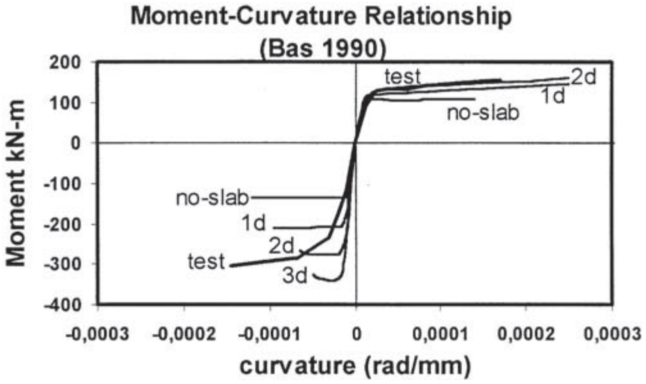

FIGURE 1.3: Moment-curvature relation of a beam with slab participation

1.2.1.2 Transverse Beam

The transverse beam is a further element affecting the amount of slab width to consider in the behaviour of the connection. Several experiments and parametric studies [4–6, 9, 12, 15, 18, 19, 22, 24–31] have been carried out on interior and exterior connections, by simulating earthquake loading, with the aim to determine how transverse beams condition the effective width of the slab acting as a tension flange for the longitudinal beam. Mainly, it was demonstrated that, for both interior and exterior joints, when the slab is in tension, the presence of the transverse beam, through its torsional stiffness, influences the strain distribution in the slab and also the stiffness and strength of the connection. In particular, torsional stiffer transverse elements increases the slab width.

As a reaction to lateral loads, a transverse element generally experiences a relative torsional rotation with respect to the column, depending on its torsional stiffness. Elements with a low torsional stiffness rotate in order to relieve the rotational demand. Elements with a high torsional stiffness experience very little torsional rotation. In [12], it was observed that, in the case of torsionally stiff transverse elements, the rotations imposed across the slab were more uniform, as uniform was also the strain in the slab reinforcement. Hence, it was found that, if subjected to large levels of drift, torsionally stiffer elements can easily mobilise the full slab width [12].

Tests on three 1/3 scaled interior joints [25] highlighted that the specimen having a large torsional stiffness exhibited greater resistance than other specimens, in the initial loading cycles, while the peak load was almost the same. In the same tests, the mere existence of the transverse beams, even if previously damaged, was demonstrated to reduce the inter-storey drift. Moreover, sub-assemblages having torsional stiffer transverse elements were found to exhibit smaller drift. The larger slab participation [25], indeed, reduced the ultimate curvature.

The transverse element, in addition, helps to confine the joint [29, 32], thus preventing the rotation and inducing larger damage in the close beams [30]. It plays a crucial role in transferring the forces from the slab to the column, by extending the joint region.

Interior and exterior connections are differently influenced by the transverse element.

In [4, 12], it was observed that transverse elements of exterior connections may experience torsional failure, due to the tensile forces in the slab longitudinal rebars. The tensile forces of the slab, indeed, cannot be transferred to another side of the slab. On the contrary, in interior connections, the tensile forces on both sides of the transverse beam tend to eliminate since, for the sake of equilibrium, the tensile forces on the slab in tension side are transferred to the slab in compression side. Therefore, in exterior connections, the slab involvement is limited by the torsional capacity of the transverse beam [12, 15, 19, 29].

As said, when the transverse beam undergoes cracking, due to the brittle behaviour of the concrete and lack of the slab on the other side of the connection [12, 15], the load transfer mechanism, conveying the forces from the slab to the joint core does not take place [12, 29]. Researchers [28] assumed that, after the cracking and yielding in the transverse beam, the flow of the forces may be reasonably modelled by a strut-and-tie mechanism, with compressive struts occurring in the concrete and ties in the slab and spandrel beam rebars. As a consequence, the number of slab rebars defining the flange of the slab in tension depends on the torsional yield capacity of the spandrel beam and the capacity of the strut-and-tie-mechanism. In other words, it depends on the torsional reinforcement and size of the spandrel beam, the slab reinforcement, and the size of the column [28].

Other researchers, instead, based on experimental evidence, related the effective slab width of exterior joints after the cracking to the column width plus twice the depth of the transverse beams [6]. In [29] the authors found that, while the behaviour of the exterior joints was insensitive to a variable width of the transverse beam, reducing the width of the transverse beam by half in interior connections reduces the story shear in the applied positive and negative loading direction.

However, many studies [27, 31] concluded that the transverse beam reinforcement is not able to enhance the total storey shear.

1.2.1.3 Bi-directional Loading

As the earthquake forces are never one-way oriented, an important parameter that may affect the slab action is the load applied in the transverse direction. A previously [9, 12, 25] or simultaneously [29] applied transverse load, may cause damage in the transverse direction, in transverse beams if these exist, thus obstructing the load-transfer mechanism from the slab to the joint and reducing the slab participation [25]. The more realistic condition is the application of a bi-directional (better if three-dimensional) loading.

Tests were performed in different steps to investigate this topic. The load was applied in one direction, firstly, and in the orthogonal one, secondly [25]. Initially, the damage, due to the previously applied transverse load, reduced the bearing capacity and stiffness of the structure. However, in [12], the authors pointed out that this evidence disappeared for imposed deformations greater than the maximum value applied in the first loading stage, in the transverse direction.

1.2.1.4 Further Factors

Hereinbefore the principal factors determining the effective width of the slab have been presented. As stated, the slab contribution is mainly a kinematically induced phenomenon, hence it is likely to be influenced by additional “secondary” occurrences, related to deformations at the boundaries of the slab. These phenomena are referred to as “secondary” since they may affect the slab participation at very large levels of drift or because of their limited effectiveness.

In [17], the slippage of the main beam reinforcement was found to increase the strain in the slab reinforcement, by promoting the beam elongation. The authors pointed this phenomenon as the reason why the entire width of the slab gets mobilised only at a very large level of drift. The bond-slip of the slab rebars may induce a redistribution of the strain in the entire bay span.

Additionally, in [19], the occurrence of the steel rebars buckling was found to affect the slab contribution. The specimens in [19] were subjected to alternated lateral load actions for increasing levels of drift. Tension and compression stress affected, successively, the top and bottom part of the beam section. The stress reversal and increased curvature ductility demand in the positive moment plastic hinge may easily cause the buckling of the bottom steel reinforcement. The slab contribution increases the curvature ductility demand in the positive moment plastic hinge. Hence, the bottom reinforcement in that section is subjected to high levels of inelastic tensile strain.

The strain in the slab may be also reduced by the in-plane deflections of the transverse beams [17], the in-plane shear forces in the slab [12] and the deformation in the beam-column joint [17].

1.2.2 Effects of the Slab Participation Phenomenon

The description of the slab role in the three-dimensional behaviour of RC connections induces some considerations about the effects of its contribution. The presence of the slab, indeed, mainly enhances the flexural strength of the beam. As a consequence, the global strength and lateral stiffness of the structure are enhanced. Also, it affects the ductility demand of the elements in the connection.

The slab, acting as a beam flange, increases the beam bearing capacity. Consider the portal frame illustrated in Figure 1.4, which is a single-span single-storey frame selected from a complete frame structure. By referring to a beam with geometrical and mechanical features constant along the bay span and supporting a monolithic slab, it is evident that, if the bearing capacity of the beam is assumed to be symmetric, the plastic hinges develop at both the beam ends, and the inflection was approximately at midspan of the beams (Figure 1.4(a)). Instead, if the slab is accounted for, hence an asymmetrical moment-curvature relation is assumed to model the behaviour of the connection, with a flexural capacity enhancement grater in hogging rather than in sagging bending, then the yielding no longer occurs simultaneously at the beam ends. The first plastic hinge develops at the beam end subjected to sagging moment, while the other end remains in a pre-yielding state (Figure 1.4(b)). As the lateral sway increases and much more slab gets mobilised, the hogging bending rises and, consequently, the inflexion point shifts from the mid-span toward the yielded end [33, 34]. This means the slab enhances not only the flexural capacity of the beam but also the curvature ductility demand in the plastic hinges, especially for the slab in compression case [33]. On the contrary, the deformation capacity of the structure [18] is reduced.

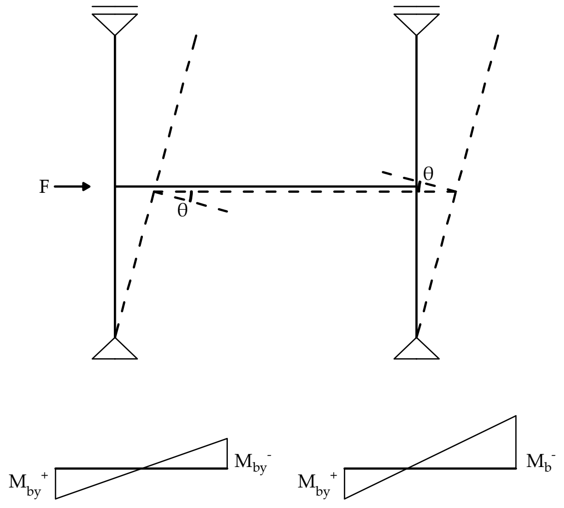

(a) **(b)**

FIGURE 1.4: Bending moment in the bay span considering the mere beam (a) and the slab contribution (b).

The slab influences the seismic performance of the structures in different ways [26]. A dangerous consequence of the increased flexural capacity of the beam due to the slab presence is the possible alteration of the failure mode of the structure, as the column-to-beam moment ratio decreases and the formation of plastic hinges in the columns is promoted [13], thus inducing a "weak column-strong beam" failure mode [15, 18, 35].

The increased flexural strength of the beam causes greater shear forces [3, 18, 36] and ductility demand [33] of the columns. Hence, the input shear to achieve a target drift is more significant and this can lead to a soft-storey mechanism or column shear failure [36].

As said at the beginning of this Chapter, the increase in the lateral load resistance of the structure was found to be the first clear effect of the over-resistance induced by the slab [3]. The over-resistance value, indeed, was far from being part of the material over-strength. Also in sub-standard detailed exterior RC beam-column subassemblies, the slab was found to increase the lateral capacity [32] [18]. Moreover, Finite Element (FE) simulations supported this evidence when the slab is included in the beam-column joint model, showing a storey shear higher in interior joints rather than in the exterior ones [29].

Not only the frame lateral resistance is increased by the slab participation, but also the stiffness [5, 6, 15, 26, 33, 34]. Indeed, in [26] the specimen with slab showed a stiffness 60-70% higher than those without slab. The degradation of stiffness was considerably delayed in [26] and it was more rapid in the slab-in-compression case than the slab-in-tension case [6]. In [29], instead, was found an increase in the initial stiffness, especially in models without spandrel beams.

However, if the stiffness is underestimated, the structure may exhibit high acceleration forces [25], as resulting from the analysis carried out on the multi-storey building in [33]. In the work, the beams were modelled by means of a modified spring element, accounting for the different behaviour of the RC connection in the slab-in-tension and slab-in-compression case. The structures experienced an increase in storey acceleration and base shear [33].

Another part of the RC structure that may be dramatically affected by the presence of the slab is the joint, due to the difficulties in repairing it and the detrimental consequences of its potential failure. Experimental tests showed that the joint shear is increased due to the slab participation [13, 26, 36] and a great part of the stress is transferred to it by torsion of the transverse beams [19]. Hence, it is necessary to account for the enhanced resistance due to the slab, as the joint and the column would undergo larger shear forces [18, 36]. However, the post-earthquake examination of interior joints in modern buildings with integral slab did not show shear failure [34]. The enhancement in the joint shear capacity was ascribed to the beneficial confinement effect of the elements surrounding the web, such as the slab and transverse beams (before cracking), which expand the effective width of the joint [22]. Experimental data [14] confirmed the slab helps confining the joint in compression [13, 22, 32].

1.3 Motivation and Objectives of the Work

The slab participation phenomenon has been described in the above with reference to the results of the last 40 years of research. The experimental campaigns analysed were carried out on RC specimens equipped with a specific typology of RC floor deck, i.e. the one composed of a monolithic floor slab cast with the beam. The results allowed not only to prove the existence of the slab contribution but also to obtain experimental formulas estimating the effective slab width, which have been adopted by different current codes. The outcomes of the previous studies, i.e. the general description of the slab participation phenomenon, as well as the parameters on which it depends and the effects of its presence in RC connections, can be easily extended to other types of RC floor decks. On the contrary, the same is not for the slab width formula, as it is experimentally derived.

The motivation of this Thesis work lies in investigating the effect of a different RC floor deck, most common in Italy and the Mediterranean area, in the behaviour of currently designed connections. The considered RC floor deck is made up of RC joists with upper slab and interlaid hollow tile blocks, depicted in Figure 1.5. Over the years, this topic has not been examined in depth. No laboratory tests have been carried out to investigate the influence of the joists and slab in the behaviour of the connections.

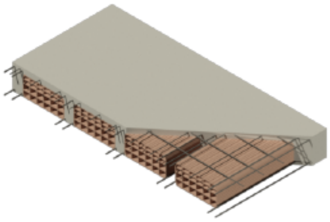

FIGURE 1.5: Reinforced Concrete floor deck made up of joists with upper slab and interlaid tile blocks.

The current knowledge in this field lies on a few parametric studies [37]. In that case, both non-ductile and ductile RC beam-to-column joint with deck were investigated, in order to understand no longer the role of the slab, but more properly the role of the joists. The authors, indeed, refer to the deck influence as the "joist contribution" [37], by suggesting that the direction of the joists (warping) is the main factor influencing the stress distribution in the deck. In particular, the joists parallel to the reference beam give a certain contribution in absorbing the bending moment, while the contribution of the joists orthogonal to the beam is reduced [37]. As resulted in specimens with integrated slab mainly analysed in Japan, USA and New Zealand, also in specimens equipped with the joists only a part of the floor deck along the bay span may be considered in the connection.

Concerning the exact estimation of the floor deck contribution, authors suggested to include in the joint resistance the part of the deck in one-meter stripe centred on the beam inter-axis [38, 39].

Others evaluated the floor deck contribution with a theoretical formula deriving from the elastic interaction between the joists and beam supporting the joists [40, 41].

The present Thesis naturally evolved from the works of the same research team [40, 41]. The main objectives can be summarised in the following as:

- the experimental validation of the theoretical formula presented in [40, 41] and properly modified, in order to exactly estimate the joists contribution in RC connections designed according to the current seismic European codes;
- the proposal of new technological detail for RC beam-to-column joints, able to overcome the negative effects of the floor-beam interaction. The new detail aims at, firstly, reducing the over-resistance due to the floor deck, secondly, shifting the plastic (and hence damage-prone) zone in a more accessible point of the connection, which could be more accessible in the case of a retrofit intervention.

In order to achieve the above goals, twelve beam-to-column specimens, designed according to the current European codes, have been tested at the STRENGTH (Structural Engineering Testing All) Laboratory of the Department of Civil Engineering of the University of Salerno. In particular, six so-called “conventional” specimens with and without floor have been tested to: (i) experimentally evaluate the difference in terms of resistance due to the floor deck made up of the joists and slab; (ii) compare the experimental and theoretical expected bending capacity. In addition, the new proposed detail of RC connections has been designed. The performances have been experimentally evaluated by testing six so-called “innovative” specimens, with and without the floor deck, with the aim to verify the achievement of the previously mentioned objectives fixed for the innovative detail.

Chapter 2

Design and Realization of Experimental Modules

2.1 Introduction

The experimental modules are the external connection of an RC residential building. As illustrated in Figure 2.1, the reference connection is located between two square-in-plan bays, whose length is $3.2m$. The dimensions of the bays were fixed in accordance with the space in which the test machine operates at the STRENGTH laboratory of the University of Salerno, where the experimental campaign was carried out. The modules are three-dimensional sub-assemblies of an RC frame external connection. Hence, they are made up of a column, extending above and below the floor level, and three beams framing in the joint region. The length of the column is equal to $2m$, which is the distance between the constraints of the test machine, where the specimen are then settled. The length of the beams is half of the bay span, indicatively.

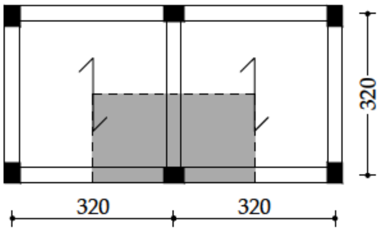

FIGURE 2.1: External connection (units: cm)

With reference to the building plan in Figure 2.1, two different typologies of modules were designed: the “conventional” and the “innovative” modules. Each typology is divided into two sub-typologies, which differ in the presence of the floor deck.

The conventional modules were so-called since they were designed according to the provisions of the current European codes [1, 42]. The reference conventional joint, made up of the mere frame structural elements, i.e. the beams and the column, was tagged as J_01. The conventional joint with the floor deck was tagged as

J_01_S. It has the same structural elements as the simple joint, but, besides, *J_01_S* is equipped with the cast-in-situ floor deck, composed of RC joists, upper slab and interlaid tile blocks.

The innovative specimens, instead, were inspired by the Reduced Beam Section (RBS) design, proper of the steel structures. According to the RBS design, the aims were to reduce the flexural strength of the connection and localise the plasticity zone in a specific area of the beam, far from the column face. In the newly defined plastic zone, the beam depth and the longitudinal reinforcement were reduced for a fixed length. The innovative modules, also, were designed without and with deck. They were tagged as, respectively, *J_02* and *J_02_S*.

The modules were designed according to the current European codes, Eurocode 2 (EC2) [42] and Eurocode 8 (EC8) [1], for the Medium Ductility Class (DCM). The design materials were concrete C25/30 and steel B450C for rebars. According to EC2, the partial factors for the material properties for obtaining the design resistances are $\gamma_c = 1.5$ for concrete and $\gamma_s = 1.15$ for steel.

2.2 Design of Experimental Specimens

2.2.1 Design of Conventional Specimens

Conventional modules are RC external connections designed without and with the floor deck. The two typologies of conventional modules are reported in Figure 2.2. The reference joint, *J_01* (Figure 2.2a), is the simplest one, made up of a column and three beams framing in the joint region. The *J_01_S* joint (Figure 2.2b) is equal to the reference joint but it is equipped with the floor deck.

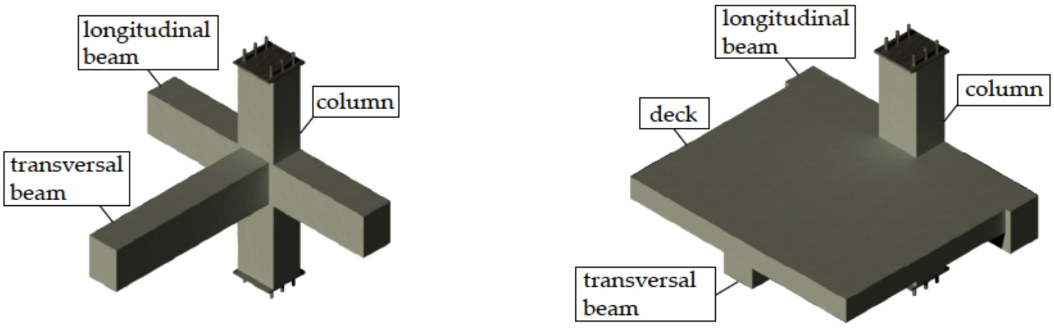

(a) J_01 (b) J_01_S

FIGURE 2.2: conventional modules without (a) and with deck (b)

In compliance with EC8, the structural elements were designed at the ultimate limit state by observing the conditions of resistance, ductility and equilibrium. In particular, the modules were designed for the Medium Ductility Class (DCM). The designed elements are hereinafter described in accordance with a certain sequence since the capacity design introduces an interdependence in the design of the various elements (joints-beams-columns). The results of the design are depicted in Figures

2.6 and 2.6, with reference to the specimen J_01_S. The simple specimen, J_01, indeed, is the same as J_01_S but without the floor deck.

The floor system consists of RC joists with upper slab and infilled hollow clay blocks. The total depth of the deck is $21cm$. The height of the RC slab is $5cm$ and that of the hollow clay blocks is $16cm$. The joist section is a T-beam section, whose upper width is equal to $50cm$, whereas the bottom one is $10cm$. The same longitudinal reinforcement was provided at the top and bottom of the joist section, consisting of $2\phi10$ (Figure 2.6).

The features of the fully designed beams are shown in Figure 2.6. Transverse and longitudinal beams had the same section dimensions. The height and width of the beams were, respectively, $40cm$ and $30cm$. Four longitudinal steel rebars were provided as top and bottom reinforcement. The design moments of resistance were $M_{Rd} = 80.12kNm$, for the transverse beam, and $M_{Rd} = 76.14kNm$, for the longitudinal beams. The resistance values were used for the capacity design of the beams in shear and the capacity design of the columns. The transverse reinforcement of the beam was designed according to the capacity design rule of Section 5.4.2.2 of EC8. The shear forces acting on the beam derive from the equilibrium conditions due to the seismic loads and the formation of the plastic hinges at the ends of the beams or columns framing in the joint. The end moments $M_{i,d}$ (with i=1,2 the end sections of the beam) were evaluated according to the following expression:

$$M_{i,d} = \gamma_{Rd} M_{Rb,i} min\left(1, \frac{\sum M_{Rc}}{\sum M_{Rb}}\right) \tag{2.2.1}$$

where γ_{Rd} is the over-strength coefficient accounting for the steel strain hardening, equal to 1 for DCM; $M_{Rb.i}$ is the design value of the bending resistance at the beam end i; $\sum M_{Rc}$ is the sum of the moment of resistance of the columns framing into the joint and $\sum M_{Rb}$ is the sum of the moment of resistance of the beams framing into the joint (Figure 2.3).

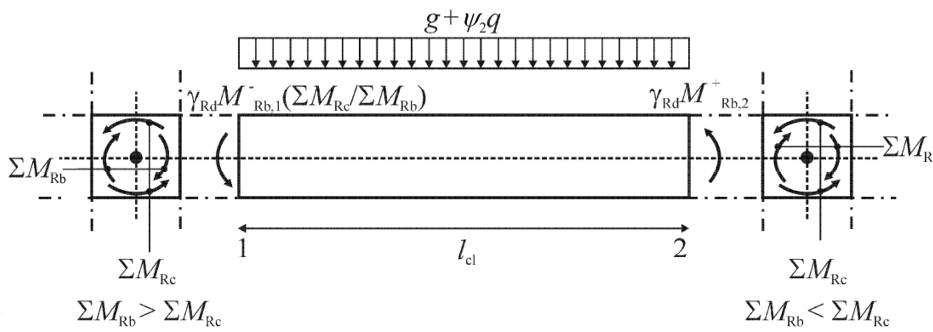

FIGURE 2.3: Shear forces acting on the beams according to the capacity design (Figure 5.1 of EC8).

In addition, the local ductility details for beams in DCM, required in Section

5.4.3.1.2 of EC8, were observed. In particular, the critical region of the beam l_{cr} is equal to the depth of the beam, hence it is $l_{cr} = h_w = 400mm$. Within this length, the diameter adopted for the shear reinforcement is $\phi = 8mm$, which is greater than the minimum admissible of $\phi = 6mm$. The hoops spacing was set equal to $80mm$ according to:

$$s = min\left(\frac{h_w}{4}; 24d_{bw}; 225; 8d_{bL}\right) \tag{2.2.2}$$

where d_{bw} is the diameter of the stirrups and d_{bL} is the minimum diameter of the longitudinal bars. In addition, the first stirrup was placed at $50mm$ from the end section of the beam, as required in Section 5.4.3.1.2 (6)P c) of EC8. Outside of the critical region, $\phi 8$ stirrups with $100mm$ spacing were adopted (Figures 2.6 and 2.6).

The column was designed by imposing the reinforcement area equal to 3% of the concrete cross-sectional area, equal to $30x40cm$. Indeed, Section 5.4.3.2.2(1)P of EC8 [1], concerning the local ductility details for columns in DCM, provides that the total longitudinal reinforcement ratio ρ_l shall be not less than 0.01 and not more than 0.04. Moreover, the same point of the Section provides that, in symmetrical cross-sections, symmetrical reinforcement should be provided ($\rho = \rho'$). In addition, in compliance with the code, intermediate bars were provided between the corner bars, for each side of the column section, in order to ensure the integrity of the beam-to-column joint. In conclusion, $\phi 20$ rebars were adopted as longitudinal reinforcement, as detailed in Figure 2.6. As prescribed in section 4.4.2.3 of EC8 in order to prevent the formation of a soft-storey plastic mechanism in frame buildings, at the joint the following check was satisfied (Figure 2.4):

$$\sum M_{Rc} \geq 1.3 \sum M_{Rb} \tag{2.2.3}$$

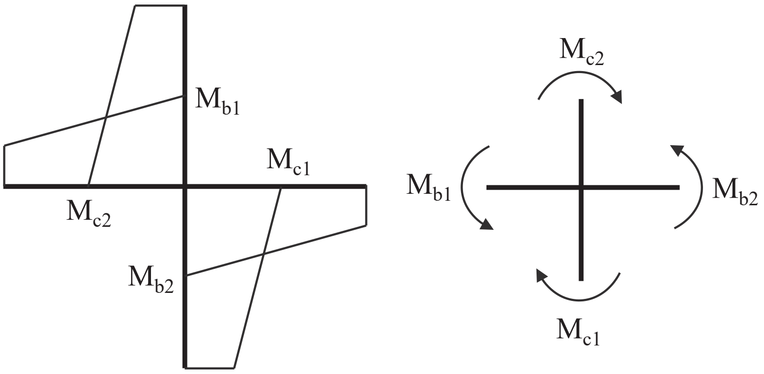

FIGURE 2.4: Equilibrium in the joint between the moments of beams M_b and columns M_c.

The moments of resistance of the columns were evaluated at zero axial loads because the experimental tests were carried out under this more conservative condition. In accordance with 5.4.3.2.1(2) section of EC8, the bi-axial bending in the columns was taken into account in a simplified way, by carrying out the verification in each direction with the uni-axial moment of resistance reduced by 30%. The design bending resistances of the column were 184.10kNm, with respect to the strong-axis, and 140.40kNm, with respect to the weak-axis. As for the beams, also for the columns, the shear forces were determined according to the capacity design provisions (5.4.2.3 EC8). The shear actions on the columns derive from the equilibrium of the column under the moments at its ends $M_{i,d}$, corresponding to the formation of the plastic hinges, according to the Formula 2.2.4:

$$M_{i,d} = \gamma_{Rd} M_{Rc,i} min \left(1, \frac{\sum M_{Rb}}{\sum M_{Rc}} \right) \tag{2.2.4}$$

where the over-strength coefficient γ_{Rd} is 1.1 for DCM.

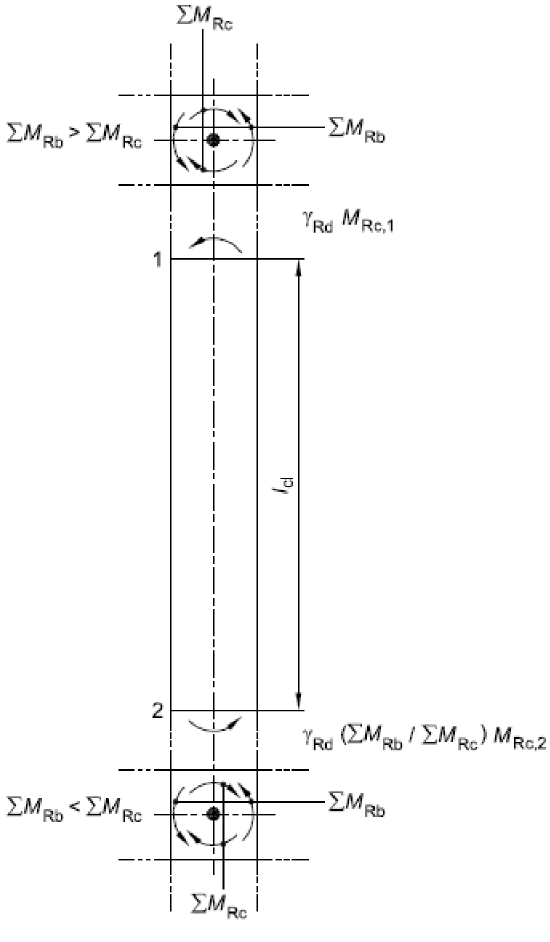

FIGURE 2.5: Shear forces acting on the columns according to the capacity design (Figure 5.2 of EC8)

The critical region of the column was evaluated staring from the column end sections, adjacent to the joint. Its length l_{cr} was evaluated according to the following expression (5.4.3.2.2-EC8):

$$l_{cr} = max \left(h_c; \frac{l_{cl}}{6}; 0.45 \right) \tag{2.2.5}$$

where h_c is the biggest width of the column cross-section and l_{cl} is the column effective length (all the values are in meters). The length of the critical region was $l_{cr} = 0.50m$. The transverse reinforcement in the critical region was designed considering the minimum diameter for hoops and ties of $\phi = 6mm$. In addition, the hoops spacing s (in millimetres) must not exceed the following value:

$$s = min\left(\frac{b_0}{2}; 175; 8d_{bL}\right) \tag{2.2.6}$$

where b_0 is the smallest dimension of the concrete core (to the centre-line of the hoops) and d_{bL} is the smallest diameter of the longitudinal bars. Moreover, the distance between consecutive longitudinal bars engaged by hoops or cross-ties must not exceed $200mm$. Also, the following check was satisfied [43]:

$$A_{st} \geq k\frac{f_{cd}}{f_{yd}}b_{st}s \tag{2.2.7}$$

in which $k = 0.08$ for DCM and $k = 0.12$ for DCH [43], A_{st} is the hoops area, b_{st} is the greatest width of the hoop, evaluated at the inter-axis. By observing the abovementioned provisions, $\phi 8$ stirrups with $7cm$ spacing and a cross-tie in each direction were adopted in the critical region. Outside of the critical region, $\phi 8$ stirrups with $10cm$ spacing were adopted.

Finally, for the joint in DCM class, EC8 does not provide any particular verification, hence the horizontal confinement reinforcement was the same as in the column critical regions.

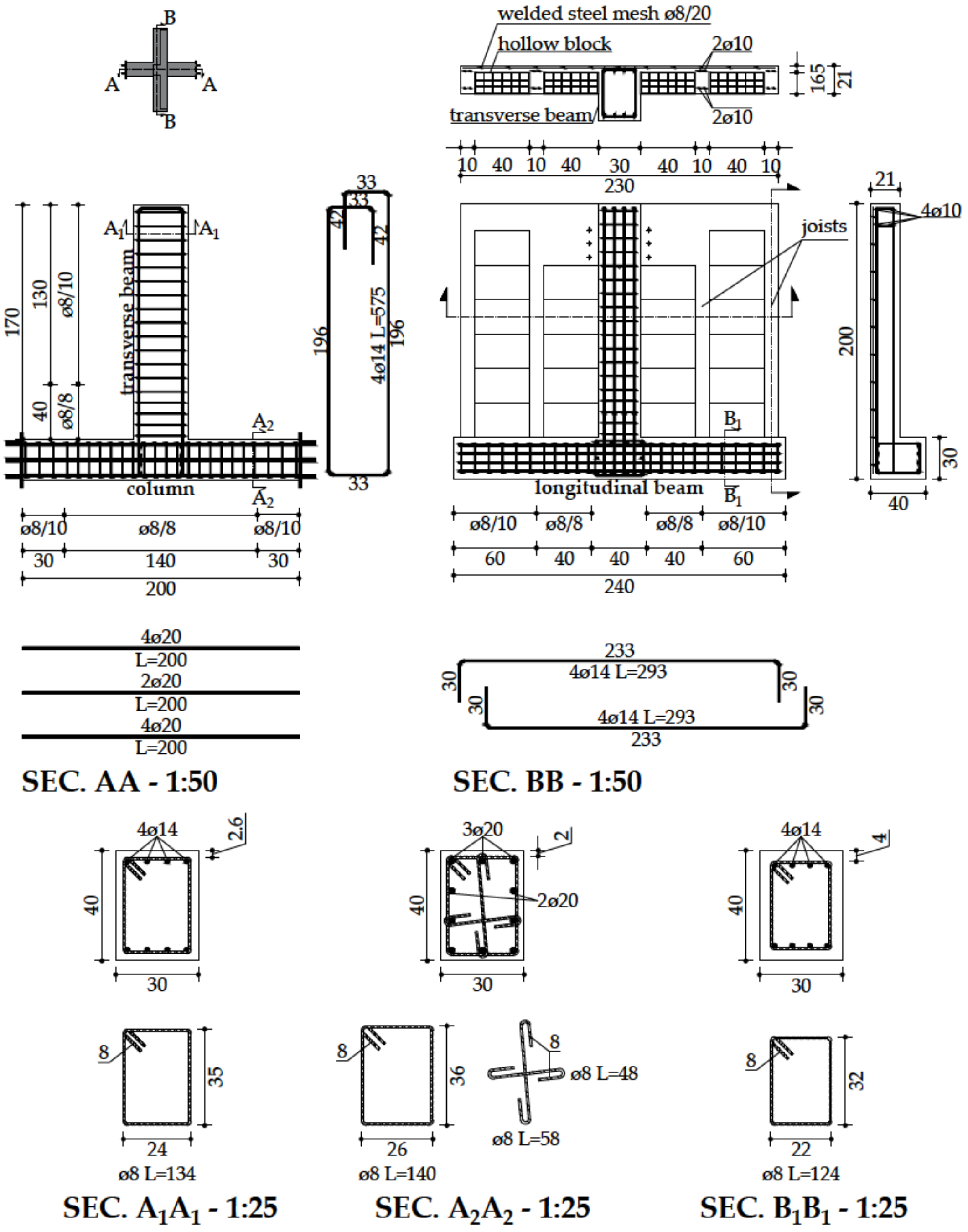

FIGURE 2.6: Technical details of the conventional module with the deck *J_01_S*.

2.2.2 Design of Innovative Specimens

The modules *J_02* and *J_02_S* are called innovative as they present a novelty. By drawing inspiration from the Reduced Beam Section (RBS) design, proper of the steel structures, the novelty consists in a reduction of the bending resistance of the beam, in order to balance the additional resistance that the floor deck may lend to the connection. The aim was pursued by reducing the depth of the beam and the reinforcement in a datum portion of the beam, which started from an arbitrary distance far from the column face and developed for a length equal to the theoretical length of the plastic hinge. A consequential result is the shift of the plastic hinge far from the joint area and toward the middle of the beam span, which would improve the beam fixing, in the perspective of potential retrofitting intervention. Since the over-resistance supplied by the presence of the floor deck is, in this work, attributed to the warping of the RC joists, the RBS detail was provided for the transverse beam only, whose axis is parallel to that of the joists.

In Figure 2.7, the innovative modules are illustrated. The *J_02* module is the simplest one, made up of a single column and three beams framing in the joint. The *J_02_S* module is the same as *J_02* but it is equipped with the deck.

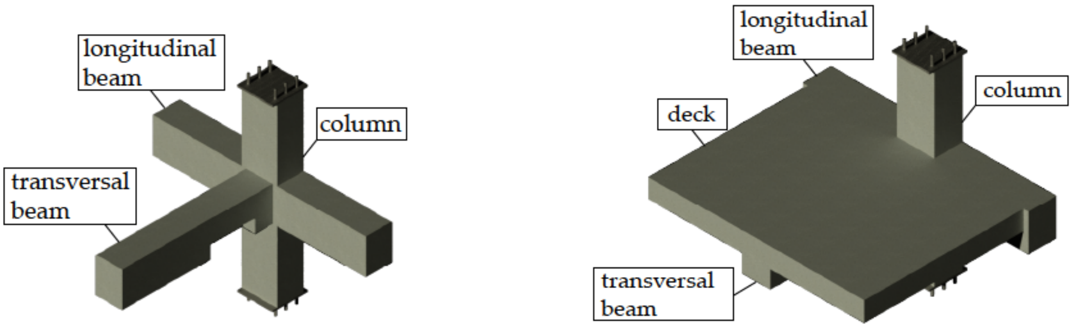

(a) J_02 (b) J_02_S

FIGURE 2.7: Innovative modules without (a) and with the floor deck (b)

The technical details of the designed specimens are shown in Figures 2.8 and 2.9, with reference to only the *J_02_S* specimen. As for conventional specimens, the simple specimen, *J_02*, was made up of the same structural elements as *J_01_S*, but it was not equipped with the floor deck. The main structural elements, i.e. the beams and the column, and the secondary elements, i.e. the cast-in-situ floor deck, had the same features of the conventional specimens, described in Section 2.2.1, with the exception of the localised reduction in the beam depth. Innovative specimens, indeed, were designed, hence tested, with the aim to decrease the bending resistance of the connection, as compared to conventional specimens.

The floor deck, shown in Figure 2.9, was equal to conventional joints, made up of RC joists, upper slab and interlaid hollow clay blocks.

The longitudinal beam and the full-depth transverse beam, depicted in Figures 2.8 and 2.9, had the same characteristics as those in conventional joints.

The only exception was the definition of the new plastic zone, i.e. the reduction of the beam depth. The depth of the RBS was fixed to the minimum allowable value deriving from the gravity-loads combinations, that was $h_{RBS} = 25cm$. The RBS longitudinal reinforcement was equal to $4\phi14$ and $3\phi14$, respectively in the top and bottom part of the section. The relation 2.2.3 previously verified with reference to conventional specimens and establishing a hierarchy criterion between the conventional dissipative zone, i.e. the beam, and the non-dissipative one, i.e. the column, was differently applied in this case. In the design of the innovative specimens, a local hierarchy criterion was applied, The hierarchy was established between the RBS, the new dissipative zone, and the full-depth beam section, the nearest non-dissipative zone, as follows:

$$M_{Rb} \geq 1.3M_{R.RBS} \tag{2.2.8}$$

The design bending resistance of the RBS was equal to $33.61kNm$, in sagging bending, and $-43.66kNm$, in hogging bending. The RBS, i.e. the plastic zone, was localised far from the end of the beam. It started at $20cm$ far from the column face and developed toward the middle span of the beam for a length equal to the theoretical length of the plastic hinge, L_{pl}, evaluated according to Equation 2.2.9 of EC8-Part 3 [44]:

$$L_{pl} = 0.1L_V + 0.17h + 0.24\frac{d_{bl}f_y}{\sqrt{f_c}} \tag{2.2.9}$$

where $L_V = M/V$ is the ratio moment/shear at the end section, h is the depth of the member, d_{bL} is the (mean) diameter of the tension reinforcement, f_y is the yield strength of the bars (MPa) and f_c is the concrete compressive strength (MPa). The length of the plastic hinge was equal to $L_{pl} = 50cm$. The whole extent of the RBS ($50cm$) was considered as a critical region and the local ductility details were set with reference to Section 5.4.3.1.2 of the EC8 [1]. For this reason, $\phi8$ stirrups with $6cm$ spacing were provided in the critical zone, while $\phi8$ stirrups with $10cm$ spacing were provided in the full-depth section of the beam.

The geometrical and mechanical features of the column were the same as in conventional modules. Hence, the column cross-section was $30x40cm$. Although the hierarchy criterion was applied as a local hierarchy criterion, between the RBS and the full-depth beam section, the column was reinforced with the same amount of longitudinal and transverse rebars, provided for conventional modules. The details are depicted in Figure 2.9.

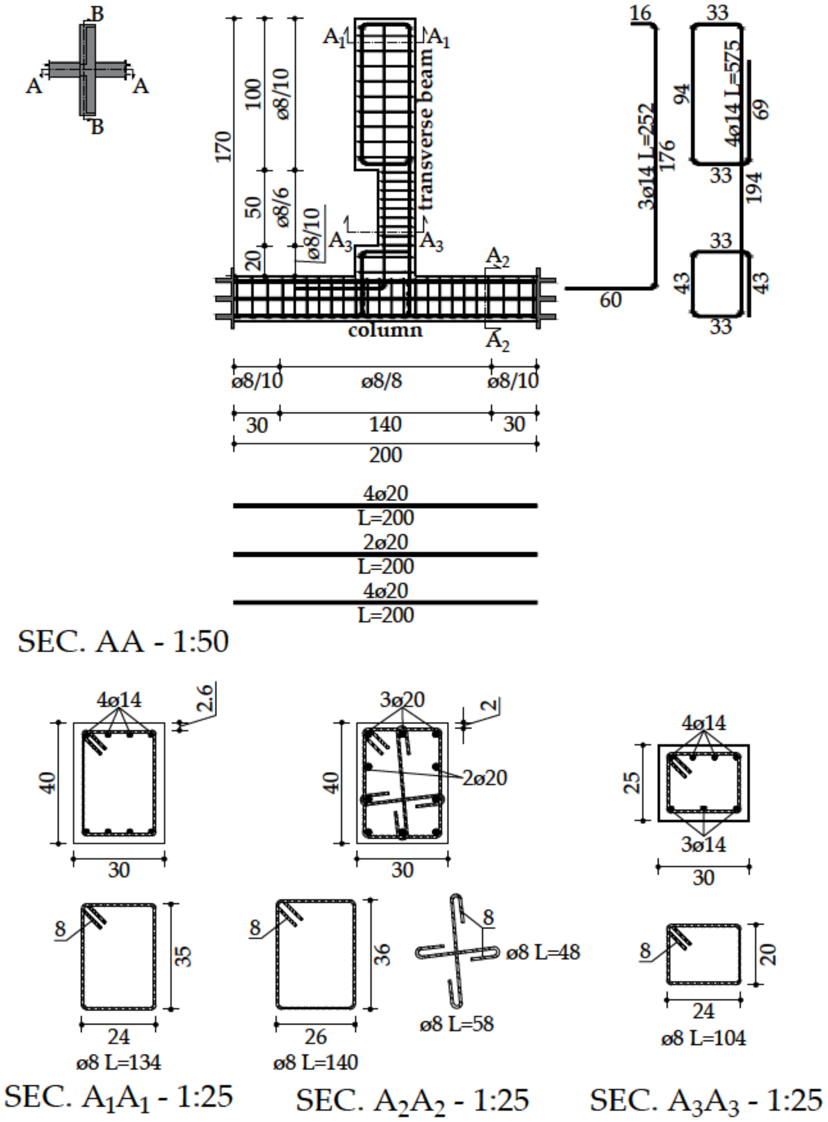

FIGURE 2.8: Technical details of the innovative module with the floor deck *J_02_S*-SEC AA (units:cm).

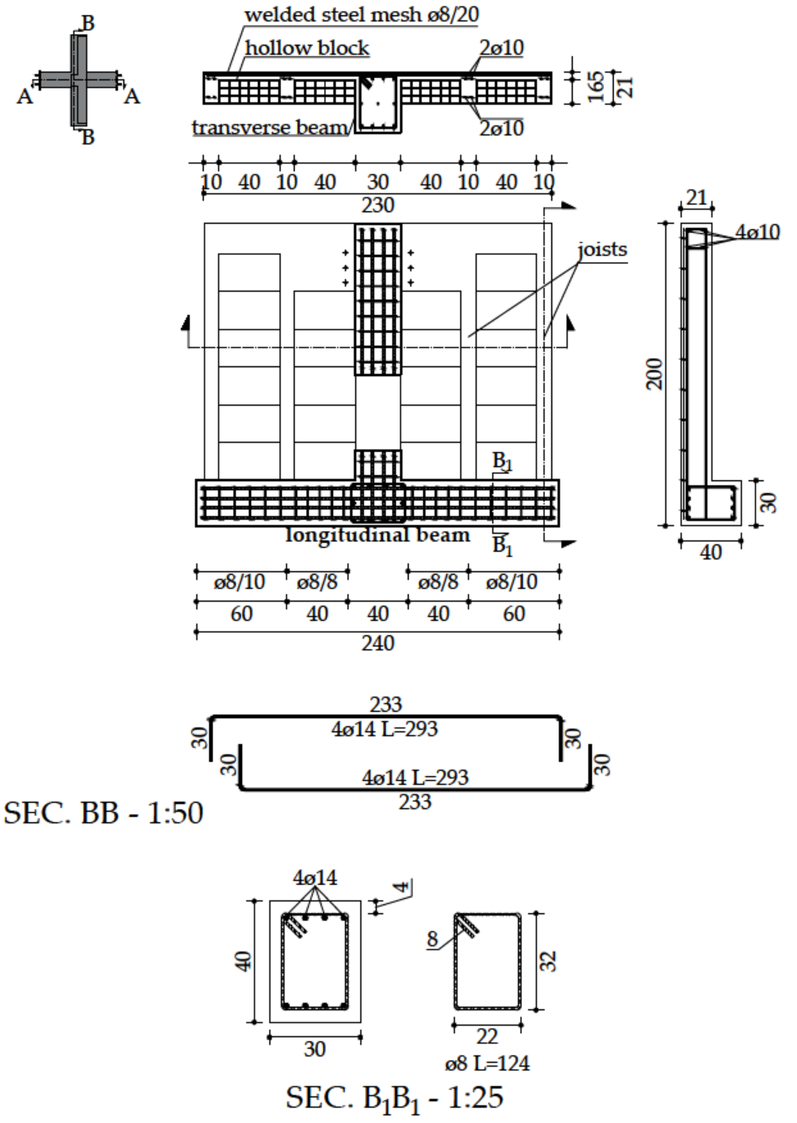

FIGURE 2.9: Technical details of the innovative module with the floor deck *J_02_S*-SEC BB (units:cm).

2.2.3 Evaluation of the Number of Collaborating Joists

The Thesis evolved from previous scientific papers of the same research team, investigating RC buildings equipped with a floor deck composed of the joists, upper slab and interlaid hollow blocks. The papers [40, 41] assumed that a certain number of joists, within the bay span length, act as a so-called "equivalent beam", parallel to them. The "equivalent beam" model, hence, provided a theoretical formula estimating the number of joists collaborating in the "beam behaviour", hence in the lateral response and resistance of the structure. In this work, the original theoretical formula was improved for buildings designed according to the current seismic codes and for the specimens.

2.2.3.1 Equivalent Beam Model for Buildings

2.2.3.1.1 Gravity-load Designed Buildings

The "equivalent beam" model is a theoretical formulation estimating the number of joists collaborating in the lateral response of the structure. In the previous work by Montuori et al. [40], which is the starting point of the experimental investigation herein presented, the "equivalent beam" model was applied to RC buildings very common in the Mediterranean area before the seismic design regulations. The frame structure of these buildings was designed only for gravity loads, hence they were mainly composed of one-way oriented frame, parallel each other, with no transverse beams connecting them. The elements linking the parallel frames were the RC joists composing the common cast-in-situ floor deck, this latter made up of RC joists, upper slab and interlaid hollow blocks. The post-earthquake analyses carried out on such a typology of buildings revealed that these structures were able to withstand moderate seismic events, also in the direction orthogonal to main frames, where no beams were provided. This evidence was attributed to the contribution exploited by the so-called "secondary" elements, i.e. the joists. The "equivalent beam" model assumes that a certain number of joists works together as a proper transverse beam, which is a T-beam resulting from the sum of the single T-section of the involved joists. The number of joists collaborating n_{cj} as a transverse beam, i.e. equivalent beam, is evaluated by means of a theoretical formula which is the result of the following considerations.

In Figure 2.10, a generic carpentry plan of buildings designed to withstand gravity loads is illustrated. As the "equivalent beam" runs parallel to the joists, the transverse frame connecting the internal column has to be considered, whose horizontal structural elements are the joists themselves. Concerning the translational behaviour, no relative horizontal displacements can happen between any two points of the floor deck, as the in-plane stiffness of the diaphragm is assumed to be infinite. Concerning the rotational behaviour, two limit schemes can be identified, shown in Figure 2.11. The first one assumes that the torsional stiffness of the longitudinal beams is negligible, so that the contribution of the floor joists to the rotational stiffness of the joint located at the end of the columns, i.e. at the floor levels, is negligible. Hence, the structural model of Figure 2.11(a) can be applied. The second limit scheme assumes that the torsional stiffness of the longitudinal beams is infinite so that all the joists of the floor have the same flexural rotations at their ends. These rotations are equal to the torsional rotation of the corresponding longitudinal beam. In this second case, all the floor joists contribute to the frame behaviour in the transverse direction, so that the structural model in such direction is the one depicted in Figure 2.11(b). However, the actual behaviour of the structural system in the transverse direction is intermediate between the two limit schemes above described. Therefore, the number of joists involved in the "beam behaviour" for seismic actions in the transverse direction depends on the relation between the torsional stiffness of the longitudinal beams and the flexural stiffness of the joists.

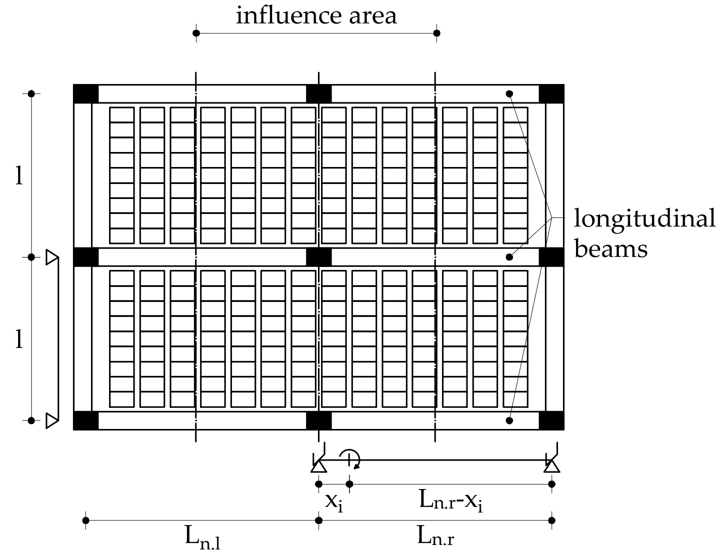

FIGURE 2.10: Carpentry plan of a building designed for gravity loads.

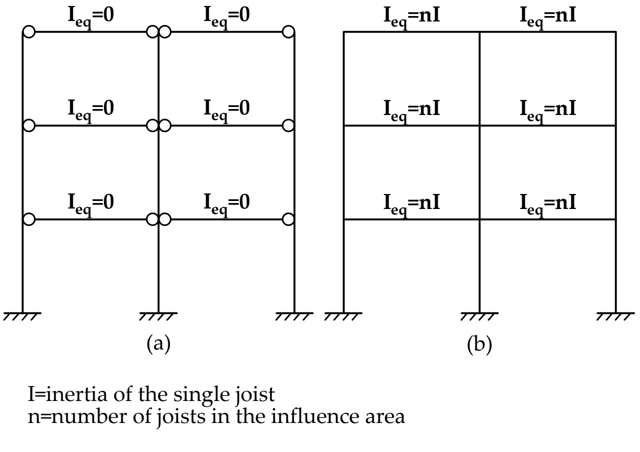

FIGURE 2.11: Limit schemes for the joists contribution to the lateral stiffness of buildings.

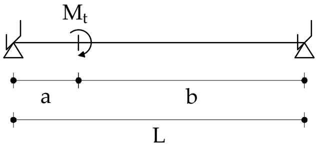

FIGURE 2.12: Structural scheme of the longitudinal beam in the "equivalent beam" model.

With reference to the structural scheme of the longitudinal beam pointed out in Figure 2.10 and better highlighted in Figure 2.12, by neglecting the torsional continuity of the longitudinal beams, the torsional moment is:

$$GJ_t\frac{d\theta}{dx} = M_t(x) \tag{2.2.10}$$

with G and J_t respectively the shear modulus and torsional inertia of the beam. For $0 < x < a$, x takes the name of x_1, so that:

$$GJ_T\frac{d\theta_1}{dx_1} = M_t\frac{b}{L} \implies \frac{d\theta_1}{dx_1} = \frac{M_t}{GJ_T}\frac{b}{L} \tag{2.2.11}$$

By integrating, the torsional rotation is obtained:

$$\theta_1 = \theta_1(x_1) = \frac{M_t}{GJ_T}\frac{b}{L}x_1 + C_1 \tag{2.2.12}$$

By defining the boundary condition:

$$\theta_1 = 0 \quad \text{for} \quad x_1 = 0 \tag{2.2.13}$$

the constant $C_1 = 0$ is obtained, hence the Equation 2.2.12 becomes:

$$\theta_1 = \theta_1(x_1) = \frac{M_t}{GJ_T}\frac{b}{L}x_1 \tag{2.2.14}$$

On the contrary, for $a < x < L$, x takes the name of x_2 and the following relation can be obtained:

$$GJ_T\frac{d\theta_2}{dx_2} = -M_t\frac{a}{L} \implies \frac{d\theta_2}{dx_2} = -\frac{M_t}{GJ_T}\frac{a}{L} \tag{2.2.15}$$

$$\theta_2 = \theta_2(x_2) = -\frac{M_t}{GJ_T}\frac{a}{L}x_2 + C_2 \tag{2.2.16}$$

The definition of the boundary condition:

$$\theta_2 = 0 \quad \text{for} \quad x_2 = b \tag{2.2.17}$$

provides:

$$C_2 = \frac{M_t}{GJ_T}\frac{ab}{L} \tag{2.2.18}$$

so the Equation 2.2.16 becomes:

$$\theta_2 = \theta_2(x_2) = \frac{M_t}{GJ_T}\frac{a}{L}(b - x_2) \tag{2.2.19}$$

In particular, for $x_1 = a$ and $x_2 = 0$ the following relation is obtained:

$$\theta_1(a) = \theta_2(0) = \frac{M_t}{GJ_T}\frac{ab}{L} \tag{2.2.20}$$

By replacing a with x, and b with $L - x$ in Equation 2.2.20, the torsional rotation of the beam at the generic abscissa x, $\theta(x)$, can be expressed as:

$$\theta(x) = \frac{M_t}{GJ_T}\frac{x(L - x)}{L} \tag{2.2.21}$$

Hence, the torsional stiffness of the longitudinal beams at the position of the generic joist, x_i, is given by:

$$k_\phi = \frac{M_t}{\theta} = \frac{GJ_tL_n}{x_i(L_n - x_i)} \quad \text{with} \quad x_i \leq \frac{L_n}{2} \tag{2.2.22}$$

with L_n the bay span length of the longitudinal beam.

FIGURE 2.13: Structural scheme of the joist under seismic actions.

Under the assumption of a bi-triangular bending moment diagram with zero moment at midspan (see Figure 2.13), i.e. under seismic actions, the end rotation of joists is due to the sum of the effects of the torsional deformation of the longitudinal beam and the flexural deformation of the joists, as follows:

$$\theta = \frac{M}{k_\phi} + \frac{Ml}{6EI} = \frac{Ml}{6EI}\left(1 + 6\frac{EI}{lk_\phi}\right) \tag{2.2.23}$$

where M and I are, respectively, the moment at the joist ends and the inertia of the single joist. In addition, l is the span length of joists. Therefore, for each joist, whose position is x_i, an equivalent inertia $I_{eq.i}$ can be defined according to Equation 2.2.24:

$$I_{eq.i} = \frac{I}{\left(1 + 6\frac{EI}{lk_\phi}\right)} \tag{2.2.24}$$

which, by recalling the Equation 2.2.22, results in:

$$I_{eq.i} = \frac{I}{1 + 6\frac{EI/l}{GJ_t/L_n}\frac{x_i}{L_n}\left(1 - \frac{x_i}{L_n}\right)} = \frac{I}{1 + 6\psi\frac{x_i}{Ln}\left(1 - \frac{x_i}{L_n}\right)} \tag{2.2.25}$$

where $\psi = \frac{EI}{l} / \frac{GJ_t}{L_n}$ is the ratio between the flexural stiffness of the single joist and the torsional stiffness of the longitudinal beam. From this relationship, it can be noted that, for $x_i = 0$ the equivalent inertia is $I_{eq.i} = I$, i.e. when the joists are directly connected to the columns, they behave like normal transverse link beams. On the contrary, when the distance of the generic joist, x_i, increases, its contribution to the "beam behaviour" is reduced, being $I_{eq.i}$ less than 1.0. Therefore, the "beam behaviour" due to the orthotropic reinforced concrete slab for seismic actions in the transverse direction can be modelled by means of an "equivalent beam". The "equivalent beam" inertia is the sum of the equivalent inertia of each joist located within the influence area of the equivalent frame as follows:

$$I_{eq} = \sum_{i=1}^{n_r} I_{eq.i} + \sum_{i=1}^{n_l} I_{eq.i} \tag{2.2.26}$$

where n_r and n_l are the number of the joists within the influence area located, respectively, on the right and left side of the "equivalent beam" axis. These values are given by:

$$n_r = \frac{L_{nr}}{2p_j} \qquad n_l = \frac{L_{nl}}{2p_j} \tag{2.2.27}$$

where p_j is the joist spacing, and L_{nr} and L_{nl} are the longitudinal beam spans, respectively on the right side and left side of the "equivalent beam" axis. The position of each joist, x_i, can be also written as $x_i = ip_j$, with i the number of the considered joist, progressively increasing with the distance from the connection. Hence, Equation 2.2.26 becomes:

$$I_{eq} = \sum_{i=1}^{n_r} \frac{I}{1 + 6\psi\frac{x_i}{L_{nr}}\left(1 - \frac{x_i}{L_{nr}}\right)} + \sum_{i=1}^{n_l} \frac{I}{1 + 6\psi\frac{x_i}{L_{nl}}\left(1 - \frac{x_i}{L_{nl}}\right)} \tag{2.2.28}$$

which, in the case of equal bay span on the right and left side of the connection ($L_{nr} = L_{nl} = L_n$ and $n_r = n_l = n$) is:

$$I_{eq} = 2\sum_{i=1}^{n} \frac{I}{1 + 6\psi\frac{x_i}{L_n}\left(1 - \frac{x_i}{L_n}\right)} \tag{2.2.29}$$

The number of the overall joists collaborating to the "beam behaviour", n_{cj}, derives from Equation 2.2.30:

$$n_{cj} = \frac{I_{eq}}{I} \tag{2.2.30}$$

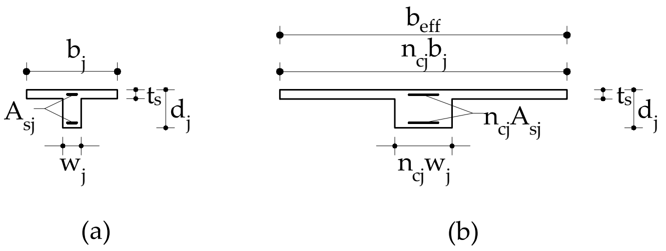

FIGURE 2.14: Joist (a) and internal "equivalent beam" (b) section in buildings designed for gravity loads.

By properly accounting for the general formulation of the joists equivalent inertia in Equation 2.2.28, the number of joists involved in the "beam behaviour" is provided by the following Equation:

$$n_{cj} = \sum_{i=1}^{n_r} \frac{1}{1 + 6\psi \frac{x_i}{L_{nr}}(1 - \frac{x_i}{L_{nr}})} + \sum_{i=1}^{n_l} \frac{1}{1 + 6\psi \frac{x_i}{L_{nl}}(1 - \frac{x_i}{L_{nl}})} \tag{2.2.31}$$

Then, the specific formulation of the joists equivalent inertia in Equation 2.2.29 is accounted for. As a consequence, the number of joists involved in the "beam behaviour", in the case of equal bay span on the right and left side of the connection, is provided by the following Equation:

$$n_{cj} = 2\sum_{i=1}^{n} \frac{1}{1 + 6\psi \frac{x_i}{L_n}(1 - \frac{x_i}{L_n})} \tag{2.2.32}$$

The resulting Equations 2.2.31 and 2.2.32 show that the number of joists involved depends on the ratio between the flexural stiffness of the joists and the torsional stiffness of the longitudinal beams, ψ, and the number of joists n_r and n_l, hence n, located within the influence area of the equivalent beam. Obviously, in the theoretical case of longitudinal beams having infinite torsional stiffness, i.e. when $\psi \to 0$, all the joists located within the influence area of the transversal frame contribute to the "beam behaviour", hence:

$$n_{cj} = n_{tot} = n_l + n_r \tag{2.2.33}$$

Conversely, in the theoretical case of longitudinal beams having no torsional stiffness, i.e. when $\psi \to \infty$, the number of collaborating joists is zero.

The number of collaborating joists, n_{cj} defines the geometrical and mechanical features of the "equivalent beam", as pointed out in Figure 2.14, where the section of the joist (Figure 2.14a) and resulting "equivalent beam" (Figure 2.14b) are depicted.

2.2.3.1.2 Seismic-load Designed Buildings

The "equivalent beam" model, in this work, is applied to buildings of modern conception, designed according to the current seismic European codes. Such buildings are made up of RC 3D spatial frames hence, beams are located in both longitudinal and transverse direction, as pointed out in the conventional carpentry plan of Figure 2.15.

In this case, the number of collaborating joists are always computed by means of Equation 2.2.31, or Equation 2.2.32 if the length of the bay span is equal on both sides of the connection. However, the formula evaluating the number of the joists within the influence area of the connection has to account for the presence of the transverse beam, and its actual dimensions. With reference to Figure 2.15, Equation 2.2.27 is modified in:

$$n_r = \frac{L_{nr} - (w_{tb} + w_{tb.r})/2}{2p_j} \quad \text{and} \quad n_l = \frac{L_{nl} - (w_{tb} + w_{tb.l})/2}{2p_j} \tag{2.2.34}$$

where w_{tb}, $w_{tb.r}$ and $w_{tb.l}$ are, respectively, the width of the transverse beam of the examining connection, and the width of the beam on the right and left side of the connection.

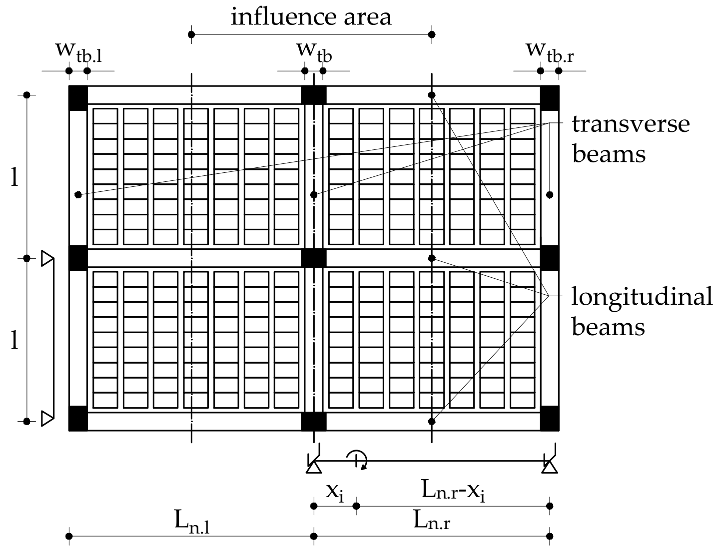

FIGURE 2.15: Carpentry plan of a generic building with 3D spatial frames

In this case, the number of collaborating joists, n_{cj}, and the transverse beam define the geometrical and mechanical features of the "equivalent beam". In Figure 2.16, the section of the joist (Figure 2.16a), transverse beam (Figure 2.16b) and resulting "equivalent beam" (Figure 2.16c) are depicted.

The number of collaborating joists for the study case has been computed by means of the relationships described above, with reference to the carpentry plan of the designed building shown in Figure 2.17.

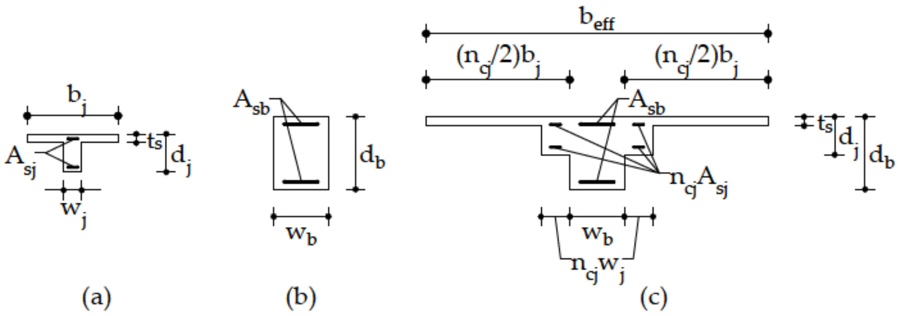

FIGURE 2.16: Joist (a), beam (b), and internal "equivalent beam" (c) section in buildings designed for seismic actions.

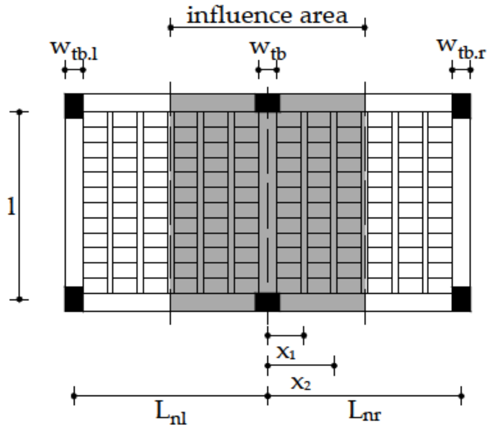

FIGURE 2.17: Carpentry plan of the designed building

Given the features of the elements designed in Section 2.2.1 the number of collaborating joists is equal to $n_{cj} = I_{eq}/I = 3.36$.

2.2.3.2 Equivalent Beam Model for Experimental Tests

The relationships reported in Section 2.2.3.1 were derived by assuming specific static schemes for the longitudinal beam and the joist. The longitudinal beam was considered as a simply supported beam with torsional constrained ends. The joist was considered as a simply supported beam with applied flexural moments at the ends. Equally, it can be considered as an embedded beam whose ends are subjected to rotations.

The formula computing the number of joists involved in the "beam behaviour" was modified according to the new static scheme of the longitudinal beam. Considering the experimental conditions, due to the test layout, the static scheme of the longitudinal beam is a cantilever beam, as depicted in Figure 2.18.

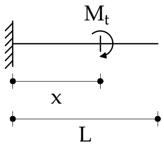

FIGURE 2.18: Structural scheme of the longitudinal beam in the "equivalent beam" model, accounting for the experimental layout.

The torsional rotation θ of the longitudinal beam is obtained integrating the following equation:

$$\frac{d\theta}{dx} = \frac{M_t}{GJ_t} \tag{2.2.35}$$

which results in:

$$\theta = \frac{M_t}{GJ_t}x + C_1 \tag{2.2.36}$$

By imposing the boundary condition:

$$\theta(0) = 0 \implies C_1 = 0 \tag{2.2.37}$$

the torsional rotation, θ, is:

$$\theta = \frac{M_t}{GJ_t}x \tag{2.2.38}$$

By replacing the so-determined torsional rotation of longitudinal beam in Equation 2.2.23, the total rotation becomes:

$$\theta = \frac{Ml}{6EI}\left(1 + 6\psi\frac{x_i}{L_n}\right) \tag{2.2.39}$$

where, as usual, x_i is the generic position of the considered joist and $\psi = \frac{EI}{l} / \frac{GJ_t}{L_n}$. Therefore, the equivalent inertia of the single joist is equal to:

$$I_{eq.i} = \frac{I}{(1 + 6\psi\frac{x_i}{L_n})} \tag{2.2.40}$$

The equivalent inertia of the joists collaborating to the "beam behaviour" is:

$$I_{eq} = \sum_{i=1}^{n_r} \frac{I}{(1 + 6\psi\frac{x_i}{L_{nr}})} + \sum_{i=1}^{n_l} \frac{I}{(1 + 6\psi\frac{x_i}{L_{nl}})} \tag{2.2.41}$$

which, in the case of an equal bay span on the right and left side of the connection, i.e. $L_{nr} = L_{nl} = L_n$ (and $n_r = n_l = n$), becomes:

$$I_{eq} = 2\sum_{i=1}^{n} \frac{I}{(1 + 6\psi\frac{x_i}{L_n})} \tag{2.2.42}$$

being n_r and n_l computed according to Equation 2.2.34.

The number of collaborating joists involved in the "beam behaviour" is $n_{cj} = I_{eq}/I$, with I the inertia of the single joist. Its general formulation is specified in Equation 2.2.43:

$$n_{cj} = \sum_{i=1}^{n_r} \frac{1}{(1 + 6\psi \frac{x_i}{L_{nr}})} + \sum_{i=1}^{n_l} \frac{1}{(1 + 6\psi \frac{x_i}{L_{nl}})} \tag{2.2.43}$$

which in the specific case of equal bay span on the right and left side of the connection becomes:

$$n_{cj} = 2 \sum_{i=1}^{n} \frac{1}{(1 + 6\psi \frac{x_i}{L_n})} \tag{2.2.44}$$

As one might expect, the number of collaborating joists evaluated with reference to the experimental test layout does not significantly change. Indeed, the number of joists collaborating in the "beam behaviour" results $n_{cj} = 3.16$. As a consequence, the experimental modules were realised with 4 collaborating joists, 2 on each side of the connection.

2.3 Realization of Experimental Specimens

All the categories of modules, conventional and innovative, as well as the subcategories, without ($J\_01 - J\_02$) and with the floor deck ($J\_01\_S - J\_02\_S$), were made up of the same structural elements, except for the deck. Therefore, the building construction system was essentially the same for all the modules, with some slight differences underlined in the following between conventional and innovative specimens.

The 3D modules in Figures 2.19 and 2.20, built in AutoCAD software, give the spatial idea of what the Sarno Prefabbricati s.r.l. company has realised for all the modules.

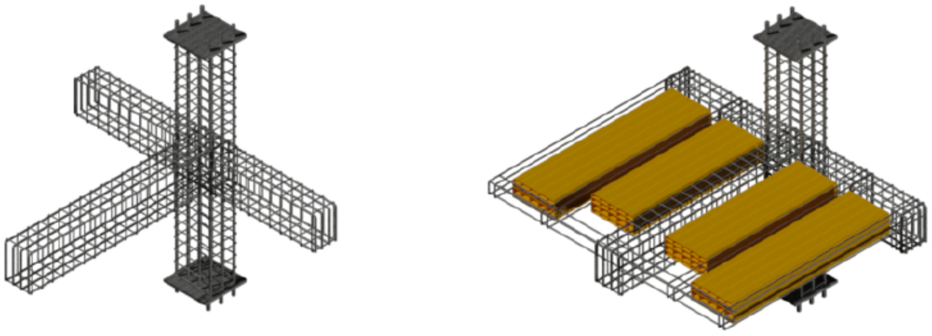

(a) (b)

FIGURE 2.19: 3D reinforcement of the J_01 (a) and J_01_S module (b).

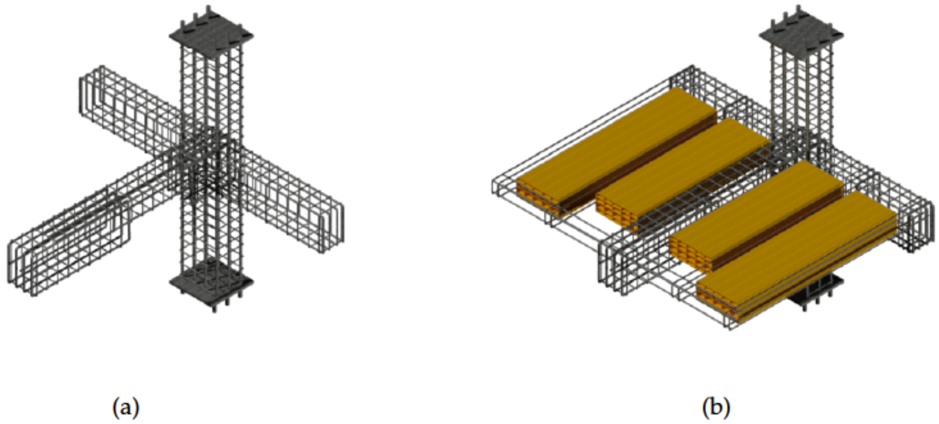
(a) (b)

FIGURE 2.20: 3D reinforcement of the *J*_02 (a) and *J*_02_*S* module (b).

With the help of the contractor committed to realising the modules, also the form-work was designed. In order to assure its reuse and versatility, the form-work is composed of several steel components, which are connected by means of bolts or spot welding. In Figure 2.21 the steps to assemble the form-work are shown in sequence. Firstly, the part housing the longitudinal beams and the column was set up on a horizontal workbench (Figure 2.21a), then it was rotated (Figure 2.21b), in order to place the floor deck on the horizontal workbench (Figure 2.21c), where the spaces for the transverse beam and the deck were created (Figure 2.21d).

The reinforcement of the modules was assembled separately constituting a unique block and then it was placed in the form-work. The reinforcement assembly was a quite complex operation as the longitudinal rebars of the transverse beam were bend again at the ends in order to avoid the slippage during the test. Clearly, this choice influenced the sequence by which the entire reinforcement had to be built, as the single elements had to perfectly intersect each other. Firstly, the rebars of the transverse beam were intersected with those of the joint area, i.e. the longitudinal bars and the stirrups of the column, as shown in Figure 2.22 with reference to a *J*_02 specimen. In the innovative modules, where the reinforcement was not constant along the beam axis because of the localised reduction of the transverse beam section, also the bottom reinforcement of the RBS is inserted before setting up the joint region. After, the stirrups of the transverse beam and those of the column were later put on the related reinforcement.

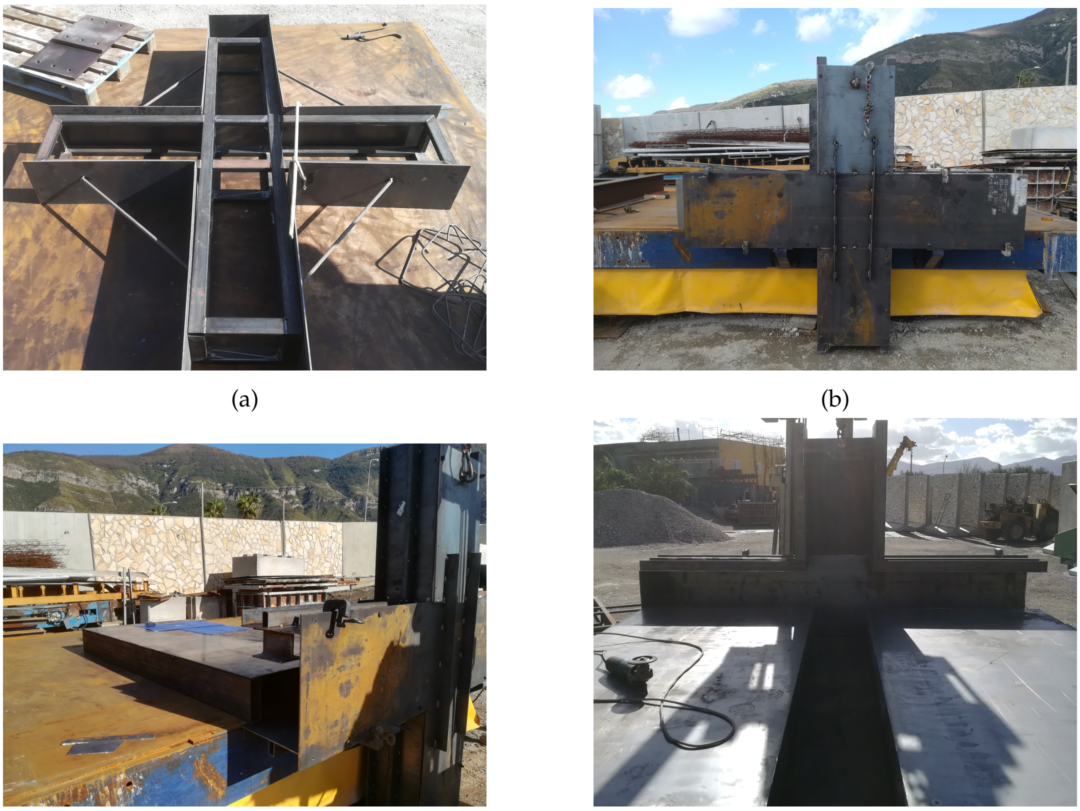

(a) (b)

(c) (d)

FIGURE 2.21: Form-work assembly.

(a) (b)

FIGURE 2.22: Reinforcement of the transverse beam (a) and joint region (b) of an innovative module.

Once connected the transverse beam and column reinforcement (Figure 2.23), then the longitudinal beam rebars were added, passing through the joint area, and, finally, the hoops were assembled. In Figure 2.24 it is possible to notice the reinforcement of the joists, which warps the beam reinforcement.

FIGURE 2.23: Transverse beam and column assembly in a conventional module.

FIGURE 2.24: Joist reinforcement warping the longitudinal beam rebars.

After, the reinforcement of the module was assembled. It was settled in the form-work and the end plates, devoted to connecting the specimen to the constraints of the test machine, were welded to the longitudinal rebars of the column. In order to realise the RBS of innovative specimens, during the concrete casting, a styrofoam was placed at the bottom of the transverse beam form-work, as depicted in Figure 2.25.

FIGURE 2.25: Realization of RBS in innovative modules.

Figure 2.26 depicts the whole reinforcement of a specimen with the floor deck settled in the form-work and before the concrete casting. It is worth to notice that around the free end of the transverse beam six holes were obtained, by means of $\phi30$ pipes, aimed at fixing the actuator plate.

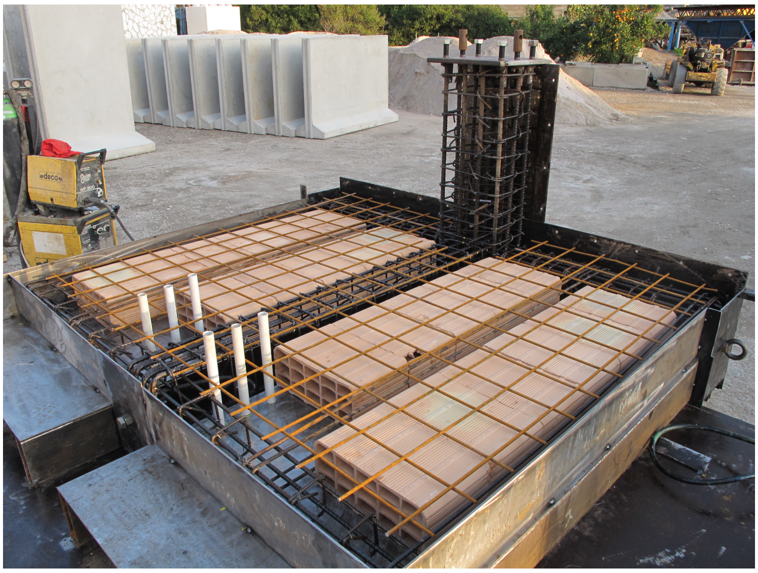

FIGURE 2.26: Reinforcement of the J_01_S module in the form-work.

The form-work was realised in order to assure optimal conditions for the concrete casting operations. For this reason, the casting was exploited in two steps. Firstly, the column was arranged vertically, with the floor deck lying horizontally on the workbench (Figures 2.27a and 2.28a). In this phase, the casting concerned the bottom part of the column, including the joint region, the transverse beam and floor deck. Secondly, the specimen was rotated, with the column settled on a horizontal plane (Figures 2.27b and 2.28b) and the remaining part of the column was cast.

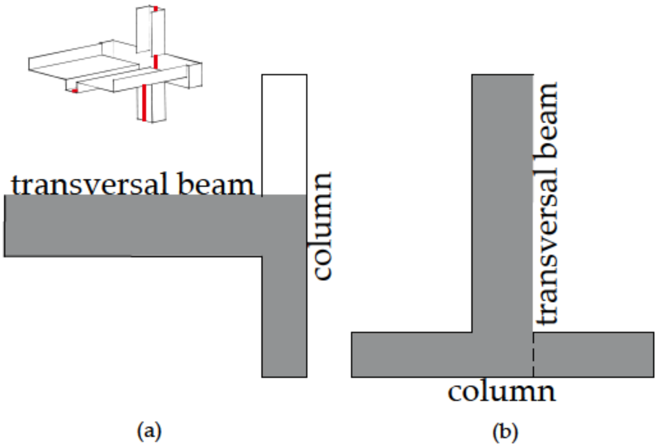

FIGURE 2.27: Planned concrete casting steps.


(a) (b)

FIGURE 2.28: Concrete casting steps.

Chapter 3

Experimental Campaign

3.1 Introduction

The chapter describes the experimental campaign carried out on the beam-to-column modules and the materials composing them. All the tests were performed at the STRuctural ENGineering Test Hall (STRENGTH) Laboratory, at the University of Salerno. Firstly, the tests performed on the materials constituting the specimens are reported, as they serve the purpose of the materials qualification. In particular, the materials tests consisted of crushing tests on concrete cubes and tensile tests on steel rebars, which have been taken as samples from the building site. Moreover, the test set up, the sensors arrangement and the loading protocol are described with reference to the beam-to-column joints. Twelve modules have been tested in whole, six of them belonging to the so-called conventional category and the other six to the so-called innovative category.

Table 3.1 summarises the name of the investigated joints. Also, it reveals in advance the type of the test protocol since the name of the modules derives from the combination of two different elements: the specimens typology and the applied loading protocol. The labels identifying the specimens are those previously defined for conventional and innovative modules without the floor deck, i.e. J_01 and J_02, and for conventional and innovative modules with the floor deck J_01_S and J_02_S. In addition, the loading protocol has been indicated with "C", for cyclic protocols, and "M^{+}" and "M^{-}" for, respectively, positive and negative monotonic loading protocols.

For the sake of clarity, in the next explanation and discussion of the results, the tests are sorted by specimen and applied loading typology, as they are hereinafter reported, rather than by the chronological order of execution.

	Module name
1	J_01-C
2	J_01-M^{+}
3	J_01_S-Geolite-C
4	J_01_S-C
5	J_01_S-M^{+}
6	J_01_S-M^{-}
7	J_02-C
8	J_02-M^{+}
9	J_02-M^{-}
10	J_02_S-C
11	J_02_S-M^{+}
12	J_02_S-M^{-}

TABLE 3.1: Performed tests.

3.2 Material Tests

The reinforced concrete is a composite material made up of concrete and steel. In the design stage, the classes chosen for concrete and steel were, respectively, C25/30 and B450C. The end-plates equipping the column ends were made up of steel of S355 grade, but they were not subjected to test as they do not influence the response of the specimens.

According to the design properties provided by EN1992-1-1 [42], the concrete characteristic compressive strength at 28 days is $R_{ck} = 30N/mm^2$, if cubes are used for testing and $f_{ck} = 25N/mm^2$, if cylinders are used for testing. The characteristic yield strength of the steel rebars is $f_{yk} = 450N/mm^2$. The tests on materials provided values of the above-mentioned quantities greater than the nominal ones. In the next Paragraphs, the protocols and results of the tests for both concrete and steel materials are reported and detailed.

3.2.1 Concrete Tests

Tests on concrete consisted of crushing tests on hardened concrete, to obtain the compressive strength value of the specimens, according to the reference regulation UNI EN 12390-3:2009 [45]. The specimens are loaded to failure in compression through a testing machine compliant with EN 12390-4 [46]. The maximum load the specimen is able to withstand is recorded and the compressive strength of concrete is evaluated.

Before running the test, the weight and the exact dimensions of the specimens are measured. The specimens were 15x15x15cm cubic samples. Then, the cube was placed between the supports of the SCHENCK/RBS 4000 E2 machine (with 4000 kN payload and ±100 mm stroke), that is a precision servo-hydraulic press. There, the specimen was subjected to pressure on the face orthogonal to the casting direction. The test ended once the force decreased by 30% as compared to the peak load achieved and the failure of the specimen was compliant with the code [45], thus stating the accuracy of the test.


(a) (b)

FIGURE 3.1: Specimen before (a) and after (b) the compressive strength test.

Concrete samples were collected during each casting in order to obtain the average value of the concrete compressive strength for each beam-to-column joint. During each casting, minimum 2 and maximum 5 specimens were collected. Hence, for each beam-to-column joint, from 5 to 10 total samples were taken. With reference to each beam-to-column joint listed in Table 3.1, the results of the crushing tests are reported, in Tables 3.2 to 3.13. The Tables point out the features of each cubic sample, i.e. the dimensions (L_x,L_y,L_z), weight, compressive cubic strength R_c. Additionally, the average value of the compressive cubic $R_{c.av.}$ and cylinder strength $f_{c.av.}$ are reported.

Specimen [-]	**L$_x$** [mm]	**L$_y$** [mm]	**L$_z$** [mm]	**Weight** [kg]	**R$_c$** [MPa]
1	150.00	153.00	150.00	7.61	35.09
2	150.00	151.00	150.00	7.86	39.40
3	150.00	151.00	150.00	7.76	37.62
4	150.00	154.00	150.00	7.96	37.73
5	150.00	151.00	150.00	8.01	41.45
6	150.00	151.00	150.00	7.82	34.46
7	150.00	151.00	149.50	7.78	34.22
8	149.00	150.00	149.00	7.82	36.25
9	150.00	148.00	150.00	7.80	34.48
10	149.50	149.00	149.00	7.81	34.93
			R$_{c.av.}$	[MPa]	36.56
			f$_{c.av.}$	[MPa]	30.35

TABLE 3.2: Results of concrete crushing tests for $J\_01 - C$ specimen.

Specimen	**L**$_x$	**L**$_y$	**L**$_z$	**Weight**	**R**$_c$
[-]	[mm]	[mm]	[mm]	[kg]	[MPa]
1	150	152	150	7.81	32.63
2	150	152	150	7.89	34.73
3	150	152	150	7.76	33.56
4	150	152	150	7.72	35.58
5	150	152	150	7.90	35.44
6	150	152	150	7.79	33.99
7	150	152	150	7.70	32.85
			R$_{c.av.}$	[MPa]	34.11
			f$_{c.av.}$	[MPa]	28.31

TABLE 3.3: Results of concrete crushing tests for $J\_01 - M^+$ specimen.

Specimen	**L**$_x$	**L**$_y$	**L**$_z$	**Weight**	**R**$_c$
[-]	[mm]	[mm]	[mm]	[kg]	[MPa]
1	150	150	149	7.90	32.94
2	150	151	150	8.03	32.88
3	150	153	150	8.22	33.17
4	150	151	150	7.89	33.43
5	151	152	150	7.87	32.14
6	151	151	151	7.98	40.11
7	150	152	150	8.00	41.52
8	150	151	150	7.86	40.48
9	151	152	150	7.88	38.19
10	150	150	150	7.75	40.49
			R$_{c.av.}$	[MPa]	36.53
			f$_{c.av.}$	[MPa]	30.32

TABLE 3.4: Results of concrete crushing tests for $J\_01\_S - Geolite - C$ specimen.

Specimen	**L**$_x$	**L**$_y$	**L**$_z$	**Weight**	**R**$_c$
[-]	[mm]	[mm]	[mm]	[kg]	[MPa]
1	151	151	151	7.98	40.11
2	151	156	151	8.14	43.45
3	150	149	150	7.90	47.29
4	150	152	150	7.89	46.18
5	151	153	150	7.91	45.10
6	151	153	150	8.70	43.79
7	150	152	150	7.99	41.52
8	150	151	150	7.85	40.48
9	151	152	150	7.88	38.19
10	150	150	150	7.75	40.49
			R$_{c.av.}$	[MPa]	42.66
			f$_{c.av.}$	[MPa]	35.41

TABLE 3.5: Results of concrete crushing tests for $J\_01\_S - C$ specimen.

Specimen	**L**$_x$	**L**$_y$	**L**$_z$	**Weight**	**R**$_c$
[-]	[mm]	[mm]	[mm]	[kg]	[MPa]
1	150	152	150	7.80	32.43
2	151	152	150	7.82	34.58
3	150	153	150	7.84	34.48
4	152	151	150	7.77	33.18
5	150	150	150	7.77	36.73
			R$_{c.av.}$	[MPa]	34.28
			f$_{c.av.}$	[MPa]	28.45

TABLE 3.6: Results of concrete crushing tests for $J\_01\_S - M^+$ specimen.

Specimen	**L**$_x$	**L**$_y$	**L**$_z$	**Weight**	**R**$_c$
[-]	[mm]	[mm]	[mm]	[kg]	[MPa]
1	150	152	150	7.81	32.63
2	150	152	150	7.89	34.73
3	150	152	150	7.76	33.56
4	150	152	150	7.72	35.58
5	150	152	150	7.90	35.44
6	150	152	150	7.79	33.99
7	150	152	150	7.70	32.85
			R$_{c.av.}$	[MPa]	34.11
			f$_{c.av.}$	[MPa]	28.31

TABLE 3.7: Results of concrete crushing tests for $J\_01\_S - M^-$ specimen.

Specimen	**L**$_x$	**L**$_y$	**L**$_z$	**Weight**	**R**$_c$
[-]	[mm]	[mm]	[mm]	[kg]	[MPa]
1	150	151	150	7.398	26.99
2	150	154	150	7.509	30.08
3	150	153	153	7.635	29.55
4	150	153	150	7.548	30.31
5	150	152	150	7.503	31.15
			R$_{c.av.}$	[MPa]	29.62
			f$_{c.av.}$	[MPa]	24.58

TABLE 3.8: Results of concrete crushing tests for $J\_02 - C$ specimen.

Specimen	**L**$_x$	**L**$_y$	**L**$_z$	**Weight**	**R**$_c$
[-]	[mm]	[mm]	[mm]	[kg]	[MPa]
1	150	150	149	7.70	33.72
2	150	152	150	7.75	33.64
3	150	150	149	7.92	38.08
4	150	153	150	7.80	38.78
5	150	152	150	7.79	38.18
			R$_{c.av.}$	[MPa]	36.48
			f$_{c.av.}$	[MPa]	30.28

TABLE 3.9: Results of concrete crushing tests for $J\_02 - M^{+}$ specimen.

Specimen	**L**$_x$	**L**$_y$	**L**$_z$	**Weight**	**R**$_c$
[-]	[mm]	[mm]	[mm]	[kg]	[MPa]
1	150	151	149	7.72	25.35
2	150	151	149	7.58	22.29
3	150	150	149	7.75	25.12
4	150	150	150	7.72	26.81
5	151	150	150	7.78	26.10
6	152	151	151	7.83	24.19
			R$_{c.av.}$	[MPa]	24.98
			f$_{c.av.}$	[MPa]	20.73

TABLE 3.10: Results of concrete crushing tests for $J\_02 - M^{-}$ specimen.

Specimen	**L$_x$**	**L$_y$**	**L$_z$**	**Weight**	**R$_c$**
[-]	[mm]	[mm]	[mm]	[kg]	[MPa]
1	150	151	150	7.40	26.99
2	150	154	150	7.51	30.08
3	150	153	153	7.64	29.55
4	150	153	150	7.55	30.31
5	150	152	150	7.50	31.15
			R$_{c.av.}$	[MPa]	29.62
			f$_{c.av.}$	[MPa]	24.58

TABLE 3.11: Results of concrete crushing tests for $J\_02\_S - C$ specimen.

Specimen	**L$_x$**	**L$_y$**	**L$_z$**	**Weight**	**R$_c$**
[-]	[mm]	[mm]	[mm]	[kg]	[MPa]
1	150	150	149	7.70	33.72
2	150	152	150	7.75	33.64
3	150	150	149	7.92	38.08
4	150	153	150	7.80	38.78
5	150	152	150	7.79	38.18
			R$_{c.av.}$	[MPa]	36.48
			f$_{c.av.}$	[MPa]	30.28

TABLE 3.12: Results of concrete crushing tests for $J\_02\_S - M^{+}$ specimen.

Specimen	**L$_x$**	**L$_y$**	**L$_z$**	**Weight**	**R$_c$**
[-]	[mm]	[mm]	[mm]	[kg]	[MPa]
1	150	151	149	7.72	25.35
2	150	151	149	7.58	22.29
3	150	150	149	7.75	25.12
4	150	150	150	7.72	26.81
5	151	150	150	7.78	26.10
6	150	152	150	7.83	24.19
			R$_{c.av.}$	[MPa]	24.98
			f$_{c.av.}$	[MPa]	20.73

TABLE 3.13: Results of concrete crushing tests for $J\_02\_S - M^{-}$ specimen.

3.2.2 Steel Tests

The mechanical characterization of the steel was carried out by performing a tensile test in accordance with the codes [47, 48], through a 630 kN SCHENCK servo-hydraulic press. Steel samples of the longitudinal and shear reinforcement (Figure3.2) of the elements composing the beam-to-column joints were examined. The tests were carried out under displacement control until the bar failure and no extensometers were used. In Figure 3.3, it is possible to observe a bar before and after the test.

The following Tables 3.14, 3.15 and 3.16 show the results of the tests carried out on the steel reinforcement, in terms of nominal diameter d_0, nominal area A, yield strength f_y, and ultimate tensile strength f_t.

FIGURE 3.2: Samples of the steel reinforcement.

(a) (b)

FIGURE 3.3: Steel rebars before (a) and after (b) the tensile test.

Number [-]	d_0 [mm]	**A** [mm^2]	f_y [MPa]	f_t [MPa]
1	8	50.27	555.34	661.55
2	8	50.27	555.25	660.40
3	8	50.27	552.66	658.73
f_{av} [MPa]			554.42	660.23
1	10	78.54	452.99	555.14
2	10	78.54	446.19	552.91
3	10	78.54	415.79	522.54
4	10	78.54	423.16	528.29
5	10	78.54	453.81	555.79
6	10	78.54	450.73	554.05
f_{av} [MPa]			439.79	542.91
1	12	113.10	451.84	559.53
2	12	113.10	450.29	554.79
3	12	113.10	477.74	584.69
f_{av} [MPa]			471.11	578.96
1	14	153.94	480.47	496.90
2	14	153.94	488.81	603.81
3	14	153.94	499.30	611.29
4	14	153.94	487.13	602.64
5	14	153.94	489.32	601.24
6	14	153.94	480.69	591.64
f_{av} [MPa]			487.62	585.78
1	20	314.16	479.06	604.85
2	20	314.16	505.21	621.89
3	20	314.16	487.29	613.89
f_{av} [MPa]			490.52	613.54

TABLE 3.14: Results of the tensile test on rebars from $J\_01 - C$, $J\_01 - M^+$, $J\_01\_S - Geolite - C$, $J\_01\_S - C$ specimens.

Number [-]	d_0 [mm]	**A** [mm^2]	f_y [MPa]	f_t [MPa]
1	8	50.27	540.38	635.46
2	8	50.27	534.00	634.73
3	8	50.27	519.22	626.69
4	8	50.27	527.19	631.80
5	8	50.27	530.71	633.17
6	8	50.27	528.86	627.34
f_{av} [MPa]			530.06	631.53
1	10	78.54	542.26	641.19
2	10	78.54	556.13	650.58
3	10	78.54	545.02	640.68
4	10	78.54	548.87	649.44
5	10	78.54	538.21	633.61
6	10	78.54	553.79	652.31
7	10	78.54	544.35	640.16
8	10	78.54	539.52	634.61
f_{av} [MPa]			546.02	642.82
1	14	153.94	540.57	629.43
2	14	153.94	538.29	631.52
3	14	153.94	542.27	634.57
4	14	153.94	546.82	636.22
5	14	153.94	542.22	635.43
6	14	153.94	542.24	633.12
7	14	153.94	542.78	634.95
8	14	153.94	541.98	633.29
f_{av} [MPa]			542.14	633.57
1	20	314.16	528.07	622.41
f_{av} [MPa]			528.07	622.41

TABLE 3.15: Results of the tensile test on rebars from $J\_01\_S - M^+$ and $J\_01\_S - M^-$ specimens.

Number [-]	d_0 [mm]	**A** [mm^2]	f_y [MPa]	f_t [MPa]
1	10	78.54	510.32	620.37
2	10	78.54	508.44	618.89
3	10	78.54	504.54	616.20
f_{av} [MPa]			507.76	618.49
1	12	113.10	534.66	640.25
2	12	113.10	533.51	637.81
3	12	113.10	527.89	633.55
f_{av} [MPa]			532.02	637.20
1	14	153.94	523.11	613.02
2	14	153.94	521.00	611.43
3	14	153.94	526.90	614.50
f_{av} [MPa]			523.67	612.99

TABLE 3.16: Results of the tensile test on rebars from $J\_02 - C$, $J\_02 - M^+$, $J\_02 - M^-$, $J\_02\_S - C$, $J\_02\_S - M^+$, $J\_02\_S - M^-$ specimens.

3.3 Beam-to-Column Joints Tests

3.3.1 Test Setup and Loading Apparatus

The set-up of the experimental tests performed on the twelve beam-to-column connections, listed in Table 3.1, is shown in Figure 3.4. The specimen is settled in the machine by bolting the end-plates of the column, properly equipped with threaded rods, to the constraint devices of the test machine, i.e. the steel hinges. Consequently, the column is arranged horizontally, i.e. with the longitudinal axis parallel to the floor, and the transverse beam vertically, i.e. with the longitudinal axis perpendicular to the floor. The test consisted of the application of horizontal displacements at the top of the transverse beam. The tests set-up was constituted by instruments and machines, that could be divided into three macro-categories: constraint devices, loading machine and measurement instruments.

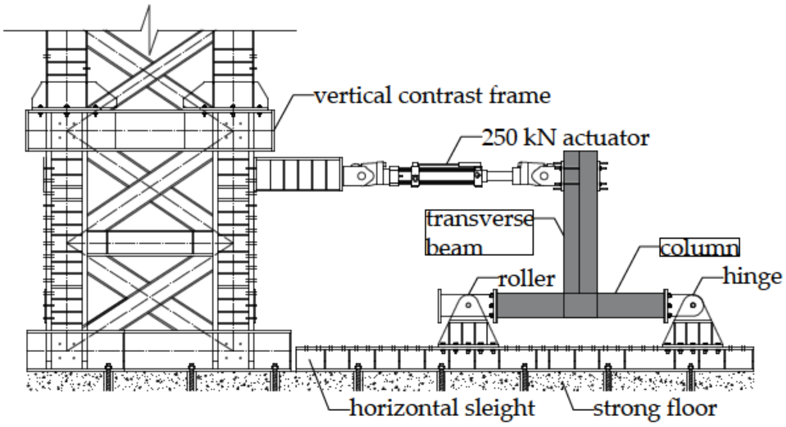

FIGURE 3.4: Layout of the experimental test.

The constraint devices counteract the actions due to the loading machine. The main constraint devices at the STRENGTH laboratory consist in the strong floor, horizontal contrast base sleight and rigid vertical contrast frame, pointed out in Figure 3.4. The laboratory strong floor is the basis to which the over-elevated structures are fixed, by means of high strength dywidag bars. The bars are settled in suitable holes of 80*mm* diameter, spaced according to a 1x1m grid in the strong floor. The horizontal base sleight is directly connected to the strong floor. Two steel hinges, between which the specimen is settled, are bolted to the horizontal base sleight. Both hinges are able to withstand 2000*kN* shear actions, but there are some differences between them. Indeed, a constraint is designed to absorb shear and axial actions, hence it is made up of a pin and calibrated holes. The other constraint enables the slippage in the horizontal direction, i.e. parallel to the column axis, and disables displacements in the orthogonal direction, i.e. out of the Figure 3.4 plane, as it is made up of a pin and slotted holes. As a consequence, in Figure 3.4 this latter device is referred to as a roller. The loading machine, then, is fixed to the vertical contrast frame.

The loading machine employed in the experimental campaign was the MTS hydraulic actuator, with a maximum load capacity equal to 250 kN. Through the actuator, the loading history is applied to the specimens. In this case, the desired protocol is given in terms of displacements. It is imposed at the free end of the transverse beam, by connecting the plate and counter-plate of the actuator through threaded bars, tightened with a predetermined torque.

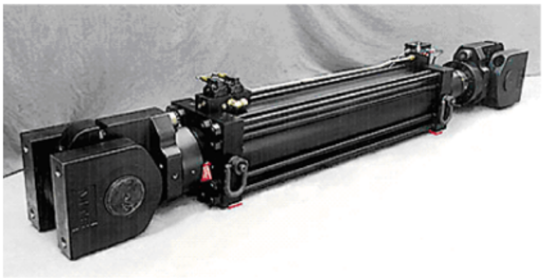

FIGURE 3.5: MTS hydraulic actuator.

3.3.2 Instrumentation

Measuring instruments were employed during the tests. In particular, the displacements exhibited by the specimens were recorded by means of Linear Displacements Transducers (LDT) and Wire Displacement Sensors (WDS) (Figure 3.6). The instruments were placed in several points of the specimens to get as much displacement data as possible, with the arrangement shown in Figures 3.7 and 3.8 with reference to conventional specimens, respectively, without and with the floor deck. The instrumentation setup was not pointed out for innovative specimens since it was equal for conventional and innovative modules.

(a) LDT

(b) WDS

FIGURE 3.6: Measuring instruments.

The total number of employed sensors was 13 and 17 for testing, respectively, simple modules, *J*_01 and *J*_02, and modules equipped with the floor deck, *J*_01_*S* and *J*_02_*S*. The absence of the floor deck obviously entails fewer parameters to monitor. H-LDT_1 to H-LDT_5 provided the relative displacements of the floor deck with respect to the longitudinal beam since they were supported by a shaft fixed to the beam. In particular, H-LDT_1, H-LDT_2, H-LDT_5 and H-LDT_6 monitored the relative displacements of the joists, while H-LDT_3 and H-LDT_4 monitored the relative displacements of the transverse beam. Except for the first test ($J\_01\_S - Geolite - C$), where LDTs with $50mm$ stroke were used, the previously mentioned sensors had $100mm$ measuring range. A further survey of relative displacements of the transverse beam with respect to the longitudinal ones was given by H-WDS_1, which was a wire sensor installed in the middle of the actuator counter-plate, having $500mm$ measuring range. The torsional rotation of the longitudinal beams, as well as the joint rotation, was evaluated through LDTs vertically arranged with a stroke of $50mm$. These transducers are V-LDT_1, V-LDT_2, V-LDT_3, V-LDT_4, V-LDT_5, V-LDT_6 in Figures 3.7 and 3.8. Finally, the displacements of the machine constraints were detected until the limit of $50mm$. H-LDT_7 and H-LDT_8 measured, respectively, the roller and hinge horizontal displacements, while V-LDT_7 and V-LDT_8 measured, respectively, the roller and hinge vertical displacements.

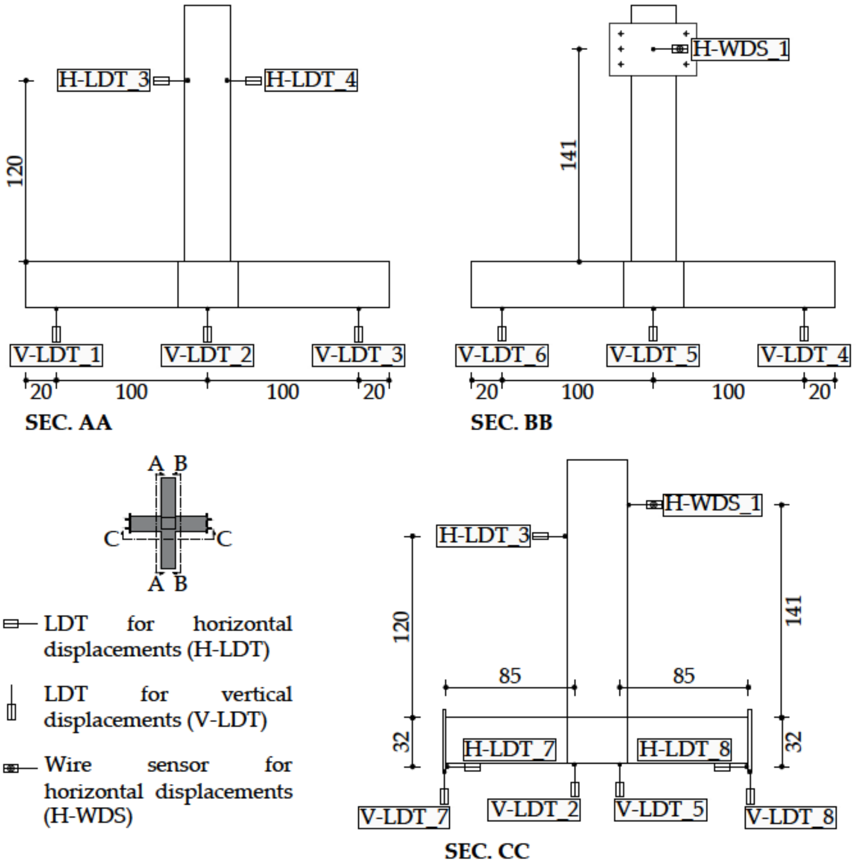

FIGURE 3.7: Setup of the instrumentation in J_01 specimen (units: cm).

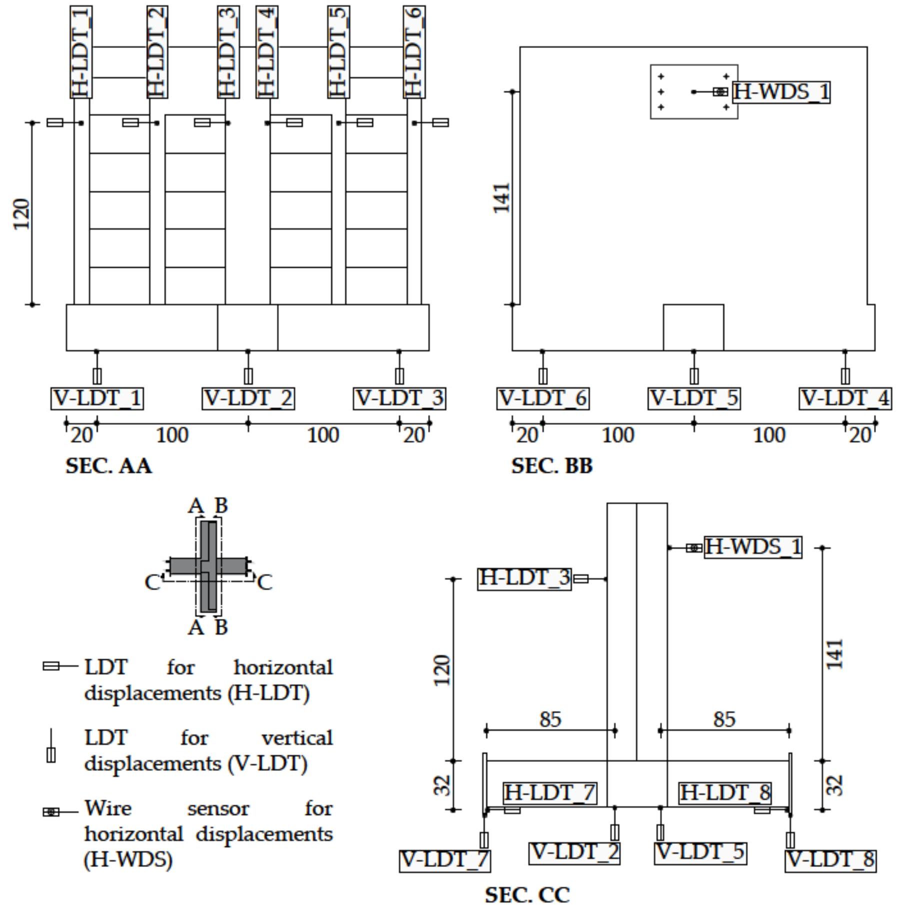

FIGURE 3.8: Setup of the instrumentation in J_01_S specimen (units: cm).

3.3.3 Testing Procedure and Loading Sequence

As revealed in advance, the tests were carried out by applying displacement-controlled loading at the top of the transverse beam with the hydraulic actuator of 250 kN loading capacity. The load corresponding to the applied displacement was properly measured by the load cell mounted in the hydraulic actuator. The load history was applied by imposing monotonic and cyclic protocols without the application of any simultaneous axial force to the column, as it is a conservative condition [49–51].

The monotonic tests were executed by applying increasing levels of displacement and keeping the velocity equal to the constant value of $v = 0.15 mm/s$. It was disrupted once about 20% loss of resistance was reached.

The cyclic protocol was set in accordance to the ACI 374.1-05 document [51], which provides a test sequence given in terms of drift ratios and the number of cycles, thus ensuring a gradual increase in steps. The drift was computed as the angular rotation θ of the beam chord with respect to the centroid of the beam-column joint, according to Equation 3.3.1 and Figure 3.9, where the static scheme of the tested specimen is shown.

$$\theta = \frac{\Delta}{L} \tag{3.3.1}$$

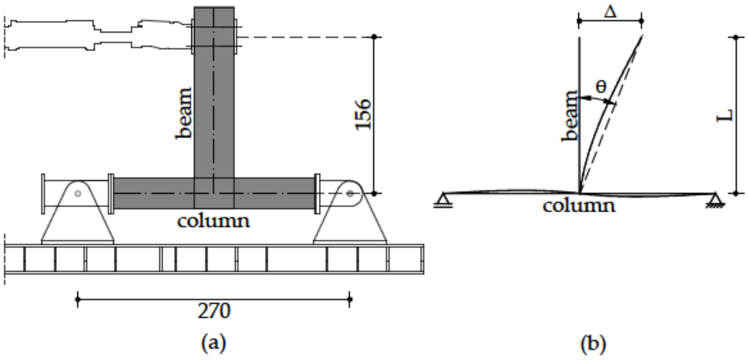

FIGURE 3.9: Test layout with actual dimensions in cm (a) and related static scheme with deformation of the beam-to-column specimen (b).

In order to implement the loading history in the test machine software, the loading protocol was converted in terms of displacement history, given in Table 3.17, by multiplying the drift by the lever arm, $L = 156cm$. In particular, three fully reversed cycles were implemented for each drift level. For the first level of drift, composed of three fully reversed cycles, the test velocity was fixed at $v = 0.15mm/s$ hence the time range was consequently derived. For the following cycles until 2.75% drift, the time range was set equal to the first one obtained, while the velocity was variable. For drift ratios greater than 2.75%, the velocity was fixed at $v = 2.06mm/s$. In Figure 3.10, the cyclic protocol is shown in terms of displacements versus time until 3.5% drift, according to [51]. Although it was implemented in the machine until a drift of 6.5%, the tests were stopped widely before the achievement of this last step, i.e. once the module attained 80% of the maximum resistance achieved during the test.

Step [-]	**Cycles/Step** [-]	**v** [mm/s]	θ [%]	Δ [mm]	Δt [s]
1	3	0.15	0.20	3.11	248.96
2	3	0.19	0.25	3.89	248.96
3	3	0.26	0.35	5.45	248.96
4	3	0.38	0.50	7.78	248.96
5	3	0.56	0.75	11.67	248.96
6	3	0.75	1.00	15.56	248.96
7	3	1.05	1.40	21.78	248.96
8	3	1.31	1.75	27.23	248.96
9	3	1.65	2.20	34.23	248.96
10	3	2.06	2.75	42.79	248.96
11	3	2.06	3.50	54.46	316.86

TABLE 3.17: Loading displacement history.

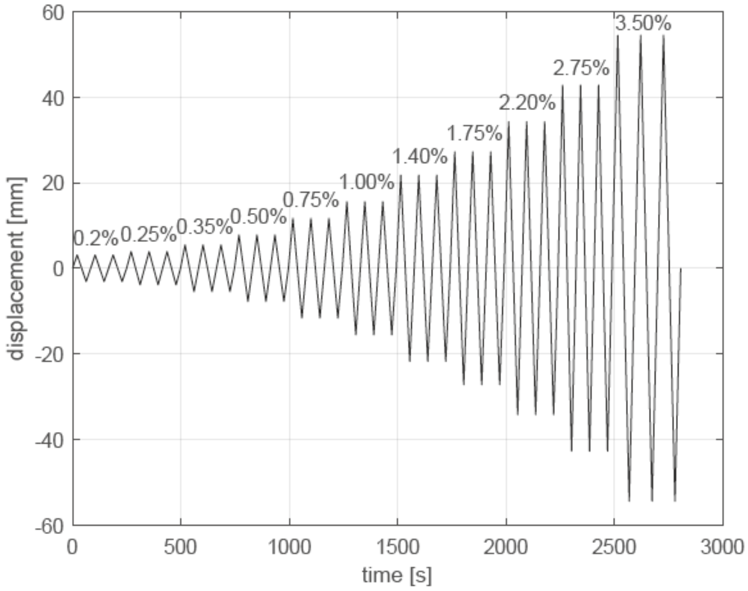

FIGURE 3.10: Cyclic loading protocol.

3.3.4 Performed Tests

The experimental campaign carried out on the beam-to-column connections was devoted to investigating their response to the monotonic and cyclic loading protocols detailed in Section 3.3.3. All the typologies of designed specimens, mentioned in Section 2.2, were tested. Firstly, the experimental investigation was carried out on conventional modules, equipped and not with the floor deck. The six tests consisted of:

- two tests on conventional specimens without the floor deck, J_01: a cyclic test, in the following referred to as $J\_01 - C$, and a monotonic test in positive loading direction, referred to as $J\_01 - M^+$;
- four tests on conventional specimens with the floor deck, J_01_S: two cyclic tests, referred to as $J\_01\_S - Geolite - C$ and $J\_01\_S - C$, and two monotonic tests, one in positive and one in negative loading direction, referred to as, respectively, $J\_01\_S - M^+$ and $J\_01\_S - M^-$.

As it may be noticed, the name $J\_01\_S - Geolite - C$ is quite different from the others. During the concrete casting, indeed, problems occurred in the column, hence it was monolithically repaired by means of a pourable geo-mortar, the GeoLite Magma from Kerakoll. Nevertheless, the specimen was tested first and used as a test set-up. As will be seen in the following Chapters, the repair intervention did not influence its response.

Secondly, six innovative specimens, with and without the floor deck, were analysed by performing:

- three tests on innovative specimens without the floor deck, J_02: a cyclic test, in the following referred to as $J\_02 - C$, and two monotonic tests, one in positive and one in negative loading direction, referred to as, respectively, $J\_02 - M^+$ and $J\_02 - M^-$;

- three tests on innovative specimens with the floor deck, J_01_S: a cyclic test, $J\_02\_S - C$, and two monotonic tests, one in positive and one in negative loading direction, referred to as, respectively, $J\_02\_S - M^+$ and $J\_02\_S - M^-$.

Positive and negative signs in the names of the specimens subjected to monotonic loads are related to the displacements imposed at the top of the transverse beam during the tests. Positive and negative displacements are highlighted in Figure 3.11, with reference to a specimen with the floor deck. Conventionally, positive displacements were assumed when the actuator pushed the specimens toward the hinge constraint, while negative displacements were assumed when the actuator pulled the specimens, toward the roller. The former and latter condition entailed, respectively, the compressive and tensile stress in the slab. As a consequence, positive displacements implied positive load and bending moment (slab-in-compression) and negative displacements implied negative load and bending moment (slab-in-tension). In conclusion, the overall tests performed are pointed out in Table 3.1.

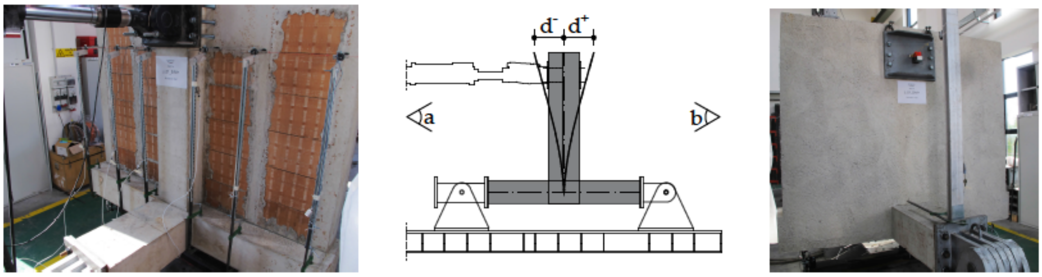

(a)

(b)

FIGURE 3.11: Conventional positive and negative displacements.

Chapter 4

Experimental Results

4.1 Introduction

In this Chapter, the results of the performed tests are provided in two main sections, concerning the two categories of analysed specimens, i.e. conventional and innovative specimens. Moreover, each category is then split into the two subcategories of beam-to-column joints without and with the floor deck.

The responses of the specimens are reported in terms of the load versus displacement curve. Loads and displacements were measured at the hydraulic actuator level, at the end of the transverse beam. The load was supposed to be applied at $L_i = 1.56m$ from the column inter-axis, and at $L_c = 1.41m$ from the column face, as depicted in Figure 4.1.

Moment versus rotation plots are also provided. The moment was evaluated at the intersection of the beam-column inter-axes, hence it was the product of the applied load and the lever arm of $L_i = 1.56m$. The rotation was evaluated from the top beam displacement and the above-mentioned lever arm.

Besides, non-dimensional moment versus rotation graphs are proposed. The non-dimensional moment was computed by dividing the experimental moment by the moment of resistance of the transverse beam (30x40cm), evaluated through the average mechanical properties of concrete and steel, given in Chapter 3. From the monotonic tests only, the moment was also plotted versus the beam rotation, calculated from the beam displacements.

The beam displacements, in *J*_01 and *J*_02 tests, together with the joists displacements, in *J*_01_*S* and *J*_02_*S* tests, are plotted against the test time.

Finally, the crack pattern and the damage evolution are described for each subcategory of specimens, i.e. for joints with and without the floor deck.

As specified in Section 3.3.4 and illustrated in Figure 3.11, displacements and forces (and moments in consequence) are conventionally assumed as positive when the actuator pushes the specimen, by inducing compressive stress in the slab, and negative when it pulls the specimen, resulting in tensile stress in the slab. The experimental data manipulation, the parameters highlighted in Tables and Figures, and the computed benchmark theoretical values are exhaustively explained in Section 4.2 of this Chapter, while they are omitted in the following Section.

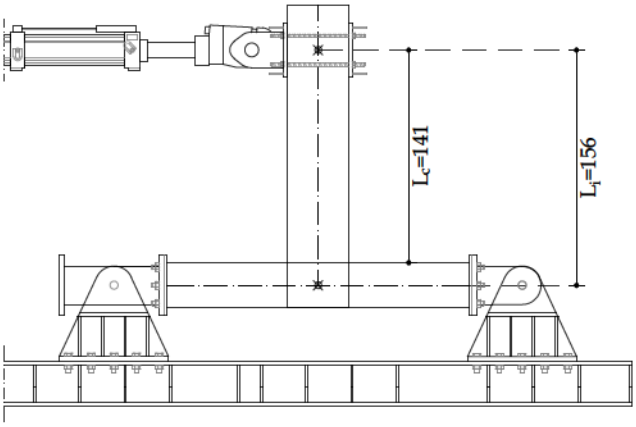

FIGURE 4.1: Test layout of conventional specimens (units:cm).

4.2 Conventional Specimens

4.2.1 Joints without Floor Deck

4.2.1.1 Load-Displacement Response

The load versus displacement chart shows the displacements imposed to the transverse beam, on the x-axis, and the forces of the hydraulic actuator, on the y-axis. However, the actuator displacements are affected by the horizontal slippage of the machine constraints, i.e. the hinge and the roller, due to the bolt hole gap, which is equal to $\pm 3mm$. As a consequence, the proper displacements were obtained by subtracting, at all times, the displacements detected by the horizontal LDTs near the constraints, H-LDT_7 and H-LDT_8 in Figure 4.2, from the actuator displacements. Alternatively, the effective displacements were obtained from the data of the wire sensor, which was integral with the specimen hence not affected by slippage. In Figure 4.3, the difference in the load-displacement curves obtained with the original and reduced displacements is pointed out.

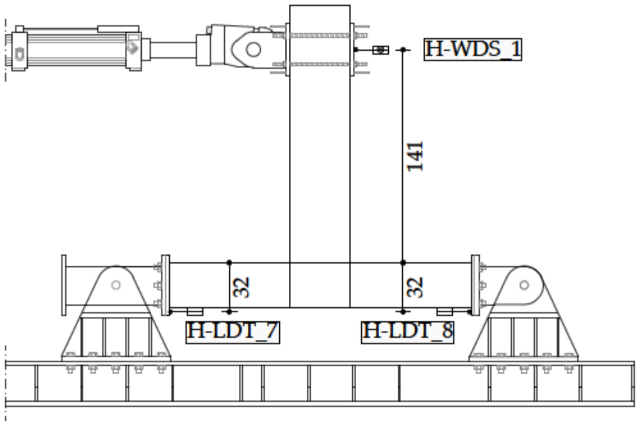

FIGURE 4.2: LDTs monitoring the horizontal displacements of the machine constraints and WDS at the top of the beam (units:cm).

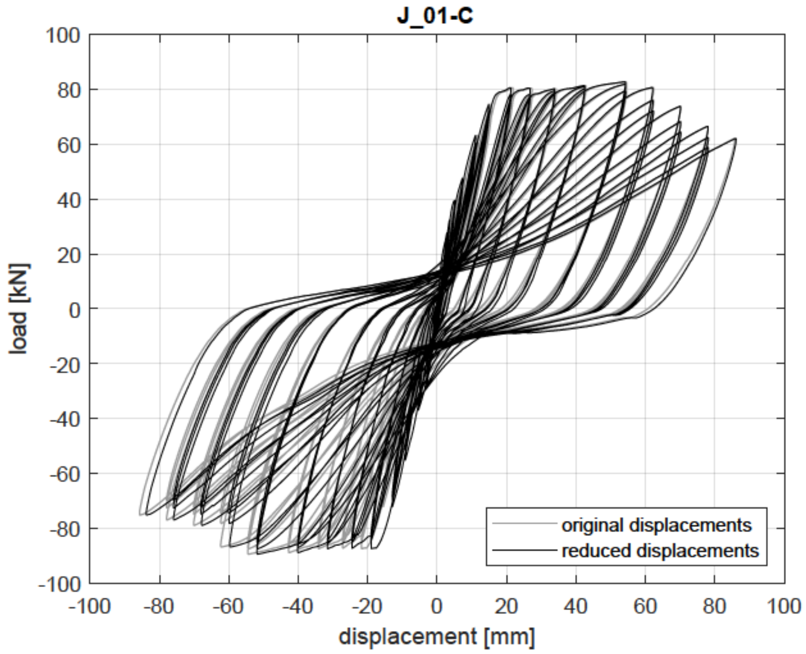

(a)

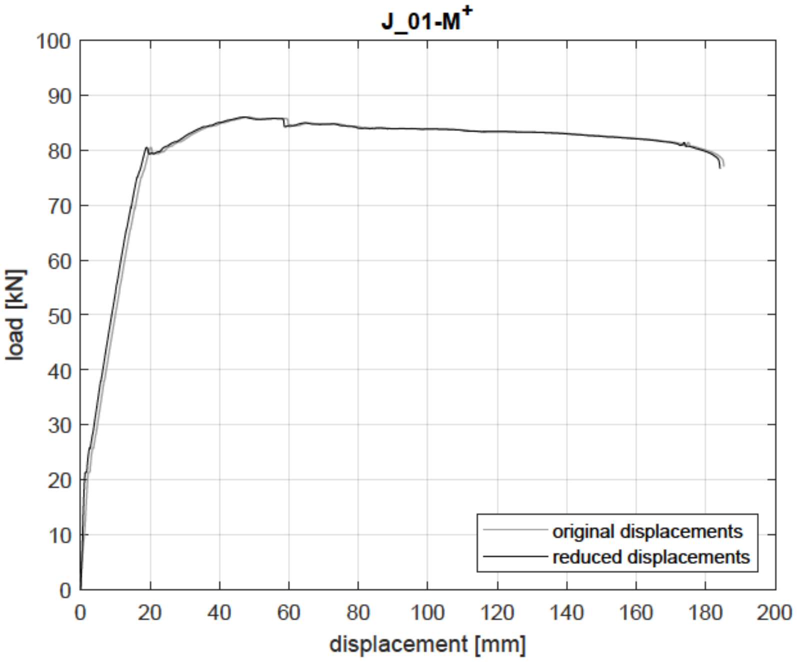

(b)

FIGURE 4.3: Effect of the displacements reduction on the load vs displacement response of $J\_01 - C$ (a) and $J\_01 - M^+$ (b) specimens.

The load vs displacement response to monotonic and cyclic tests performed on the conventional joints without the floor deck are shown in Figure 4.4 and Figure 4.5, with reference to, respectively, $J\_01 - C$ and $J\_01 - M^+$ specimens. On these curves, the first cracking, the general yielding and the maximum load points were identified. For the specimen subjected to the cyclic test, the load vs displacement curve was also plotted by pointing out the monotonic envelope, i.e. the skeleton curve. The skeleton curve, indeed, is the red curve over the hysteresis loops, which envelopes the values of maximum and minimum loads achieved for each level of drift.

The first cracking of the main beam is reported in Table 4.1, with reference to each test. In particular:

- F_{cr}^+ and d_{cr}^+ are the load and relative displacement corresponding to the first cracking when positive displacements are applied (i.e. when the actuator is in the pushing stage);
- F_{cr}^- and d_{cr}^- are the load and relative displacement corresponding to the first cracking when negative displacements are applied (i.e. when the actuator is in the pulling stage).

The first cracking of the transverse beam, in positive loading (displacement) direction, occurred at $+17.97kN$ in $J\_01 - C$ specimen, and $+21.00kN$ in $J\_01 - M+$ specimen, corresponding to a positive cracking moment M_{cr}^+ of, respectively, $+28.03kNm$ and $+32.76kNm$. In the negative loading (displacement) direction, first cracking was at $-15.02kN$, corresponding to a negative cracking moment M_{cr}^- of $-23.43kNm$. The cracking moments can be checked in following Section 4.2.1.2, where the moment-rotation graphs are reported. The cracking moments were predicted to be $\pm 27.67kNm$ for $J\_01 - C$ beam and $+25.97kNm$ for $J\_01 - M^+$ beam. In particular, the previous experimental cracking moments were evaluated as $F_{cr}^{+/-} \times L_i$. However, the first cracking, as will be widely explained in Section 4.2.1.4, appeared around the beam-to-column intersection, hence, by considering $L_c = 1.41m$ as a lever arm, the experimental cracking moments become $+25.34kNm$ and $-21.18kNm$ for $J\_01 - C$ test, and $+29.61kNm$ for $J\_01 - M^+$.

In addition, the point at which the general yielding of the beam longitudinal reinforcement had certainly occurred was identified. Loads and displacements corresponding to the general yielding are shown in Table 4.2. In detail:

- F_y^+ and d_y^+ are the load and displacement corresponding to the yielding of the beam longitudinal rebars when the specimen was subjected to positive displacements;
- F_y^- and d_y^- are the load and displacement corresponding to the yielding of the beam longitudinal rebars when the specimen was subjected to negative displacements.

The yielding of the transverse beam reinforcement, in the positive loading direction, was supposed to occur at a load of $+74.56kN$ and a displacement of $+14.86mm$ in $J\_01 - C$, and at $+80.52kN$ load and $+19.05mm$ displacement in $J\_01 - M^+$ specimen. In the negative loading direction, the yielding was assumed to take place at $-80.73kN$ load and $-15.08mm$ displacement. The corresponding yielding moments, evaluated through L_i, were $M_y^+ = +116.31kNm$ and $M_y^- = -125.93kNm$ in $J\_01 - C$, and $M_y^+ = +125.62kNm$ in $J\_01 - M^+$. The corresponding yielding moments, evaluated through L_c, were $M_y^+ = +105.13kNm$ and $M_y^- = -113.82kNm$ in $J\_01 - C$, and $M_y^+ = +113.54kNm$ in $J\_01 - M^+$. The expected values of the yielding moment were $M_y^{+/-} = \pm 96.66kNm$.

The peak loads and the corresponding displacements are summarised in Table 4.3, where:

- F_E^+ and d_E^+ are the maximum load and the corresponding displacement, when positive displacements are applied;
- F_E^- and d_E^- are the minimum load and the corresponding displacement, when negative displacements are applied.

During the test on $J\_01 - C$ module, the peak positive load achieved was $+82.75kN$ at a displacement of $+53.95mm$ and a displacement ductility of $d_E/d_y = 3.63$. The peak negative load was $-89.54kN$, corresponding to a displacement of $-51.72mm$ and a displacement ductility of $d_E/d_y = 3.43$. $J\_01 - M+$ specimen withstood the maximum positive load of $+86.06kN$, occurring at a displacement of $+47.47mm$, hence at a displacement ductility of $d_E/d_y = 2.49$. Upon further loading, the peak loads sustained by the specimens in both load directions were quite similar to the yielding load. The testing on $J\_01 - C$ specimen was discontinued at a positive load of $+62.08kN$, corresponding to a displacement of $+85.93mm$, and at a negative load of $-75.27kN$, whose relative displacement was $-83.63mm$. The attained loss of resistance was 25% in the first case, and 16% in the second one. During the test, the hysteresis loops are increasingly larger. The testing on $J\_01 - M+$ module was interrupted at a load of $76.70kN$ and a displacement of $+184.05mm$, when the resistance reduced by 11%.

As a general rule, the tests were disrupted once about the 20% loss of resistance was attained, a considerable concrete spalling occurred and before the rebars buckling.

Specimen	F_{cr}^+ [kN]	d_{cr}^+ [mm]	F_{cr}^- [kN]	d_{cr}^- [mm]
$J\_01 - C$	17.97	1.29	-15.02	-1.21
$J\_01 - M^+$	21.00	1.25	-	-

TABLE 4.1: Positive and negative first cracking loads and corresponding displacements for specimens $J\_01 - C$ and $J\_01 - M^+$.

Specimen	F_y^+ [kN]	d_y^+ [mm]	F_y^- [kN]	d_y^- [mm]
$J\_01 - C$	74.56	14.86	-80.73	-15.08
$J\_01 - M^+$	80.52	19.05	-	-

TABLE 4.2: Positive and negative yielding loads and corresponding displacements for specimens $J\_01 - C$ and $J\_01 - M^+$.

Specimen	F_E^+ [kN]	d_E^+ [mm]	F_E^- [kN]	d_E^- [mm]
$J\_01 - C$	82.75	53.95	-89.54	-51.72
$J\_01 - M^+$	86.06	47.47	-	-

TABLE 4.3: Maximum and minimum loads and corresponding displacements for specimens $J\_01 - C$ and $J\_01 - M^+$.

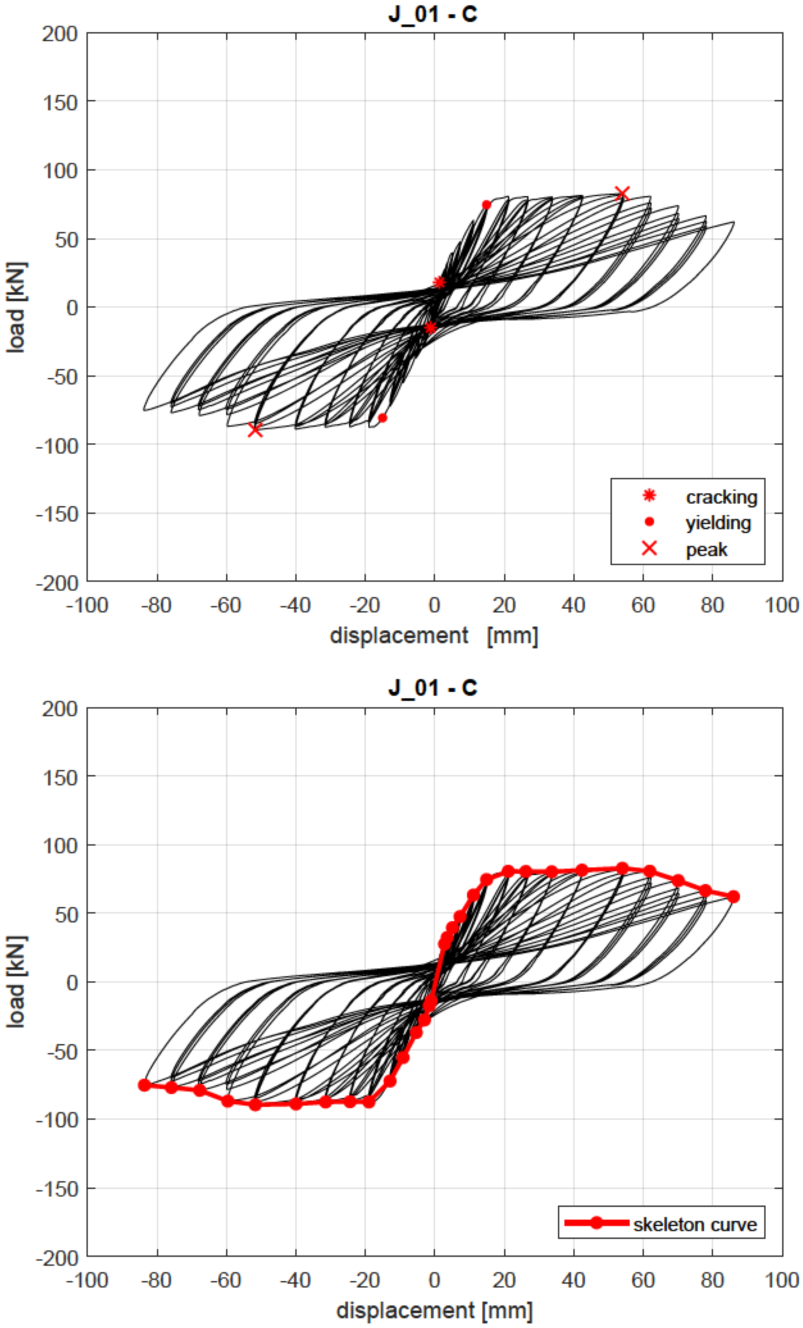

FIGURE 4.4: Load vs displacement response of $J\_01 - C$ specimen.

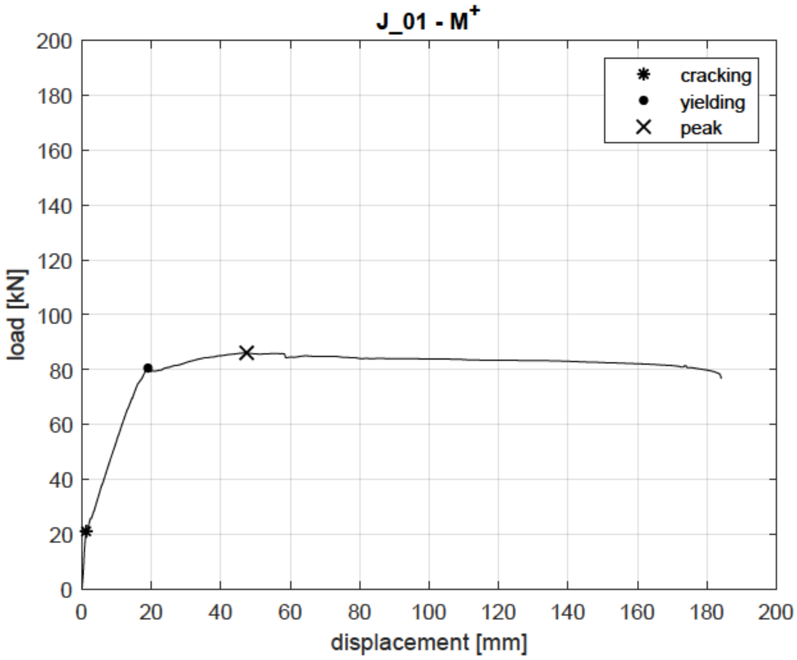

FIGURE 4.5: Load vs displacement response of $J\_01 - M^{+}$ specimen.

4.2.1.2 Moment-Rotation Response

The response of conventional joints without the floor deck was also analysed in terms of moment versus rotation. The moment, on the y-axis, is the product of the experimental force multiplied by the lever arm. The lever arm, shown in Figure 4.1, is the distance between the middle of the actuator plate, where the load resultant is supposed to be applied, and the intersection of the beam and column inter-axes. Its length is $L_i = 1.56m$. On the x-axis, the chord rotation, θ, was plotted. The angle was evaluated from the top displacement of the transverse beam, at the actuator level, Δ, divided by the lever arm, L_i, as illustrated in Figure 3.9.

In Figure 4.6 and Figure 4.7, the moment vs rotation curves of, respectively, $J\_01 - C$ and $J\_01 - M^{+}$ specimens are reported. The specific events occurred during the test, cracking, yielding, and peak load can be identified on these curves, as done in the load-displacement graphs. As a matter of fact, moments and rotations are directly derived from, respectively, forces and displacements. The peak moments, in positive and negative loading direction, sustained by the $J\_01 - C$ specimen, were $129.09kNm$ and $-139.68kNm$, while the maximum moments reached by the $J\_01 - M^{+}$ specimen was $134.25kNm$.

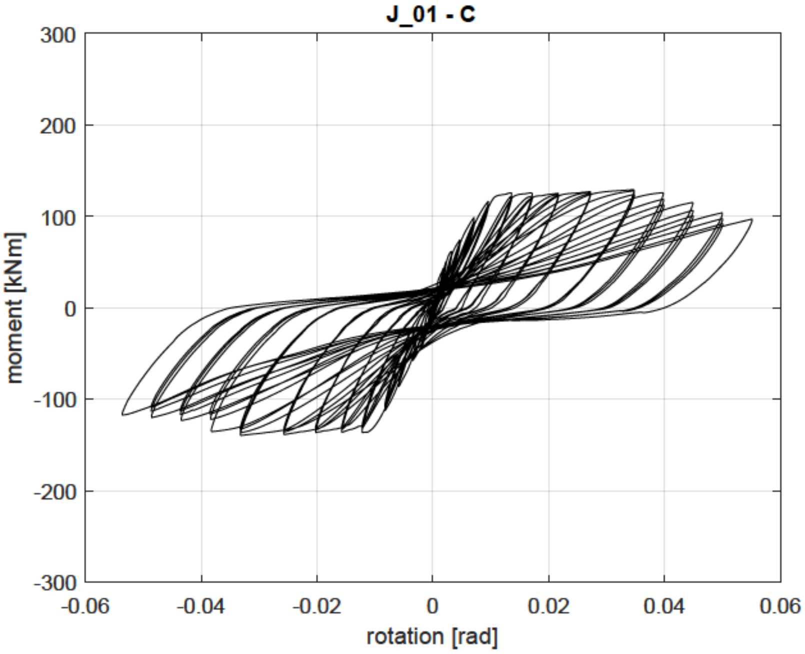

FIGURE 4.6: Moment vs rotation response of $J\_01 - C$ specimen.

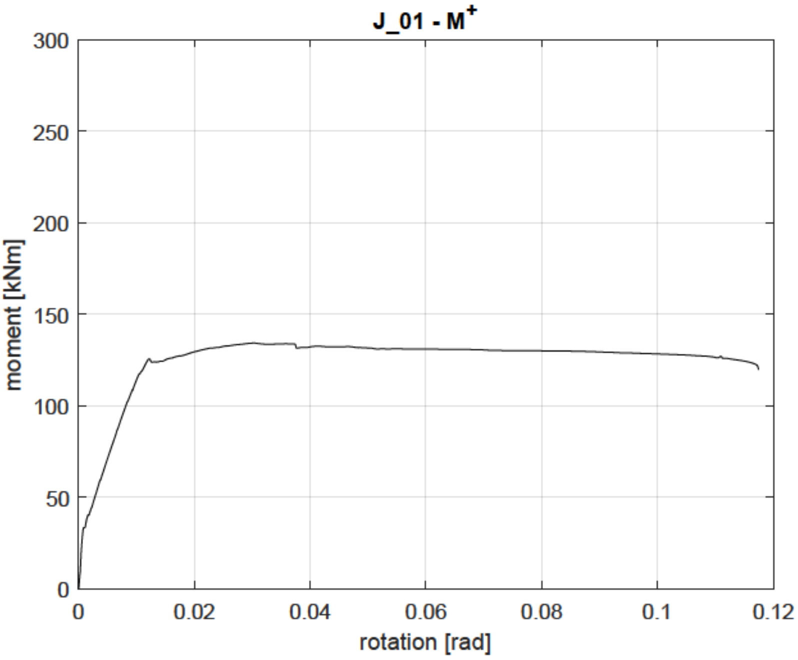

FIGURE 4.7: Moment vs rotation response of $J\_01 - M^+$ specimen.

The moment-rotation graph was used to build the non-dimensional moment versus rotation chart graph. It is shown in Figure 4.8 and Figure 4.9, with reference to, respectively, J_01-C and J_01-M^{+} specimen. The non-dimensional moment was the ratio between the experimental moment and the moment of resistance of the transverse beam, $M_R^{+/-}$. The bending resistance of the transverse beam $M_R^{+/-}$ was computed by referring to the average mechanical properties of the tested materials, reported in Chapter 3. The stress-block model was adopted as a constitutive law for the concrete and the elastic-perfectly plastic mechanical behaviour was assumed for the steel reinforcement. The resulting moments of resistance, in absolute value, were $M_R^{+/-} = 102.83kNm$ and $M_R^{+} = 102.40kNm$, for the transverse beam of, respectively, J_01-C and J_01-M^{+} . The non-dimensionalization process is useful to make the experimental measurements homogeneous. By properly accounting for the slight differences in the material features, a comparison between the typologies of analysed specimens can be finally stated. The non-dimensionalization is particularly suitable for the estimation of the over-resistance that the presence of the floor deck supplied to the connection, as will be seen in the next Chapter 3. Obviously, in the joints without the floor deck, the ratio between the maximum experimental and resistance moment was expected to be one or around it. In particular, it was equal to 1.26 and -1.36 in, respectively, positive and negative loading direction of J_01-C test, and 1.31 in J_01-M^{+} test.

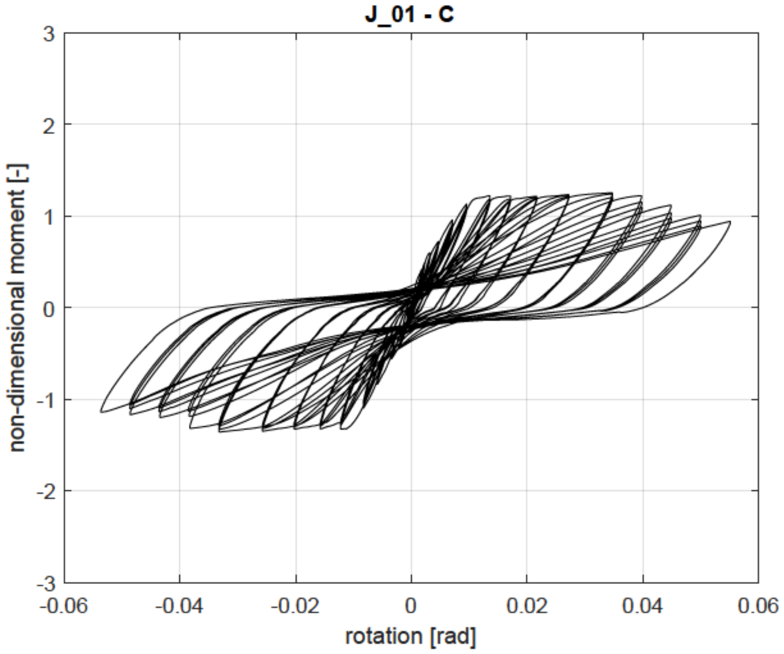

FIGURE 4.8: Non-dimensional moment vs rotation response of J_01-C specimen.

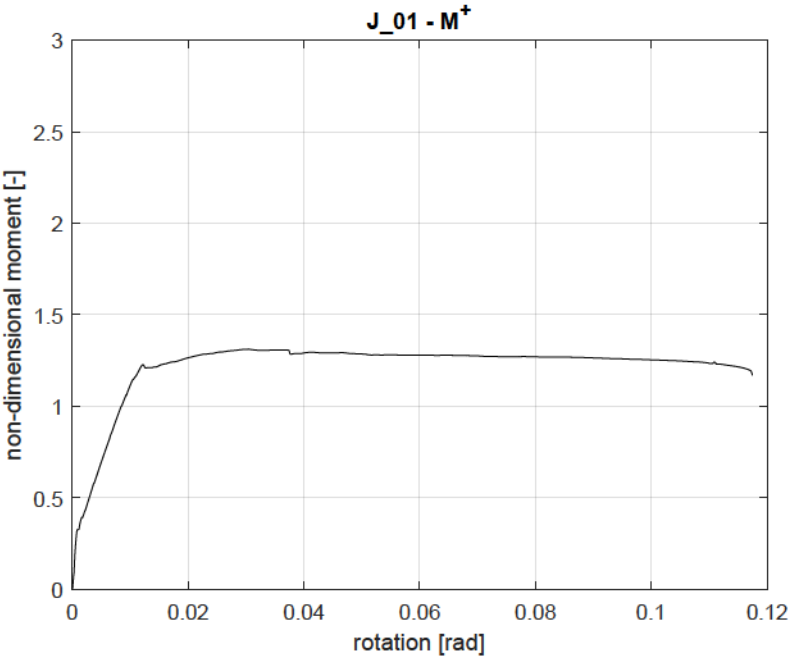

FIGURE 4.9: Non-dimensional moment vs rotation response of $J\_01 - M^{+}$ specimen.

Finally, for the monotonic tests only, the moment versus beam rotation curve was plotted. The moment was the same quantity as previously defined, i.e. the load multiplied by the lever arm ($M = F \times L$). The beam rotation was evaluated in two different ways. The first and easier one consisted in dividing the average of the displacements detected by the LDTs near the transverse beam (H-LDT_3, in Figure 4.10, and that on the opposite side, labelled H-LDT_4) by the lever arm (b_{3-4}, in Figure 4.10). Those sensors, indeed, detected the displacements of the beam, since they were integral to the joint area, hence they rotated together with the joint. The rotation of the beam was alternatively obtained by subtracting, from the actuator total displacement, Δ, the displacement due to the joint rotation, δ_j (Equation 4.2.1). The top beam displacements due to the joint rotation were evaluated according to Equation 4.2.2, in which the joint rotation, θ_j, was multiplied by the lever arm, L_i (Figure 4.11). The joint rotation was the angle formed by the deformed inclined and the undeformed horizontal joint configuration. Hence, it was computed by dividing the difference of the vertical displacements, detected by the two LDTs under the joint area, V-LDT_2 and V-LDT_5 (Figure 4.10), by their distance, b_{25} (Figure 4.10).

$$\delta_b = \Delta - \delta_j \tag{4.2.1}$$

$$\delta_j = \arctan\left(\frac{\eta_2 - \eta_5}{b_{25}}\right) \times L_i \tag{4.2.2}$$

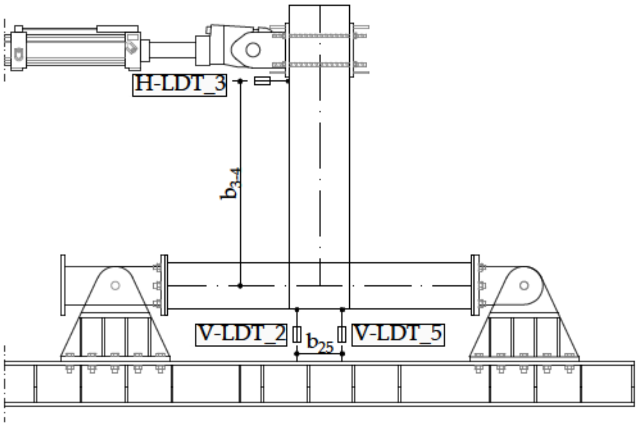

FIGURE 4.10: Instrumentation to derive the beam rotation.

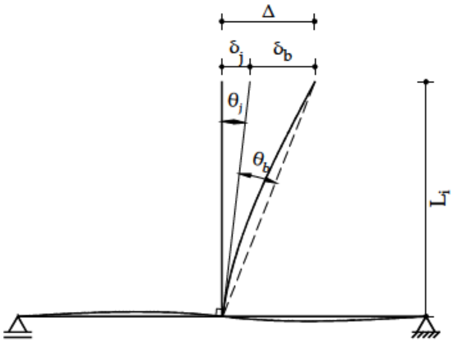

FIGURE 4.11: Top displacement components.

Figure 4.12 shows the comparison between the moment vs beam rotation curves provided by computing the beam rotation in both the ways previously explained. In the black curve, the beam rotation was evaluated from H-LDT_3 and H-LDT_4 sensors, while in the red dotted one, Equation 4.2.1 was applied. In theory, the two curves should coincide, but the H-LDT_3 and H-LDT_4 data were supposed to be more reliable, since they were directly applied to obtain the beam rotation, without being further processed. However, the information was provided until the end stroke of H-LDT_3 and H-LDT_4 sensors, which was always reached before the test end. On the contrary, the red dotted line measured the beam rotation throughout the test. The final beam rotation, indeed, was $0.07 rad$ on the black curve and $0.11 rad$ on the red one.

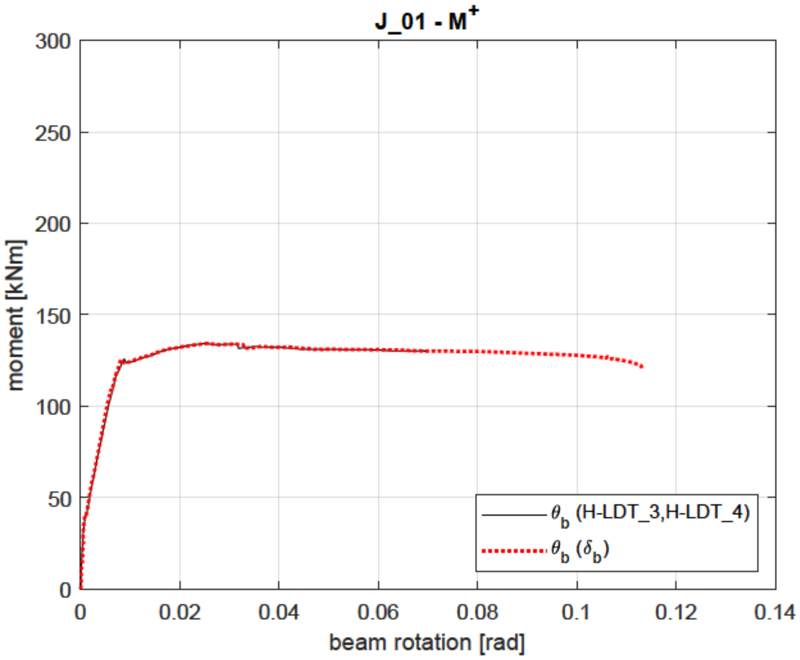

FIGURE 4.12: Moment vs beam rotation response of $J\_01 - M^+$ specimen.

4.2.1.3 Beam Response

The displacements of the main beam, i.e. the transverse beam, detected by H-LDT_3 and H-LDT_4 linear transducers, and used to derive the proper rotation of the beam in moment vs beam rotation graphs, are reported in Figure 4.13 and Figure 4.14, with reference to, respectively, $J\_01 - C$ and $J\_01 - M^+$ specimen. The LDTs applied in the tests had a stroke of $100mm$. The peak displacements of $J\_01 - C$ beam in the positive loading direction were $+53.15mm$ (H-LDT_3) and $+54.77mm$ (H-LDT_4), while in the negative one were $-45.33mm$ (H-LDT_3) and $-44.48mm$ (H-LDT_4). The maximum beam displacements in $J\_01 - M+$ were $+95.74mm$ (H-LDT_3) and $+95.24mm$ (H-LDT_4). In conclusion, the displacements on both the beam sides were very similar and they could be considered quite symmetric for loading in the positive and negative direction.

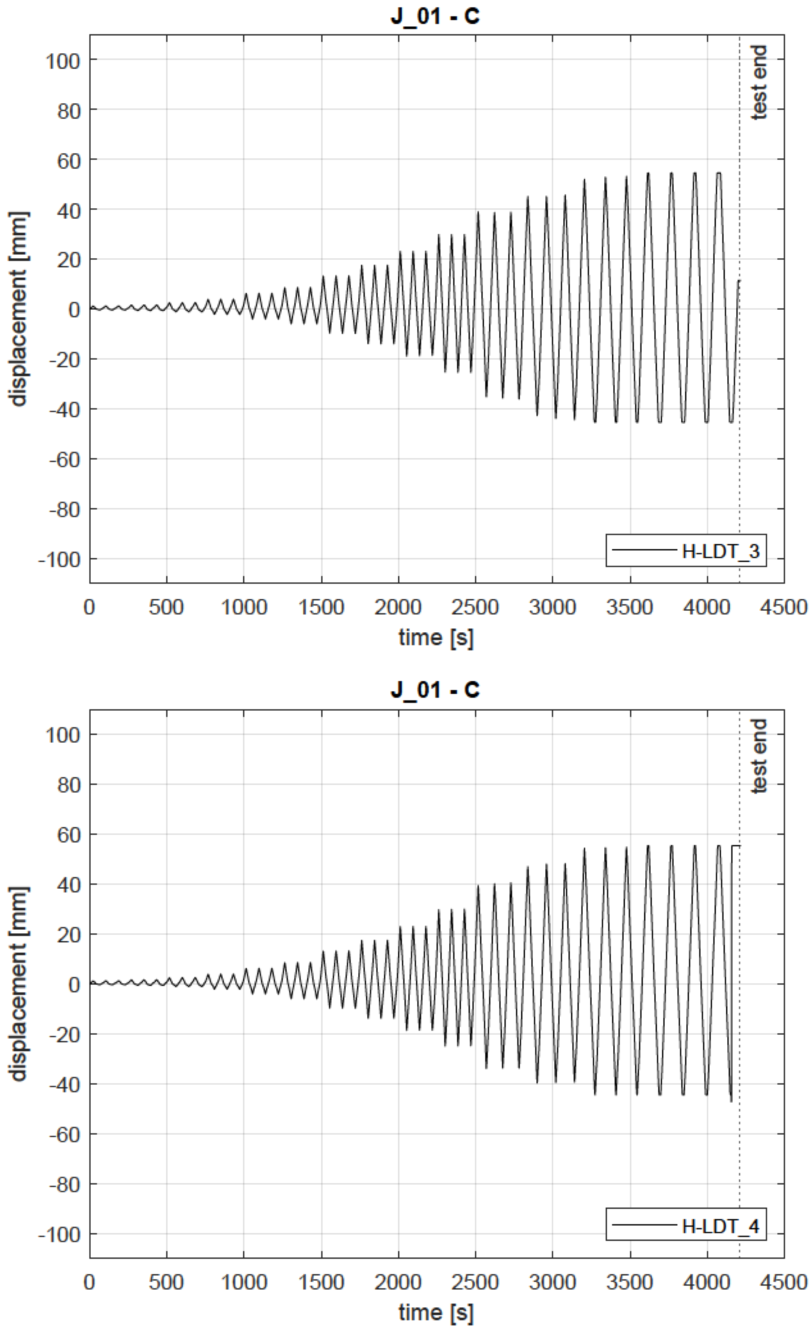

FIGURE 4.13: Beam displacement vs time of $J\_01 - C$ specimen.

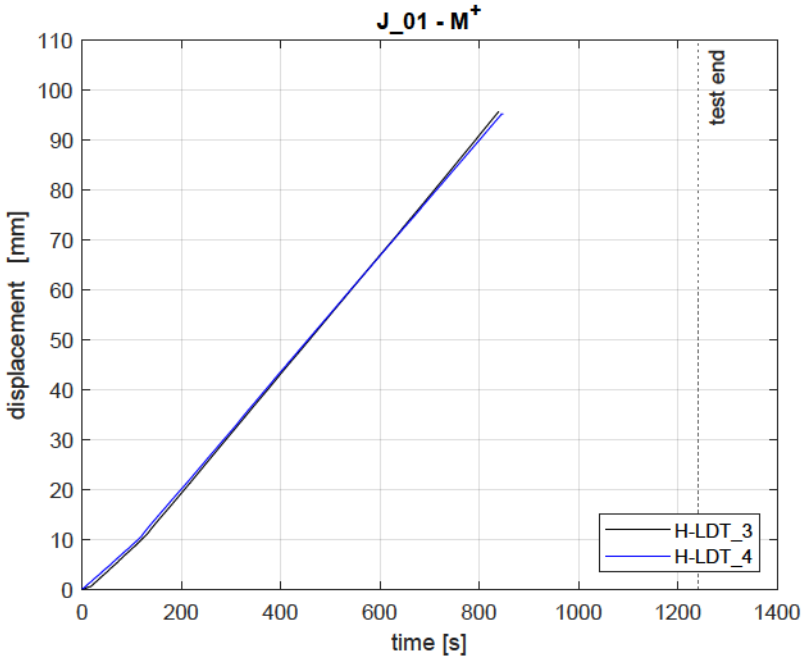

FIGURE 4.14: Beam displacement vs time of $J\_01 - M^{+}$ specimen.

4.2.1.4 Crack Pattern

As the specimens have been designed according to the EC8 provisions [1], a ductile failure was expected. The damaging pattern confirmed the expectation, as the plastic hinge, in conventional specimens without the floor deck, developed in the proper conventional dissipative zone, i.e. the beam end. The crack pattern evolution and the plastic hinge are shown in Figures 4.15 and 4.16, for $J\_01 - C$ specimen, and in Figures 4.17 and 4.18, for $J\_01 - M^{+}$ specimen.

During the cyclic test, the first crack appeared at few centimetres from the beam-column interface. As the test progressed, new cracks grew in the beam at increasing distance from the column until, at a high level of imposed displacements, new cracks gathered near the first one, thus pulling out the RC cover (Figure 4.16).

In the monotonic test, the first crack appeared at the beam-column interface. In a short while and almost simultaneously, the second and third cracks occurred at about, respectively, $30cm$ and $60cm$ from the beam-column interface. Upon further loading, the damage mainly affected the area between the first and second crack.

At the end of the tests, no damage was observed in the column (and in the joint area) and the longitudinal beams.

FIGURE 4.15: Crack pattern evolution in J_01-C specimen.

FIGURE 4.16: Final damage in the beam of $J\_01 - C$ specimen.

FIGURE 4.17: Crack pattern evolution in $J\_01 - M^{+}$ specimen.

(a) (b)

FIGURE 4.18: Final damage on beam tension (a) and compression (b) sides of $J\_01 - M^{+}$ specimen.

4.2.2 Joints with Floor Deck

4.2.2.1 Load-Displacement Response

The load versus displacement curves obtained from the monotonic and cyclic tests on the conventional beam-to-column joints equipped with the floor deck are reported in Figure 4.19, Figure 4.20, Figure 4.21 and Figure 4.22, with reference to, respectively, $J\_01\_S - Geolite - C$, $J\_01\_S - C$, $J\_01\_S - M^{+}$ and $J\_01\_S - M^{-}$ specimens.

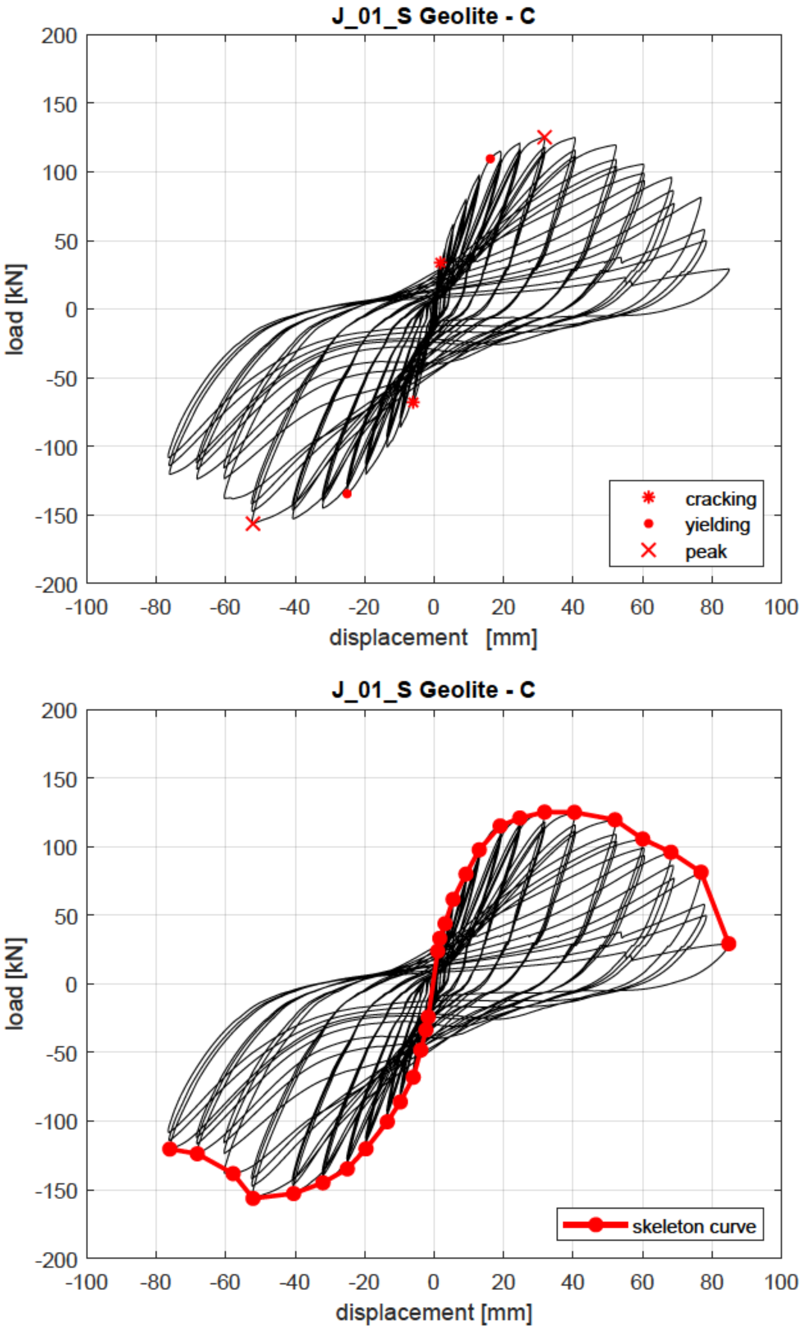

FIGURE 4.19: Load vs displacement response of $J\_01\_S - Geolite - C$ specimen.

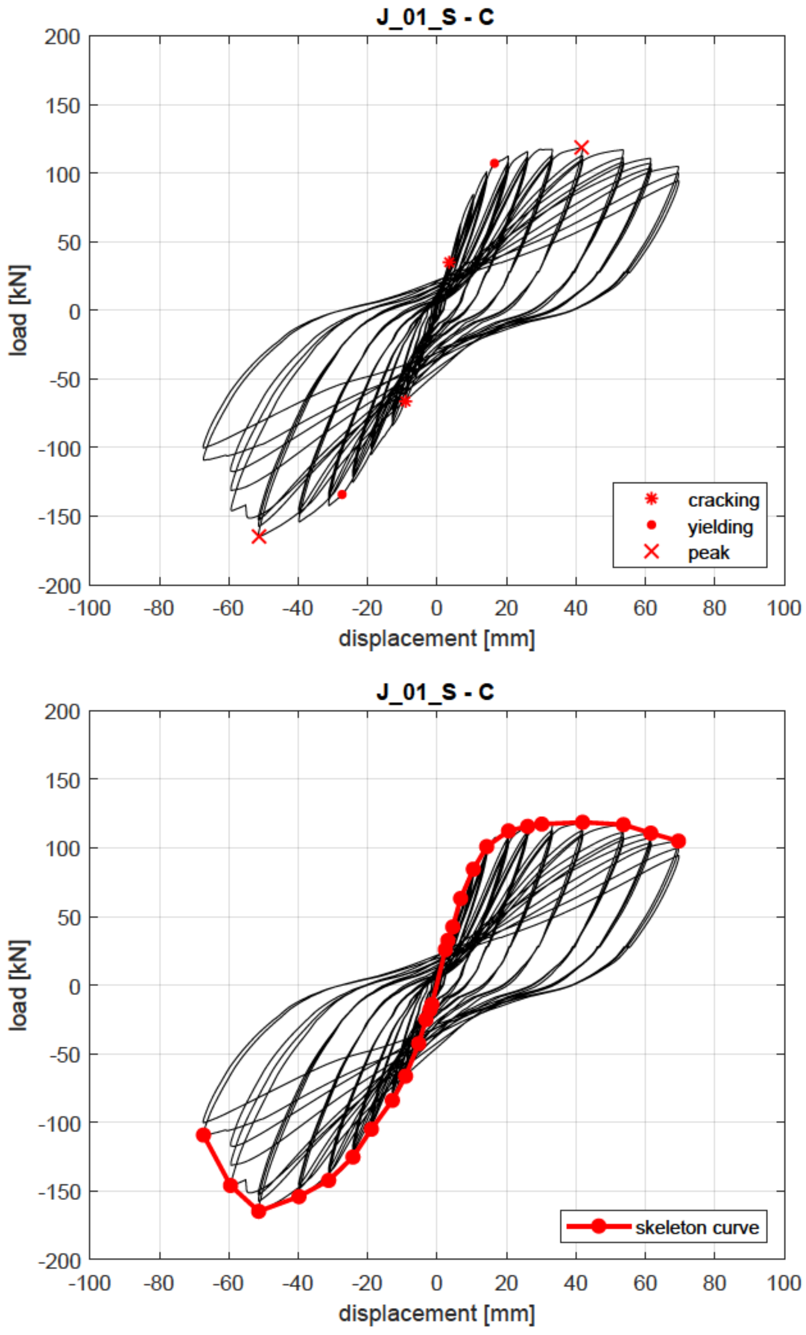

FIGURE 4.20: Load vs displacement response of $J\_01\_S - C$ specimen.

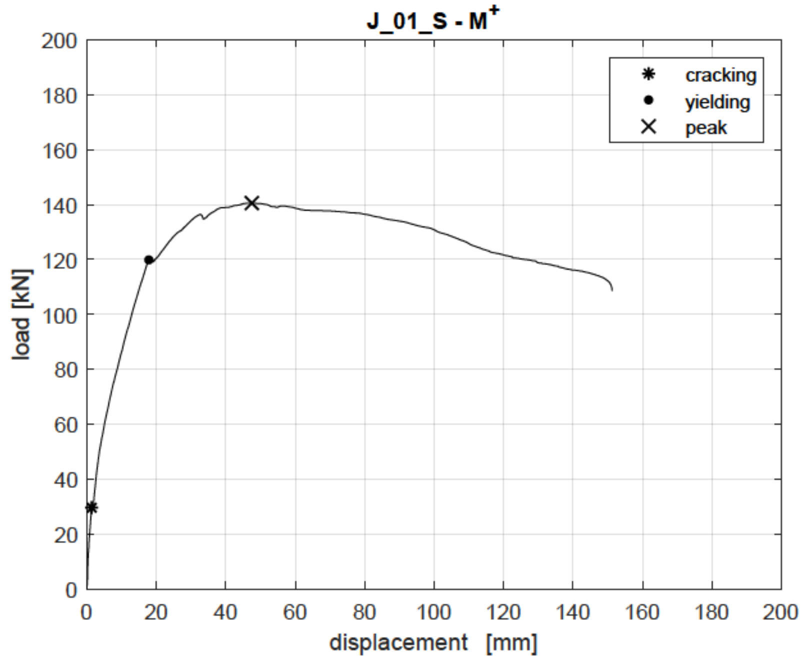

FIGURE 4.21: Load vs displacement response of $J\_01\_S - M^{+}$ specimen.

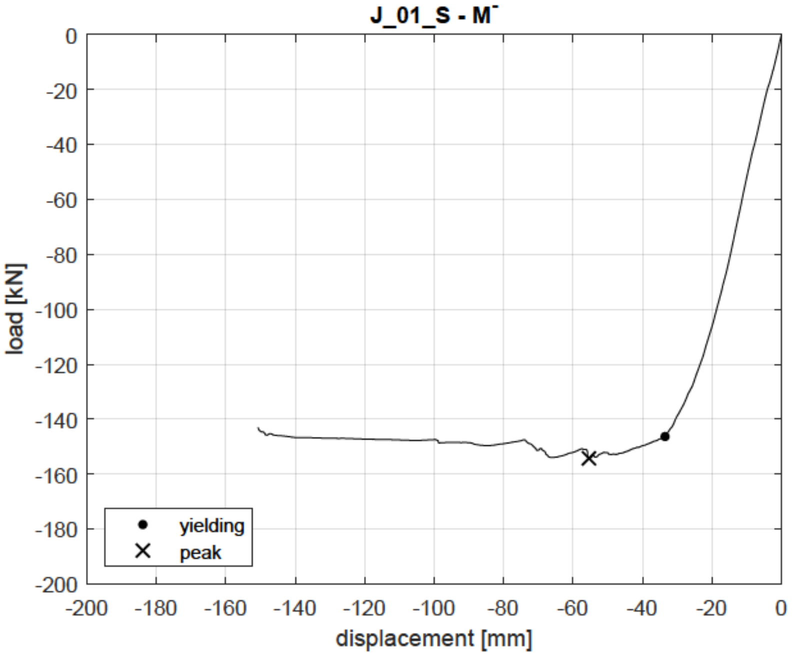

FIGURE 4.22: Load vs displacement response of $J\_01\_S - M^{-}$ specimen.

The first cracking was experimentally evaluated from the curves and the values are reported in Table 4.4, with reference to each test. In particular, the first cracking in positive loading direction was found at $+33.73kN$ in the $J\_01\_S - Geolite - C$ specimen, at $+35.05kN$ in $J\_01\_S - C$, and $+29.55kN$ in $J\_01\_S - M^+$, corresponding to a positive cracking moment, M^+_{cr}, of, respectively, $+52.62kNm$, $+54.68kNm$ and $+46.10kNm$. In the negative loading direction, first cracking was supposed to occur at $-68.04kN$ and $-66.29kN$ in, respectively, $J\_01\_S - Geolite - C$ and $J\_01\_S - C$ test, corresponding to negative cracking moments, M^-_{cr}, of $-106.14kNm$ and $-103.41kNm$. The response of $J\_01\_S - M^-$ specimen did not show clearly the first cracking point, hence no values were reported. The cracking moments can be also checked from the moment versus rotation plots in the following Section 4.2.2.2. Alternatively, the experimental values of the cracking moments, evaluated by considering the $L_c = 1.41m$ lever arm, were $+47.56kNm$ and $-95.94kNm$ in $J\_01\_S - Geolite - C$ specimen, $+49.42kNm$ and $-93.47kNm$ in $J\_01\_S - C$ and $+41.66kNm$ in $J\_01\_S - M^+$. Also for specimens equipped with the deck, the first cracking moments were predicted with reference to the transverse beam section (30x40cm). The values were $27.65kNm$ and in $J\_01\_S - Geolite - C$ specimen, $31.70kNm$ in $J\_01\_S - C$, $26.09kNm$ in $J\_01\_S - M^+$, and $25.97kNm$ in $J\_01\_S - M^-$.

The general yielding values for J_01_S specimens are shown in Table 4.5. In detail, in the positive loading direction, the general yielding was supposed to occur at a load of $+109.50kN$ in $J\_01\_S - Geolite - C$, $+107.18kN$ in $J\_01\_S - C$ and $+119.84kN$ in $J\_01\_S - M^+$, corresponding to a displacement of, respectively, $+16.16mm$, $+16.51mm$ and $+17.85mm$. In the negative loading direction, the general yielding was assumed to take place at a load of $-134.59kN$ in $J\_01\_S - Geolite - C$, $-134.16kN$ in $J\_01\_S - C$, and $-146.31kN$ in $J\_01\_S - M^-$, at the displacements of, respectively, $-25.07mm$, $-27.39mm$ and $-33.52mm$. The corresponding yielding moments, evaluated through L_i, were $M^+_y = +170.82kNm$ and $M^-_y = -209.96kNm$ in $J\_01\_S - Geolite - C$, $M^+_y = +167.20kNm$ and $M^-_y = -209.96kNm$ in $J\_01\_S - C$, $M^+_y = +186.95kNm$ in $J\_01\_S - M^+$, and $M^-_y = -228.24kNm$ in $J\_01\_S - M^-$. The corresponding yielding moments, evaluated through L_c, were $M^+_y = +154.40kNm$ and $M^-_y = -189.77kNm$ in $J\_01\_S - Geolite - C$, $M^+_y = +151.12kNm$ and $M^-_y = -189.17kNm$ in $J\_01\_S - C$, $M^+_y = +168.98kNm$ in $J\_01\_S - M^+$, and $M^-_y = -206.30kNm$ in $J\_01\_S - M^-$. The expected yielding moments were evaluated by referring to the transverse beam section (30x40cm). The values are $M^{+/-}_y = \pm 96.66kNm$ for $J\_01\_S - Geolite - C$ and $J\_01\_S - C$, $M^{+/-}_y = \pm 107.47kNm$ for $J\_01\_S - M^+$ and $J\_01\_S - M^-$. Note that the theoretical and expected values are strongly different due to the presence of the floor deck. Moreover, in the case of applied negative displacements, the general yielding point was not readily identified, as resulted in the examined bibliography [14]. The resistance in negative bending did not stop growing as large displacements were imposed and more slab reinforcement was activated.

The peak loads and the corresponding displacements are summarised in Table

4.6. The maximum loads achieved for positive displacements from the specimens $J\_01\_S - Geolite - C$, $J\_01\_S - C$ and $J\_01\_S - M^{+}$, were, respectively, $+125.18kN$, $+118.72kN$ and $+140.55kN$, at the displacements of $+31.79mm$, $+41.62mm$ and $+47.51mm$. The corresponding displacement ductility d_E/d_y was, in an orderly manner, 1.97, 2.52 and 2.66. The maximum loads achieved when the specimens were subjected to negative displacements, i.e. in $J\_01\_S - Geolite - C$, $J\_01\_S - C$ and $J\_01\_S - M^{-}$ tests, were $-156.33kN$, $-164.79kN$ and $-154.27kN$, at the pertaining displacements of $-52.14mm$, $-51.32mm$ and $-55.44mm$. As a consequence, the displacement ductility d_E/d_y was, respectively, 2.08, 1.87 and 1.65.

Since $J\_01\_S - Geolite - C$ specimen was the first module to be tested and it was employed as a test set-up, the loading protocol was applied until the buckling of the transverse beam reinforcement. The peak load in the last performed positive drift level was $+29.25kN$ at a displacement of $+84.80mm$. The peak load in the last performed negative drift level was $-120.40kN$ at a displacement of $-76.10mm$. In conclusion, the test ended once the decrease in resistance reached 77%, in a positive loading direction, and 23% in the negative one. The hysteresis loops increased as the imposed displacements were greater.

On the contrary, in the homologous $J\_01\_S - C$ specimen, a considerable resistance drop, about 34%, was observed only in the hogging moment condition, i.e. when the slab undergoes tensile stresses. In sagging bending conditions, the loss of resistance was 12%. For positive loading, the peak load was quite similar to the yielding one. This test, indeed, was discontinued before the test performed on $J\_01\_S - Geolite - C$ specimen. It was stopped at the positive peak load of $+105.00kN$, corresponding to $+69.50mm$ displacement, and at the peak negative load of $-109.20kN$, related to a displacement of $-67.32mm$. Concerning the dissipative behaviour, the hysteresis loops are increasingly larger, especially under negative loading where a fat cycle was observed at the 11th drift level.

The test on $J\_01\_S - M+$ specimen ended at a load of $+108.56kN$ and a displacement of $+151.23mm$, at about 23% of the resistance loss. The test on $J\_01\_S - M-$ specimen was disrupted at a load of $-143.00kN$ and a displacement of $-150.70mm$, at about 7% of the resistance loss, since, in this case, the load settled on a plateau branch.

Specimen	F_{cr}^{+} [kN]	d_{cr}^{+} [mm]	F_{cr}^{-} [kN]	d_{cr}^{-} [mm]
$J\_01\_S - Geolite - C$	33.73	1.78	-68.04	-6.01
$J\_01\_S - C$	35.05	3.49	-66.29	-9.11
$J\_01\_S - M^{+}$	29.55	1.42	-	-
$J\_01\_S - M^{-}$	-	-	-	-

TABLE 4.4: Positive and negative first cracking loads and corresponding displacements for specimens $J\_01\_S - Geolite - C$, $J\_01\_S - C$, $J\_01\_S - M^{+}$ and $J\_01\_S - M^{-}$.

Specimen	F_y^+ [kN]	d_y^+ [mm]	F_y^- [kN]	d_y^- [mm]
$J\_01\_S - Geolite - C$	109.50	16.16	-134.59	-25.07
$J\_01\_S - C$	107.18	16.51	-134.16	-27.39
$J\_01\_S - M^+$	119.84	17.85	-	-
$J\_01\_S - M^-$	-	-	-146.31	-33.52

TABLE 4.5: Positive and negative yielding loads and corresponding displacements for specimens $J\_01\_S - Geolite - C$, $J\_01\_S - C$, $J\_01\_S - M^+$ and $J\_01\_S - M^-$.

Specimen	F_E^+ [kN]	d_E^+ [mm]	F_E^- [kN]	d_E^- [mm]
$J\_01\_S - Geolite - C$	125.18	31.79	-156.33	-52.14
$J\_01\_S - C$	118.72	41.62	-164.79	-51.32
$J\_01\_S - M^+$	140.55	47.51	-	-
$J\_01\_S - M^-$	-	-	-154.27	-55.44

TABLE 4.6: Maximum and minimum loads and corresponding displacements for specimens $J\_01\_S - Geolite - C$, $J\_01\_S - C$, $J\_01\_S - M^+$ and $J\_01\_S - M^-$.

4.2.2.2 Moment-Rotation Response

The response of the conventional joints with the deck, in terms of moment versus rotation, was herein reported. The moment vs rotation curves of J_01_S specimens subjected to the cyclic load protocol, i.e. $J\_01\_S - Geolite - C$ and $J\_01\_S - C$, are given, respectively, in Figure 4.23, where the peak moments observed were $+195.29kNm$ and $-243.88kNm$, and in Figure 4.24, where the peak moments were $+185.20kNm$ and $-257.07kNm$. Figure 4.25 and Figure 4.26 show the moment-rotation plots of J_01_S specimens subjected to the monotonic loading protocol, i.e. $J\_01\_S - M^+$ and $J\_01\_S - M^-$. The maximum moment sustained by the former specimen was $+219.25kNm$ while the minimum moment sustained by the latter was $-240.66kNm$.

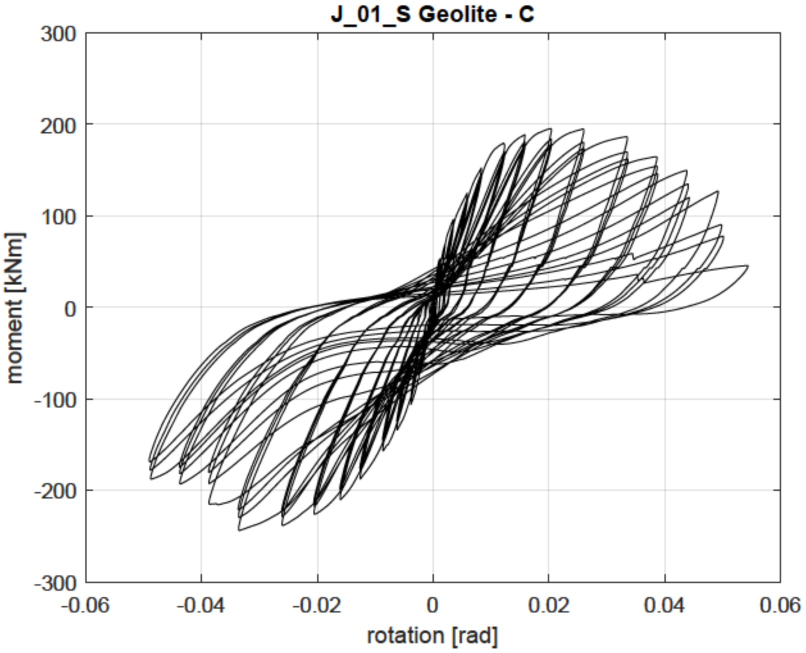

FIGURE 4.23: Moment vs rotation response of $J\_01\_S - Geolite - C$ specimen.

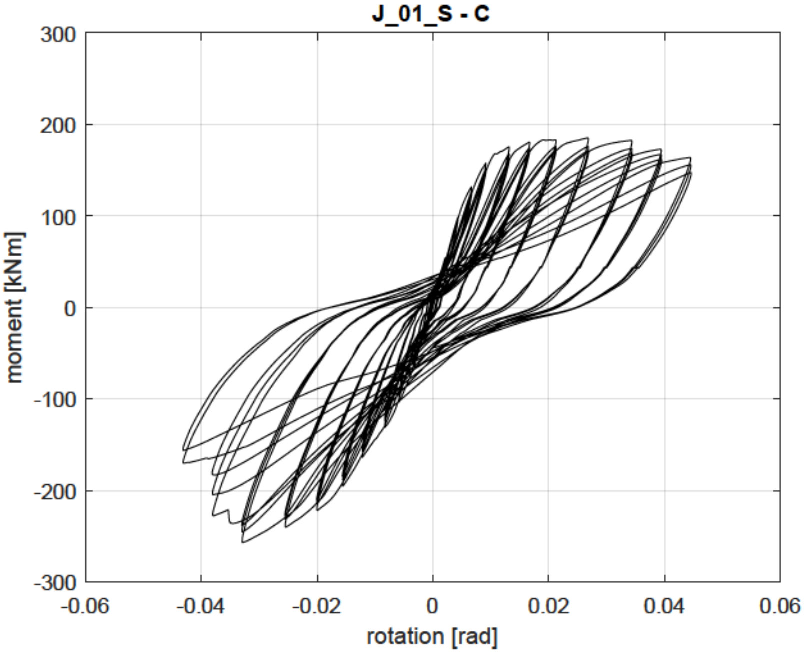

FIGURE 4.24: Moment vs rotation response of $J\_01\_S - C$ specimen.

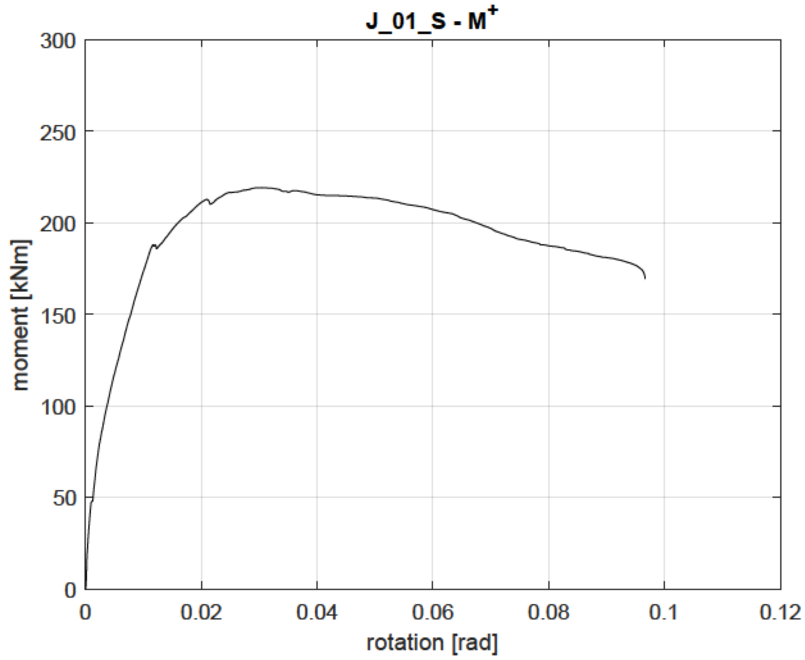

FIGURE 4.25: Moment vs rotation response of $J\_01\_S - M^{+}$ specimen.

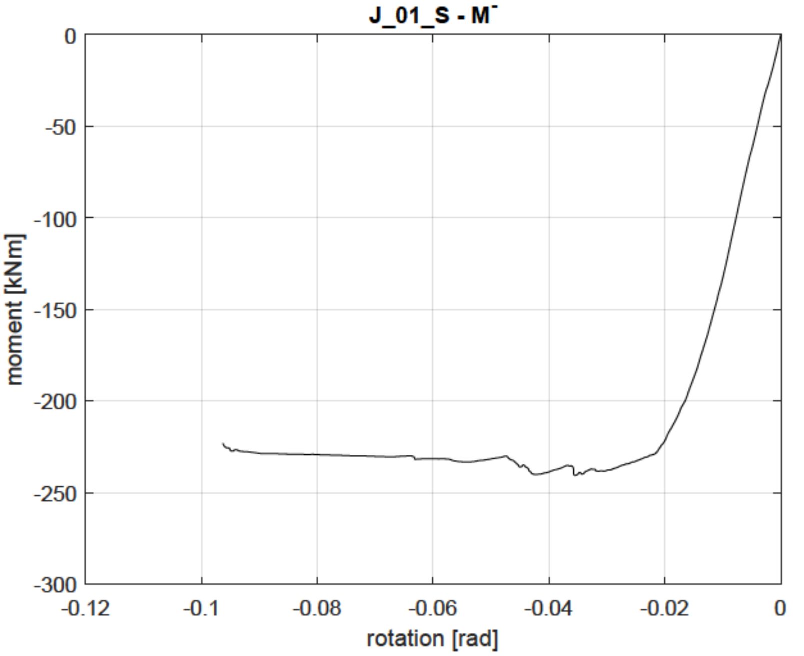

FIGURE 4.26: Moment vs rotation response of $J\_01\_S - M^{-}$ specimen.

In addition, the non-dimensional moment versus rotation curves are reported in Figure 4.27 and Figure 4.28, for $J\_01\_S - Geolite - C$ and $J\_01\_S - C$ specimens, and in Figure 4.29 and Figure 4.30 for $J\_01\_S - M^{+}$ and $J\_01\_S - M^{-}$ specimens. The moment of resistance of the transverse beam, by which the experimental moment was divided in order to obtain the non-dimensional moment, was evaluated according to the hypothesis given in the previous Section 4.2.1.2. The computed absolute values were $M_R^{+/-} = 102.83kNm$ for the transverse beam of $J\_01\_S - Geolite - C$ module and $M_R^{+/-} = 103.86kNm$ for that of $J\_01\_S - C$, while it was $M_R^{+} = 113.19kNm$ for $J\_01\_S - M^{+}$ and $M_R^{-} = 113.16kNm$ for $J\_01\_S - M^{-}$. The maximum and minimum non-dimensional moment of 1.90 and -2.37 were observed in $J\_01\_S - Geolite - C$ test and 1.78 and -2.48 in $J\_01\_S - C$. During the monotonic test for positive displacements, $J\_01\_S - M^{+}$ test, the maximum value of 1.94 was observed, while for negative displacements, in $J\_01\_S - M^{-}$ specimen, the minimum value of -2.13 was noticed. Compared to J_01 beam-to-column joints, the overall resistance was greatly increased by the floor deck presence.

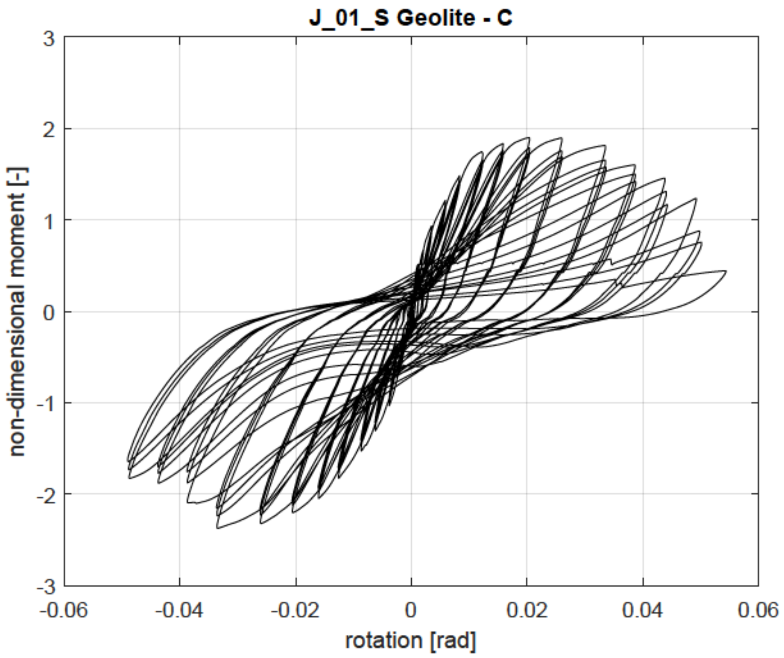

FIGURE 4.27: Non-dimensional moment vs rotation response of $J\_01\_S - Geolite - C$ specimen.

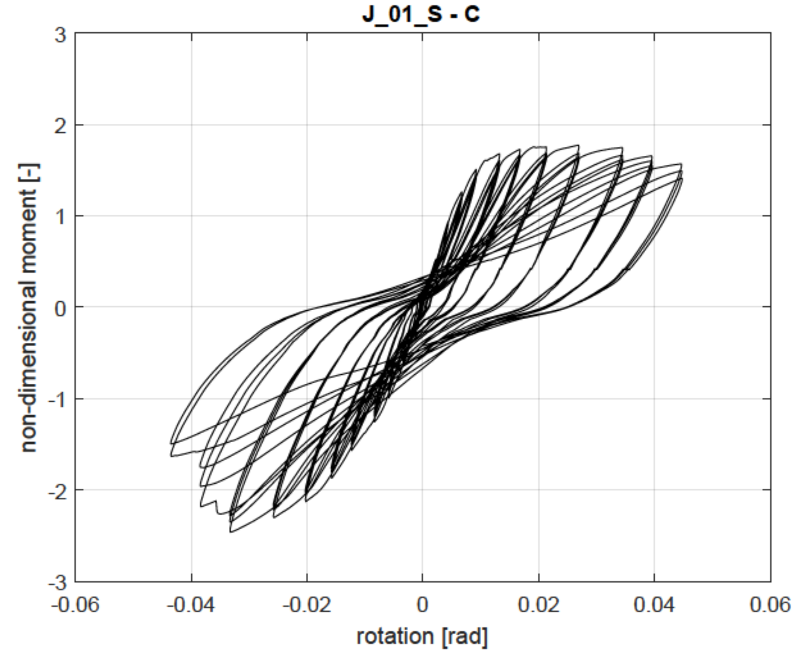

FIGURE 4.28: Non-dimensional moment vs rotation response of $J\_01\_S - C$ specimen.

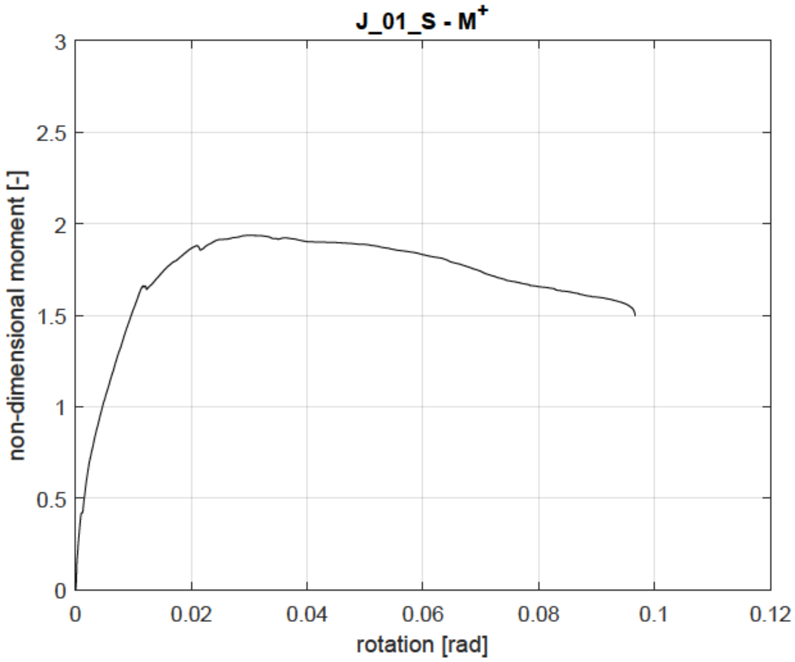

FIGURE 4.29: Non-dimensional moment vs rotation response of $J\_01\_S - M^+$ specimen.

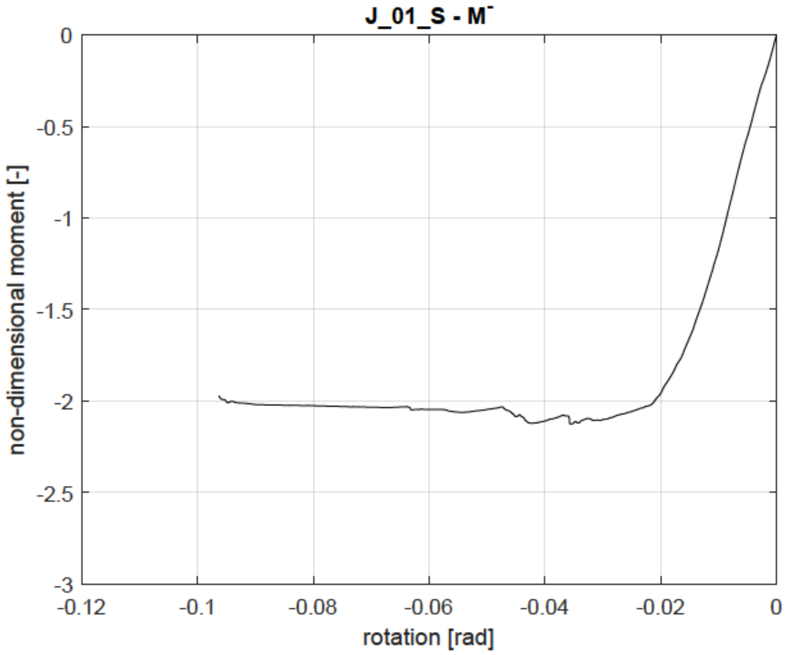

FIGURE 4.30: Non-dimensional moment vs rotation response of $J\_01\_S - M^-$ specimen.

Finally, for the monotonic tests, the moment versus beam rotation was plotted with reference to the rotation deriving from the displacements detected by the LDTs near the transverse beam, H-LDT_3 and H-LDT_4, and those obtained from Equations 4.2.1 and 4.2.2. The two curves are represented with, respectively, a black continuous line and a red dotted line, where the last values of the beam rotation were about $0.07rad$ and $0.09rad$, in $J\_01\_S - M^+$ specimen (Figure 4.31) and $-0.06rad$ and $-0.08rad$ in $J\_01\_S - M^-$ specimen (Figure 4.32).

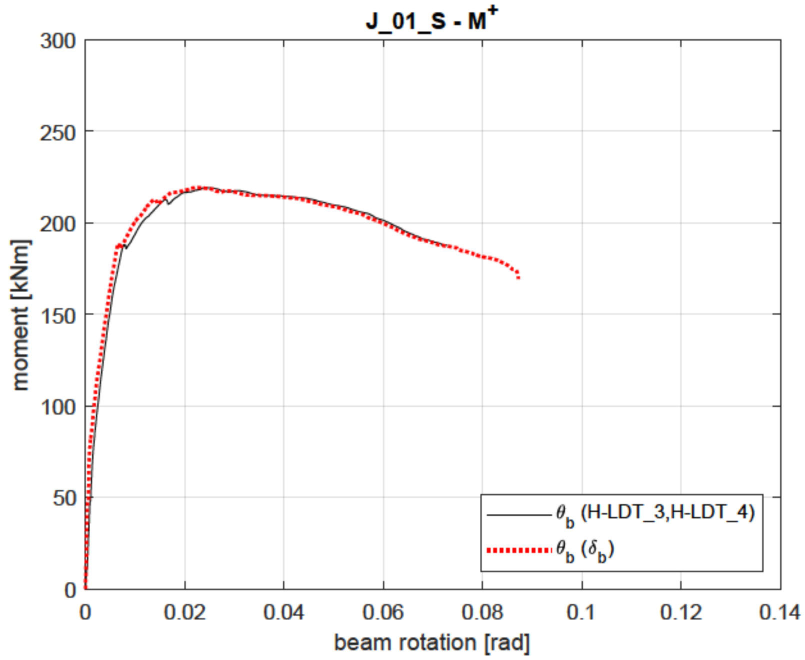

FIGURE 4.31: Moment vs beam rotation response of $J\_01\_S - M^{+}$ specimen.

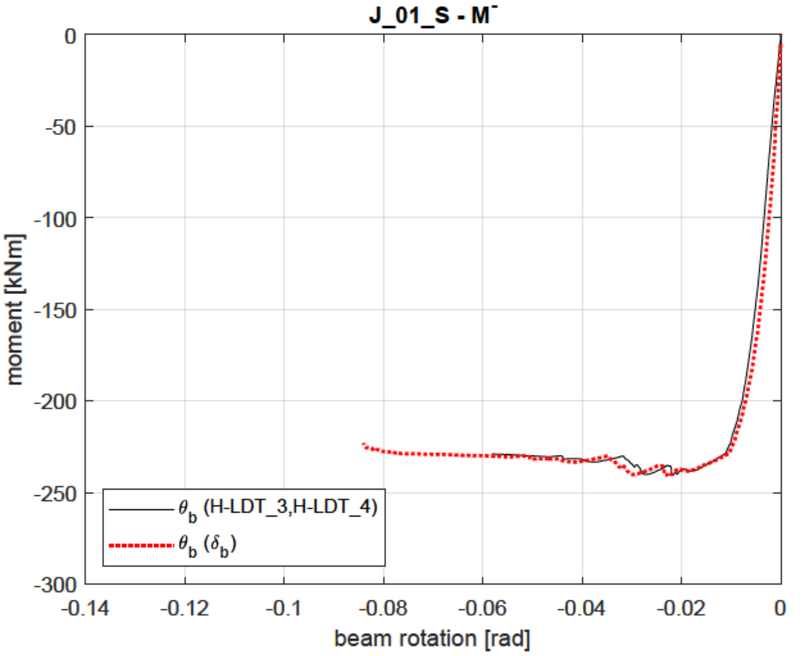

FIGURE 4.32: Moment vs beam rotation response of $J\_01\_S - M^{-}$ specimen.

4.2.2.3 Joists and Beam Response

The displacements exhibited by the joists and beam during the test are herein reported. Figure 4.33 reminds the position of the horizontal LDTs equipping specimens with the floor deck.

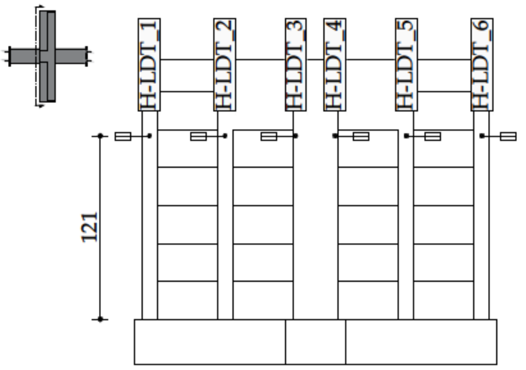

FIGURE 4.33: Arrangement of the joists and beam LDTs equipping specimens with the floor deck.

In Figure 4.34 the joists and beam displacements are plotted with reference to $J\_01\_S - Geolite - C$ specimen. For the test set-up, linear transducers having $50mm$ total stroke were employed, The stroke limit, which is the plateau line in the final cycles of the curves, was achieved widely before the test end. This resulted in an incomplete and asymmetric reading of the sensors. The peak displacements of the joists in positive and negative loading direction were $+24.58mm$ and $-18.24mm$ for H-LDT_1, $+24.58mm$ and $-20.57mm$ for H-LDT_2, $+26.82mm$ and $-23.16mm$ for H-LDT_5. Instead, some problems occurred in the H-LDT_6 sensor. The maximum and minimum displacements of the beam were $+32.34mm$ and $-17.63mm$ from H-LDT_3, $+18.15mm$ and $-31.82mm$ from H-LDT_4.

In the following tests, LDTs having a stroke of $100mm$ were employed. In this way, reliable information was collected for a considerable extent of the test. Figure 4.35 illustrates the response of $J\_01\_S - C$ specimen in terms of the joists and beam displacements versus time. H-LDT_1 showed peak displacements of $+40.05mm$ and $-13.54mm$; H-LDT_2 displacements of $+45.06mm$ and $-23.47mm$; H-LDT_5 $+40.72mm$ and $-21.37mm$, and H-LDT_6 $+40.82mm$ and $-12.29mm$. The maximum and minimum displacements detected by H-LDT_3 were $+57.44mm$ and $-34.44mm$, and those detected by H-LDT_4 were $+60.73mm$ and $-29.45mm$. The response under positive and negative loading is not symmetric, with higher absolute values recorded in positive direction. The displacements histories of the homologous sensors, i.e. those equidistant from the main beam (the couples H-LDT_1 and H-LDT_6, H-LDT_3 and H-LDT_4, and H-LDT_2 and H-LDT_5), are quite similar.

The horizontal floor deck displacements of $J\_01\_S - M^+$ module are pointed out in Figure 4.36 and they are very similar to each other. The blue and black curves, representing the displacements of the main beam, overlapped. The maximum displacements reached by H-LDT_3 and H-LDT_4 are, respectively, $+99.29mm$ and

$+88.38mm$, but the latter stopped reading before the former. Peaks achieved by the other sensors were $+93.74mm$ for H-LDT_1, $+96.22mm$ for H-LDT_2, $+99.25mm$ for H-LDT_5, and $+92.71mm$ for H-LDT_6. From the chart, it can be concluded that the response of the joists was substantially equal along the bay span.

In the monotonic test where the beam underwent a hogging bending, i.e. in the $J\_01\_S - M^{-}$ test, the gap among the displacements of the coupled deck elements became larger. The displacements of the main beam and joists were clearly different. The homologous joists exhibited quite the same displacements trend. Nevertheless, it is evident that something went wrong in H-LDT_6 curve, which, at the beginning of the test, perfectly followed the curve of H-LDT_1. However, the peak displacements achieved during the test were: $-49.96mm$ and $-19.54mm$ in H-LDT_1 and H-LDT_6, $-72.29mm$ and $-78.39mm$ in H-LDT_2 and H-LDT_5, and $-81.37mm$ and $-79.39mm$ in H-LDT_3 and H-LDT_4.

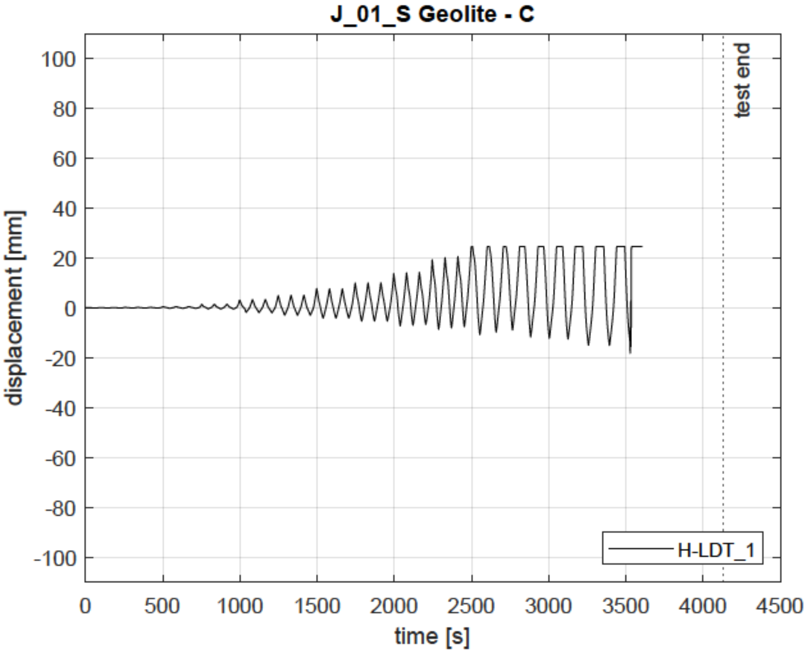

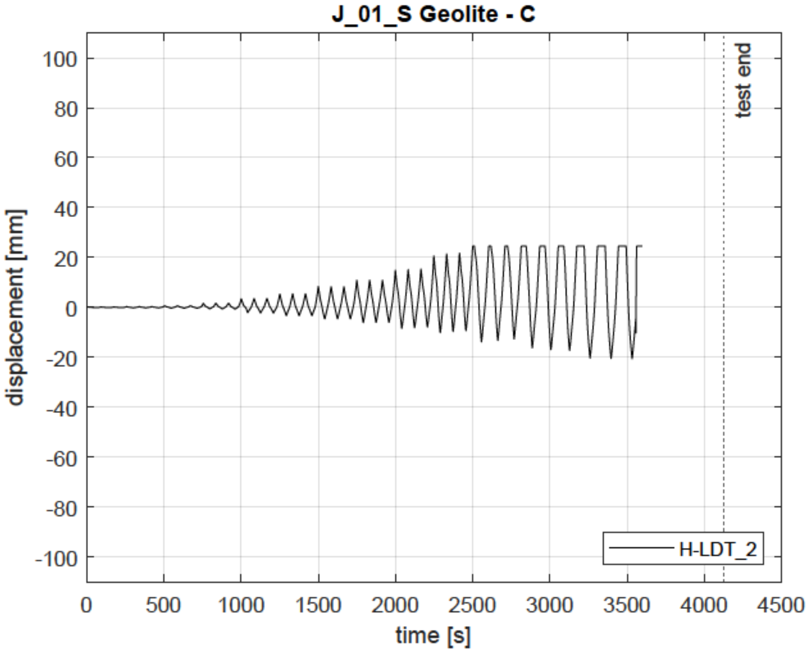
J_01_S Geolite - C
displacement [mm]
100
80
60
40
20
0
-20
-40
-60
-80
-100
time [s]
0
500
1000
1500
2000
2500
3000
3500
4000
4500
test end
H-LDT_2

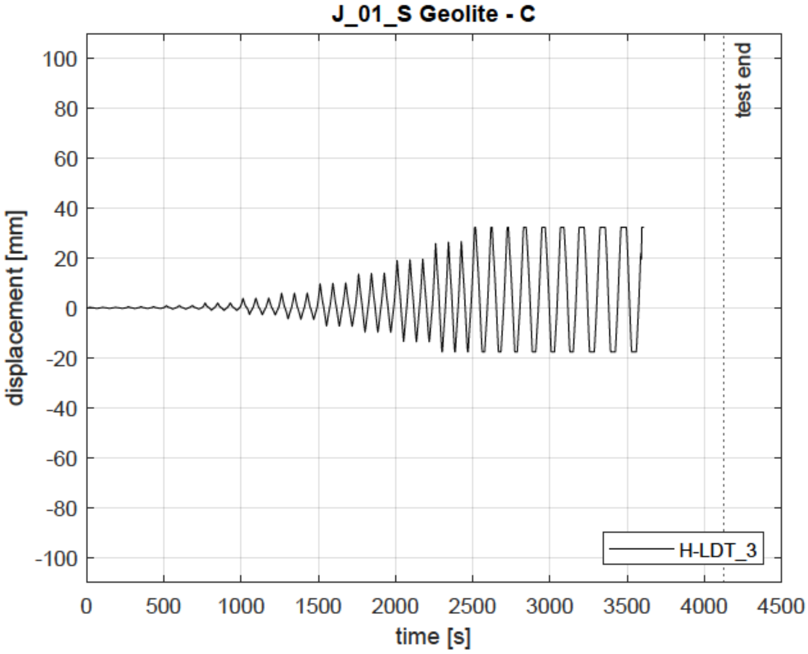
J_01_S Geolite - C
displacement [mm]
100
80
60
40
20
0
-20
-40
-60
-80
-100
time [s]
0
500
1000
1500
2000
2500
3000
3500
4000
4500
test end
H-LDT_3

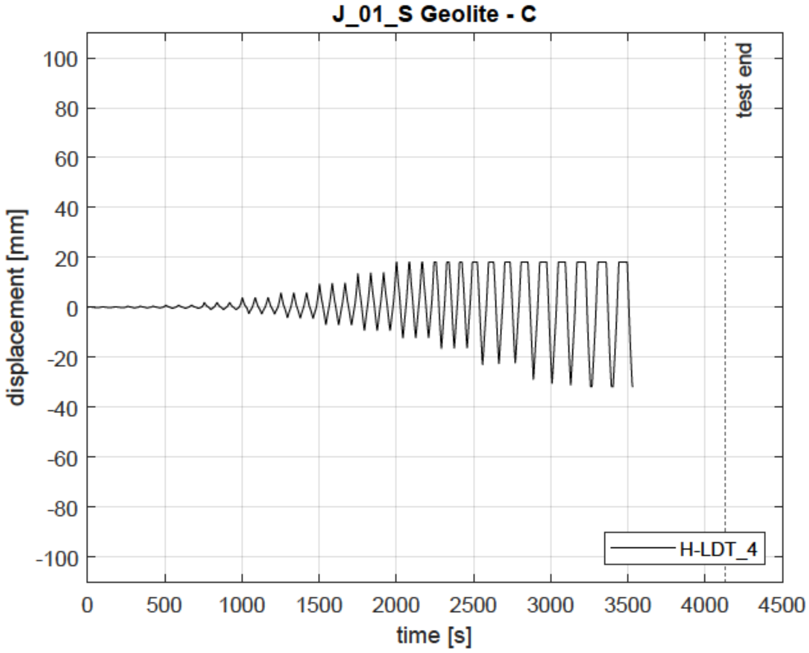
J_01_S Geolite - C
displacement [mm]
time [s]
100
80
60
40
20
0
-20
-40
-60
-80
-100
0
500
1000
1500
2000
2500
3000
3500
4000
4500
test end
H-LDT_4

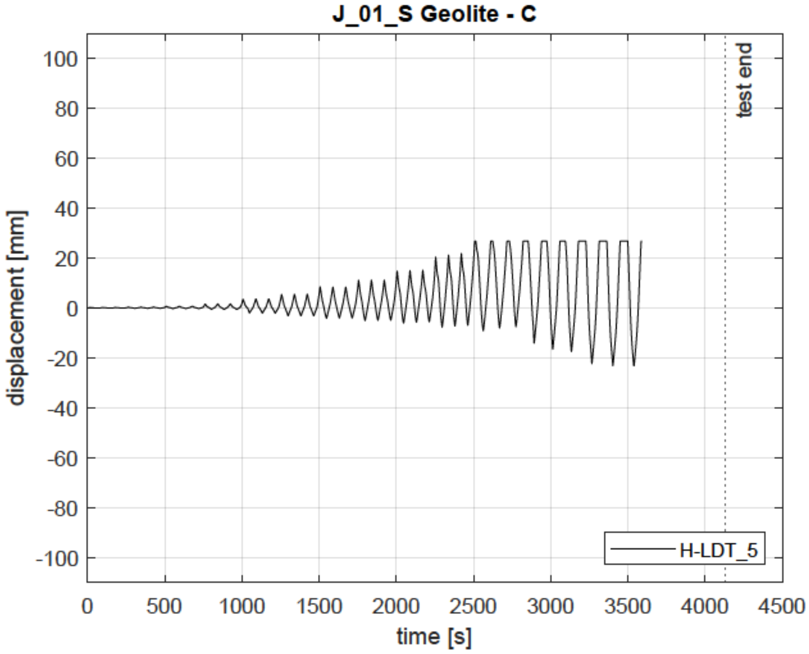
J_01_S Geolite - C
displacement [mm]
time [s]
100
80
60
40
20
0
-20
-40
-60
-80
-100
0
500
1000
1500
2000
2500
3000
3500
4000
4500
test end
H-LDT_5

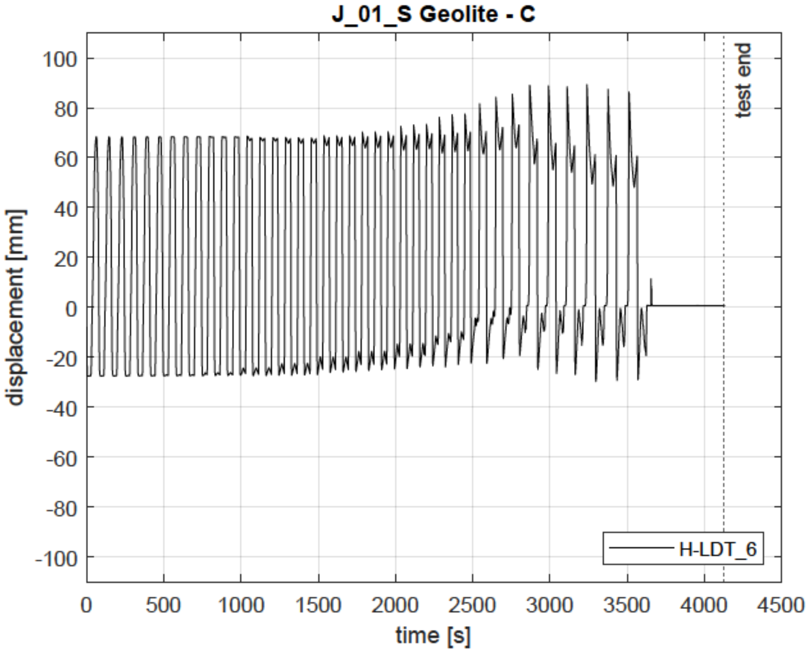

FIGURE 4.34: Joists displacements vs time of $J\_01\_S - Geolite - C$ specimen.

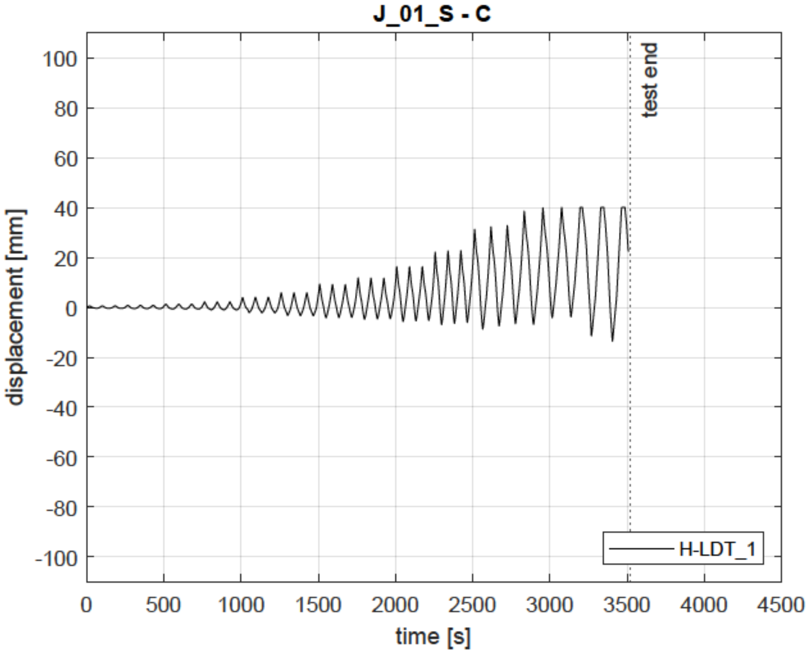

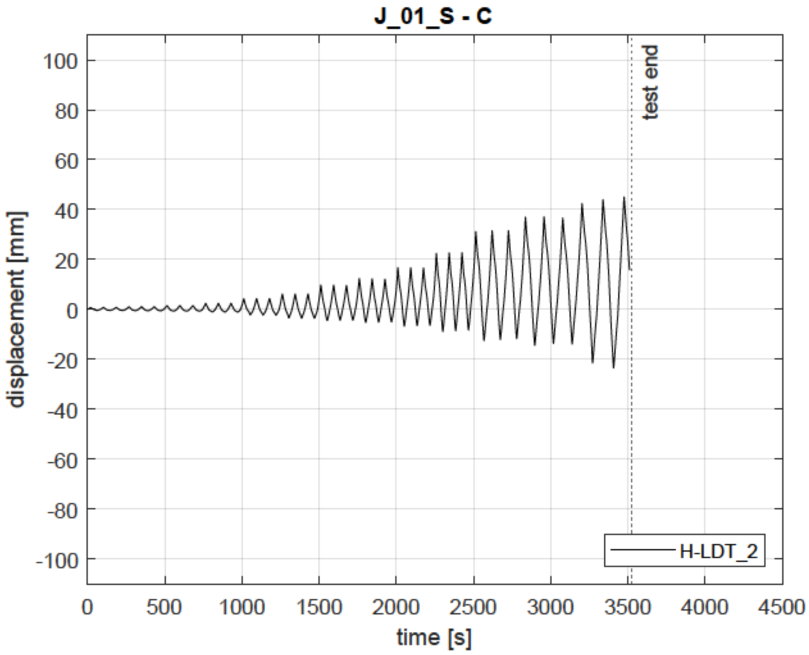
J_01_S - C
displacement [mm]
time [s]
100
80
60
40
20
0
-20
-40
-60
-80
-100
0
500
1000
1500
2000
2500
3000
3500
4000
4500
test end
H-LDT_2

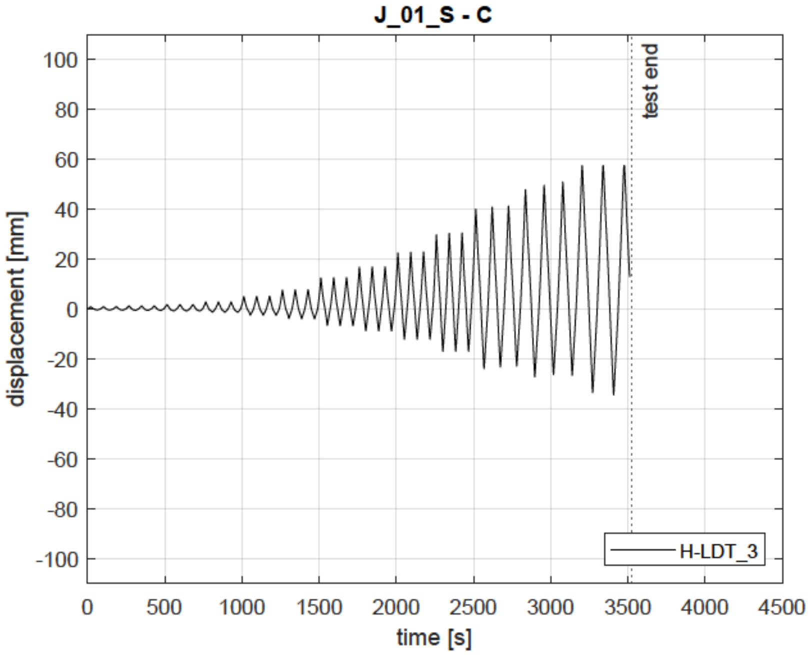
J_01_S - C
displacement [mm]
time [s]
100
80
60
40
20
0
-20
-40
-60
-80
-100
0
500
1000
1500
2000
2500
3000
3500
4000
4500
test end
H-LDT_3

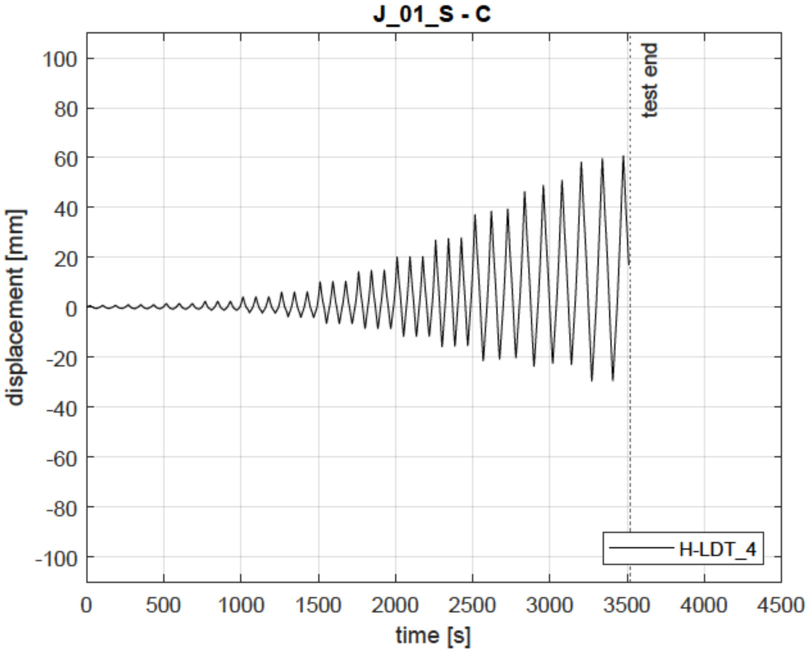
J_01_S - C
displacement [mm]
time [s]
100
80
60
40
20
0
-20
-40
-60
-80
-100
0
500
1000
1500
2000
2500
3000
3500
4000
4500
test end
H-LDT_4

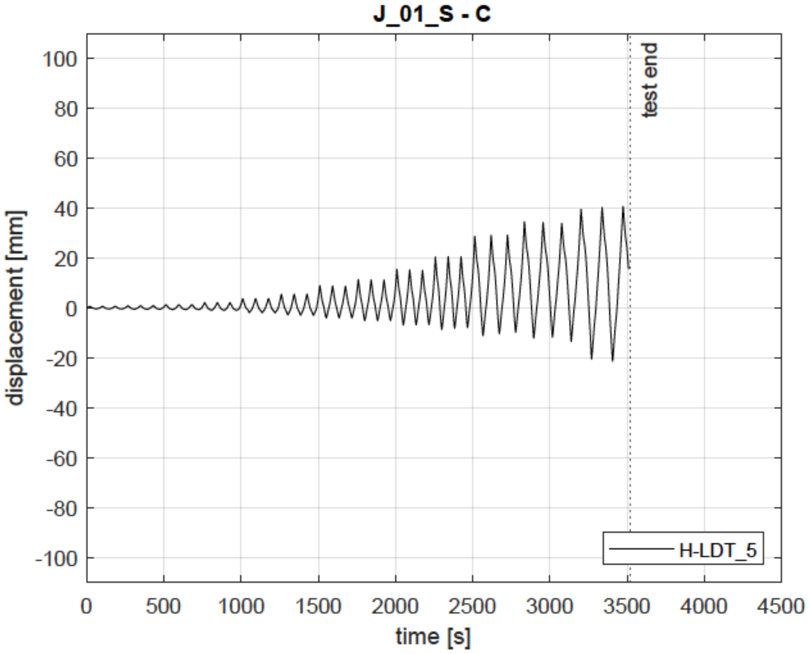
J_01_S - C
displacement [mm]
time [s]
100
80
60
40
20
0
-20
-40
-60
-80
-100
0
500
1000
1500
2000
2500
3000
3500
4000
4500
test end
H-LDT_5

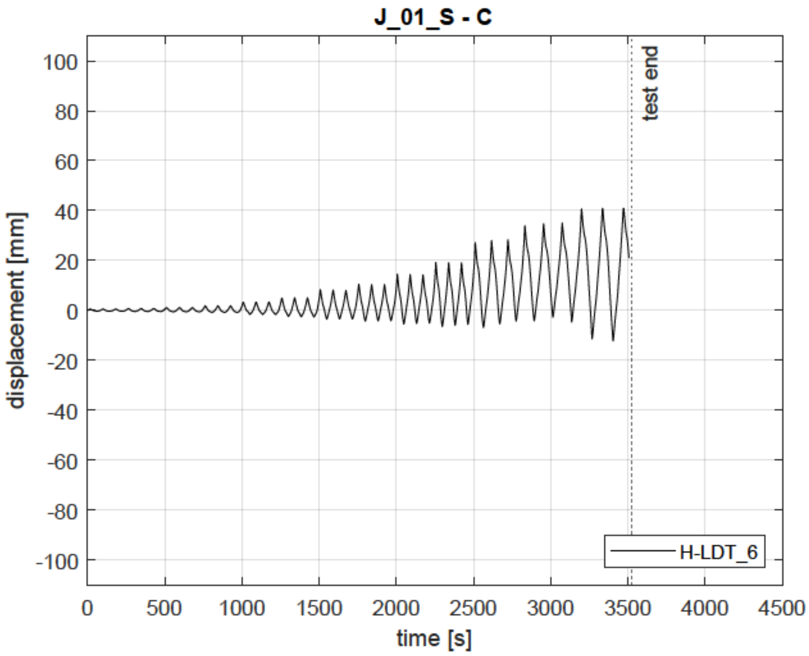

FIGURE 4.35: Joists displacements vs time of J_01_S-C specimen.

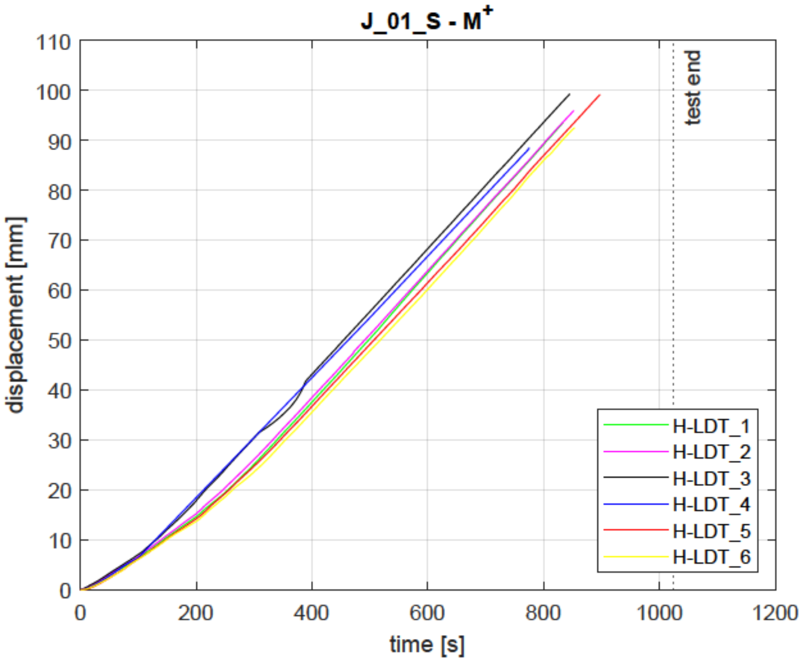

FIGURE 4.36: Joists displacements vs time of $J\_01\_S-M^{+}$ specimen.

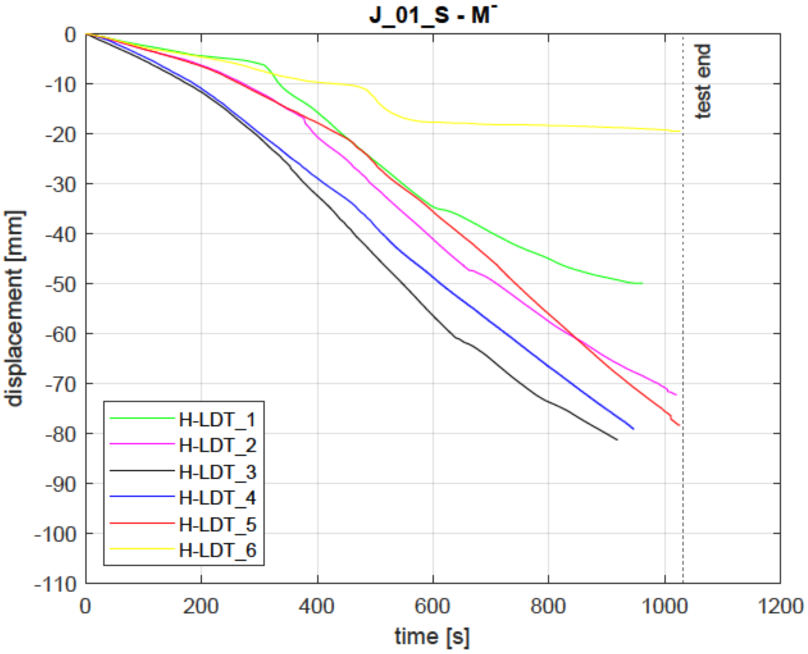

FIGURE 4.37: Joists displacements vs time of $J\_01\_S - M^-$ specimen.

4.2.2.4 Crack Pattern

The crack pattern evolution of conventional specimens equipped with the floor deck is explained for each test, but the general behaviour, deduced from the experimental evidence, is described in advance. The damage in J_01_S modules was primarily localised in the dissipative zone, which, for specimens with the deck as for those without it, is properly the end of the main beam. However, its extent varied, since it was greater in joints without the deck, as can be checked by comparing Figure 4.16 with Figures 4.41 and 4.45. Moreover, cracks spread over the slab and the beams supporting the joists. The cracks in the longitudinal beams were 45° oriented and they were rather diffused when the slab underwent tensile stress. On the contrary, in the column and joint area, no damage was observed.

The damage progression in the cyclic test on $J\_01\_S - Geolite - C$ module is depicted in Figures 4.38, 4.39, 4.40 and 4.41. On the side of the joists (Figure 4.38), the first crack appeared at the beam-column interface and it, gradually, spread at the intersection between the deck and longitudinal beams. Upon further loading, other cracks, parallel to the first one, appeared at a gradually increasing distance from the column face, until the spalling of the concrete cover.

On the slab side (Figure 4.39), horizontal cracks started at the slab-column intersection and then propagated on both sides of the connection. The third crack appeared in the slab, parallel to the previous ones, at about $30cm$ from the column. Then, cracks with different slope spread near the smallest sides of the column, toward the exterior part of the connection. At increasing displacement levels, the cracks, firstly appeared at the beam-column interface, extended along the deck span (label 6 in Figure 4.39), until the external left and right sides of the deck and another crack, number 7, arose at about $50cm$ from the column face.

When the test ended, the external side of the connection appeared as in Figure 4.40. The cracks $4-5$ proceeded from the slab to spandrel beams, with an inclination of approximately 45°. By the point in which they intersected the longitudinal beams external side, a wide fracture originated around the slab thickness ($5cm$), crossing the entire length of the beams. No damage, instead, affected the joint area.

As the final state of the beam reinforcement in the plastic hinge zone suggests (Figure 4.41), the test on $J\_01\_S - Geolite - C$ specimen was disrupted once the bars buckling occurred. For this reason, although they are similar, the crack pattern of the $J\_01\_S - Geolite - C$ specimen was more widespread as compared to that of $J\_01\_S - C$, which is depicted in Figures 4.42, 4.43, 4.44 and 4.45. For this latter, the width of cracks also reduced.

FIGURE 4.38: Crack pattern evolution on the joists side of $J\_01\_S - Geolite - C$ specimen.

FIGURE 4.39: Crack pattern evolution on the slab side of $J\_01\_S - Geolite - C$ specimen.

FIGURE 4.40: Crack pattern evolution in the joint and longitudinal beams of $J\_01\_S - Geolite - C$ specimen.

(a) (b)

FIGURE 4.41: Final damage on beam front (a) and lateral (b) sides of $J\_01\_S - Geolite - C$ specimen.

FIGURE 4.42: Crack pattern evolution on the joists side of $J\_01\_S - C$ specimen.

FIGURE 4.43: Crack pattern evolution on the slab side of J_01_S-C specimen.

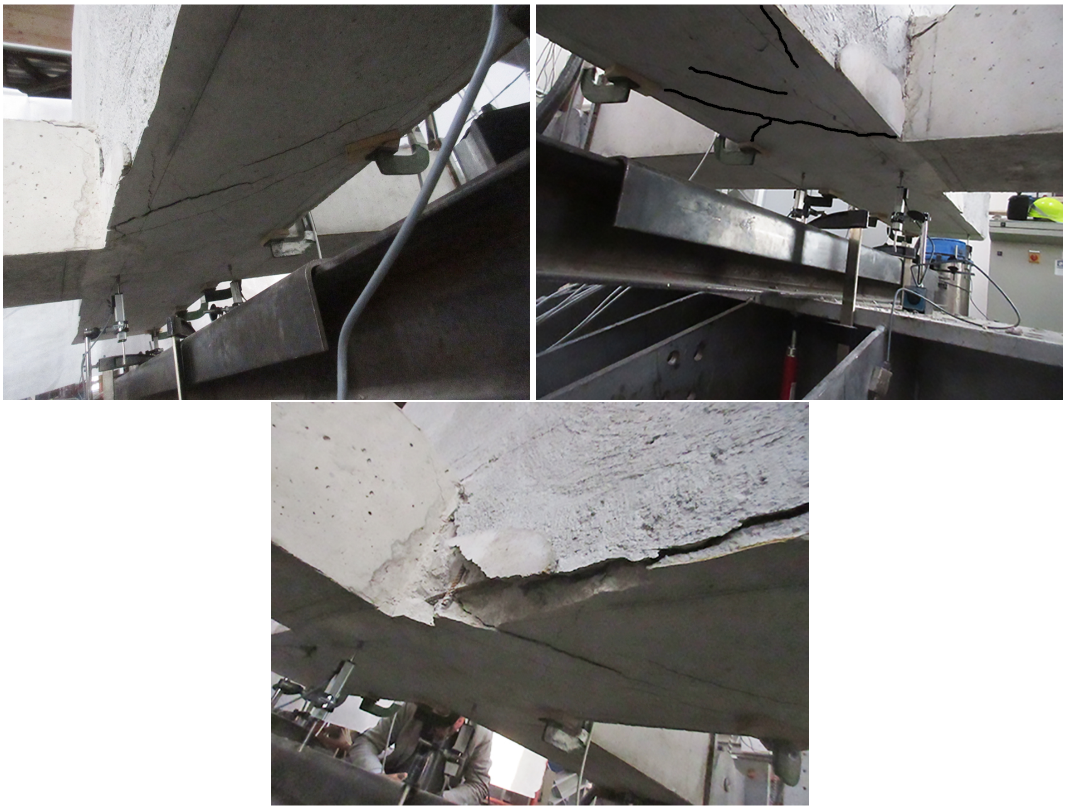

FIGURE 4.44: Crack pattern evolution in the joint and longitudinal beams of J_01_S-C specimen.

FIGURE 4.45: Final damage in the beam of $J\_01\_S - C$ specimen.

The crack pattern in the monotonic tests, illustrated in Figures 4.46, 4.47, 4.48 and 4.49 for $J\_01\_S - M^{+}$ specimen, and in Figures 4.50, 4.51 and 4.52 for $J\_01\_S - M^{-}$, was obviously similar to that of the cyclic tests. However, by separately applying the uni-directional loading histories, the damage due to the positive and negative displacements can be distinguished.

In $J\_01\_S - M^{+}$ specimen, the first crack appeared at the transverse beam-column interface and, then, it ran over the deck-spandrel beams interface. Later, the damage increased in a localised area of about $20cm$ length from the column face, which was the plastic hinge zone (Figure 4.49). Because of the greater displacements imposed in the monotonic tests, on the side of the joists, the damage affected also the hollow tile blocks, especially near the plastic hinge area, as underlined in Figure 4.46. On the slab side, the crushing damage was limited to a few centimetres above the beam-column intersection (Figure 4.47). On the external side of the connection, whose final condition is depicted in Figure 4.48, the damage was noticed neither in the joint area nor in spandrel beams. Longitudinal beams, instead, were only damaged at their ends, by differently inclined cracks flowing also in the slab, for few centimetres (the photo on the right of Figure 4.47).

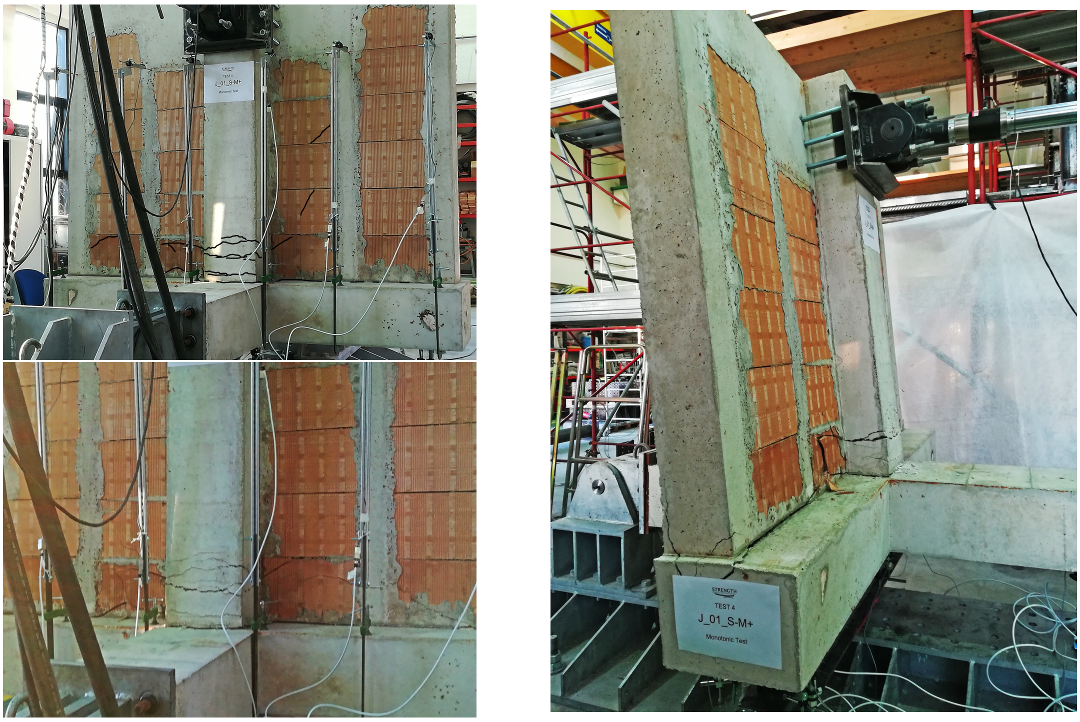

FIGURE 4.46: Crack pattern evolution on the joists side of $J\_01\_S-M^+$ specimen.

FIGURE 4.47: Crack pattern evolution on the slab side of $J\_01\_S-M^+$ specimen.

FIGURE 4.48: Crack pattern evolution in the joint and longitudinal beams of $J\_01\_S-M^{+}$ specimen.

FIGURE 4.49: Final damage in the beam of $J\_01\_S-M^{+}$ specimen.

Conversely, in $J\_01\_S-M^{-}$ specimen, the external side of the connection was particularly damaged, except for the joint area. In Figure 4.52, the torsional cracks in the longitudinal beams and the detachment between the slab and the beams, where the tensile stress are high, can be clearly seen. The deep fracture, parallel to the slab plane, ran across the bay span of the beams supporting the joists, until their ends (Figure 4.51). The longitudinal beams inclined cracks were also observed from the joists side view. In the slab, the cracking started from the slab-column interface and propagated with inclined cracks along the smallest sides of the column (Figure 4.51). In the main beam, on the opposite side of the specimen, the only damage observed consisted of the concrete crushing (Figure 4.50).

FIGURE 4.50: Final damage in the beam of $J\_01\_S - M^-$ specimen.

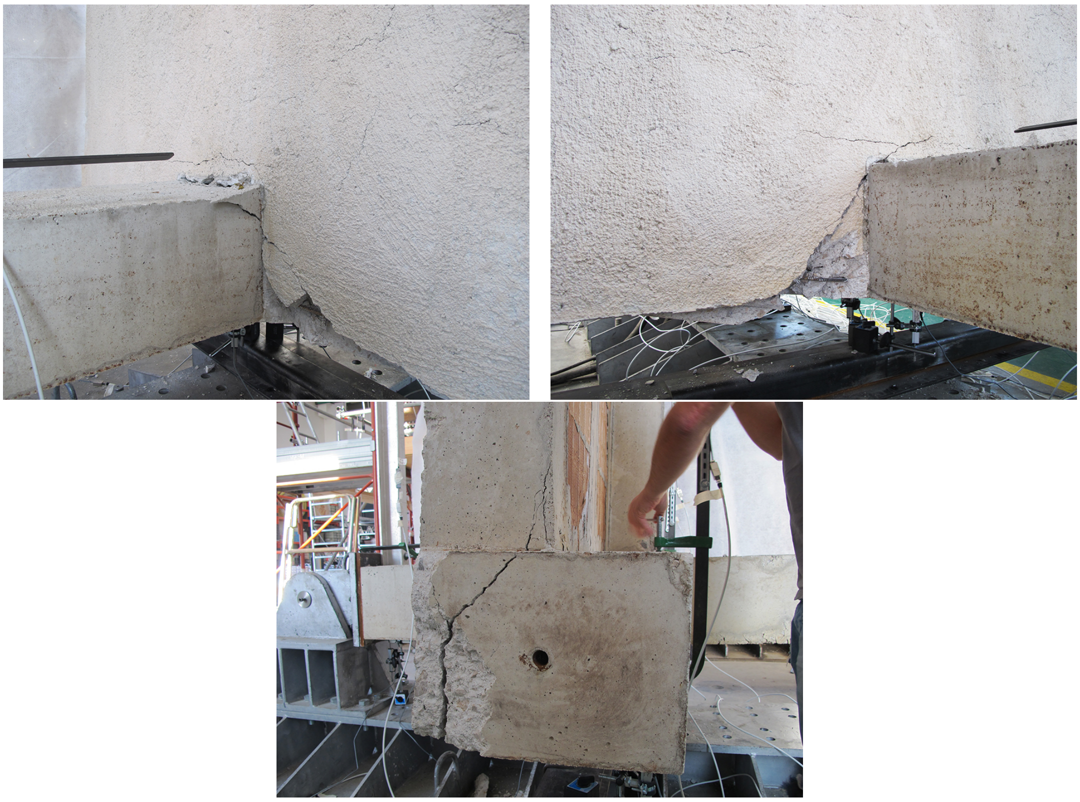

FIGURE 4.51: Crack pattern evolution on the slab side of $J\_01\_S - M^-$ specimen.

FIGURE 4.52: Crack pattern evolution in the joint and longitudinal beams of $J\_01\_S - M^-$ specimen.

4.3 Innovative Specimens

4.3.1 Joints without Floor Deck

4.3.1.1 Load-Displacement Response

The load versus displacement response of innovative specimens without the floor deck, subjected to cyclic and monotonic tests in positive and negative loading direction, are herein analysed. In particular, Figure 4.53 shows the response of $J\_02 - C$ specimen, Figure 4.54 that of $J\_02 - M^+$, and Figure 4.55 that of $J\_02 - M^-$. For the cyclic test, as usual, the monotonic envelope, in other words the skeleton curve, was plotted and it was also useful to compare the monotonic and cyclic results. Indeed, the load-displacement curve in negative loading direction (Figure 4.55) showed a particular behaviour, with very low stiffness and a continuously increasing resistance, as compared to the cyclic test skeleton curve. This was due to an incident occurred before the test, when the specimen underwent a little pre-stress, with the application of $5kN$ of load in the positive loading direction, which caused the starting crack at the RBS level illustrated in Figure 4.72. As a consequence, the results reliability is not sure, especially for what concerns the displacements.

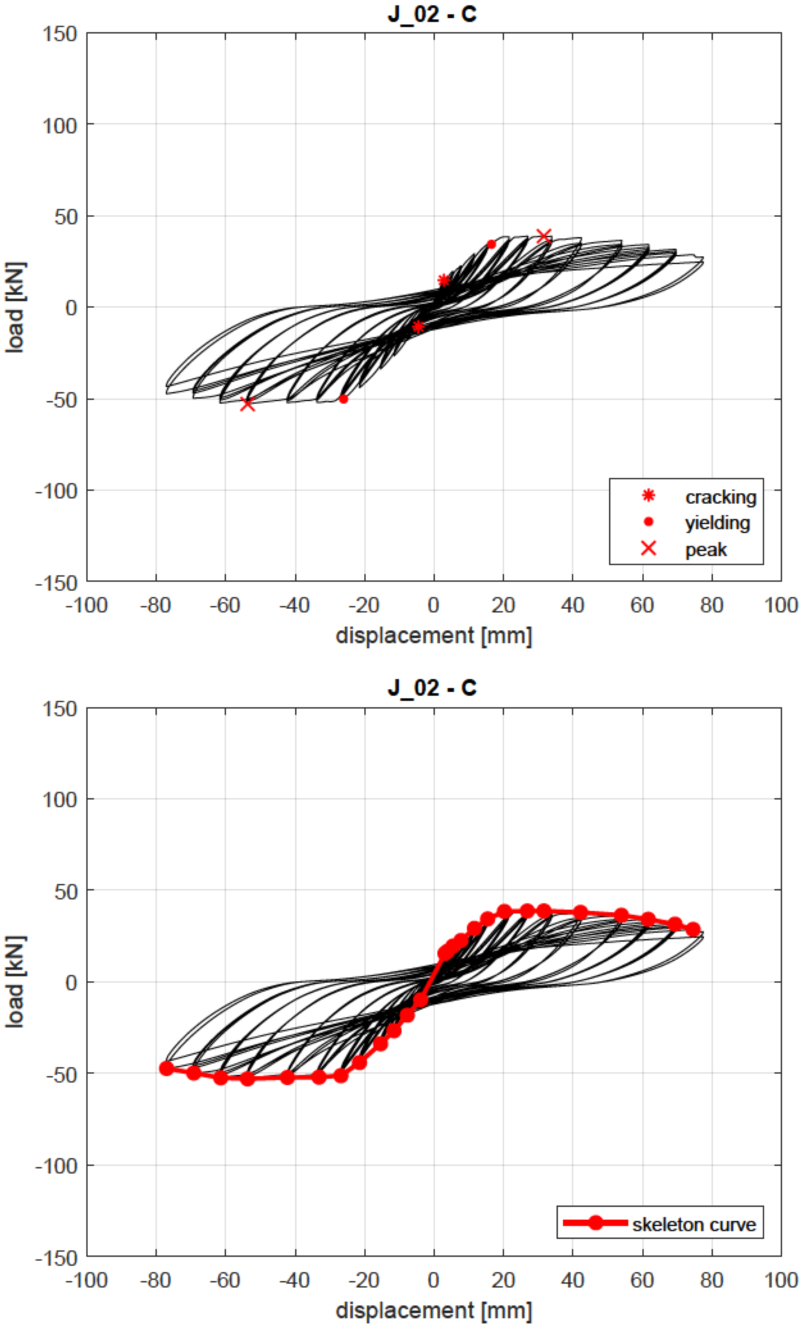

FIGURE 4.53: Load vs displacement response of $J\_02 - C$ specimen.

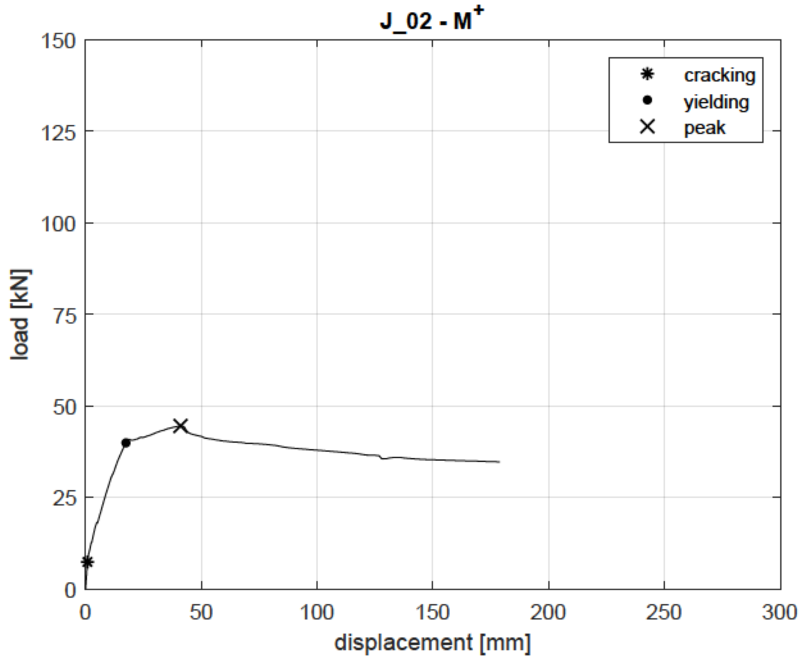

FIGURE 4.54: Load vs displacement response of $J\_02 - M^{+}$ specimen.

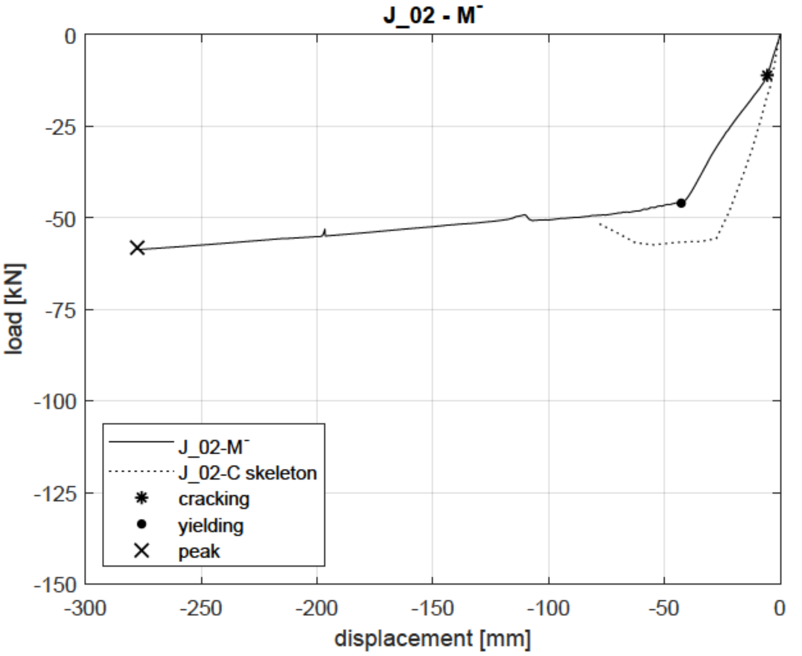

FIGURE 4.55: Load vs displacement response of $J\_02 - M^{-}$ specimen.

The first cracking of the main beam was evaluated from the experimental curves and is reported, for each test, in Table 4.7. With reference to the positive loading direction, i.e. when the transverse beam is subjected to sagging bending, the first cracking was supposed to occur at $+14.67kN$, during the cyclic test, and at $+7.35kN$, during the monotonic test. These values correspond to positive cracking moments of, respectively, $+22.88kNm$ and $+11.47kNm$, which were evaluated with the usual lever arm of $1.56m$, hence they can be checked also in the moment-rotation plots of the following Section 4.3.1.2. However, especially in the case of innovative specimens, it would be more appropriate to consider as lever arm the distance between the middle of the actuator plate and the starting point of the reduced beam section, which was $20cm$ far from the column face, as depicted in Figure 4.56. Indeed, this latter was the exact point where the first crack appeared and the plasticity was concentrated. Considering the new length of the lever arm, equal to $L_{RBS} = 1.21m$, the first cracking moments are $+17.75kNm$, for the $J\_02 - C$ transverse beam, and $+8.89kNm$, for $J\_02 - M^+$ specimen. The theoretical values of the first cracking moment for the beam with the reduced section (30x25cm) are $+9.54kNm$ and $+11.62kNm$ for, respectively, $J\_02 - C$ and $J\_02 - M^+$ specimen. In the negative loading direction, i.e. when the main beam is subjected to a hogging bending moment, the first cracking occurred at $-10.66kN$, in the cyclic test, and at $-11.13kN$, in the monotonic one. The corresponding cracking moments are, respectively, $-16.63kNm$ and $-17.36kNm$, evaluated with the lever arm of $1.56m$, and $-12.90kNm$ and $-13.47kNm$, with the shorter lever arm of $1.21m$. The theoretical values of cracking moments computed for the RBS were $-9.92kNm$ and $-8.32kNm$ for, respectively, $J\_02 - C$ and $J\_02 - M^-$ specimen.

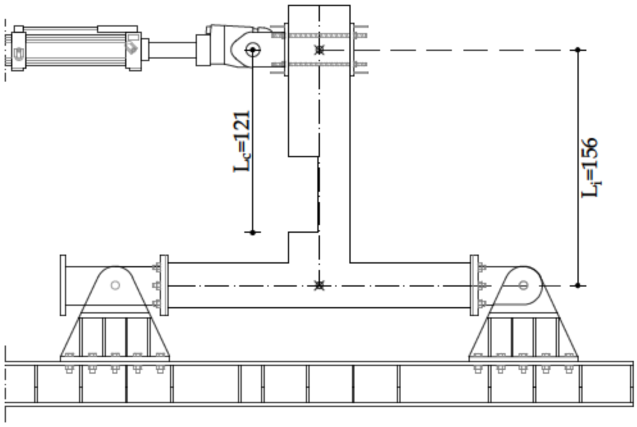

FIGURE 4.56: Test layout of innovative specimens (units: cm).

The general yielding was identified for each test and the values are summarised in Table 4.8. In the specific case of positive loading direction, the yielding is supposed to occur at a load of $+34.31kN$, in $J\_02 - C$ specimen, and $+39.82kN$ in $J\_02 - M^+$, corresponding to the displacements of, respectively, $+16.52mm$ and $+17.41mm$. In the case of negative loading direction, the yielding was located at a load of $-50.26kN$, in $J\_02 - C$ specimen, and of $-46.00kN$, in $J\_02 - M^-$ specimen, at the related displacements of $-26.07mm$ and $-42.78mm$. The corresponding yielding moments, evaluated through L_i, were $M_y^+ = +53.52kNm$ and $M_y^- = -78.41kNm$ in $J\_02 - C$, $M_y^+ = +62.11kNm$ in $J\_02 - M^+$ and $M_y^- = -71.76kNm$ in $J\_02 - M^-$. The corresponding yielding moments, evaluated through L_{RBS}, were $M_y^+ = +41.51kNm$ and $M_y^- = -60.82kNm$ in $J\_02 - C$, $M_y^+ = +48.18kNm$ in $J\_02 - M^+$ and $M_y^- = -55.66kNm$ in $J\_01\_S - M^-$. The expected yielding moments were evaluated by referring to the RBS of the transverse beam (30x25cm). The values are $M_y^+ = +43.83kNm$ and $M_y^- = -57.86kNm$.

Table 4.9, moreover, shows the peak loads and the corresponding displacements. The positive peak load achieved in $J\_02 - C$ test was $+38.75kN$ at $+31.60mm$ displacement, and in $J\_02 - M^+$ it was $+44.50kN$ at $+41.00mm$. The displacement ductility, d_E/d_y, hence, was, respectively, 1.91 and 2.35. The negative peak load achieved in $J\_02 - C$ test was $-52.97kN$, at the pertaining displacement of $-53.70mm$, and, in $J\_02 - M^-$ test, it was $-58.17kN$ at $-277.68mm$ displacement. Hence, the displacement ductility, d_E/d_y, was, respectively, 2.06 and 6.49.

The test on $J\_02 - C$ specimen was interrupted, in the positive loading direction, once the peak load in the last performed drift level decreased by 26% compared to the maximum load, i.e. at a load of $+28.66kN$ and a displacement of $+74.55mm$. The test was interrupted, in the negative loading direction, when the peak load of the last performed drift level attained 11% loss of the resistance, i.e. at a load of $-47.33kN$ and a displacement of $-77.02mm$.

The monotonic test by which the transverse beam is subjected to sagging bending, i.e. the test performed on $J\_02 - M^+$ specimen, was ended at a load of $+34.67kN$ and a displacement of $+178.78mm$, once the drop in resistance was 22%, as compared to the peak load. The test on $J\_02 - M^-$ specimen showed increasing resistance until the displacement of $-277.80mm$, at which the test was stopped. The final value of the load, in this case, was equal to the maximum load achieved, i.e. $-58.02kN$.

Specimen	F_{cr}^+ [kN]	d_{cr}^+ [mm]	F_{cr}^- [kN]	d_{cr}^- [mm]
$J\_02 - C$	14.67	2.78	-10.66	-4.51
$J\_02 - M^+$	7.35	0.79	-	-
$J\_02 - M^-$	-	-	-11.13	-5.65

TABLE 4.7: Positive and negative first cracking loads and corresponding displacements for specimens $J\_02 - C$, $J\_02 - M^+$ and $J\_02 - M^-$.

Specimen	F_y^+ [kN]	d_y^+ [mm]	F_y^- [kN]	d_y^- [mm]
$J\_02 - C$	34.31	16.52	-50.26	-26.07
$J\_02 - M^+$	39.82	17.41	-	-
$J\_02 - M^-$	-	-	-46.00	-42.78

TABLE 4.8: Positive and negative yielding loads and corresponding displacements for specimens $J\_02 - C$, $J\_02 - M^+$ and $J\_02 - M^-$.

Specimen	F_E^+ [kN]	d_E^+ [mm]	F_E^- [kN]	d_E^- [mm]
$J\_02 - C$	38.75	31.60	-52.97	-53.70
$J\_02 - M^+$	44.50	41.00	-	-
$J\_02 - M^-$	-	-	-58.17	-277.68

TABLE 4.9: Maximum and minimum loads and corresponding displacements for specimens $J\_02 - C$, $J\_02 - M^+$ and $J\_02 - M^-$.

4.3.1.2 Moment-Rotation Response

The moment versus rotation response of innovative specimens without the floor deck was reported for the joint subjected to the cyclic test, $J\_02 - C$, in Figure 4.57, and for the joints subjected to monotonic tests, $J\_02 - M^+$ and $J\_02 - M^-$, in Figures 4.58 and 4.59. To compare the two typologies of specimens, the moment was evaluated as in the conventional modules, i.e. by multiplying the experimental load by the lever arm ($M = F \times L_i$) of $L_i = 1.56m$ (Figure 4.56). It goes without saying that the plastic zone, in this case, developed at the RBS, hence the effective lever arm was $L_{RBS} = 1.21m$. The peak moments achieved during the cyclic test were $+60.45kNm$ and $-82.64kNm$. The maximum moment observed in the monotonic test under positive displacements was $+69.42kNm$, while the minimum in the monotonic test in negative displacements was $-90.74kNm$.

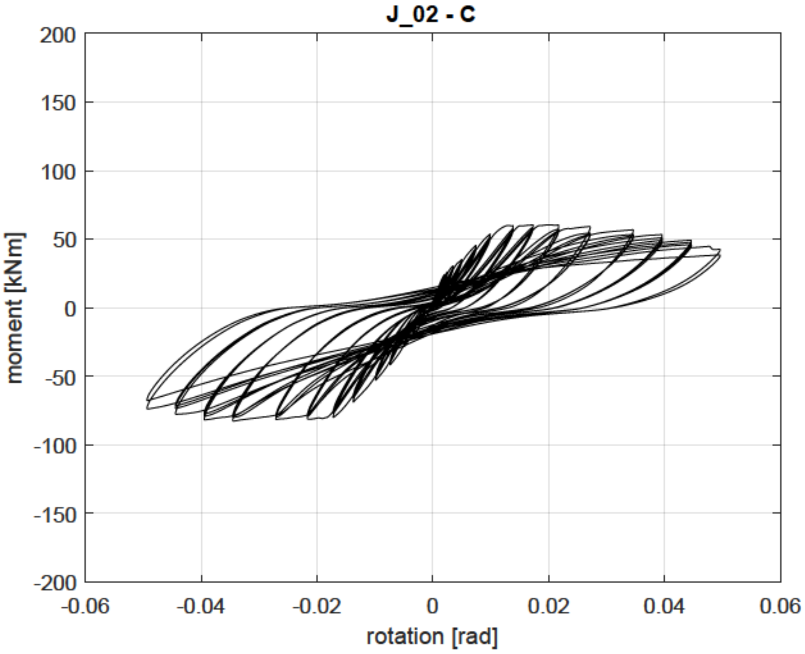

FIGURE 4.57: Moment vs rotation response of $J\_02 - C$ specimen.

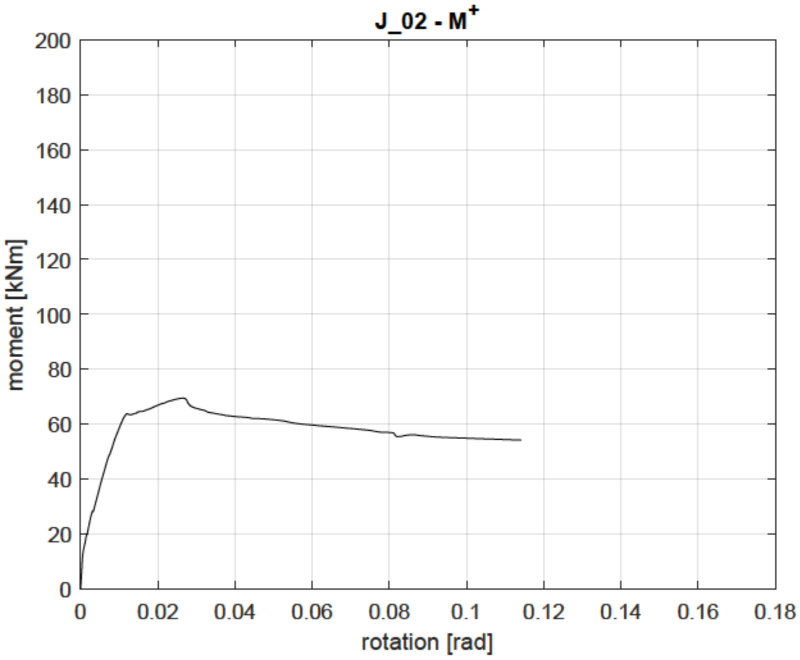

FIGURE 4.58: Moment vs rotation response of $J\_02 - M^+$ specimen.

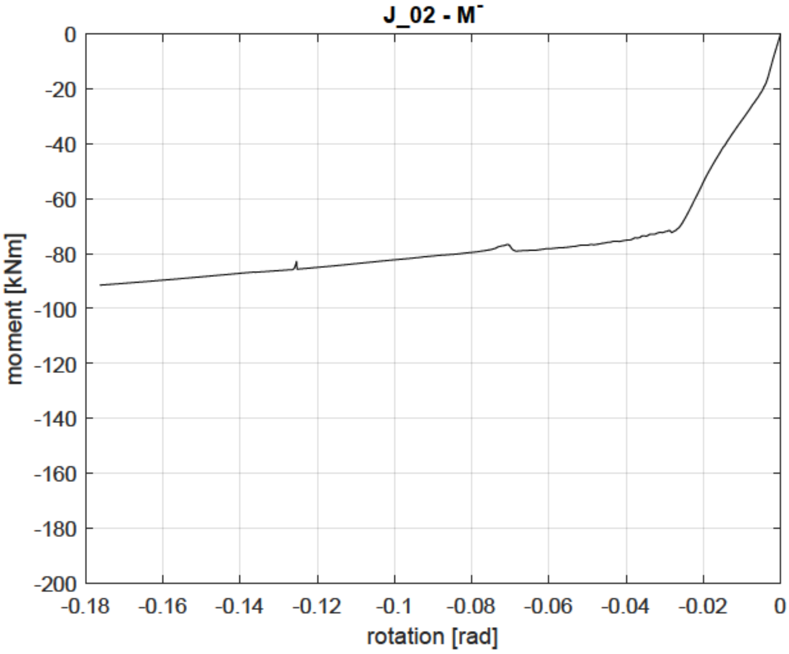

FIGURE 4.59: Moment vs rotation response of $J\_02 - M^-$ specimen.

In addition, the non-dimensional moment versus rotation curves are reported in Figure 4.60 for $J\_02 - C$ specimen, and in Figure 4.61 and Figure 4.62 for $J\_02 - M^+$ and $J\_02 - M^-$ specimens. The experimental moment was divided by the moment of resistance of the full-depth beam section (30x40 cm), $M_R^{+/-}$, in order to evaluate the effectiveness of the RBS solution. The non-dimensional moment, indeed, was useful to estimate the loss of resistance due to the reduced beam section compared to the full-depth one. A greater loss of resistance was expected in positive loading direction, because of the RBS and 3ϕ14 bottom bars. A lower drop of resistance was expected in the negative loading direction, where only the RBS affected the moment value since the top reinforcement was continuous along the whole beam and equal to 4ϕ14. The resistance moment of the transverse beam in $J\_02 - C$ specimen was, in absolute value, $M_R^{+/-} = 108.68kNm$. The non-dimensional moment reached the maximum value of 0.56 and the minimum value of -0.76. Hence, the resistance decreased by around 44% and 24%, respectively in positive and negative loading direction, as compared to the conventional specimens without the floor deck (J_01). The moment of resistance was $M_R^+ = 109.95kNm$ for $J\_02 - M^+$ transverse beam. The maximum value of the non-dimensional moment was 0.63, hence the drop in resistance, as compared to that of conventional modules, was around 40%. The resisting moment of the beam in $J\_02 - M^-$ was, in absolute value, $M_R^- = 107.76kNm$. The resistance loss, due to the RBS, was around 20% since the minimum non-dimensional moment was -0.84.

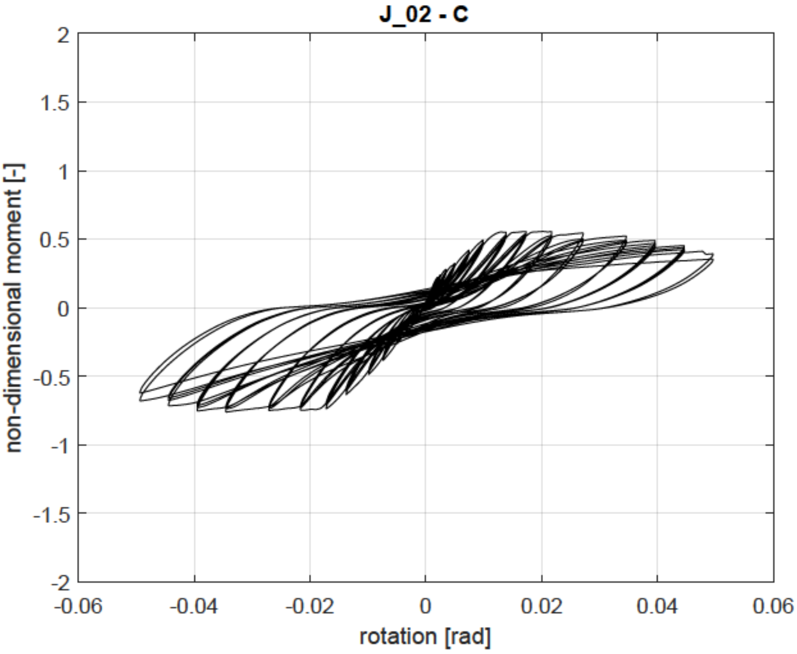

FIGURE 4.60: Non-dimensional moment vs rotation response of $J\_02 - C$ specimen.

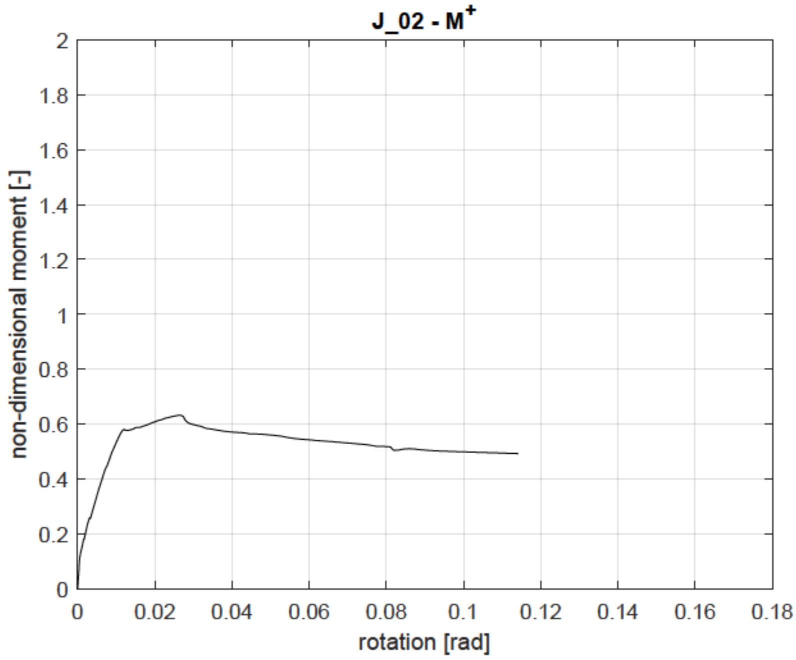

FIGURE 4.61: Non-dimensional moment vs rotation response of $J\_02 - M^+$ specimen.

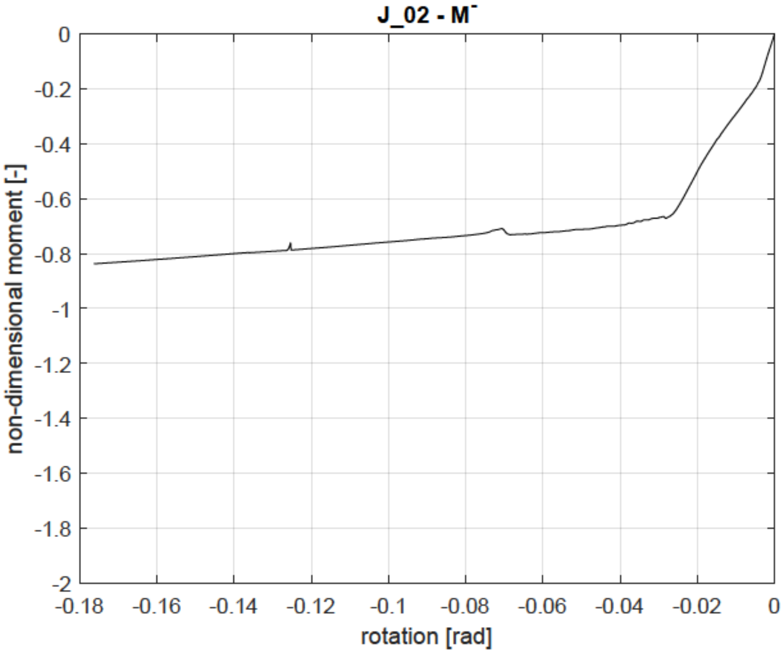

FIGURE 4.62: Non-dimensional moment vs rotation response of $J\_02 - M^-$ specimen.

In addition, for the monotonic tests, the moment was plotted versus the beam rotation. As usual, the beam rotation was evaluated in the two previously described ways, represented in the chart by a black and red curve. Figure 4.63 shows the response of $J\_02 - M^+$ specimen, and Figure 4.64 that of $J\_02 - M^-$. In $J\_02 - M^+$ specimen, the maximum value of the beam rotation was $0.07rad$ on the black curve, which stopped when the LDTs reached the end stroke, and $0.10rad$ on the red one, which reached the test end. In $J\_02 - M^-$ specimen, the minimum beam rotation on the shorter curve was $-0.06rad$, while on the longer curve it reached $-0.17rad$.

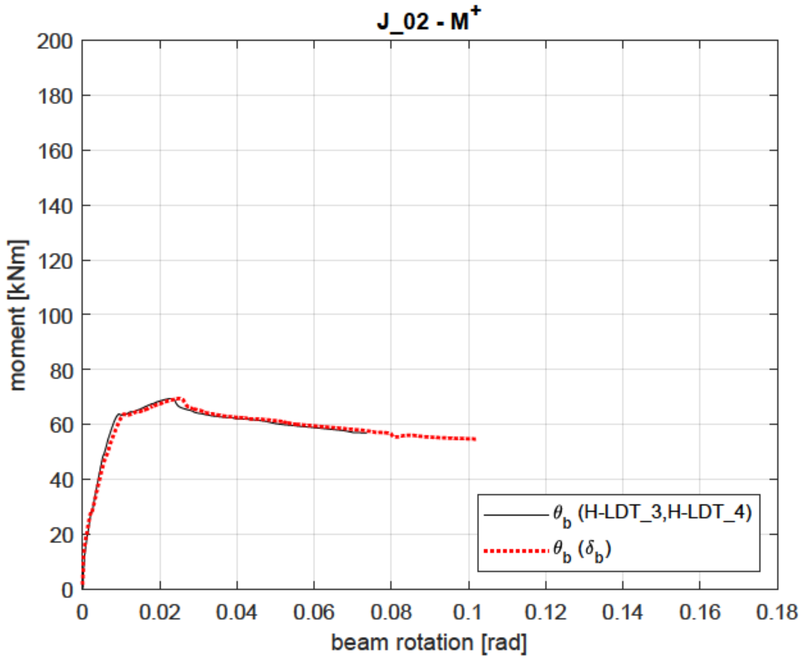

FIGURE 4.63: Moment vs beam rotation response of $J\_02 - M^+$ specimen.

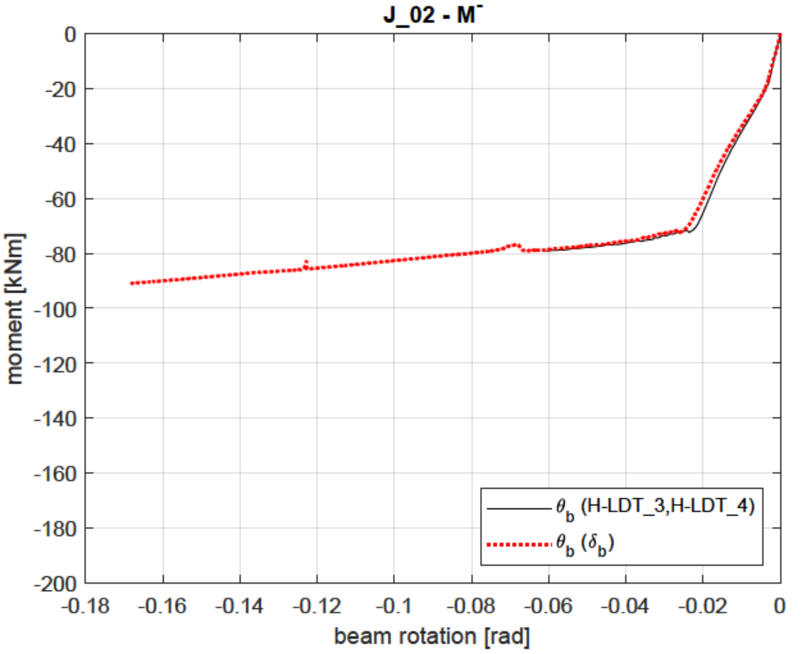

FIGURE 4.64: Moment vs beam rotation response of $J\_02 - M^-$ specimen.

4.3.1.3 Beam Response

The displacements exhibited by the beam during the test were monitored by H-LDT_3 and H-LDT_4 sensors, having a stroke of $100mm$, and are reported in Figure 4.65, Figure 4.66, and Figure 4.67, concerning, respectively, $J\_02 - C$, $J\_02 - M^+$, and $J\_02 - M^-$ specimen. The peak displacements of $J\_02 - C$ beam, in positive loading direction, were $+48.74mm$ (H-LDT_3) and $+45.18mm$ (H-LDT_4), but this latter value was achieved at about 3000s, due to the end stroke of the linear transducer. The peak negative displacements were $-53.72mm$ (H-LDT_3) and $-52.84mm$ (H-LDT_4). The beam maximum displacements in $J\_02 - M^+$ specimen were $+100.30mm$ (H-LDT_3) and $+99.24mm$ (H-LDT_4), while the minimum displacements in $J\_02 - M^-$ test were $-81.82mm$ (H-LDT_3) and $-87.88mm$ (H-LDT_4). The test end line is not visible in Figure 4.67 since it is located after the maximum limit of the x-axis. The linear transducers detected quite the same amount of displacements, which can be considered symmetrical in the positive and negative loading direction.

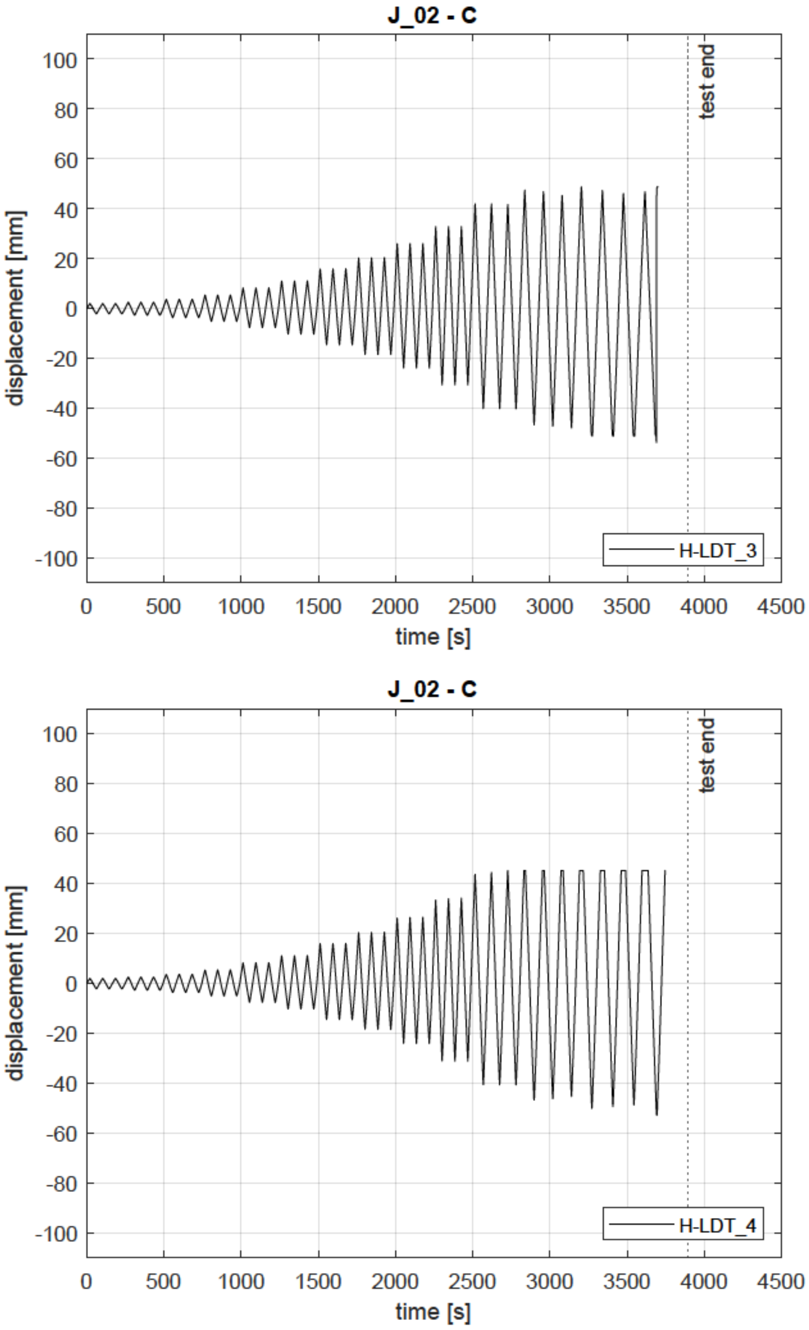

FIGURE 4.65: Beam displacement vs time of $J\_02 - C$ specimen.

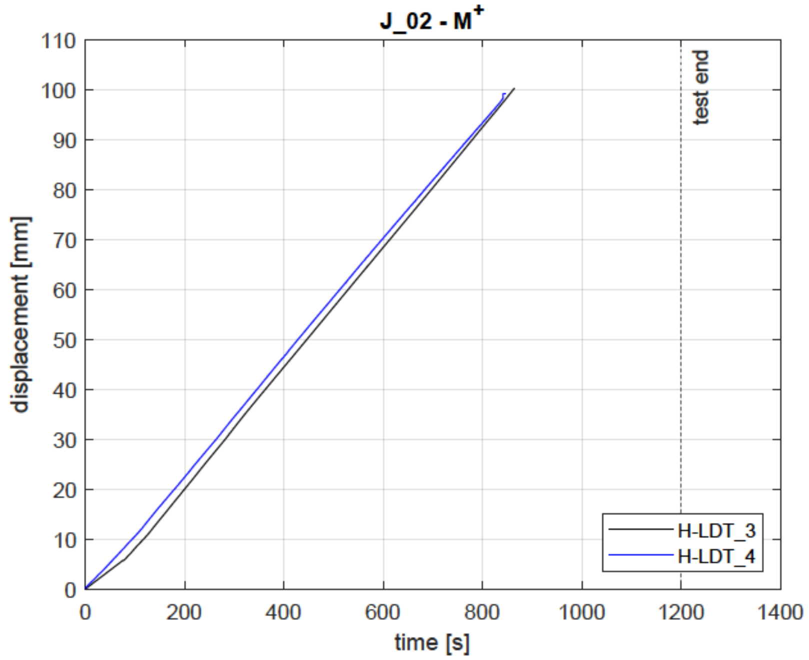

FIGURE 4.66: Beam displacement vs time of $J\_02 - M^{+}$ specimen.

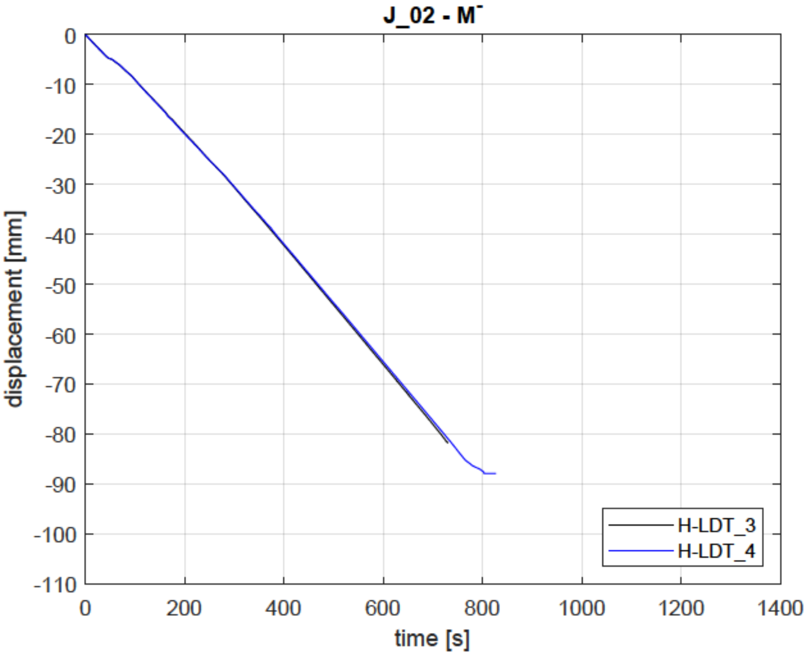

FIGURE 4.67: Beam displacement vs time of $J\_02 - M^{-}$ specimen.

4.3.1.4 Crack Pattern

The damage in J_02 specimens was localised in the transverse beam, without affecting the longitudinal beams or the joint area. The plasticity area of the beam was no longer exactly located at the beam-column interface, but it moved toward the middle span, showing an asymmetrical behaviour. On the RBS side, the plasticity is localised where the beam height reduced while, on the continuous side of the beam, it affected a grater area, extending from the beam reduction starting point, at least, toward the column face. The asymmetrical response was due to the difference in the top and bottom reinforcement. The top beam reinforcement, indeed, was constant along the entire beam span. On the contrary, the bottom reinforcement was not continuous between the full and reduced beam section. In the following, the damage evolution is described in detail about each test.

During the cyclic test, cracking phenomena, illustrated in Figure 4.68, mainly affected the RBS area, but asymmetrically. Indeed, on the side of the section reduction, the cracking arose at the beginning of the beam cut ($20cm$ from the column face) and it ran, with a certain slope, toward the opposite side of the beam (crack 1 in Figure 4.68). As a consequence, on the side where the beam is continuous, the first crack was at about $10cm$ from the column face. The following cracks, 2 and 3, appeared, respectively, at the middle and the end of the reduced beam section, by horizontally crossing the element. Upon further loading, the damage became more intense around the first crack and on both sides of the beam. On the RBS side, greater damage was limited near the first crack; on the opposite beam side, a new crack spread, at the beam section reduction level ($20cm$ from the column face), hence the plastic hinge developed between this latter and the first one, as shown in Figure 4.69.

The crack pattern was amplified in monotonic tests as compared to the cyclic one. As it can be checked in Figure 4.70, the first, second and third cracks exactly occurred in the same points as in the cyclic test but, because of the increasing displacements imposed to $J\_02 - M^+$ specimen, more cracks affected the entire length of the RBS, subjected to tensile stress, until the final stage depicted in Figure 4.71. The crushing damage, instead, affected the continuous side of the beam, until a final length extending from $2cm$ to $20cm$ from the column face.

The top left photo in Figure 4.72 points out the state of the specimen $J\_02 - M^-$ before the test. As previously said, it was accidentally subjected to $+5kN$ load, hence an initial cracking started at the beginning of the section reduction. By applying the loading protocol inducing a negative moment to the beam, the first cracks, 1 and 2, on the beam tension side, spread at about, respectively, $10cm$ and $30cm$ from the column face and they converged, on the beam compressed side, at the same point, which was the beginning of the RBS. On the continuous side of the beam, cracks 3 and 4, due to further loading, developed with different depths. The final damage in the beam of $J\_02 - M^-$ specimen is pointed out in Figure 4.73.

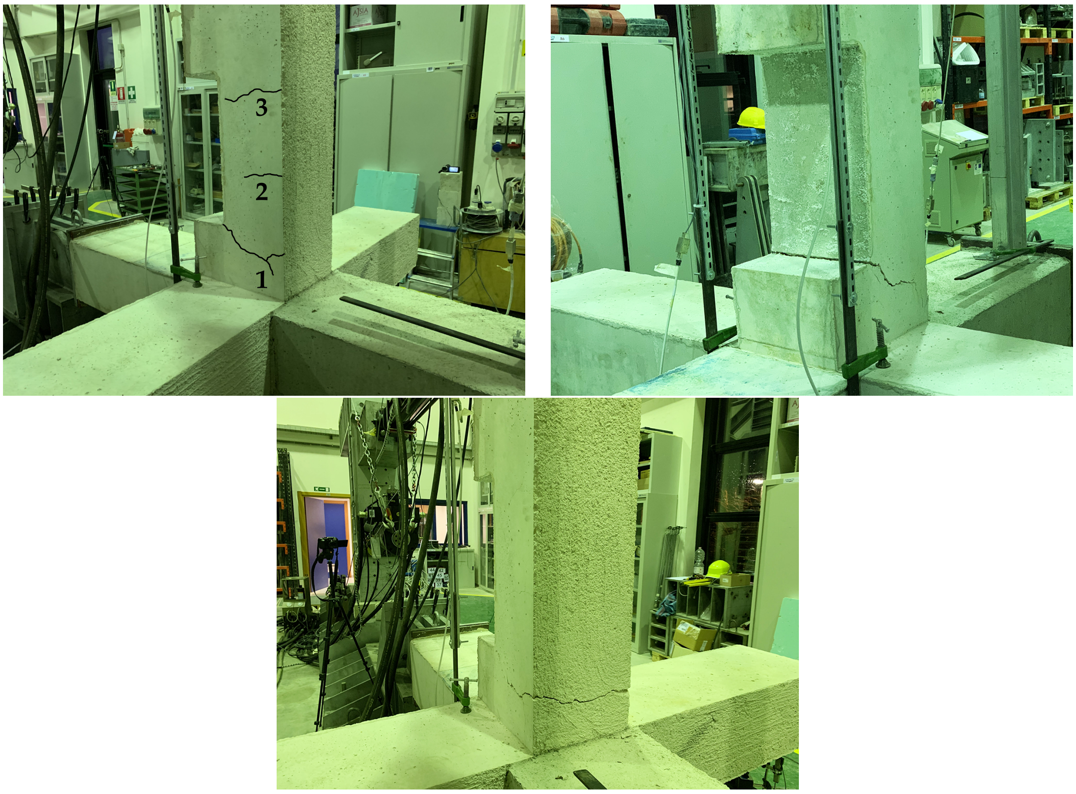

FIGURE 4.68: Crack pattern evolution in J_02-C specimen.

FIGURE 4.69: Final damage in the beam of $J\_02 - C$ specimen.

FIGURE 4.70: Crack pattern evolution in $J\_02 - M^{+}$ specimen.

FIGURE 4.71: Final damage in the beam of $J\_02 - M^{+}$ specimen.

FIGURE 4.72: Crack pattern evolution in $J\_02 - M^{-}$ specimen.

FIGURE 4.73: Final damage in the beam of $J\_02 - M^{-}$ specimen.

4.3.2 Joints with Floor Deck

4.3.2.1 Load-Displacement Response

The cyclic and monotonic responses of innovative specimens equipped with the deck are given, in terms of load versus displacement, in Figure 4.74, Figure 4.75 and Figure 4.76, with reference to, respectively, $J\_02\_S - C$, $J\_02\_S - M^{+}$ and $J\_02\_S - M^{-}$ specimen.

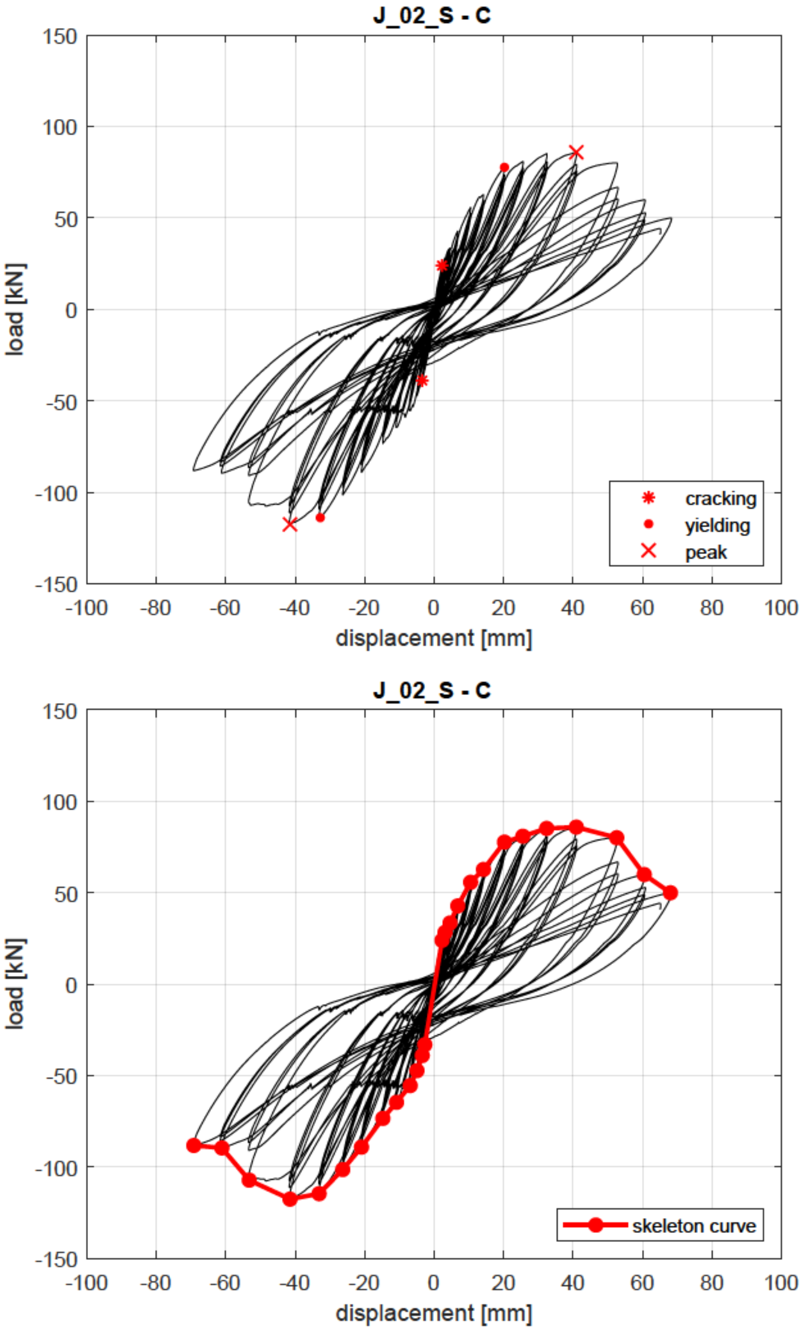

FIGURE 4.74: Load vs displacement response of $J\_02\_S - C$ specimen.

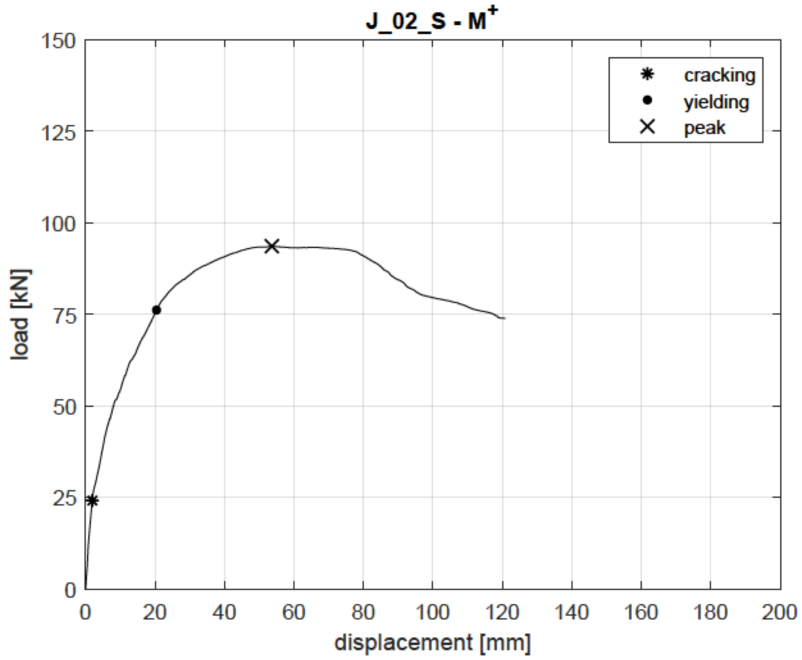

FIGURE 4.75: Load vs displacement response of $J\_02\_S - M^+$ specimen.

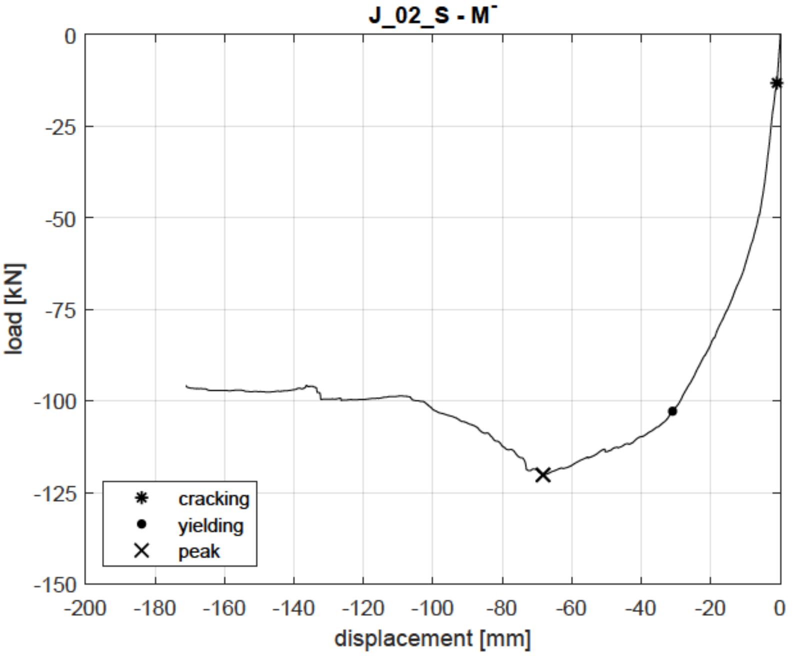

FIGURE 4.76: Load vs displacement response of $J\_02\_S - M^-$ specimen.

The first cracking identified in each experimental curve is reported in Table 4.10. In the positive loading direction, it was supposed to occur at $+23.97kN$ in $J\_02\_S - C$ specimen and $+24.11kN$ in $J\_02\_S - M^+$, corresponding to a positive cracking moment M_{cr}^+ of, respectively, $+37.39kNm$ and $+37.61kNm$, which can be checked in the moment vs rotation chart of the following Section 4.3.2.2. The experimental cracking moments evaluated with the lever arm of $L_{RBS} = 1.21m$ are $+29.00kNm$ and $+29.17kNm$. The theoretical values of the cracking moment, concerning the beam with the reduced section (30x25 cm), were, respectively, $+9.54kNm$ and $+11.62kNm$. The first cracking in the negative loading direction was identified at $-38.88kN$ and $-13.19kN$ in, respectively, $J\_02\_S - C$ and $J\_02\_S - M^-$ specimen, corresponding to the negative cracking moments M_{cr}^- of $-60.65kNm$ and $-20.58kNm$, evaluated through the lever arm $L_i = 1.56m$. The cracking moments provided by the lever arm $L_{RBS} = 1.21m$ are equal to $-47.04kNm$ and $-15.96kNm$. The theoretical cracking moments of the RBS were $-9.91kNm$ and $-12.08kNm$. A large difference occurs between the theoretical and experimental values of the cracking moment in the J_02_S because of the floor deck presence.

The general yielding was identified for each test and it is pointed out in Table 4.11. In particular, in the positive loading direction, the yielding was supposed to occur at a load of $+77.66kN$ in $J\_02\_S - C$ module and $+76.18kN$ in $J\_02\_S - M^+$, corresponding to a displacement of $+20.24mm$ and $+20.41mm$. In the negative loading direction, the yielding was assumed to take place at a load of $-113.84kN$ in $J\_02\_S - C$ module and $-102.83kN$ in $J\_02\_S - M^-$, at the displacements of, respectively, $-32.78mm$ and $-31.01mm$. The corresponding yielding moments, evaluated through L_i, were $M_y^+ = +121.14kNm$ and $M_y^- = -177.59kNm$ in $J\_02\_S - C$, $M_y^+ = +118.84kNm$ in $J\_02\_S - M^+$ and $M_y^- = -160.41kNm$ in $J\_02\_S - M^-$. The corresponding yielding moments, evaluated through L_{RBS}, were $M_y^+ = +93.96kNm$ and $M_y^- = -137.74kNm$ in $J\_02\_S - C$, $M_y^+ = +92.18kNm$ in $J\_02\_S - M^+$ and $M_y^- = -124.42kNm$ in $J\_02\_S - M^-$. The expected yielding moments were evaluated by referring to the RBS of the transverse beam (30x25cm). The values are $M_y^+ = +43.83kNm$ and $M_y^- = -57.86kNm$. Note that, as in conventional specimens, the values in specimens with the floor deck were strongly higher than in simple specimens. Moreover, the general yielding point was not easy to identify in innovative specimens as well.

The peak loads sustained by each specimen and the related displacements are summarised in Table 4.12. The maximum positive loads displayed by $J\_02\_S - C$ and $J\_02\_S - M^+$ specimens were $+85.85kN$ and $+93.62kN$, at the corresponding displacements of $+40.92mm$ and $+53.62mm$. The displacement ductility, d_E/d_y, was, in the same order as before, 2.02 and 2.63. The maximum negative loads reached during the tests on $J\_02\_S - C$ and $J\_02\_S - M^-$ modules, were $-117.48kN$ and $-120.22kN$, at the displacements of $-41.50mm$ and $-68.31mm$. The consequent displacement ductility, d_E/d_y, was, respectively, 1.27 and 2.20.

The test on $J\_02\_S - C$ specimen was interrupted once the peak load of the drift level reached, in negative loading direction, the 25% drop in resistance, at a load of $-88.14kN$ and a displacement of $-69.19mm$. At that moment, the positive load was $+49.97kN$, at a displacement of $+68.02mm$, and the loss of resistance was 42%. Concerning the dissipative behaviour, the hysteresis loops are increasingly larger, with a fat hysteresis loop observed for high deformation, between $\pm 40/60mm$ of displacement.

The test on $J\_02\_S - M+$ specimen was disrupted at a load of $+73.91kN$ and a displacement of $+120.77mm$, at 21% loss of resistance. The test on $J\_02\_S - M-$ specimen was stopped at a load of $-95.74kN$ and a displacement of $-171.02mm$, once the resistance was the 80% of the peak one.

Specimen	F_{cr}^{+} [kN]	d_{cr}^{+} [mm]	F_{cr}^{-} [kN]	d_{cr}^{-} [mm]
$J\_02\_S - C$	23.97	2.26	-38.88	-3.42
$J\_02\_S - M^{+}$	24.11	1.95	-	-
$J\_02\_S - M^{-}$	-	-	-13.19	-1.00

TABLE 4.10: Positive and negative first cracking loads and corresponding displacements for specimens $J\_02\_S - C$, $J\_02\_S - M^{+}$ and $J\_02\_S - M^{-}$.

Specimen	F_{y}^{+} [kN]	d_{y}^{+} [mm]	F_{y}^{-} [kN]	d_{y}^{-} [mm]
$J\_02\_S - C$	77.66	20.24	-113.84	-32.78
$J\_02\_S - M^{+}$	76.18	20.41	-	-
$J\_02\_S - M^{-}$	-	-	-102.83	-31.01

TABLE 4.11: Positive and negative yielding loads and corresponding displacements for specimens $J\_02\_S - C$, $J\_02\_S - M^{+}$ and $J\_02\_S - M^{-}$.

Specimen	F_{E}^{+} [kN]	d_{E}^{+} [mm]	F_{E}^{-} [kN]	d_{E}^{-} [mm]
$J\_02\_S - C$	85.85	40.92	-117.48	-41.50
$J\_02\_S - M^{+}$	93.62	53.62	-	-
$J\_02\_S - M^{-}$	-	-	-120.22	-68.31

TABLE 4.12: Maximum and minimum loads and corresponding displacements for specimens $J\_02\_S - C$, $J\_02\_S - M^{+}$ and $J\_02\_S - M^{-}$.

4.3.2.2 Moment-Rotation Response

Innovative specimens equipped with the floor deck exhibited the moment versus rotation response depicted in Figure 4.77 with reference to $J\_02\_S - C$ specimen, in Figure 4.78 for the $J\_02\_S - M^{+}$ one, and in Figure 4.79 for the $J\_02\_S - M^{-}$ one. The peak moments reached $+133.92kNm$ and $-183.27kNm$ during the cyclic test, while the peak positive moment in $J\_02\_S - M^{+}$ achieved $+146.05kNm$ and the peak negative moment in $J\_02\_S - M^{-}$ attained $-187.54kNm$.

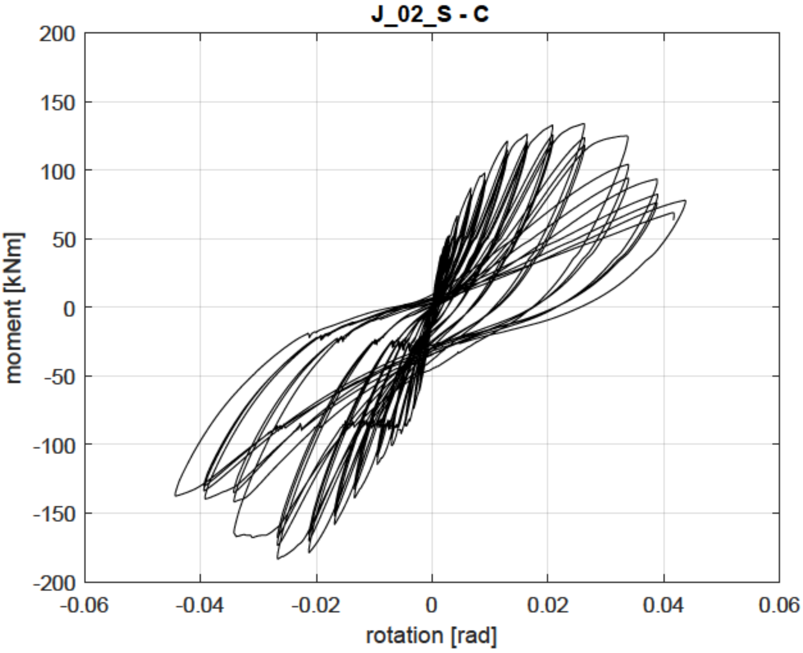

FIGURE 4.77: Moment vs rotation response of $J\_02\_S - C$ specimen.

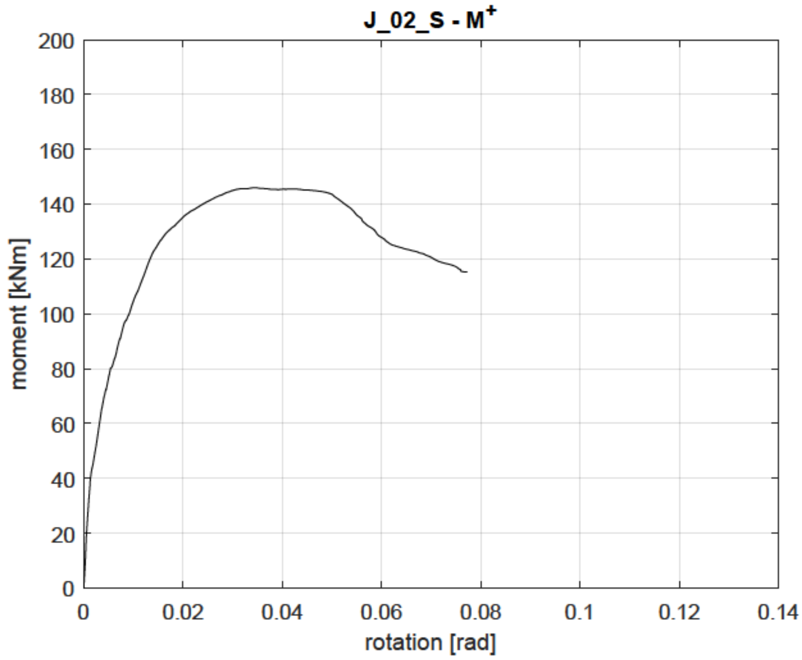

FIGURE 4.78: Moment vs rotation response of $J\_02\_S - M^+$ specimen.

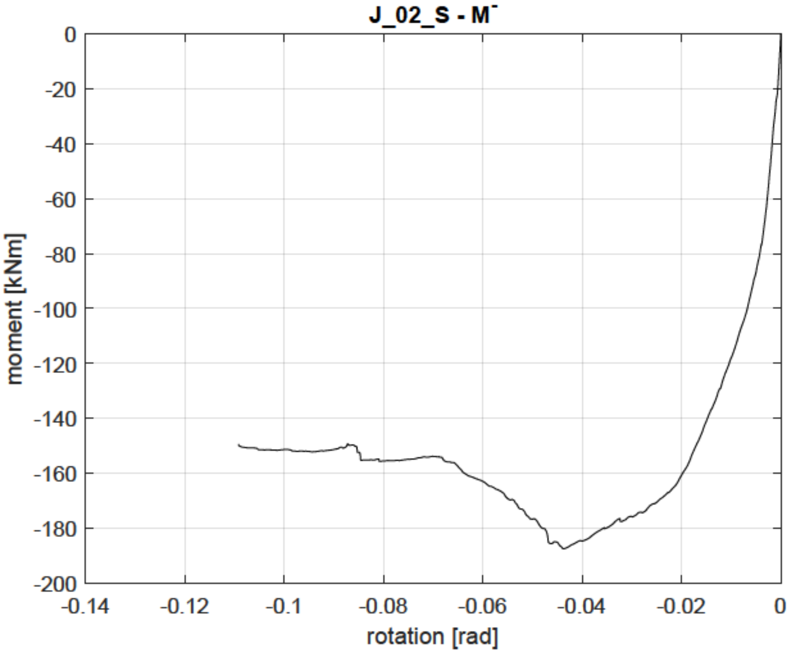

FIGURE 4.79: Moment vs rotation response of $J\_02\_S - M^-$ specimen.

Moreover, the non-dimensional moment versus rotation plots are pointed out in Figure 4.80 for $J\_02\_S - C$ specimen, and in Figure 4.81 and Figure 4.82, for $J\_02\_S - M^+$ and $J\_02\_S - M^-$ specimens. The experimental moment was divided, as usual, by the moment of resistance of the full-depth beam section, $M_R^{+/-}$, i.e. the 30x40 cm section, in order to evaluate, in terms of resistance, the effect of the RBS design on specimens with the deck and to make a comparison with the conventional specimens. The absolute values of resistance moments were $M_R^{+/-} = 108.68kNm$ for the $J\_02\_S - C$ beam, $M_R^+ = 109.95kNm$ for the $J\_02\_S - M^+$ beam and $M_R^- = 107.76kNm$ for the $J\_02\_S - M^-$ beam. Due to the delimited section reduction and the difference in the top and bottom reinforcement, also the response of J_01_S modules was asymmetric. The maximum and minimum values of non-dimensional moments observed in the cyclic test were, respectively, $+1.23$ and -1.69, meaning that the RBS detail caused the floor to add, respectively, 23% and 69% over-strength to the connection. Note that these values were much higher in J_01_S specimens. Moreover, the peak non-dimensional moment in $J\_02\_S - M^+$ test was $+1.33$, while it was -1.74 in $J\_02\_S - M^-$ test.

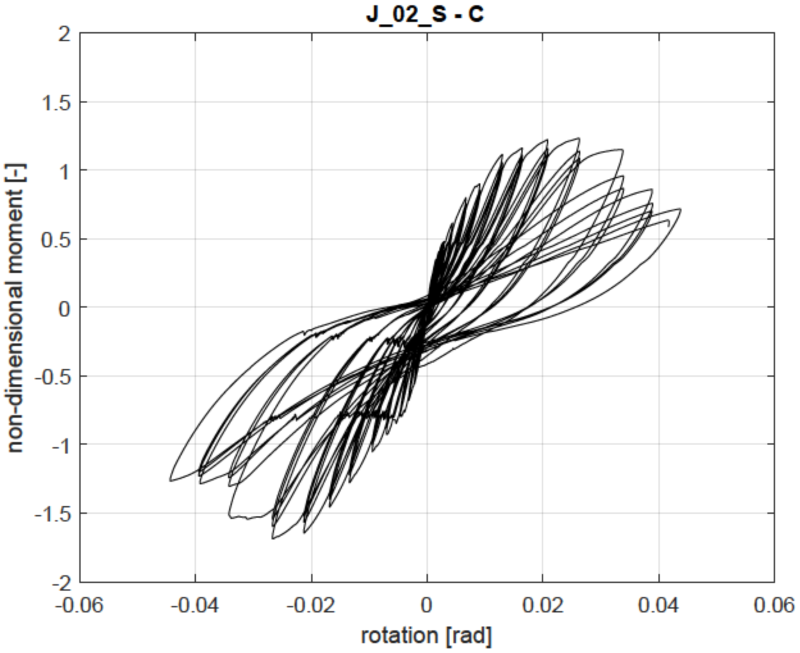

FIGURE 4.80: Non-dimensional moment vs rotation response of $J\_02\_S - C$ specimen.

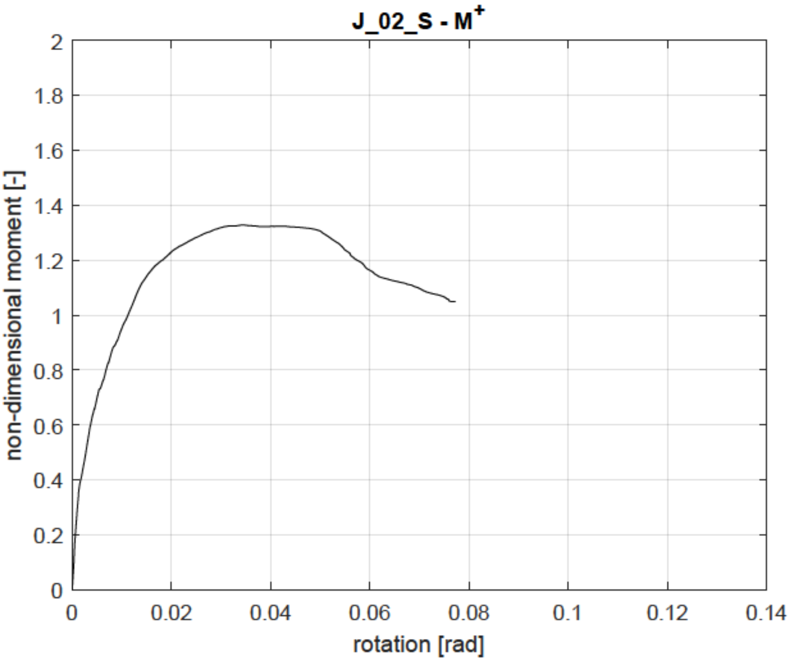

FIGURE 4.81: Non-dimensional moment vs rotation response of $J\_02\_S - M^{+}$ specimen.

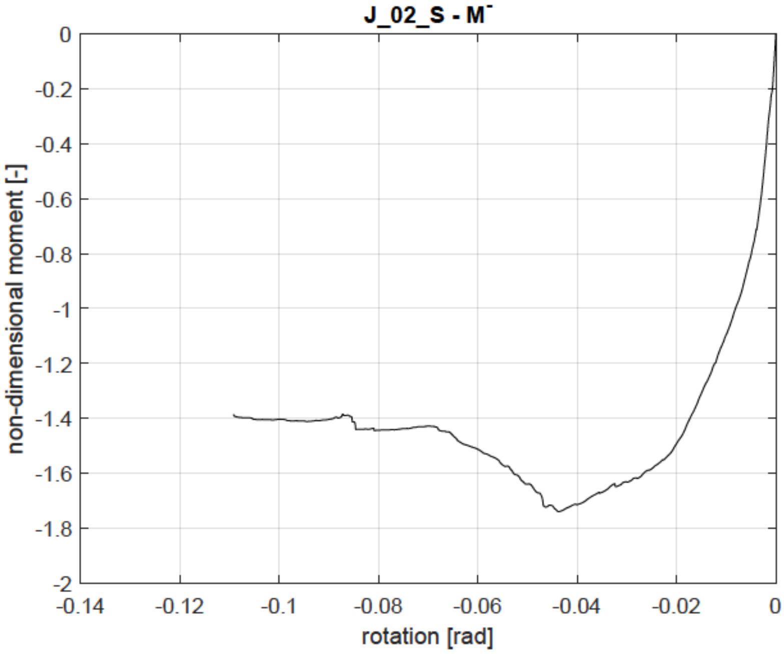

FIGURE 4.82: Non-dimensional moment vs rotation response of $J\_02\_S - M^{-}$ specimen.

From the monotonic tests, through which the transverse beam was subjected to sagging and hogging bending, the moment versus beam rotation plots were extrapolated and are given, respectively, in Figure 4.83 and Figure 4.84. The maximum beam rotation in $J\_02\_S - M^{+}$ specimen was around $0.06rad$ if evaluated directly from the beam LDTs, and it was $0.07rad$ if evaluated by subtracting the joint rotation from the total rotation. The maximum beam rotation in $J\_02\_S - M^{-}$ specimen, instead, were around $-0.05rad$ and $-0.10rad$.

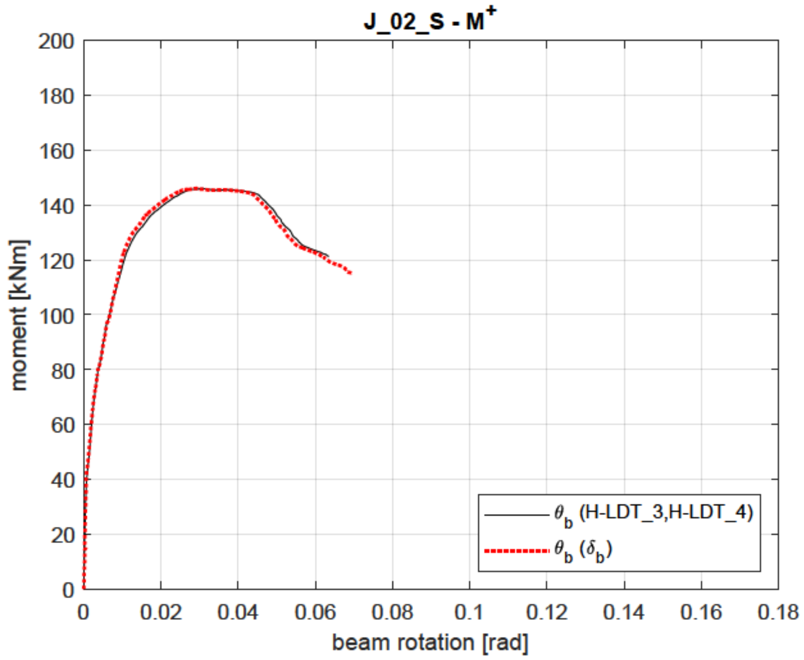

FIGURE 4.83: Moment vs beam rotation response of $J\_02\_S - M^{+}$ specimen.

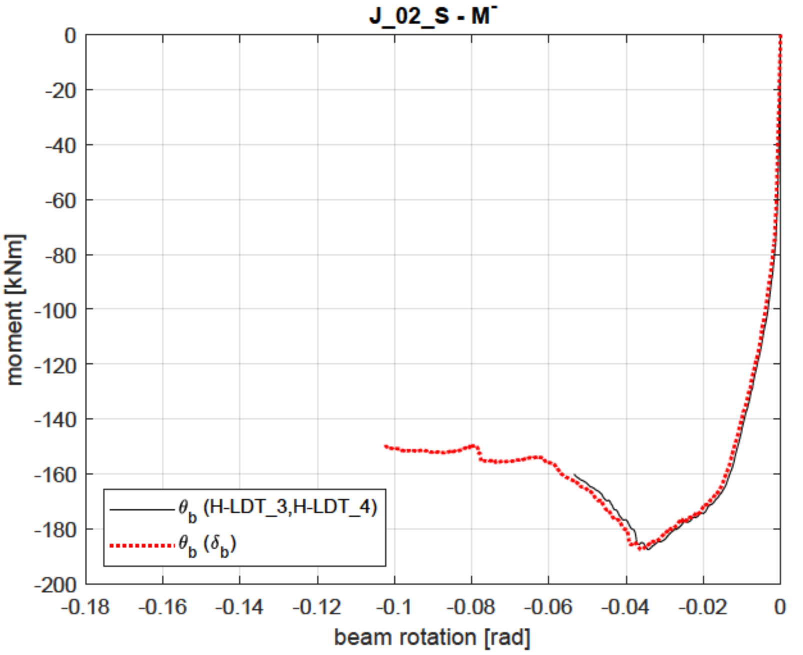

FIGURE 4.84: Moment vs beam rotation response of $J\_02\_S - M^{-}$ specimen.

4.3.2.3 Joists and Beam Response

As it was done in Section 4.2.2.3, the displacements of the joists and beam are reported for cyclic and monotonic tests. The LDTs employed in the tests had a stroke of $100mm$.

The displacement vs time graph of the cyclic test is shown in Figure 4.85. The peak displacements of the joists in positive and negative loading were $+40.40mm$

and $-32.99mm$ for H-LDT_1, 39.08mm and $-35.97mm$ for H-LDT_2, $+36.40mm$ and $-34.32mm$ for H-LDT_5, and $+38.24mm$ and $-31.64mm$ for H-LDT_6. The maximum and minimum displacements of the beam were $+41.07mm$ and $-43.01mm$ in H-LDT_3, $+41.43mm$ and $-47.07mm$ in H-LDT_4.

The beam and joists displacements in $J\_02\_S - M^+$ test are illustrated in Figure 4.86. The blue and black curves, representing the beam displacements, perfectly overlapped. The maximum displacements reached by H-LDT_3 and H-LDT_4 were, respectively, $+84.80mm$ and $+89.46mm$. The peak achieved by the other sensors were $+75.89mm$ for H-LDT_1, $+83.51mm$ for H-LDT_2, $+85.02mm$ for H-LDT_5, and $+86.62mm$ for H-LDT_6. The homologous sensors, located at the equal distance from the main beam but on the opposite sides of it, did not show the same trend.

Under hogging bending, homologous elements (H-LDT_1 and H-LDT_6, H-LDT_2 and H-LDT_5, H-LDT_3 and H-LDT_4) exhibited the same trend, but the displacements of the joists were much smaller than those of the main beam. In particular, the peak displacements achieved during the test were: $-99.19mm$ and $-99.83mm$ for the couple H-LDT_1 and H-LDT_6, $-88.08mm$ and $-93.47mm$ for H-LDT_2 and H-LDT_5, and $-83.59mm$ and $-70.82mm$ for H-LDT_3 and H-LDT_4. The reading of H-LDT_4, however, stopped before that of H-LDT_3.

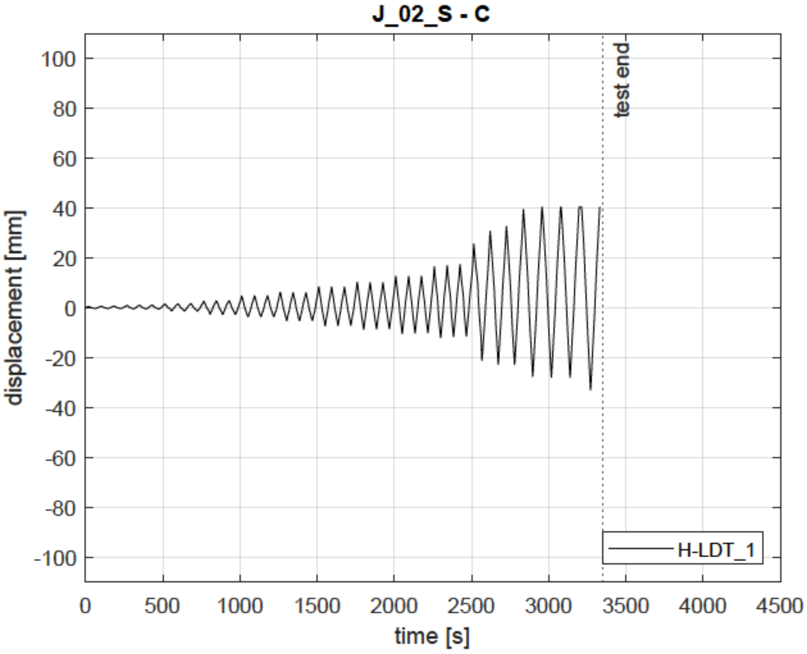

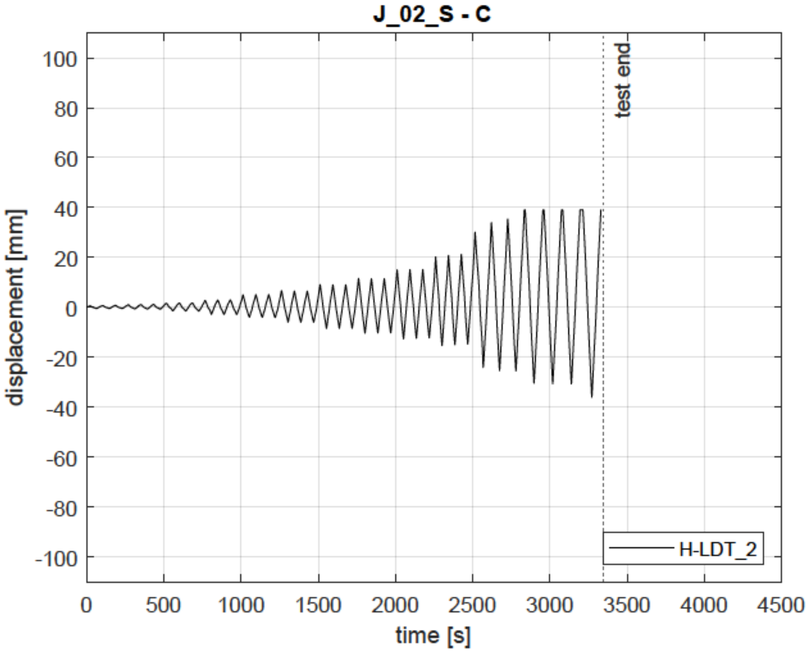
J_02_S - C
displacement [mm]
100
80
60
40
20
0
-20
-40
-60
-80
-100
0
500
1000
1500
2000
2500
3000
3500
4000
4500
time [s]
test end
H-LDT_2

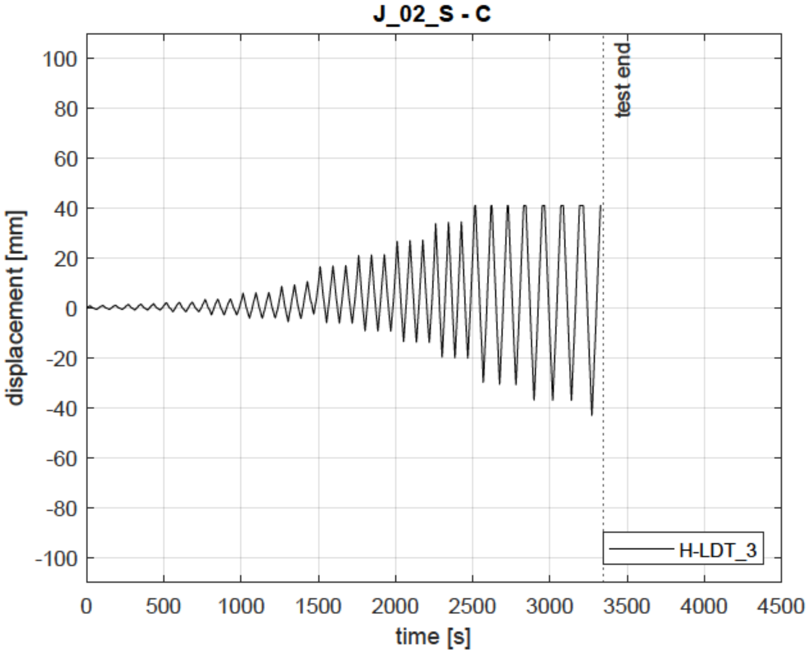
J_02_S - C
displacement [mm]
100
80
60
40
20
0
-20
-40
-60
-80
-100
0
500
1000
1500
2000
2500
3000
3500
4000
4500
time [s]
test end
H-LDT_3

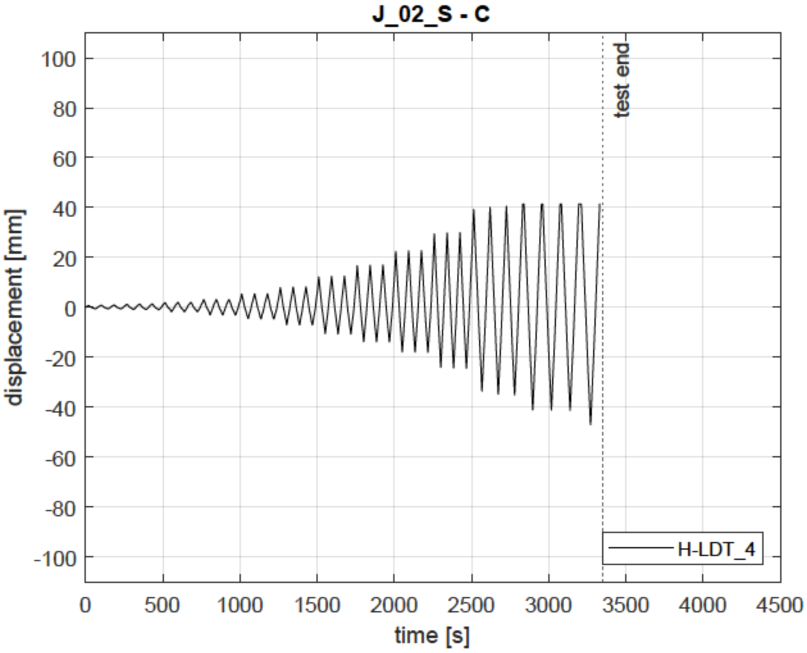
J_02_S - C
displacement [mm]
100
80
60
40
20
0
-20
-40
-60
-80
-100
time [s]
0
500
1000
1500
2000
2500
3000
3500
4000
4500
test end
H-LDT_4

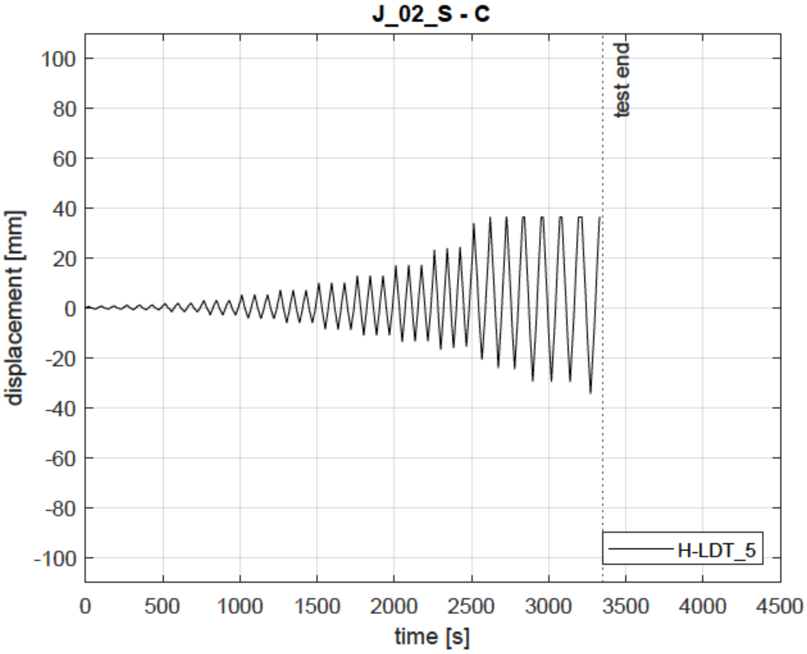
J_02_S - C
displacement [mm]
100
80
60
40
20
0
-20
-40
-60
-80
-100
time [s]
0
500
1000
1500
2000
2500
3000
3500
4000
4500
test end
H-LDT_5

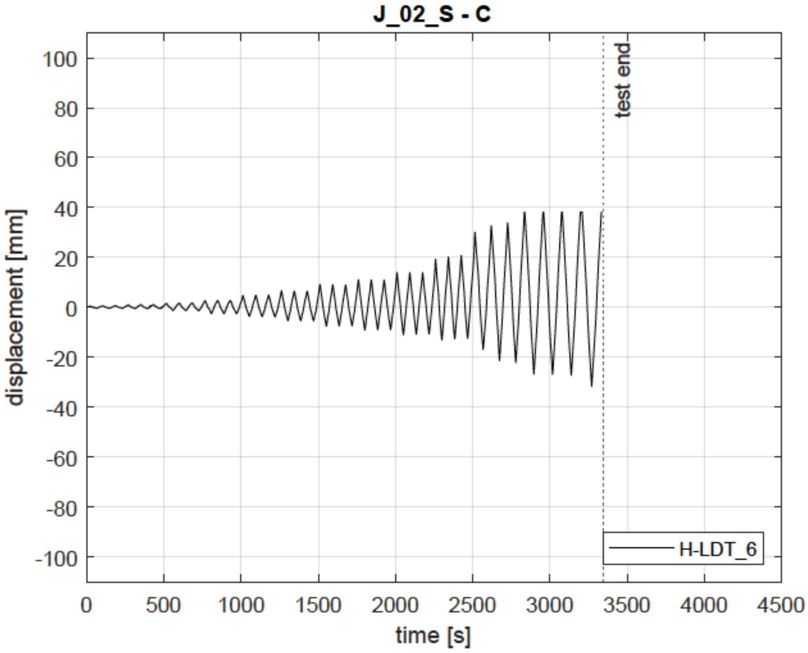

FIGURE 4.85: Joists displacements vs time of $J\_02\_S - C$ specimen.

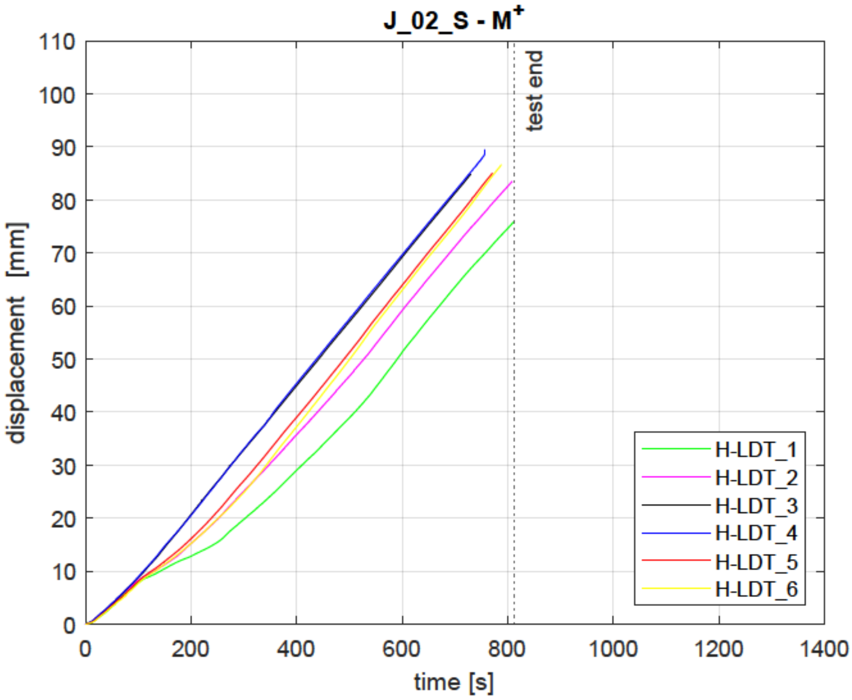

FIGURE 4.86: Joists displacements vs time of $J\_02\_S - M^+$ specimen.

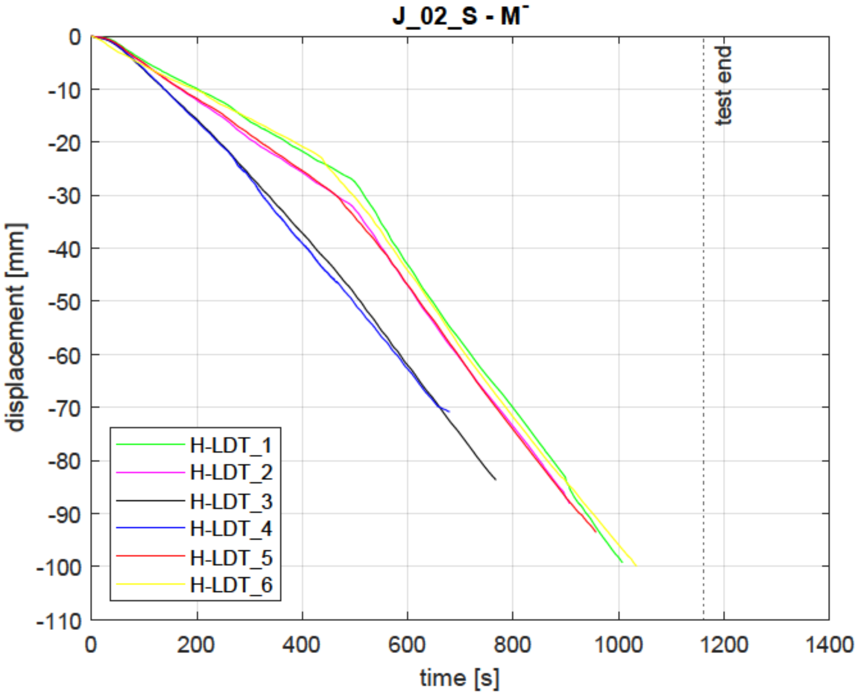

FIGURE 4.87: Joists displacements vs time of $J\_02\_S - M^-$ specimen.

4.3.2.4 Crack Pattern

The damage evolution in innovative specimens with the floor deck affected a reduced area of the beam, as compared to the simple specimens without the deck, but it involved other elements, like the longitudinal beams.

During the cyclic test, on the side of the joists, the first crack appeared at the reduction of the beam section. Cracks propagated also in the nearest hollow tile blocks and, then, at the intersection between the joists and longitudinal beams, as shown in Figure 4.88. Upon further top displacements, damage concentrated near the first crack, until the plasticity (Figure 4.91). On the slab side, in Figure 4.89, the cracking started at the beam-column interface and continued, with an inclination of about 45°, on the smallest sides of the column toward the end of the slab. Cracking also involved the longitudinal beams, by causing, upon further loading, the slab concrete spalling. These cracks originated the crack ones depicted in Figure 4.90, which ran until the end of the longitudinal beams. At high levels of load, these spread parallel to the slab plane, crossing the longitudinal beams and the slab itself, for about $50cm$, as depicted in Figure 4.89.

FIGURE 4.88: Crack pattern evolution on the joists side of $J\_02\_S - C$ specimen.

FIGURE 4.89: Crack pattern evolution on the slab side of $J\_02\_S - C$ specimen.

FIGURE 4.90: Crack pattern evolution in the joint and longitudinal beams of $J\_02\_S - C$ specimen.

FIGURE 4.91: Final damage in the beam of $J\_02\_S - C$ specimen.

The damage evolution in the $J\_02\_S - M^+$ specimen is illustrated in Figure 4.92, Figure 4.93 and Figure 4.94. The first crack, on the joists side view, appeared at the reduction of the beam section and it propagated in the near hollow blocks. In addition, cracks appeared also in the two joists near the transverse beam, at about 25 and 50 centimeters from the longitudinal beams. Upon further loading, damage crossed along the spandrel beams span, where they intersect the joists. On the slab side, the crushing damage mainly affected the beam-to-column intersection. Cracks $5cm$ parallel to the slab plane crossed the longitudinal beams and the slab, with different emphasis between the two opposite sides, as illustrated in Figure 4.93. Torsional cracks with approximately 45° slope arose in the longitudinal beams. Contrary to conventional modules, they were not so evident. They were located on the joists side, while did not affect the external part of the connection. Moreover, no damage involved the joint area.

FIGURE 4.92: Crack pattern evolution on the joists side of $J\_02\_S - M^{+}$ specimen.

FIGURE 4.93: Crack pattern evolution on the slab side of $J\_02\_S - M^{+}$ specimen.

FIGURE 4.94: Crack pattern evolution in the joint and longitudinal beams of $J\_02\_S - M^{+}$ specimen.

FIGURE 4.95: Crack pattern at the end of the test in the beam of $J\_02\_S - M^{+}$ specimen.

On the joists side of $J\_02\_S - M^{-}$ specimen, in Figure 4.96, the crushing affected the point where the beam section is cut and the joists-longitudinal beam intersection, thus resulting in a crushing break of the first line hollow tile blocks. On the slab side, depicted in Figure 4.97, i.e. the tension part, cracks started from the beam-column interface and then ran, with a certain slope, until the spandrel beams. Horizontal cracks appeared also along the slab-spandrel beam intersection. The cracks running from the beam-column intersection to the external side of the longitudinal beams, deeply crossed the longitudinal beams with an inclination of about 45°. A deep crack parallel to the slab plane ran through the entire longitudinal beam span.

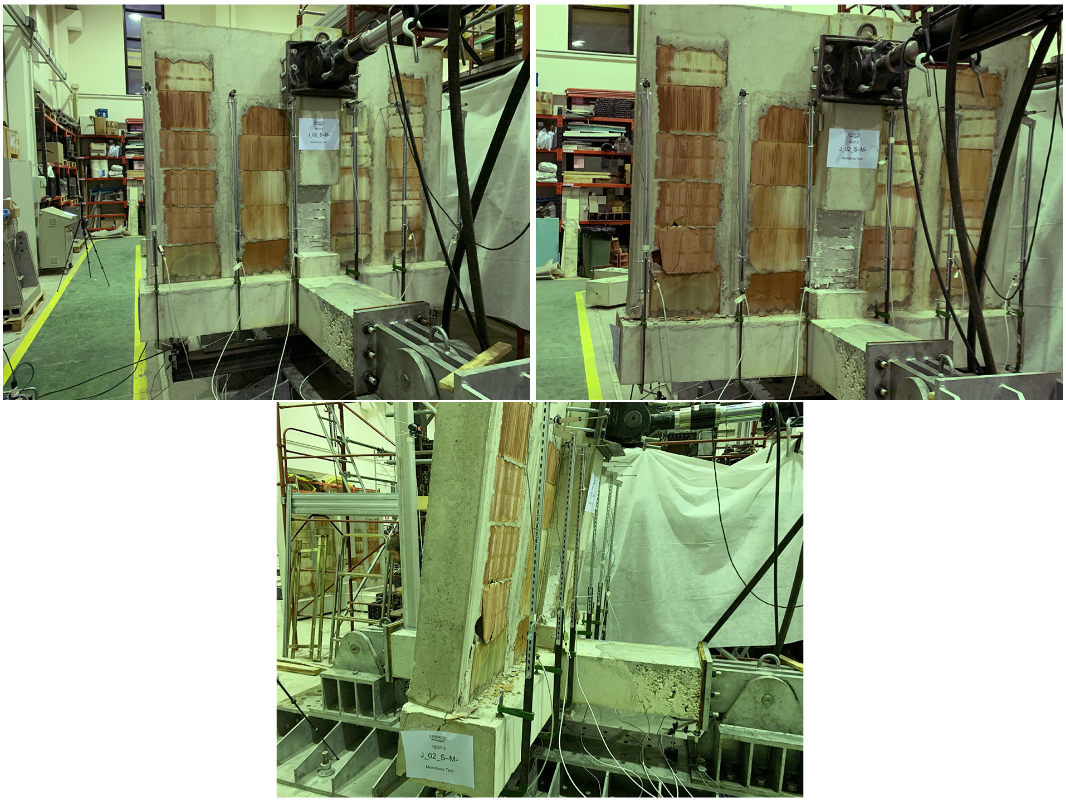

FIGURE 4.96: Crack pattern evolution on the joists side of $J\_02\_S - M^{-}$ specimen.

FIGURE 4.97: Crack pattern evolution on the slab side of $J\_02\_S - M^{-}$ specimen.

FIGURE 4.98: Crack pattern evolution in the joint and longitudinal beams of $J\_02\_S - M^{-}$ specimen.

Chapter 5

Analysis and Comparison of Tests Results

5.1 Introduction

A critical analysis of the tests results is pointed out in this Chapter, by focusing on the behaviour of the specimens, then highlighting the differences between the typologies. Firstly, a comparison is established between conventional specimens with and without the floor deck, in order to estimate the over-resistance due to the floor deck presence and, consequently, validate the theoretical formula evaluating the floor deck contribution in the joint resistance. Secondly, the response of innovative specimens is discussed. A comparison between the behaviour of innovative modules with and without the floor deck is established. Moreover, a comparison between the two different specimens typologies, i.e. conventional and innovative joints, is made, with the purpose of validating the effectiveness of the new proposed detail, realised through the localised reduction of the beam section. The results are analysed in terms of resistance, torsional rotations of the longitudinal beams and joists displacements. Aiming at highlighting the different response of the specimens once the transverse beam underwent sagging and hogging bending, the longitudinal beams torsional rotations and joists displacements are discussed with reference to the monotonic tests.

5.2 Conventional Specimens

5.2.1 Strength Response

The conventional joints, designed in compliance with the current European codes ([42],[1]), were tested for two main reasons. The first objective was to experimentally determine the increased flexural resistance due to the floor deck. The second objective was to compare the experimental value of the previously defined over-resistance with the expected theoretical value. The "equivalent beam" model predicted the expected value, by means of the theoretical formula evaluating the exact number of joists collaborating in the beam behaviour (Chapter 2).

With reference to the load-displacement graphs and the related data given in Chapter 4, Table 5.1 summarises the peak experimental loads exhibited by each specimen during the test. By recalling the terminology used in Chapter 4:

- F_E^+ is the maximum load achieved by the specimen subjected to positive displacements, i.e. when the actuator thrust forward the module;
- d_E^+ is the positive displacement at which the maximum load occurred;
- F_E^- is the minimum load achieved by the specimen subjected to negative displacements, i.e. when the actuator draw the module up;
- d_E^- is the negative displacement at which the minimum load occurred;

Specimen	F_E^+ [kN]	d_E^+ [mm]	F_E^- [kN]	d_E^- [mm]
J_01-C	82.75	53.95	-89.54	-51.72
J_01-M^+	86.06	47.47	-	-
$F_{E.av}$	**84.40**		**-89.54**	
$J\_01\_S-Geolite-C$	125.18	31.79	-156.33	-52.14
J_01_S-C	118.72	41.62	-164.79	-51.32
$J\_01\_S-M^+$	140.55	47.51	-	-
$J\_01\_S-M^-$	-	-	-154.27	-55.44
$F_{E.av}$	**128.15**		**-158.46**	
$\Delta F_{E.av}$ [%]	**+52**		**+77**	

TABLE 5.1: Positive and negative peak loads and related displacements in conventional specimens J_01 and J_01_S.

Conventional specimens without the floor deck, J_01, exhibited a peak load, induced by positive displacements, ranging from $+82.75kN$ to $+86.06kN$, with an average value, $F_{E.av}$, of $+84.40kN$. The same quantity in conventional specimens with the floor deck, J_01_S, varied from $+118.72kN$ to $+140.55kN$, with an average value of $+128.15kN$. The peak load in J_01 specimen subjected to negative displacements was $-89.54kN$, while in J_01_S specimens ranged from $-154.27kN$ to $-164.79kN$, which was, on average, $-158.46kN$. The scatter, $\Delta F_{E.av}$, between the average peak loads sustained by conventional specimens without and with the floor deck, was equal to $+52\%$ in the positive displacements direction, and $+77\%$ in the negative one. The response of specimens with the floor deck, hence, was not symmetric. The modules exhibited a greater resistance when subjected to negative displacements, i.e. when the slab underwent to tensile stresses. Table 5.1, however, provides rough information about the increase in resistance due to the presence of the floor deck. The resistance gap is more accurately provided by normal values in the following.

Before establishing a comparison through normal values, the percentage difference between the experimental and expected values is discussed. The overall values are given in Table 5.2, which summarises the maximum and minimum experimental moment for each tested specimen, M_E^+ and M_E^-, and the positive and negative moment of resistance of the transverse beam, M_R^+ and M_R^-, evaluated with the average mechanical properties of the materials. Besides, the difference between experimental and theoretical quantities, $\Delta M^{+/-}$, is given.

In *J*_01 specimens, the scatter between experimental and resistance moments should have tended to 0, theoretically. However, the average value of the differences in simple specimens was 28% and 36%, respectively for positive and negative applied displacements. Although the gap existing between the experimental and expected values, the simple specimens were considered as a benchmark. The gap was mainly due to the constitutive law model assumed for the steel in the computation of the beam moment of resistance. Indeed, the elastic-perfectly plastic behaviour was employed, hence the hardening branch was not accounted for. In addition, the length of the lever arm, through which the experimental moment was obtained, was evaluated as the distance between the middle of the actuator plate, where the load is supposed to be applied, and the intersection of the beam and column inter-axis. The plastic hinge, however, developed at the beam ends, starting from the beam-column interface. As a consequence, being the actual lever arm shorter than the considered one, the experimental moment should be greater. In addition, the actual position of the rebars in the cross-section, as compared to the design condition, can affect the slight difference in the response to positive and negative applied displacements. The reinforcement location affects the lever arm of the internal couple, hence the moment of resistance value.

In *J*_01_*S* specimens, the scatter between the experimental moment and the transverse beam resistance moment ranged, for applied positive displacements (positive bending moment), between 78% and 94%. The average value, ΔM_{av}, was 87%. The percentage difference for negative displacements (hogging bending moment) varied from 113% to 148%, with an average value of 132%. The difference between the experimental and the theoretical moments in *J*_01_*S* specimens was greater than that of *J*_01 specimen and it was not only imputable to the above-mentioned factors.

Specimen	M_E^+ [kNm]	M_R^+ [kNm]	ΔM^+ [%]	M_E^- [kNm]	M_R^- [kNm]	ΔM^- [%]
$J\_01 - C$	129.09	102.83	+26	-139.68	-102.83	+36
$J\_01 - M^+$	134.25	102.40	+31	-	-	-
$\boldsymbol{\Delta M_{av}}$			**+28**			**+36**
$J\_01\_S - Geolite - C$	195.29	102.83	+90	-243.88	-102.83	+137
$J\_01\_S - C$	185.20	103.86	+78	-257.07	-103.86	+148
$J\_01\_S - M^+$	219.25	113.19	+94	-	-	-
$J\_01\_S - M^-$	-	-	-	-240.66	-113.16	+113
$\boldsymbol{\Delta M_{av}}$			**+87**			**+132**

TABLE 5.2: Maximum and minimum experimental moments and moments of resistance of conventional specimens *J*_01 and *J*_01_*S*.

An effective method to directly compare the resistance of specimens with and without the floor deck, by proposing the same scheme of Table 5.1, consists in referring to normalised values. Normal values were evaluated as the ratio between the experimental quantities, $M_E^{+/-}$, and the resistance ones, $M_R^{+/-}$. This method, indeed, makes the quantities homogeneous, hence comparable.

In Chapter 4, a non-dimensional moment versus rotation graph was provided for each test. On the y-axis, the ratio between the experimental moment and the moment of resistance of the transverse beam, in absolute value, was plotted. The x-axis showed the joint rotation in radians. Figure 5.1 shows the overlapping of the non-dimensional moment vs rotation charts of the conventional specimens. The dashed curves refer to specimens with the floor deck, while the continuous ones refer to simple specimens. As expected, the simple joints flexural resistance is lower than that of the joints with the floor deck, which show also an asymmetric behaviour in hogging and sagging bending.

Normal values of conventional specimens are shown in Table 5.3. The difference in the normal values, $\Delta(M_E/M_R)_{av}$, of the simple joints, *J*_01, and the joints with the floor deck, *J*_01_*S*, was evaluated. *J*_01_*S* specimens showed a greater flexural resistance as compared to *J*_01 specimens, especially when the slab undergoes to tensile stresses. The scatter, indeed, was equal to +46% in sagging bending and to +71% in hogging bending.

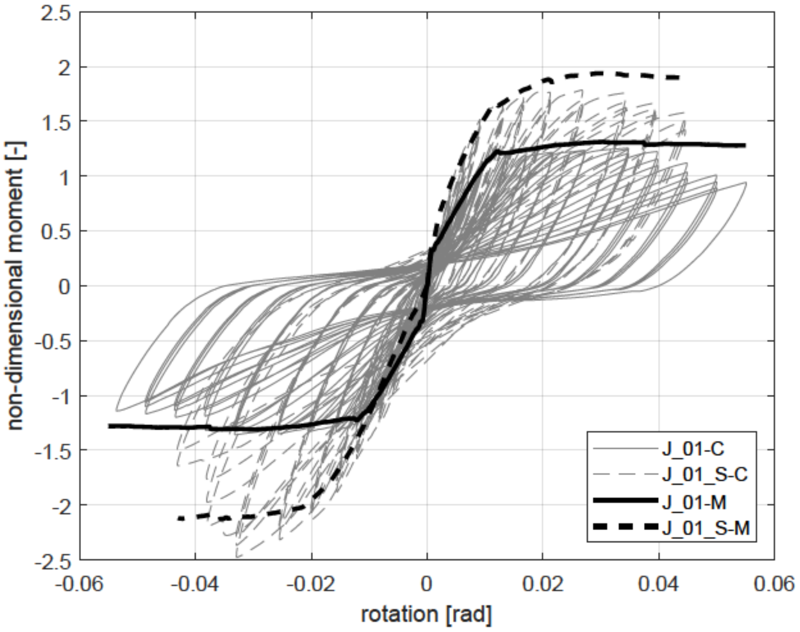

FIGURE 5.1: Overlapping of the non-dimensional moment vs rotation response of all the conventional specimens, *J*_01 and *J*_01_*S*.

Specimen	M_E^+/M_R^+ [-]	M_E^-/M_R^- [-]
J_01-C	1.26	1.36
J_01-M^+	1.31	-
$(M_E/M_R)_{av}$	**1.28**	**1.36**
$J\_01\_S-Geolite-C$	1.90	2.37
J_01_S-C	1.78	2.48
$J\_01\_S-M^+$	1.94	-
$J\_01\_S-M^-$	-	2.13
$(M_E/M_R)_{av}$	**1.87**	**2.32**
$\Delta(M_E/M_R)_{av}$[%]	**+46**	**+71**

TABLE 5.3: Peak values of normal moments in conventional specimens J_01 and J_01_S.

In the case of specimens with the floor deck, the expected resistance was more properly evaluated by means of the "equivalent beam" model. Table 5.4 shows the experimental moments for positive and negative applied displacements, $M_E^{+/-}$, the moment of resistance of the "equivalent beam" in sagging and hogging bending, $M_{R.Eq.b}^{+/-}$, and their percentage difference, $\Delta M^{+/-}$. The scatter between experimental and theoretical data ranged from $+18\%$ to $+26\%$ for positive displacements, with the average value, ΔM_{av}, of $+23\%$. The ratio for negative displacements varied between -1% and $+21\%$, being the average equal to $+12\%$. In J_01_S specimens, the percentage differences obtained through the "equivalent beam" theoretical model resistance are lower than those obtained with respect to the transverse beam (30x40cm) resistance. On average, they decreased from $+87\%$ to $+23\%$ in positive loading direction, and from $+132\%$ to $+12\%$ in negative loading direction. Moreover, the differences evaluated with reference to the "equivalent beam" resistance, in Table 5.4, were close to that of the simple joints, J_01, given in Table 5.2, which are the benchmark. They slightly differ, especially in hogging bending condition, rather than in the sagging bending. This means that the "equivalent beam" theoretical model catches the resistance of joints with the floor deck quite accurately for positive displacements while, on the contrary, for negative displacements the resistance is overrated.

Specimen	M_E^+ [kNm]	$M_{R.Eq.b}^+$ [kNm]	ΔM^+ [%]	M_E^- [kNm]	$M_{R.Eq.b}^-$ [kNm]	ΔM^- [%]
$J\_01\_S-Geolite-C$	195.29	155.64	+25	-243.88	-210.55	+16
J_01_S-C	185.20	157.00	+18	-257.07	-212.49	+21
$J\_01\_S-M^+$	219.25	173.63	+26	-	-	-
$J\_01\_S-M^-$	-	-	-	-240.66	-244.10	-1
ΔM_{av}			**+23**			**+12**

TABLE 5.4: Maximum and minimum experimental moments and "equivalent beam" moments of resistance in conventional specimens J_01_S.

Figure 5.2 summarises, by means of a bar chart, the normal values with respect to the transverse beam section (light blue and light green bars) and with respect to the "equivalent beam" section (dark blue and dark green bars). The over-resistance exhibited by *J_01_S* specimens as compared to *J_01* specimens and the accuracy of the “equivalent beam” model are clearly shown. The normal values evaluated through to the “equivalent beam” resistance are pointed out in Table 5.5.

Specimen	$M_E^+/M_{R.Eq.b}^+$ [-]	$M_E^-/M_{R.Eq.b}^-$ [-]
$J\_01\_S - Geolite - C$	1.25	1.16
$J\_01\_S - C$	1.18	1.21
$J\_01\_S - M^+$	1.26	-
$J\_01\_S - M^-$	-	0.99
$(M_E/M_{R.Eq.b})_{av}$	**1.23**	**1.12**

TABLE 5.5: Peak values of normal moments in conventional specimens *J_01_S*.

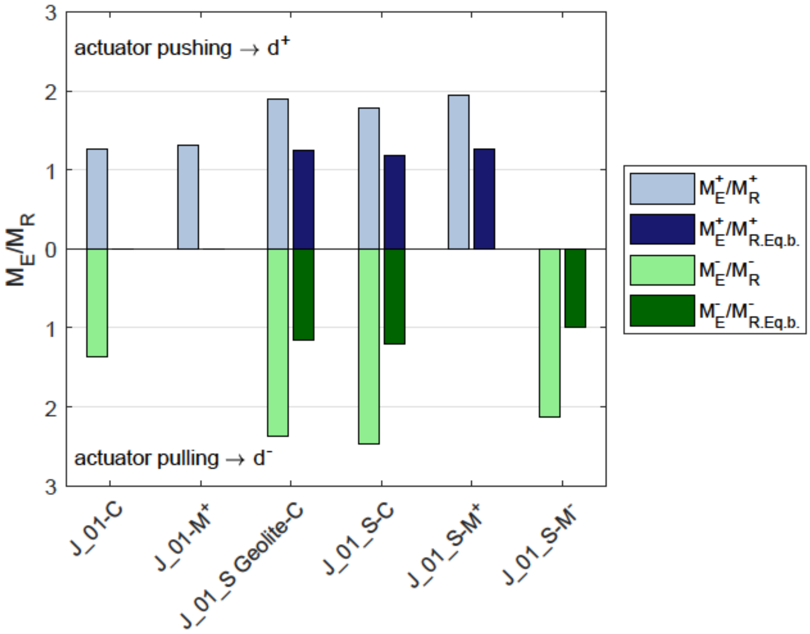

FIGURE 5.2: Validation of the “equivalent beam” model.

Provided the over-resistance that the floor deck add to the connection, an observation on the joint area is necessary. According to Eurocode 8 [1], since the specimens were designed for the Medium Ductility Class (DCM), the beam-column joint area was equipped with the same shear reinforcement provided in the critical region of the column. For the High Ductility Class (DCH), instead, further checks on beam-to-column joints are mandatory. Although the greater resistance due to the floor deck presence, at the end of the tests, no damage affected the joint area of both the specimens. This evidence led to conclude that the DCH shear reinforcement would be oversized. Finally, as a "corollary" of the experimentation carried out, it can be stated that the DCM joints are sufficiently strong.

5.2.2 Longitudinal Beams Response

The rotations exhibited by the external side of conventional connections are discussed in this Section. The vertical LDTs providing information about rotations are pointed out in Figure 5.3. They were located on both sides of the connection under the longitudinal beams, at the same abscissa. Their distance, specified in "SEC CC" of Figure 5.3, was equal to $30cm$. The rotations, θ, were evaluated as the difference between the displacements of the coupled LDTs (V-LDT_1-V-LDT_4 V-LDT_2-V-LDT_5; V-LDT_3-V-LDT_6), divided by their distance. The arrangement of linear transducers is shown in Figure 5.3 concerning the simple specimen, but it was the same as for the specimens with the floor deck.

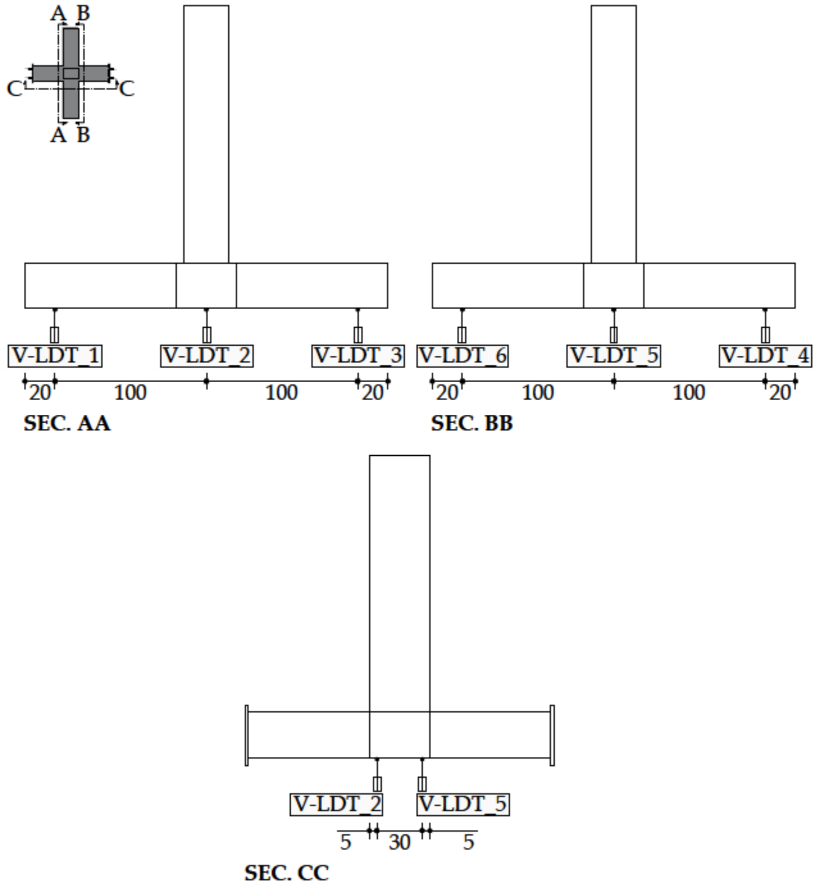

FIGURE 5.3: LDTs monitoring the vertical displacements of the longitudinal beams (units:cm).

The rotations, in radians, were plotted with respect to the drift imposed at the top of the transverse beam. In the graphs, the red and the blue curves are the torsional rotations of the longitudinal beams. They were evaluated from, respectively, V-LDT_1 and V-LDT_4, and V-LDT_3 and V-LDT_6. The black curve shows the joint rotation, derived from the V-LDT_2 and V-LDT_5 sensors. The rotations exhibited by the longitudinal beams and the joint of the $J\_01 - M^{+}$ connection are given in Figure 5.4. The rotations are quite similar to each other. Indeed, the maximum value of the joint rotation was θ(V-LDT_2-V-LDT_5)=$0.0037rad$, while those of the longitudinal beams rotation were θ(V-LDT_1-V-LDT_4)=0.0032*rad* and θ(V-LDT_3-V-LDT_6)=0.0034*rad*.

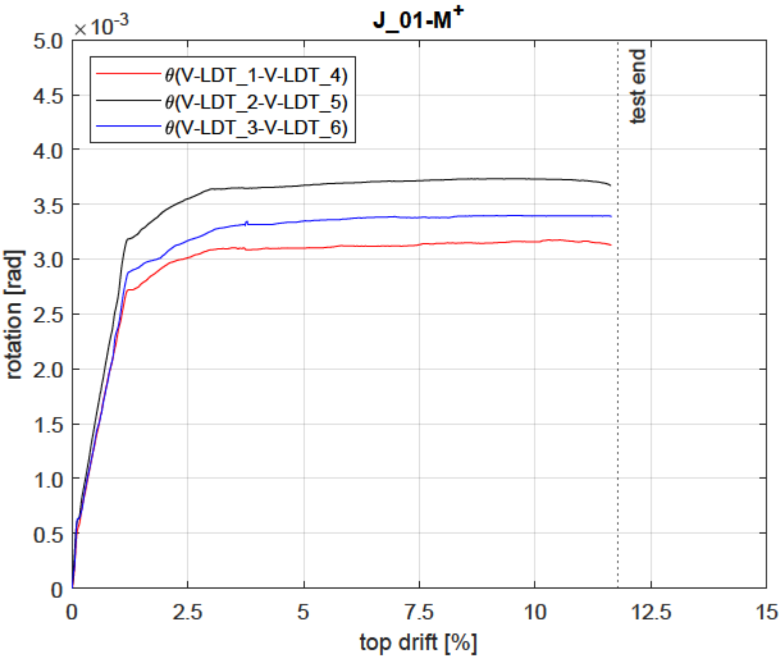

FIGURE 5.4: Rotations of longitudinal beams and joint in J_01-M^{+} specimen.

The longitudinal beams torsional rotation and the joint rotation of connections with the floor deck are shown in Figure 5.5, for $J\_01\_S-M^{+}$ specimen, and in Figure 5.6, for $J\_01\_S-M^{-}$ specimen.

For applied positive displacements at the top of the transverse beam, i.e. in $J\_01\_S-M^{+}$ specimen, the peak rotation of the joint was θ(V-LDT_2-V-LDT_5)=0.0092*rad*, while the peak longitudinal beams rotations were θ(V-LDT_1-V-LDT_4)=0.0229*rad* and θ(V-LDT_3-V-LDT_6)=0.0237*rad*.

For applied negative displacements at the top of the transverse beam, i.e. in $J\_01\_S-M^{-}$ specimen, the peak rotation of the joint was θ(V-LDT_2-V-LDT_5)=$-$0.0112*rad*, while the peak longitudinal beams rotations were θ(V-LDT_1-V-LDT_4)=$-$0.0746*rad* and θ(V-LDT_3-V-LDT_6)=$-$0.0756*rad*.

The rotations exhibited by specimens equipped with the floor deck were greater than those observed in the simple specimen. In this latter, indeed, the joint and longitudinal beams rotations were quite similar to each other and equal to, on average, 0.0034*rad*. In J_01_S specimens, instead, the response of the longitudinal beams was different from that of the joint. The joint showed fairly equal absolute rotations under positive and negative loading, equal to the peak values of 0.0092*rad*, in $J\_01\_S-M^{+}$ specimen, and -0.0112*rad* in $J\_01\_S-M^{-}$ specimen. The peak values of the longitudinal beams rotations were, on average, 0.0233*rad* in $J\_01\_S-M^{+}$ specimen, and $|-0.0751|$*rad* in $J\_01\_S-M^{-}$ specimen. Moreover, the response of the longitudinal beams rotations in J_01_S specimens was different for applied positive and negative loads. At the drift level of 6%, the longitudinal beams torsional rotations were, on average, $0.0155 rad$ in $J\_01\_S - M^+$ specimen, and $0.0471 rad$ in $J\_01\_S - M^-$ specimen. Therefore, the torsional rotation of the longitudinal beams was much higher when the slab underwent tensile stresses.

The difference in the response of J_01_S specimens to unidirectional positive and negative loading protocols was also proved by the photographic documentation in Figure 5.7, in which the damage at the end of the monotonic tests is shown. Slight damage affected the exterior side of $J\_01\_S - M^+$ connection (Figure 5.7a), while it was significant in the $J\_01\_S - M^-$ specimen (Figure 5.7b). In this latter case, a continuous crack ran over the span length and torsional cracks 45 degrees oriented spread in the longitudinal beams on both the slab and joists sides.

The torsional damage in the longitudinal beams proved the interaction between the joists and the beams supporting the floor deck, assumed in the theoretical "equivalent beam" model. The interaction, which was greater in hogging rather than in sagging bending moment, is of crucial relevance in the estimation of the number of joists collaborating in the resistance of the connection.

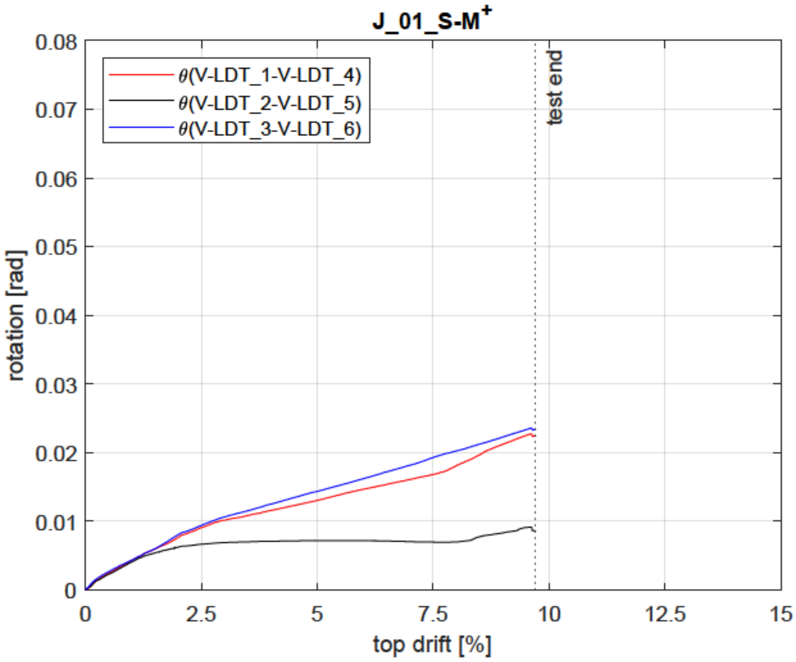

FIGURE 5.5: Rotations of longitudinal beams and joint in $J\_01\_S - M^+$ specimen.

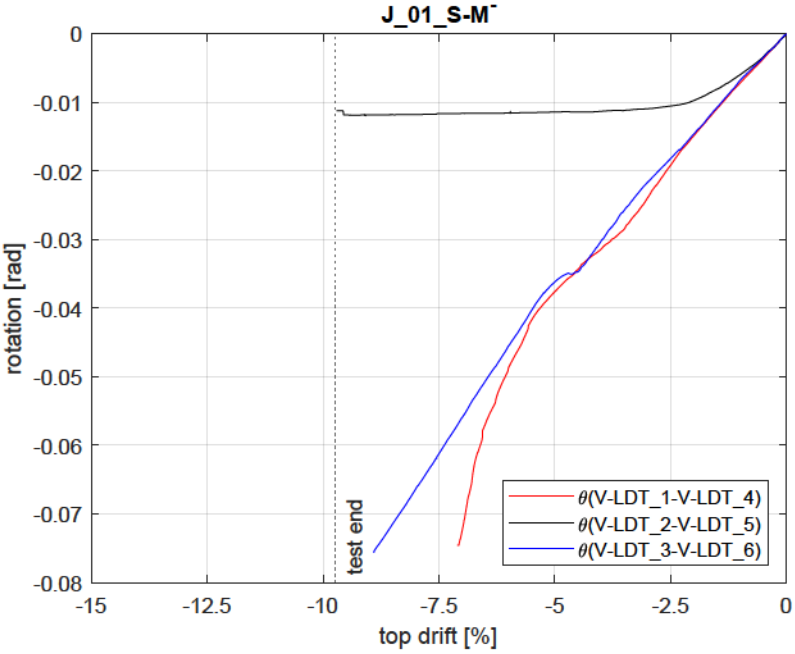

FIGURE 5.6: Rotations of longitudinal beams and joint in $J\_01\_S-M^-$ specimen.


(a) (b)

FIGURE 5.7: Longitudinal beams crack pattern in $J\_01\_S-M^+$ and $J\_01\_S-M^-$ specimens.

5.2.3 Joists Response

The difference in the response of conventional modules with the deck to positive and negative loading direction was also analysed in terms of joists displacements versus top drift applied to the specimens. The joists displacements in $J\_01\_S-M^+$ specimen, shown in Figure 5.8, exhibited the same trend during the test. At the 7% level of drift, indeed, H-LDT_1=80.54mm, H-LDT_2=80.71mm, H-LDT_5=78.22mm and H-LDT_6=77.05mm. On the contrary, in $J\_01\_S-M^-$ specimen, although the presence of the top edge beam, the response of the joists was more differentiated and their contribution decreased at increasing distance from the transverse beam. The homologous joists, i.e. those located at the same distance from the transverse beam, displayed the same history of displacements, as illustrated in Figure 5.9. At the -7% level of drift, indeed, H-LDT_1=$-41.97mm$, H-LDT_2=$-52.87mm$, H-LDT_5=$-50.55mm$ and H-LDT_6=$-18.23mm$. The different response of the homologous joists, depending on their distance from the transverse beam, proved that they provided different contributions in the resistance of the connection. This assumption is the basis of the "equivalent beam" theoretical model.

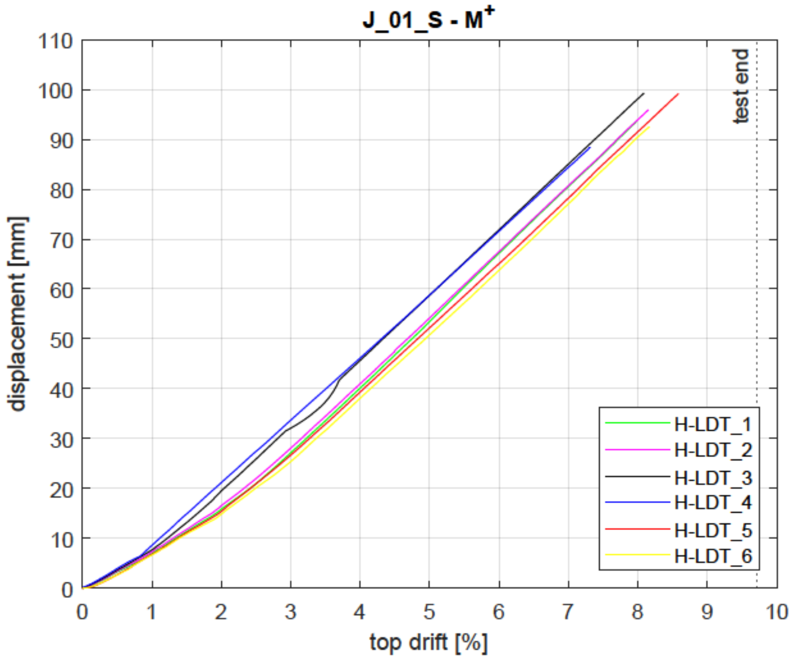

FIGURE 5.8: Joists and beam displacements versus top drift in $J\_01\_S - M^+$ specimen.

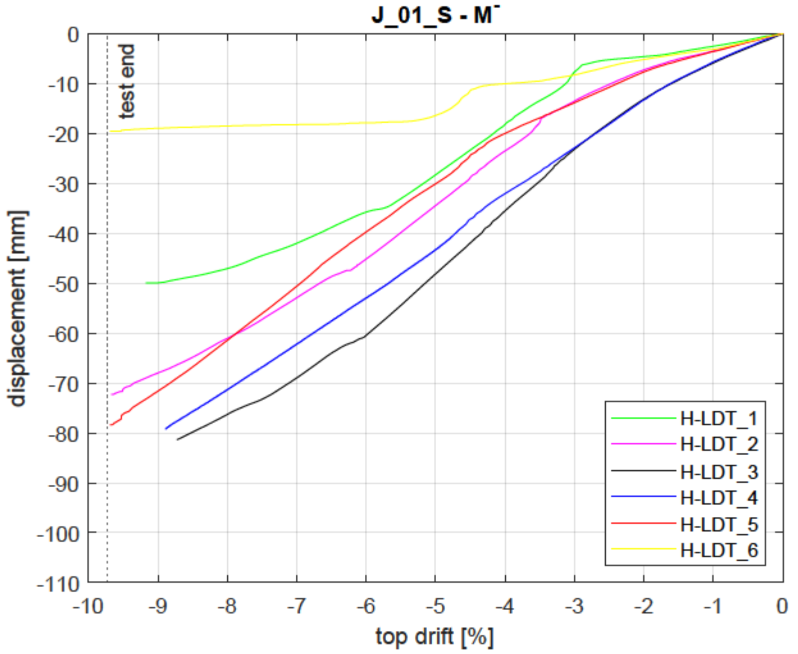

FIGURE 5.9: Joists and beam displacements versus top drift in $J\_01\_S - M^-$ specimen.

5.3 Innovative Specimens

5.3.1 Strength Response

The novelty in innovative specimens, *J*_02 and *J*_02_*S*, consisted in reducing the depth and bottom reinforcement of the transverse beam in a specific area (RBS). The reduction started at 20*cm* from the beam-column interface and extended for 50*cm* towards the middle of the beam span. Its length was that of the RBS plastic hinge, L_{pl}, properly evaluated according to the EC8 [44] formula. Both the design choices, i.e. the reduction in the beam depth and in the bottom reinforcement, aimed at reducing the flexural resistance of innovative connections as compared to the conventional ones. The extent of the reduction had to balance the over-resistance added by the floor deck and confirmed by the conventional specimens tests results, discussed in Section 5.2 of this Chapter. For the sake of comparison, indeed, the structural elements of conventional and innovative specimens were equal, being the only difference the reduced section detail of *J*_02 modules. In conclusion, the innovative specimens with the floor deck, *J*_02_*S*, were expected to exhibit a flexural resistance close to that of the conventional specimens without the floor deck *J*_01.

As for conventional specimens in Section 5.2.1, in Table 5.6, the peak experimental loads (F_E^+ and F_E^-), reached by the innovative specimens during the tests, and the related displacements (d_E^+ and d_E^-) are reported. In addition, in Table 5.7 a comparison between the average values, $F_{E.av}$, sustained by conventional and innovative connections, is proposed. The RBS in simple innovative joints, *J*_02, entailed an asymmetric reduction of the connection resistance, as compared to simple conventional joints, *J*_01. Strength decreased by 51% and 38%, respectively in positive and negative loading directions. The resistance of innovative specimens with the floor deck, *J*_02_*S*, reduced by 30% and 25% for, respectively, positive and negative applied displacements, as compared to the same type of conventional specimens, *J*_01_*S*. Finally, the resistance of innovative specimens with the slab, *J*_02_*S*, was compared to that of conventional simple specimens, *J*_01. The resistance of *J*_02_*S* connections was greater than that of *J*_01 by, respectively, 6% and 33% in, respectively, positive and negative loading directions. The analysis of the connections resistance, given in terms of load, is the first approximate evaluation of the reduced resistance due to the innovative detail, which will be provided below by accounting for the mechanical features of the materials constituting the joints.

Specimen	F_E^+ [kN]	d_E^+ [mm]	F_E^- [kN]	d_E^- [mm]
J_02-C	38.75	31.60	-52.97	-53.70
J_02-M^+	44.50	41.00	-	-
J_02-M^-	-	-	-58.17	-277.68
$\boldsymbol{F_{E.av}}$	**41.62**		**-55.57**	
J_02_S-C	85.85	40.92	-117.48	-41.50
$J\_02\_S-M^+$	93.62	53.62	-	-
$J\_02\_S-M^-$	-	-	-120.22	-68.31
$\boldsymbol{F_{E.av}}$	**89.73**		**-118.85**	

TABLE 5.6: Positive and negative peak loads and related displacements for in innovative specimens, J_02 and J_02_S.

Specimen	$F_{E.av}^+$ [kN]	$F_{E.av}^-$ [kN]
J_01	84.40	-89.54
J_02	41.62	-55.57
$\boldsymbol{\Delta F_{E.av}}$ [%]	**-51**	**-38**
J_01_S	128.15	-158.46
J_02_S	89.73	-118.85
$\boldsymbol{\Delta F_{E.av}}$ [%]	**-30**	**-25**
J_01	84.40	-89.54
J_02_S	89.73	-118.85
$\boldsymbol{\Delta F_{E.av}}$ [%]	**+6**	**+33**

TABLE 5.7: Comparison between the peak loads of conventional and innovative specimens.

Before comparing the flexural resistance of conventional and innovative specimens by means of normalised values, the experimental and expected moments of innovative modules are discussed, by referring to Table 5.8 and Table 5.9 contents. For simple innovative specimens, J_02, the expected values of the flexural strength were evaluated with reference to the RBS geometry (30x25cm) while, for innovative specimens with the floor deck J_02_S, the expected values were evaluated with reference to the "equivalent beam" section. As usual in this work, the moments of resistance were computed by assuming the stress-block and elastic-perfectly plastic constitutive laws for, respectively, the concrete and steel material behaviour.

Table 5.8 summarises the peak experimental moments $M_E^{+/-}$, evaluated as the product between the peak load and the lever arm $L_i = 1.56m$, the moment of resistance of the RBS and their percentage difference, ΔM. In J_02 specimens, the average percentage differences between experimental and expected values of bending moment were $\Delta M_{av}^+ = +37\%$, in positive moment, and $\Delta M_{av}^- = +45\%$ in negative moment. Obviously, in J_02_S specimens a greater average difference occurred, both in positive, $\Delta M_{av}^+ = +197\%$, and negative, $\Delta M_{av}^- = +210\%$, loading direction.

The expected values of innovative specimens with the floor deck were, more correctly, computed by referring to the "equivalent beam" moments of resistance, reported in Table 5.9. In this case, the difference percentage between experimental and expected resistances reduced. It was $\Delta M_{av}^{+} = +35\%$ in sagging moment, and $\Delta M_{av}^{-} = +81\%$ in hogging moment.

In general, the experimental moments were found to be greater than the expected ones. This was due to several factors. Firstly, as already found in conventional specimens, the moment of resistance was underrated due to the steel mechanical behaviour assumed in the resistance evaluation, not accounting for the hardening branch. Secondly, the experimental moment M_E, in specimens with RBS, was affected by the actual lever arm ($L_c = 1.21m$ see Figure 4.56), which was surely shorter than the adopted one ($L_i = 1.56m$). In the innovative detail, indeed, the plastic hinge was shifted far from the beam-column interface. However, the experimental and theoretical moments of simple conventional specimens, J_01, which can be considered as a benchmark, also diverged by $28\% - 36\%$. Hence a difference in this range was considered acceptable. Although the previously listed factors can reduce the divergence between experimental and theoretical expected values, a greater difference percentage persists in hogging bending as compared to the sagging bending case.

For the sake of clarity, Tables 5.8 and 5.9 are reported by referring to the experimental moment computed through the lever arm $L_c = 1.21m$, in Tables 5.10 and 5.11.

Specimen	M_E^+ [kNm]	$M_{R.RBS}^+$ [kNm]	ΔM^+ [%]	M_E^- [kNm]	$M_{R.RBS}^-$ [kNm]	ΔM^- [%]
$J\_02 - C$	60.45	46.58	+30	-82.64	-60.34	+37
$J\_02 - M^+$	69.42	47.75	+45	-	-	-
$J\_02 - M^-$	-	-	-	-90.74	-59.40	+53
$\boldsymbol{\Delta M_{av}}$			**+37**			**+45**
$J\_02\_S - C$	133.92	46.58	+188	-183.27	-60.34	+204
$J\_02\_S - M^+$	146.05	47.75	+206	-	-	-
$J\_02\_S - M^-$	-	-	-	-187.54	-59.40	+216
$\boldsymbol{\Delta M_{av}}$			**+197**			**+210**

TABLE 5.8: Maximum and minimum experimental moments and RBS moments of resistance of innovative specimens, J_02 and J_02_S.

Specimen	M_E^+ [kNm]	$M_{R.Eq.b}^+$ [kNm]	ΔM^+ [%]	M_E^- [kNm]	$M_{R.Eq.b}^-$ [kNm]	ΔM^- [%]
$J\_02\_S - C$	133.92	101.50	+32	-183.27	-103.30	+77
$J\_02\_S - M^+$	146.05	105.68	+38	-	-	-
$J\_02\_S - M^-$	-	-	-	-187.54	-100.85	+86
$\boldsymbol{\Delta M_{av}}$			**+35**			**+81**

TABLE 5.9: Maximum and minimum experimental moments and "equivalent beam" moments of resistance in innovative specimens, J_02 and J_02_S.

Specimen	M_E^+ [kNm]	$M_{R.RBS}^+$ [kNm]	ΔM^+ [%]	M_E^- [kNm]	$M_{R.RBS}^-$ [kNm]	ΔM^- [%]
$J\_02 - C$	46.89	46.58	+1	-64.10	-60.34	+6
$J\_02 - M^+$	53.84	47.75	+13	-	-	-
$J\_02 - M^-$	-	-	-	-70.38	-59.40	+18
$\boldsymbol{\Delta M_{av}}$			**+7**			**+12**
$J\_02\_S - C$	103.88	46.58	+123	-142.15	-60.34	+136
$J\_02\_S - M^+$	113.28	47.75	+137	-	-	-
$J\_02\_S - M^-$	-	-	-	-145.46	-59.40	+145
$\boldsymbol{\Delta M_{av}}$			**+130**			**+140**

TABLE 5.10: Maximum and minimum experimental moments (L_c) and RBS moments of resistance of innovative specimens, J_02 and J_02_S.

Specimen	M_E^+ [kNm]	$M_{R.Eq.b}^+$ [kNm]	ΔM^+ [%]	M_E^- [kNm]	$M_{R.Eq.b}^-$ [kNm]	ΔM^- [%]
$J\_02\_S - C$	103.88	101.50	+2	-142.15	-103.30	+38
$J\_02\_S - M^+$	113.28	105.68	+7	-	-	-
$J\_02\_S - M^-$	-	-	-	-145.46	-100.85	+44
$\boldsymbol{\Delta M_{av}}$			**+5**			**+41**

TABLE 5.11: Maximum and minimum experimental moments (L_c) and "equivalent beam" moments of resistance in innovative specimens, J_02 and J_02_S.

Table 5.12 provides information about the flexural resistance reduction in innovative connections as compared to the conventional ones. In general, through the localised section reduction (RBS), innovative beam-to-column joints were expected to exhibit lower resistance as compared to the same type of conventional specimens. In particular, the innovative design aimed at providing beam-to-column joints with the floor deck, J_02_S, having a resistance similar to that of simple conventional joints, J_01. Hence, the percentage difference between the peak experimental moment, $M_E^{+/-}$, and the moment of resistance of the full-depth beam section (30x40cm), $M_R^{+/-}$, was given. The moment of resistance was evaluated through the materials properties of each innovative joint and the assumptions on materials constitutive laws made so far.

As compared to the ideal simple specimens having constant beam section along the transverse beam longitudinal axis, simple innovative specimens, J_02, showed a flexural resistance reduced, in average, by 40% and 20% in, respectively, sagging and hogging bending moment. The RBS detail obviously entailed a resistance reduction, which was of the different amount in positive and negative bending conditions. As expected, indeed, due to the asymmetry in the top and bottom RBS reinforcement, the experimental negative moment is higher than the positive one.

As compared to the full-depth transverse beam moment of resistance, innovative specimens equipped with the floor deck, J_02_S, showed a flexural resistance increased, in average, by 28% and 71% in, respectively, positive and negative moment. Also in this case, the response of the specimens was not symmetric. The percentage difference in sagging bending was comparable to the values obtained for the simple conventional specimens, *J*_01 (28%-36%). Hence, the design objective was achieved. On the contrary, the average percentage difference in hogging bending was outside the over-strength admissible range. This means that the floor deck still had a significant impact on the flexural strength of innovative connections, once the slab underwent tensile stress.

However, this evidence was expected. As seen from the conventional specimens tests results, when the slab is subjected to tensile stress, the connection resistance is enhanced, due to the greater amount of the top steel reinforcement in tension. Consequently, the innovative detail should have resulted in resistance greatly decreased in the negative moment rather than in the positive one, the exact opposite of what resulted. It is important to stress again that the top steel reinforcement of the transverse beam was continuous along the beam, in the full-depth as well as in the reduced-depth parts, due to technological reasons. In the early stage of innovative specimens design, a different and separated steel reinforcement was provided for the full-depth and reduced-depth beam sections. However, the first sketch provided more rebars merging in the joint area, due to the anchorage length, which could have prevented a proper concrete vibration at the time of casting.

Specimen	M_E^+ [kNm]	M_R^+ [kNm]	ΔM^+ [%]	M_E^- [kNm]	M_R^- [kNm]	ΔM^- [%]
J_02-C	60.45	108.68	-44	-82.64	-108.68	-24
J_02-M^+	69.42	109.94	-37	-	-	-
J_02-M^-	-	-	-	-90.74	-107.76	-16
ΔM_{av}			**-40**			**-20**
J_02_S-C	133.92	108.68	+23	-183.27	-108.68	+69
$J\_02\_S-M^+$	146.05	109.94	+33	-	-	-
$J\_02\_S-M^-$	-	-	-	-187.54	-107.76	+74
ΔM_{av}			**+28**			**+71**

TABLE 5.12: Flexural strength reduction in innovative specimens, *J*_02 and *J*_02_*S*.

As roughly done in Table 5.7 in terms of peak loads sustained by the specimens, and by following the same scheme, in Table 5.14 a comparison between the innovative specimens and the conventional counterparts is given. Table 5.13 shows the values of the peak experimental moments normalised through the moment of resistance of the full-depth beam section (30x40cm), in order to be properly compared with the normal moments of conventional specimens. For each type of innovative specimens, the average value of the ratio, $(M_E/M_R)_{av}^{+/-}$ was evaluated. It was used, in Table 5.14, to evaluate the difference between the average normal moments of conventional and innovative specimens, $\Delta(M_E/M_R)_{av}^{+/-}$. The RBS in simple innovative joints, *J*_02, entailed an asymmetric reduction of the connection resistance, as compared to simple conventional joints, *J*_01. It was by 54% and 41%, respectively in positive and negative loading direction. The resistance of innovative specimens with the floor deck, *J*_02_*S*, reduced by 32% and 26% for, respectively, positive and negative applied displacements, as compared to the same type of conventional specimens, *J_01_S*. Finally, the resistance of innovative specimens with the slab, *J_02_S*, was compared to that of conventional simple specimens, *J_01*. Both the specimens reached the same resistance in positive bending conditions, while *J_02_S* connections showed 26% greater resistance in negative bending.

The same concepts, just expressed by discussing the contents of Table 5.14, are illustrated by means of the non-dimensional moment versus rotation curves overlapping. It was plotted for simple specimens, *J_01* and *J_02*, in Figure 5.10, for specimens with the floor deck, *J_01_S* and *J_02_S*, in Figure 5.11, and for simple conventional specimens, *J_01*, versus innovative specimens with the slab, *J_02_S*, in Figure 5.12.

Finally, the normal values are also reported in the bar chart of Figure 5.13, with reference to *J_01*, *J_01_S* and *J_02_S* specimens, respectively in light blue, dark blue and red. The resistance of innovative specimens with the floor deck was clearly much smaller than that of conventional specimens with the slab and, moreover, in perfect agreement with the simple conventional specimens ratio, especially for positive loading direction.

Specimen	M_E^+/M_R^+ [-]	M_E^-/M_R^- [-]
$J\_02 - C$	0.56	0.76
$J\_02 - M^+$	0.63	-
$J\_02 - M^-$	-	0.84
$(M_E/M_R)_{av}$	**0.59**	**0.80**
$J\_02\_S - C$	1.23	1.69
$J\_02\_S - M^+$	1.33	-
$J\_02\_S - M^-$	-	1.74
$(M_E/M_R)_{av}$	**1.28**	**1.71**

TABLE 5.13: Peak valued of normal moments in innovative specimens, *J_02* and *J_02_S*.

Specimen	$(M_E^+/M_R^+)_{av}$ [-]	$(M_E^-/M_R^-)_{av}$ [-]
J_01	1.28	1.36
J_02	0.59	0.80
$\Delta(M_E/M_R)_{av}$[%]	**-54**	**-41**
J_01_S	1.87	2.32
J_02_S	1.28	1.71
$\Delta(M_E/M_R)_{av}$[%]	**-32**	**-26**
J_01	1.28	1.36
J_02_S	1.28	1.71
$\Delta(M_E/M_R)_{av}$[%]	**0**	**26**

TABLE 5.14: Comparison between the peak normal moments of conventional and innovative specimens.

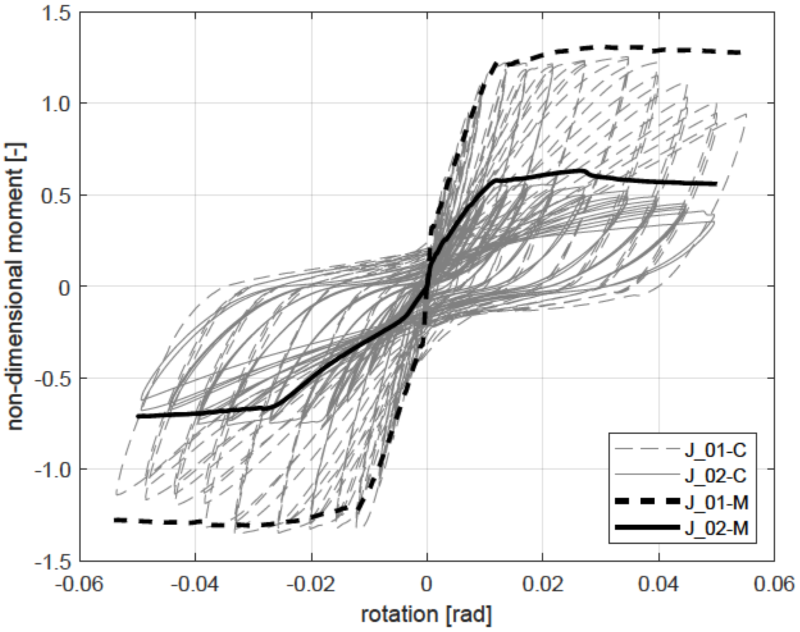

FIGURE 5.10: Overlapping of the non-dimensional moment vs rotation response of simple conventional and innovative specimens, *J*_01 and *J*_02.

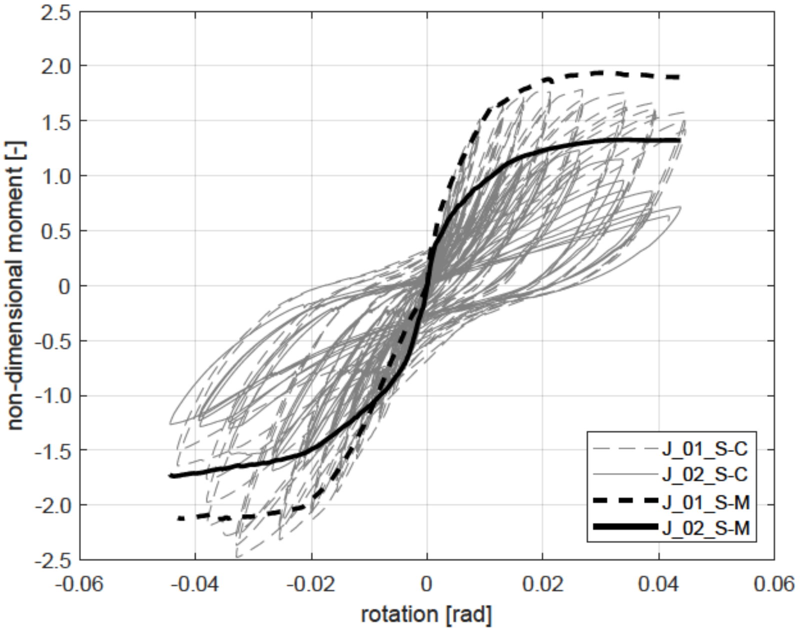

FIGURE 5.11: Overlapping of the non-dimensional moment vs rotation response of conventional and innovative specimens with the floor deck, *J*_01_*S* and *J*_02_*S*.

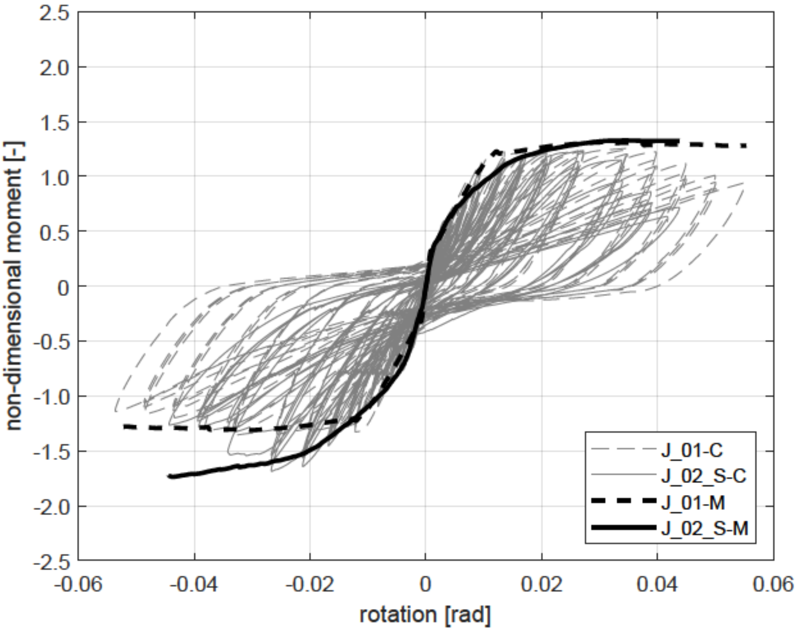

FIGURE 5.12: Overlapping of the non-dimensional moment vs rotation response of simple conventional specimens, *J_01*, and innovative specimens with the floor deck, *J_02_S*.

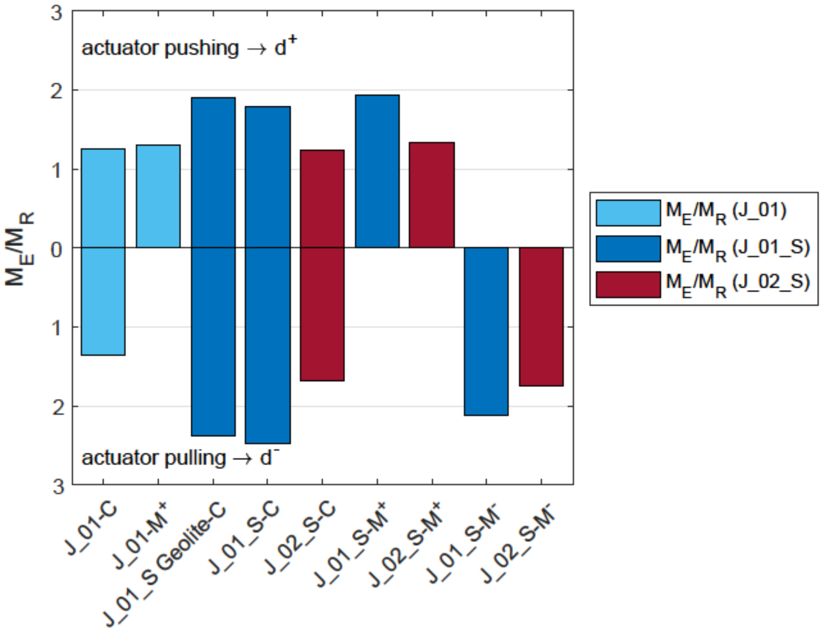

FIGURE 5.13: Validation of the innovative specimens design.

5.3.2 Longitudinal Beams Response

The longitudinal beams torsional rotations, detected by the LDTs pairs V-LDT_1 - V-LDT_4 and V-LDT_3 - V-LDT_6, as well as the joint rotations, detected by V-LDT_2 - V-LDT_5, are plotted versus the top drift imposed to the specimen. The innovative specimens results are compared to the conventional ones, discussed in Section 5.2.2.

The rotations, θ, exhibited by the longitudinal beams and joint of simple innovative specimens are given in Figure 5.14 and Figure 5.15, with reference to, respectively, $J\_02 - M^+$ and $J\_02 - M^-$ modules. In positive loading direction, rotations on the connection external side were essentially similar to each other, especially until the 2.5% drift level. The maximum value of the joint rotation was θ(V-LDT_2-V-LDT_5)=0.0015rad, while in the longitudinal beams were θ(V-LDT_1-V-LDT_4)=0.0014rad and θ(V-LDT_3-V-LDT_6)=0.0014rad. In the simple conventional module, $J\_01 - M^+$ (Figure 5.4), rotations provided by the same LDTs were θ(V-LDT_2-V-LDT_5)=0.0037rad, θ(V-LDT_1-V-LDT_4)=0.0032rad and θ(V-LDT_3-V-LDT_6)=0.0034rad. Hence, by referring to the positive loading direction, the rotations in simple innovative specimens reduced by half. In negative loading direction, instead, rotations were greater and reached values closer to those of $J\_01 - M^+$ module, i.e. θ(V-LDT_2-V-LDT_5)=$-0.0029rad$, θ(V-LDT_1-V-LDT_4)=$-0.0033rad$ and θ(V-LDT_3-V-LDT_6)=$-0.0024rad$. Clearly, some problems occurred in V-LDT_1 and V-LDT_4 signals during the test.

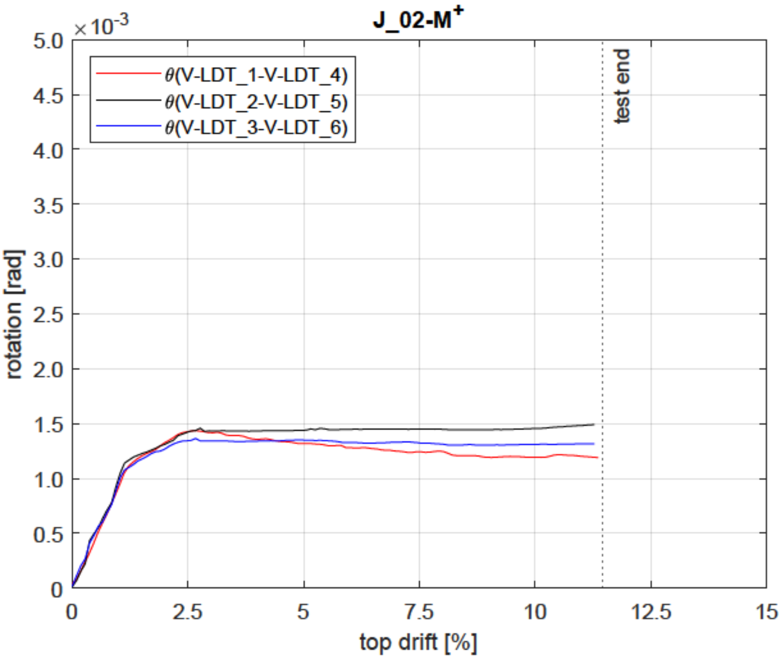

FIGURE 5.14: Rotations of longitudinal beams and joint in $J\_02 - M^+$ specimen.

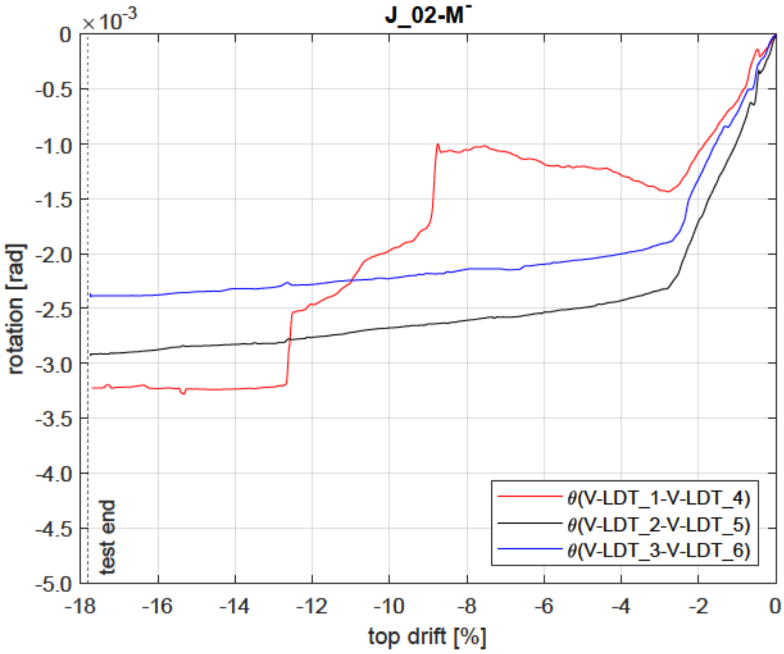

FIGURE 5.15: Rotations of longitudinal beams and joint in J_02-M^- specimen.

The response of innovative specimens equipped with the floor deck to positive and negative applied uni-directional displacements history is depicted, respectively, in Figure 5.16 and Figure 5.17. The peak rotations of joint and longitudinal beams in $J\_02\_S-M^+$ module were θ(V-LDT_2-V-LDT_5)=0.0070rad, θ(V-LDT_1-V-LDT_4)=0.0225rad and θ(V-LDT_3-V-LDT_6)=0.0208rad. The peak rotations of the joint and longitudinal beams in $J\_02\_S-M^-$ module were θ(V-LDT_2-V-LDT_5)=$-0.0069rad$, θ(V-LDT_1-V-LDT_4)=$-0.0150rad$ and θ(V-LDT_3-V-LDT_6)=$-0.0269rad$. Note that the former rotation stopped at -5.64% drift level, being the top drift at the test end equal to -10.96%. Consequently, the curve provided by V-LDT_3 and V-LDT_6 was considered to be the effective trend of the rotation of the longitudinal beams.

For the innovative specimens as well as for the conventional ones, modules with the floor deck exhibited greater rotations than the simple ones. Moreover, their response was not symmetric, showing higher rotations of the longitudinal beams for negative applied displacements. The average peak rotations were, respectively, $|-0.0269|$ and 0.0216. As opposed to simple specimens, the average peak values of the longitudinal beams rotations were greater than the joint rotation, which was equal to $|-0.0069|$ and 0.0070.

A comparison is established with the rotations of conventional joints with the floor deck. Recalling that, for J_01_S specimens, the joint rotations were 0.0092rad (in $J\_01\_S-M^+$) and $-0.0112rad$ (in $J\_01\_S-M^-$), and the average longitudinal beams rotations were 0.0233rad (in $J\_01\_S-M^+$) and $-0.0751rad$ (in $J\_01\_S-M^-$), innovative specimens with the floor deck were observed to exhibit smaller rotations, especially in the longitudinal beams in negative loading direction.

In conclusion, the innovative detail reduced the rotations, hence the damage, on the external side of the connection, as proved by the crack pattern at the end of the tests. Indeed, whereas in sagging bending conditions the damage in innovative and conventional specimens with the floor deck was slight, in hogging bending, i.e. once the slab undergoes tensile stress, it was wider spread and more significant, especially in conventional specimens (Figure 5.18 and Figure 5.19).

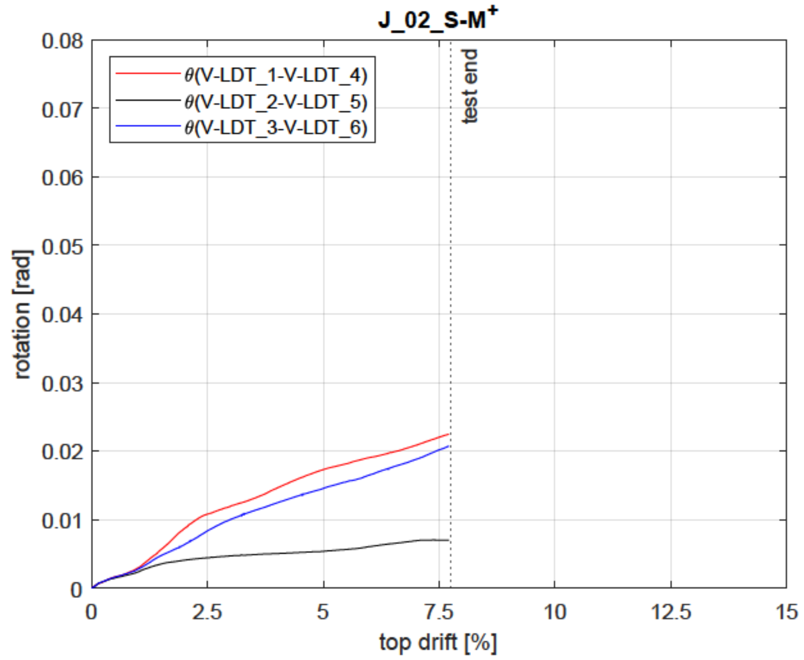

FIGURE 5.16: Rotations of longitudinal beams and joint in $J\_02\_S - M^+$ specimen.

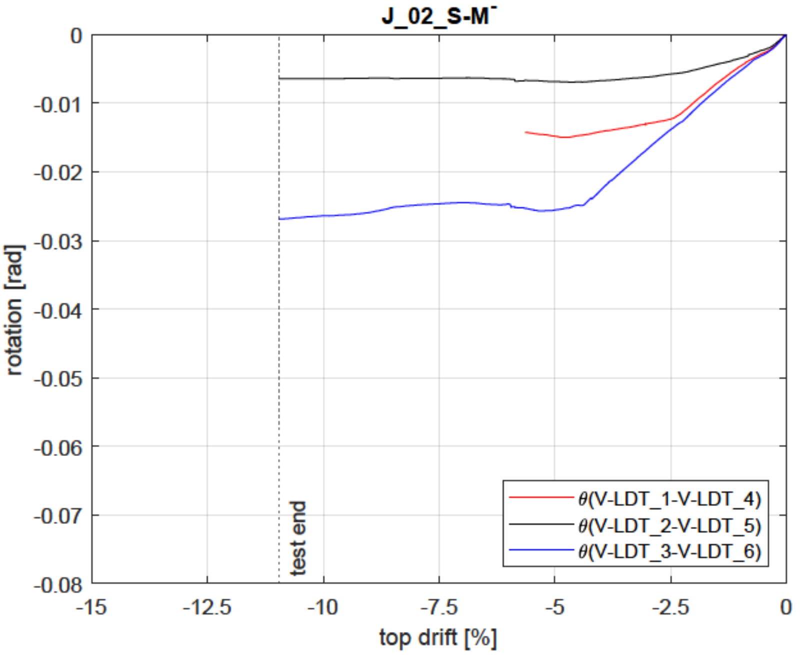

FIGURE 5.17: Rotations of longitudinal beams and joint in $J\_02\_S - M^-$ specimen.

(a) (b)

FIGURE 5.18: Joint crack pattern in $J\_01\_S - M^{+}$ (a) and $J\_02\_S - M^{+}$ (b) specimens.

(a) (b)

FIGURE 5.19: Longitudinal beams crack pattern in $J\_01\_S - M^{+}$ a and $J\_02\_S - M^{+}$ b specimens.

5.3.3 Joists Response

The response of innovative specimens to uni-directional positive and negative loading direction is discussed in terms of joists and transverse beam displacements versus the drift applied at the top of the transverse beam.

In Figure 5.20, the displacements of the floor deck in $J\_02\_S - M^+$ specimen are illustrated. The transverse beam displacements curves (H-LDT_3-H-LDT_4) overlapped perfectly. The joists curves, instead, showed lower slopes and quite the same displacements, with the exception of H-LDT_1. At the 7% level of drift, H-LDT_1=67.86mm, H-LDT_2=75.31mm, H-LDT_5=80.82mm and H-LDT_6=79.98mm.

In Figure 5.21, the floor deck displacements versus the top drift of $J\_02\_S - M^-$ specimen are given. The displacements were equal for the homologous elements, i.e. those located at the same distance from the transverse beam axis. Hence, the LDT pairs, H-LDT_1-H-LDT_6, H-LDT_2-H-LDT_5 and H-LDT_3-H-LDT_4 had an independent trend. At the -7% level of drift the joists displacements were H-LDT_1=$-63.43mm$, H-LDT_2=$-66.78mm$, H-LDT_5=$-67.14mm$ and H-LDT_6=$-63.75mm$.

In summary, the joists displacements in innovative connections showed a different response to positive and negative applied loads. In the former case, at a given drift level, greater joists displacements were observed. In the latter case, the same behaviour of the floor deck homologous elements and the independent trend of the so-defined elements pairs were found. Similar findings were obtained for conventional specimens. However, as compared to J_01_S modules, with reference to the same drift level, the displacements of the joists in J_02_S modules were slightly smaller for applied positive uni-directional loading, i.e. when the slab underwent compressive stress, and greater when a negative load protocol was applied. Although greater, the displacements exhibited in negative loading direction did not result in greater torsional rotation, hence damage, of the longitudinal beams, due to the position of the centre of rotation of the connection, shifted in the RBS.

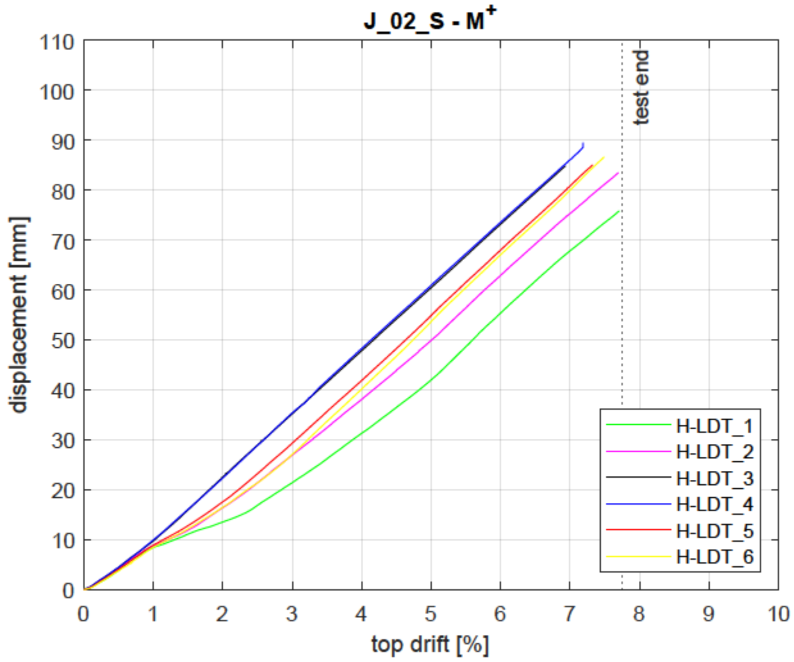

FIGURE 5.20: Joists and beam displacements versus top drift in $J\_02\_S - M^+$ specimen.

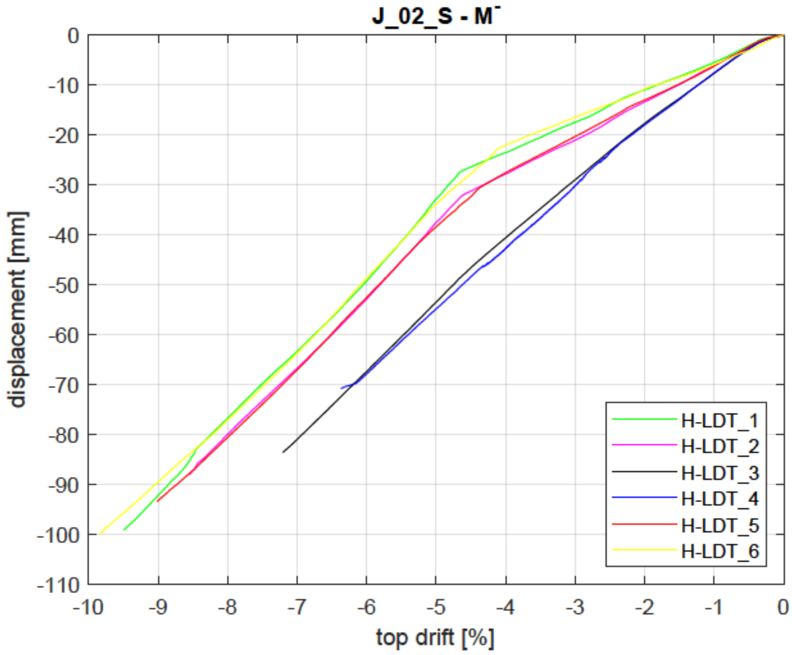

FIGURE 5.21: Joists and beam displacements versus top drift in $J\_02\_S - M^-$ specimen.

Chapter 6

Finite Element Modelling

6.1 Introduction

When a quite complex structure is subjected to an experimental campaign, the behaviour of all its parts is hard to be gathered. Many parameters, indeed, can affect the experimental data due, for example, to particular features of the test machine. Others simply can not be investigated during the test, for instance the occurrence of the plasticity in the elements. Hence, a Finite Element Model (FEM) of the investigated structure is useful to better understand what happened in a precise moment of the test. Furthermore, it is useful to evaluate the behaviour of the structure under different boundary conditions, loading history and so on. For these reasons, a 3D FEM of the tested specimen was implemented in the Abaqus [52] software.

In this chapter, firstly general information about the geometry and the mesh size of the FE models are referred. Secondly, the boundary conditions and the applied load history are shown. Then, great attention is paid in defining the material model for the reinforced concrete composing the tested specimens. The constitutive law of concrete, both in compression and in tension, is built based upon the information of the laboratory tests in Chapter 3 and on well-known literature references. The overall response of the concrete is described, both in the elastic and plastic field, by means of the 'Concrete Damaged–Plasticity' (CDP) model implemented in Abaqus. The CDP model is able to account for the concrete plasticity and the damage storage as well, typical of brittle-materials. CDP is especially useful in cyclic tests because of the possibility to control the stiffness recovery effects during cyclic load reversals. The main objective, indeed, is to calibrate the model according to the cyclic test. In the following, the calibration of monotonic tests is reported, as it is a preliminary stage before running cyclic analyses, according to the steps summarised in the flow chart of Figure 6.1. Similarly, the constitutive law of the steel is built from the results of the rebars tensile tests pointed out in Chapter 3. The assumed behaviour is reported without particular details, since it has, theoretically, a symmetrical constitutive law in tension and compression and a significant plastic deformation capacity. The results of the calibrated numerical models are reported in terms of load-displacement curve and evolution of damage.

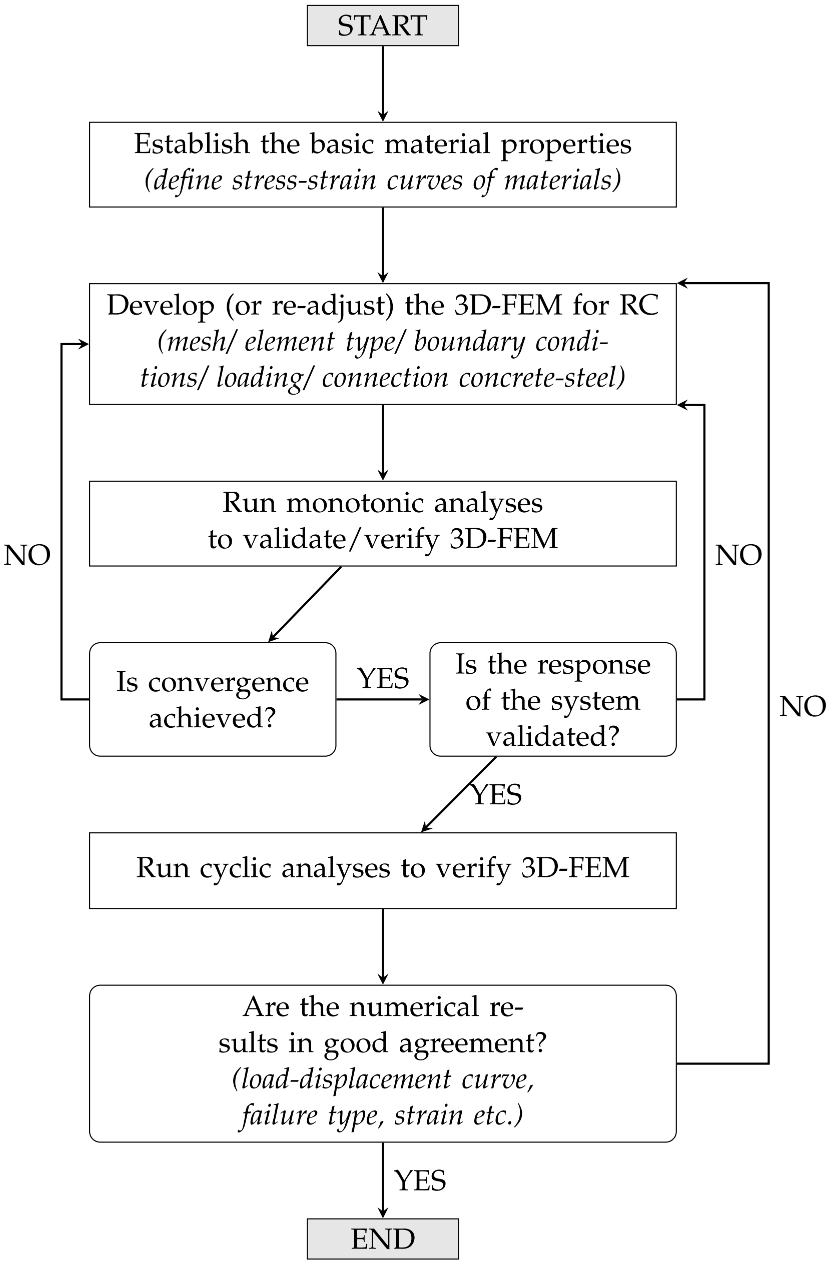

FIGURE 6.1: Steps to implement a Finite Element Model.

6.2 Finite Element Geometry and Mesh

The geometry of the specimens was implemented in Abaqus software in full compliance with the design technical details, illustrated in Chapter 2.

Each structural element composing the specimen (transverse beam, column, longitudinal beams) was implemented as a single part. After, all the parts were merged by means of constraints. The transverse beam, the one subjected to load, is a solid homogeneous element, whose length is $1.70m$. The longitudinal beams are two solid homogeneous elements of $1.00m$ length. Also the column is modelled as single solid homogeneous element of $2.00m$ length. Different typologies of constraints, like coupling, tie and merge, were used in order to find the best solution in connecting each part of the model. It turned out that they lead, more or less, to the same results but some of them entailed premature convergence problems. Finally, the continuity of the concrete has been simulated by applying tie constraints between the in-contact surfaces of the different parts. Rebars and stirrups were modelled as 3D wire deformable beam elements. Structured mesh technique was employed in the model. In particular, 3D 8–node hexahedral elements (C3D8R) were used for concrete and 3D linear beam (B31) elements for steel of rebars and stirrups. C3D8R, shown in Figure 6.2, is a general purpose linear brick element, with reduced integration, such as 1 integration point. The reduced integration implicates both advantages and shortcomings. On one hand, there are no locking phenomena observed and the computational cost is moderate. On the other hand, it is not too stiff in bending and small elements are required to adequately capture the information (stresses, strains, etc.), since those are located at the integration point [53]. B31 element used for the steel is a Timoshenko shear flexible beam (B) in space (3) with first order (1) linear interpolation. The beam orientation was assigned to enable the model work properly. The assigned mesh size was $50mm$, for all the elements in the model.

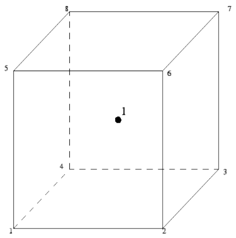

FIGURE 6.2: 1x1x1 integration point scheme in hexahedral elements.

The interaction between steel and concrete was modelled by means of the beam-in-solid embedded technique. The steel, the guest element, was embedded in the concrete, the host region. In this way, a perfect bond between reinforcement and concrete was assumed, since the embedded elements have the same translational degrees of freedom of the host region [53]. The usual real effects arising from the reinforcement-concrete interaction, such as bond slip and dowel action, was implicitly considered by defining "tension stiffening" in the reinforced concrete model, in order to indirectly simulate the load transfer through the rebars between the cracks

[53]. This technique is particularly effective for monotonic behaviour of reinforced concrete, however is not adequate in describing cyclic test, since pinching phenomena, due to the sliding, could not be captured.

The geometry and mesh of the modelled specimens are illustrated in Figure 6.3 and Figure 6.4 concerning, respectively, *J*_01 and *J*_02 specimen.

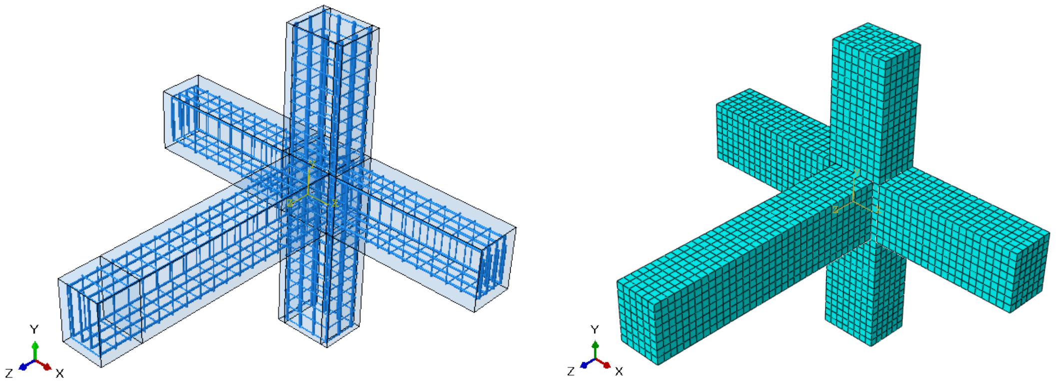

(a) (b)

FIGURE 6.3: Geometry (a) and mesh (b) of *J*_01 specimen.

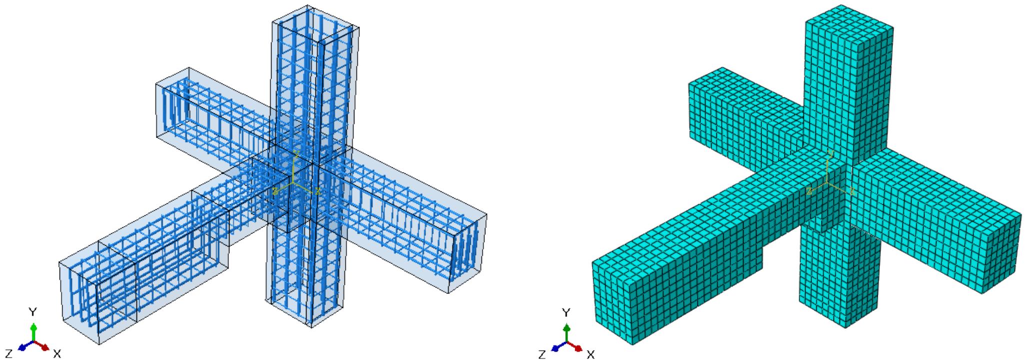

(a) (b)

FIGURE 6.4: Geometry (a) and mesh (b) of *J*_02 specimen.

6.3 Boundary Conditions and Load Application

The test machine is made up of an hydraulic actuator pushing (or pulling) the transverse beam of the specimen and one hinge and one roller constraining the column ends. The experimental layout of the loading machine and its FE implementation are shown in Figure 6.5.

In the model, boundary conditions were applied to proper sections by means of "reference points", such as points associated with a part. The column end sections were coupled to "reference points" located at the effective position of hinge and roller axes. Hence, constrains were not applied directly on the sections, but 35*cm* horizontally out of their centroid, as shown in 6.5. Finally, displacement/rotation boundary conditions were applied to the defined 'reference points', enabling the horizontal displacement (y-direction in Figure 6.5) for the roller and the rotation around the axis (x-direction in Figure 6.5) for both the constraints.

Experimental tests were carried out in displacements control and, consequently, in the software, the displacements history, for each test, was applied to the section of the transverse beam located at $141cm$ from the beam-column inter-face. At this level, indeed, representing the actuator plate centroid, the load is supposed to be applied. The horizontal displacements were directly applied to the "reference point" to which the above mentioned section is coupled.

6.4 Material Models

Reinforced concrete is a composite material, made up of steel rebars embedded into a cement-based matrix. Therefore, its structural behaviour is complex to be modelled through FE packages, both in the elastic and plastic stage, because of the joined action of concrete and steel and their interaction. Concrete exhibits a brittle failure under tension, with the possibility, under cycling reversal loading, to recover part of the original stiffness. Steel, instead, shows a ductile behaviour until the occurrence of cracks, which make impossible to connect the separated parts anymore.

The main point in modelling reinforced concrete is defining the constitutive laws, in particular the post-elasticity of the concrete. Experimentally, two main failure mechanisms affect concrete: compression crushing and tensile cracking. While the former can be well described by the theory of plasticity, the latter is well fitted by the damage theory. Consequently, the theory of plasticity, which is severely defined for metals, is not suitable for quasi-brittle materials like concrete, which can be better represented by damage models [54].

Abaqus materials library offers many models for concrete in-elasticity: the "Concrete smeared cracking" in Abaqus/Standard, the "Cracking model for concrete" in Abaqus/Explicit and the "Concrete damaged-plasticity" in both Abaqus/Standard and Abaqus/Explicit. Given the above considerations, a model coupling the two theories of plasticity and damage was chosen, i.e. the "Concrete Damaged–Plasticity" (CDP) model, in order to catch both the concrete plastic behaviour and the stiffness loss due to the damage storage [55], [56]. CDP is particularly recommended for arbitrary and cyclic loading applications. The elastic stiffness is properly modified as a function of the plastic deformations, both in tension and in compression, which is calculated by means of damage parameters. Moreover, it takes into account the stiffness recovery effects under cyclic loading [53]. Analyses were run with Abaqus/Standard solver, although the FE standard implicit procedure could bring about convergence problems when cracking and damage are involved [57]. However, to overcome any convergence problem, it is possible to apply a viscoplastic regularization of the constitutive equations.

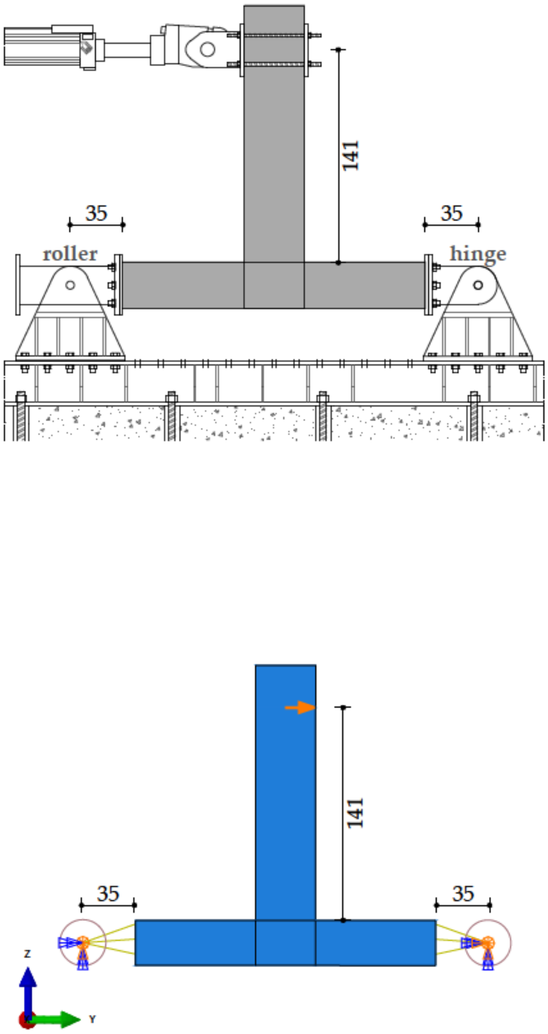

FIGURE 6.5: Test layout simulation in Abaqus environment.

As mentioned above, the mechanical properties of the concrete were investigated by means of crushing tests on concrete cubes, thus evaluating the compressive strength. The complete behaviour of concrete, instead, has to be simulated both under tension and under compression and both in elastic and in inelastic field, since the equivalent plastic strains control the evolution of the yield surface. In particular, the tensile inelastic behaviour is quite complex to be described, since tension stiffening and bond effects have to be accounted for. CDP requires many parameters to be implemented in the software. The parameters can be properly calibrated, this is the case, or experimentally evaluated [58].

A uni-axial plasticity model was employed for the behaviour of the steel constituting the rebars. The yield and ultimate strength values were those evaluated through tensile tests in Chapter 3. As first attempt, an elastic-plastic constitutive law was implemented, in order to reduce the computational time.

6.4.1 Concrete Damaged-Plasticity Model

The CDP theory was firstly proposed by Lubliner et al.[55], for monotonic, cyclic and dynamic behaviour, and it was further developed by Lee and Fenves [56]. The constitutive model is suitable for different types of concrete structures (beams, trusses, shells, and solids) exhibiting a quasi-brittle behaviour, such as subjected to low confining pressure. The main failure mechanisms of cracking in tension and crushing in compression, occurring under limited confining pressure, manage the brittle behaviour of the concrete. Conversely, a significant hydrostatic pressure, avoiding the crack propagation, ensures the concrete macroscopically behaves in a ductile manner.

The inelastic behaviour of concrete is obtained by combining the isotropic damaged elasticity theory and the isotropic tensile and compressive plasticity theory. Figure 6.6 clarifies the differences among uni-axial stress-strain curves of "Plasticity" (a), "Damage" (b) and "Plastic Damage" (c) models [59]. In the "Plasticity Model", the unloading branch has the slope of the elastic one, provided by the initial modulus of elasticity E_0. Besides, the total strain (ε) is the sum of an elastic (ε^{el}) and plastic component ($\tilde{\varepsilon}^{pl}$). In the "Damage Model", the unloading branch is not only dependent on the deformation modulus E_0, but on the damage variable d too, which causes stiffness degradation and the impossibility to know the irreversible strain. The "Plastic Damage Model" overestimates neither the plastic strain, like the elastic-plastic relation, nor the damage, like the damage law, since combines these two approaches by catching the constitutive experimental unloading behaviour. By means of the damage part, it reproduces the softening behaviour and the reduction of the elastic modulus; in the meantime, through the plasticity part, it estimates the plastic unrecoverable strain [60].

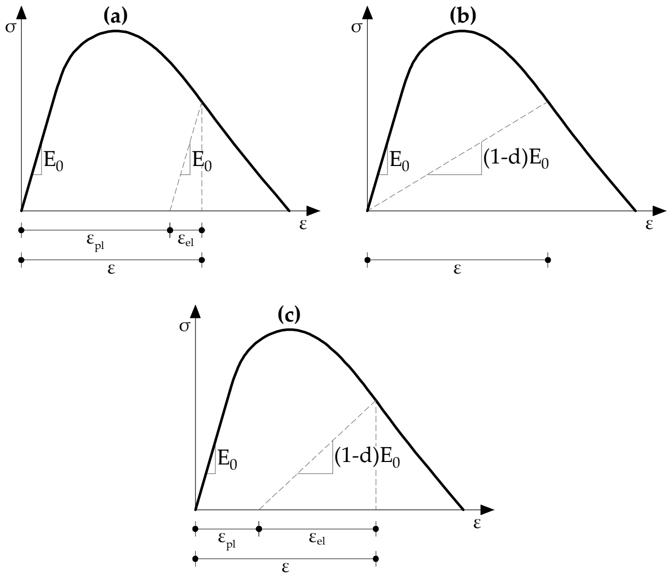

FIGURE 6.6: CDP constitutive law.

In other words, CDP describes the irreversible damage occurring during the fracture evolution, by combining non-associated multi-hardening plasticity and scalar (isotropic) damaged elasticity [53]. The two hardening variables controlling the yield surface are the tensile and compressive equivalent plastic strain, respectively $\tilde{\varepsilon}_t^{pl}$ and $\tilde{\varepsilon}_c^{pl}$. These variables are linked to the two main failure mechanisms of tensile cracking and compressive crushing and are calculated by the software from the uni-axial stress behaviour in tension and compression.

By means of specific parameters, w, to be defined both in tension and in compression (w_t and w_c, respectively), is also possible to take into account the stiffness recovery effects under reversed cyclic loading, as illustrated in Figure 6.7.

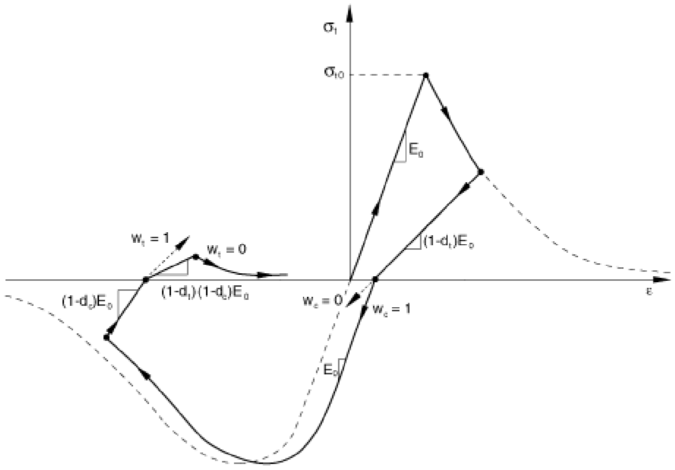

FIGURE 6.7: Uni-axial load cycle (tension-compression-tension).

6.4.1.1 Uni-axial Concrete Tensile Behaviour

The uni-axial tensile behaviour of the concrete was difficult to calibrate for different reasons. Firstly, the experimental ultimate tensile strength was unknown, since no specific tests were led up to find out it. Secondly, many different formula computing this value are available in literature and in codes. Finally, according to [61], [62], [63], the ultimate tensile strength of the concrete, f_{tm} was evaluated, in megapascal (MPa), as a function of the concrete compressive strength f_{cm}:

$$f_{tm} = 0.33\sqrt{f_{cm}} \tag{6.4.1}$$

The tensile stress-strain response of the concrete is elastic until the failure stress, with a slope corresponding to the modulus of elasticity E_0, equal to the compressive one reported in detail in the following Section 6.4.1.2.

After the failure stress, micro-cracks spread throughout the concrete, inducing strain localization, which has to includes both the crack width and tensile strain between the cracks. Noticeably, such a tensile model is called "smeared" and shows a softening stress-strain response [64]. The tension softening behaviour, also known as tension stiffening, is required in the CDP model, as it allows to take into account the interaction between concrete and reinforcement. Abaqus User's Guide [53] provides different ways to implement the tension stiffening. For instance, it suggested a value for the ultimate tensile strain (10^{-3} for standard concrete), in order to achieve the numerical solution. Indeed, more tension stiffening helps to achieve convergence more easily. On the contrary, less tension stiffening can lead to instability in the model response.

In this work, the softening segments of the constitutive laws were implemented throughout a post-failure stress-strain parameters, based on the "Fracture Energy Cracking" criterion. In the tension case, it assumes that the stress is a decreasing function of the crack opening, w. The descending branches, both for compressive and tensile behaviour, are generated in order to assure the mesh independency of the model, according to one of the so-called mesh regularization techniques, i.e. the "Crack Band Method" [65]. Therefore, the softening branch is obtained from the fracture energy per unit area. Consequently, both fracture and crushing energy, G_F and G_{ch} respectively, which are material parameter, have been set on the equivalent length l_{eq} of the finite element. As one might imagine, the characteristic (or equivalent) length l_{eq} depends on the finite element integration point, such as on the mesh size and on the type, form and quadratic rule of the element [59], [66]. In this work, the characteristic length of the first-order solid brick elements meshing the concrete was derived by dividing the volume by the largest face area [59].

Many different post-elastic tensile relations can be implemented, applying the "Fracture Energy Cracking" criterion. The simplest one consists in assuming a linear function until the critical crack width is reached [53]. This approximation can considerably reduce the computational time of the analysis, on one side, and it can cause a more stiff response, on the other side. Bi-linear [67, 68] and exponential expressions [69] can lead to more accurate results. In this case, the exponential formulation [69] was chosen. The ratio between the generic tensile stress at crack width, $\sigma(w)$, and the ultimate tensile strength, f_{tm} is:

$$\frac{\sigma_t(w)}{f_{tm}} = \left[1 + \left(c_1 \frac{w}{w_c}\right)^3\right] e^{-c_2 \frac{w}{w_c}} - \frac{w}{w_c}\left(1 + c_1^3\right) e^{-c_2} \tag{6.4.2}$$

in which $c_1 = 3$, $c_2 = 6.93$ are material constants [69] and w_c is the crack-opening displacement at complete release of fracture energy, G_F, since $\sigma_t(0) = f_{tm}$ and $\sigma_t(w_c) = 0$. Therefore, the critical crack-opening is equal to:

$$w_c = 5.14 \frac{G_F}{f_{tm}} \tag{6.4.3}$$

and the fracture energy G_F (N/mm) can be evaluated, according to [68], as:

$$G_F = 0.073 f_{tm}^{0.18} \tag{6.4.4}$$

Alternatively, G_F can be also estimated as $G_F = G_{F0}(f_{cm}/f_{cm0})^{0.7}$ [70], in which

G_{F0} is the base value of the fracture energy, depending on the maximum aggregate size, and $f_{cm0} = 10MPa$.

The whole tensile constitutive law is shown in Figure 6.8.

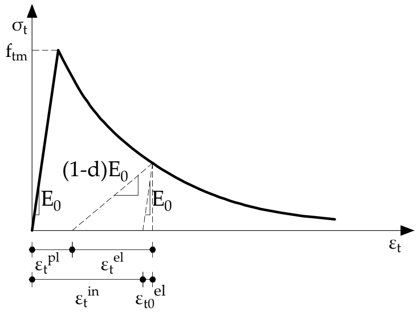

FIGURE 6.8: Uni-axial concrete tensile behaviour.

According to [57], the crack distribution was not studied in this work and was assumed a single crack per element. Therefore, the stress-crack opening displacement curve was switched into a stress-strain curve, by means of the kinematic relation from the "Crack Band Model":

$$\varepsilon_t = \varepsilon_{tm} + \frac{w}{l_{eq}} \tag{6.4.5}$$

where ε_{tm} is clearly the strain corresponding to f_{tm}.

The obtained stress-strain values were implemented in Abaqus as stress versus inelastic strain values, $\tilde{\varepsilon}_t^{ck}$ in Figure 6.8. Once the damage parameters have been implemented, according to Section 6.4.1.3, the software automatically deduces the plastic strain. The cracking strain is the total strain minus the elastic strain of the undamaged material, i.e. $\tilde{\varepsilon}_t^{ck} = \varepsilon_t - \varepsilon_{0t}^{el}$, with $\varepsilon_{0t}^{el} = \sigma_t / E_0$ [53].

6.4.1.2 Uni-axial Concrete Compressive Behaviour

The uni-axial compressive constitutive law of the concrete follows the general damaged-plasticity curve shown in Figure 6.9. It is composed of three parts: a first linear branch, until the value of the initial yield stress, a hardening part, until the failure strength, and a last softening field.

The uni-axial constitutive law was derived according to [68], by means of the average ultimate stress value, obtained from the compressive strength tests on concrete cubes, f_{cm}, occurring at the conventional strain rate $\varepsilon_{cm} = 0.0022$ [68]. The first linear segment follows the Hooke law:

$$\sigma_c^{(1)} = E_0 \varepsilon_c \tag{6.4.6}$$

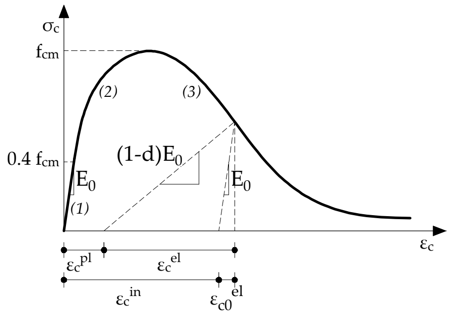

FIGURE 6.9: Uni-axial concrete compressive behaviour.

starting from zero stress until $0.4f_{cm}$. In Equation 6.4.6, ε_c is the generic strain value, and E_0 is the secant modulus of elasticity, equal to (in MPa):

$$E_0 = \left(0.8 + 0.2\frac{f_{cm}}{88}\right) E_{ci} \tag{6.4.7}$$

In Equation 6.4.7, E_{ci} is the initial deformation modulus for zero stress, which is equal to (in MPa):

$$E_{ci} = 10000 f_{cm}^{1/3} \tag{6.4.8}$$

The assumption of an initial linear behaviour is not in accordance with experimental results, as the $\sigma - \varepsilon$ law is not linear even starting from very low load values. Nevertheless, for normal concrete, the linear $\sigma - \varepsilon$ relation is a fair approximation until 30-40% of the maximum stress, before the internal micro-cracking occurs, reducing the stiffness.

For stress values ranging from $0.4f_{cm}$ to f_{cm}, the concrete shows a hardening behaviour, with a stiffness progressively decreasing to 0 (horizontal tangent) at ultimate strength. The second segment of the $\sigma - \varepsilon$ law is well fitted by the quadratic analytical function in [68]:

$$\sigma_c^{(2)} = \frac{E_{ci}\frac{\varepsilon_c}{f_{cm}} - \left(\frac{\varepsilon_c}{\varepsilon_{cm}}\right)^2}{1 + \left(E_{ci}\frac{\varepsilon_{cm}}{f_{cm}} - 2\right)\frac{\varepsilon_c}{\varepsilon_{cm}}} f_{cm} \tag{6.4.9}$$

The third softening field, after the peak strength f_{cm} and its relative strain ε_{cm}, is characterized by the localization of the damage. As tension, also the compressive softening branch has been derived by means of the "Crack Band Method" [65]. Therefore, the fracture energy under compression, which is the material parameter of the crushing energy per unit area G_{ch}, and the equivalent length l_{eq} of the finite element were employed. In consequence, fixed the mesh size, the third segment, describing the softening behaviour, was defined according to the following relation [66]:

$$\sigma_c^{(3)} = \left(\frac{2 + \gamma_c f_{cm}\varepsilon_{cm}}{2f_{cm}} - \gamma_c\varepsilon_c + \frac{\varepsilon_c^2\gamma_c}{2\varepsilon_{cm}}\right)^{-1} \tag{6.4.10}$$

in which:

$$\gamma_c = \frac{\pi^2 f_{cm}\varepsilon_{cm}}{2\left[\frac{G_{ch}}{l_{eq}} - 0.5 f_{cm}\left(\varepsilon_{cm}\left(1-b\right) + b\frac{f_{cm}}{E_0}\right)\right]^2} \tag{6.4.11}$$

with:

$$b = \frac{\tilde{\varepsilon}_c^{pl}}{\tilde{\varepsilon}_c^{ch}} \tag{6.4.12}$$

and:

$$G_{ch} = \left(\frac{f_{cm}}{f_{tm}}\right)^2 G_F \tag{6.4.13}$$

The scalar parameter b splits inelastic strains, $\tilde{\varepsilon}_c^{ch}$, into plastic strains, $\tilde{\varepsilon}_c^{pl}$. It can be assumed $b = 0.9$, as first approximation, according to experimental observations. The value of b changes during the iterative procedure explained in Section 6.4.1.4, hence it has to be uploaded each step until convergence is reached.

In Equation 6.4.13, G_F is the fracture energy described in Section 6.4.1.1. Since the softening branch asymptotically drops to zero, G_{ch} is used to evaluate the maximum fictitious strain value of the curve, as the product between the area under the curve and the characteristic length is the target to achieve.

As for tension, for compression as well the stress-strain curve was implemented in the FE software throughout stress versus inelastic strain values. The compressive inelastic (or crushing) strain is obtained as the total strain minus the elastic strain corresponding to the undamaged material, $\tilde{\varepsilon}_c^{ch} = \varepsilon_c - \varepsilon_{0c}^{el}$, with $\varepsilon_{0c}^{el} = \sigma_c / E_0$ [53].

6.4.1.3 Damage Variables

As above explained and illustrated in Figures 6.8 and 6.9, the CDP model requires the definition of damage parameters, describing the unloading response in the softening branch of constitutive laws, both in tension and in compression. Indeed, if the damage is not defined as a function of inelastic strains, $\tilde{\varepsilon}_t^{ck}$ and $\tilde{\varepsilon}_c^{ch}$, the material model behaves like a plasticity model, as already reported in Figure 6.6, thus $\tilde{\varepsilon}_t^{ck} = \tilde{\varepsilon}_t^{pl}$ and $\tilde{\varepsilon}_c^{ch} = \tilde{\varepsilon}_c^{pl}$.

Conversely, the CDP model assumes that the unloading of the concrete specimen in the softening branch of the stress-strain curve is affected by a degradation of the elastic stiffness. It means that the material response is weakened since the material has been affected by damage. The parameters to be defined in order to account for the degradation of the stiffness are scalar variables, d_t and d_c, respectively for tensile and compressive behaviour, which depend on the plastic strains, $\tilde{\varepsilon}_t^{pl}$ and $\tilde{\varepsilon}_c^{pl}$. The damage parameters values vary between 0 and 1, representing respectively the undamaged condition and the total loss of strength. They serve a purpose of defining the 'effective' tensile and compressive cohesion stress, in Equations 6.4.14 and 6.4.15, characterizing the size of the yield (or failure) surface:

$$\bar{\sigma}_t = \frac{\sigma_t}{(1-d_t)} = E_0(\varepsilon_t - \tilde{\varepsilon}_t^{pl}) \tag{6.4.14}$$

$$\bar{\sigma}_c = \frac{\sigma_c}{(1-d_c)} = E_0(\varepsilon_c - \tilde{\varepsilon}_c^{pl}) \tag{6.4.15}$$

Actually, Abaqus documentation does not provide any recommendation about how to evaluate the scalar damage parameters. A highly regarded method to define damage variables was provided by Lubliner et al.[55]. This method related the stiffness to the material cohesion, hence to the strength of the concrete. Over the years, many researchers proposed modifications. Constant factors [71], fitting with the experimental data of cyclic tests, were added to the main expression proposed by Lubliner et al.[55]. Alternatively, exponential functions were employed to calculate the damage variables for both compression and tension [72].

In this work, a new methodology proposed by [59] was applied to compute the damage variables since it provided a good accordance between experimental and FEM load versus displacement curve. Hence, tensile and compressive damage functions are:

$$d_t = 1 - \frac{1}{2+a_t}\left[2\left(1+a_t\right)e^{-b_t\tilde{\varepsilon}_t^{ck}} - a_t e^{-2b_t\tilde{\varepsilon}_t^{ck}}\right] \tag{6.4.16}$$

$$d_c = 1 - \frac{1}{2+a_c}\left[2\left(1+a_c\right)e^{-b_c\tilde{\varepsilon}_c^{ch}} - a_c e^{-2b_c\tilde{\varepsilon}_c^{ch}}\right] \tag{6.4.17}$$

where:

$$a_t = 2\left(\frac{f_{tm}}{f_{t0}}\right) - 1 + 2\sqrt{\left(\frac{f_{tm}}{f_{t0}}\right)^2 - \left(\frac{f_{tm}}{f_{t0}}\right)} \tag{6.4.18}$$

$$a_c = 2\left(\frac{f_{cm}}{f_{c0}}\right) - 1 + 2\sqrt{\left(\frac{f_{cm}}{f_{c0}}\right)^2 - \left(\frac{f_{cm}}{f_{c0}}\right)} \tag{6.4.19}$$

and:

$$b_t = \frac{f_{t0} l_{eq}}{G_F}\left(1 + \frac{a_t}{2}\right) \tag{6.4.20}$$

$$b_c = \frac{f_{c0} l_{eq}}{G_{ch}}\left(1 + \frac{a_c}{2}\right) \tag{6.4.21}$$

In Equations 6.4.18, 6.4.19, 6.4.20 and 6.4.21, the a_t, a_c, b_t and b_c parameters are expressed as a function of $f_{t0} = f_{tm}$ and $f_{c0} = 0.4 f_{cm}$.

6.4.1.4 Implementation of CDP Parameters

In this Section, the detailed implementation of the previously defined CDP parameters is reported. The iterative procedure, proposed by [59], is herein reported step by step, by expressing all the stresses in MPa. Once the convergence is achieved, the definitive curves of stress versus strain and damage variables versus cracking/crushing strain are obtained, for tensile and compressive behaviour. The output of the iterative procedure for each modelled specimen, i.e. the parameters implemented in the software, are reported in Table 6.1 and in Figures 6.10, 6.11 and 6.12. However, the constitutive parameters implemented were limited to damage values of about 90%, as for higher values Abaqus exited with errors.

1. Define the starting data. Firstly, the average value of the concrete compressive strength, f_{cm}, and the value of the strain at the peak compressive strength, $\varepsilon_{cm} = 0.0022$, as indicated in Section 6.4.1.2. In addition, the average value of the concrete tensile strength, f_{tm}, according to Equation 6.4.1. Moreover, the equivalent length of the mesh size, l_{eq}, fixed a priori. Finally, the b parameter in Equation 6.4.12, initially assumed equal to 0.9.

2. Evaluate the concrete tangent and the secant modulus of deformation, respectively $E_{ci} = 10000 f_{cm}^{1/3}$ and $E_0 = (0.8 + 0.2 f_{cm}/88)$, as pointed out in Section 6.4.1.2.

3. Calculate the fracture and crushing energy, according to Equation 6.4.4 and 6.4.13, in N/mm, i.e. $G_F = 0.073 f_{cm}^{0.18}$ and $G_{ch} = (f_{cm}/f_{tm})^2 G_F$.

4. Define, according to Equation 6.4.3, $w_c = 5.14 G_F / f_{tm}$, the critical crack opening.

5. Build the whole concrete compressive constitutive law, through its first, Equation 6.4.6, second, Equation 6.4.9, and third, Equation 6.4.10 branch. It is reminded to limit the crushing strain in order to develop the entirely crushing energy, G_{ch}.

6. Build the two segments of the tensile stress-strain constitutive law, by using the linear relation $\sigma_t^{(1)} = E_0 \varepsilon_t$ and by referring to Equation 6.4.2 and Equation 6.4.5, for respectively stress and strain of the second branch.

7. Evaluate the a_t, a_c, b_t and b_c parameters according to Equations 6.4.18, 6.4.19, 6.4.20 and 6.4.21, remembering that $f_{t0} = f_{tm}$ and $f_{c0} = 0.4 f_{cm}$.

8. Define both the tensile and the compressive damage evolution parameters, d_t and d_c, by following the Equations 6.4.16 and 6.4.17, respectively.

9. Calculate the tensile and compressive plastic strain $\tilde{\varepsilon}_t^{pl} = \tilde{\varepsilon}_t^{ck} - \sigma_t d_t / [(1 - d_t) E_0]$ and $\tilde{\varepsilon}_c^{pl} = \tilde{\varepsilon}_c^{ch} - \sigma_c d_c / [(1 - d_c) E_0]$, as reported in Figures 6.8 and 6.9.

10. Evaluate the average value of ratio $b = \tilde{\varepsilon}_c^{pl} / \tilde{\varepsilon}_c^{ch}$, compare it with the value in step 1 and iterate the procedure until convergence is reached.

Specimen	l_{eq} [mm]	f_{cm} [MPa]	f_{tm} [MPa]	G_{ch} [N/mm]	G_F [N/mm]	b [-]	a_t [-]	a_c [-]	b_t [-]	b_c [-]
$J\_01 - M^+$	50	28.31	1.76	16.16	0.06	0.86	1	7.87	2119	173
$J\_02 - M^+$	50	30.28	1.82	37.50	0.13	0.96	1	7.87	1010	80
$J\_02 - M^-$	50	20.73	1.50	9.51	0.05	0.81	1	7.87	2255	215

TABLE 6.1: Concrete parameters defining the uni-axial tensile and compressive constitutive laws.

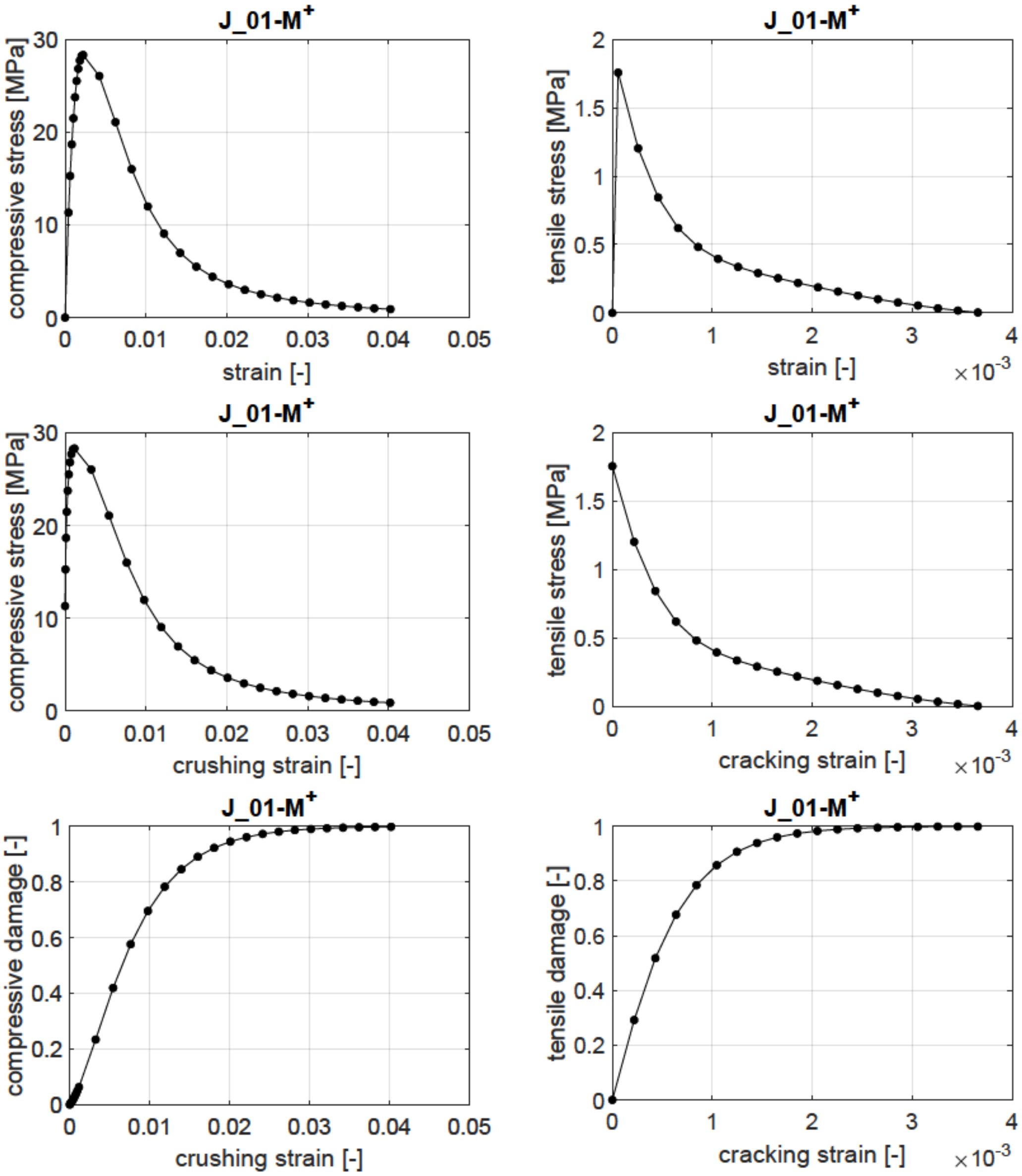

FIGURE 6.10: Stress, strain and damage for uni-axial tensile and compressive behaviour of concrete in $J\_01 - M^+$ specimen.

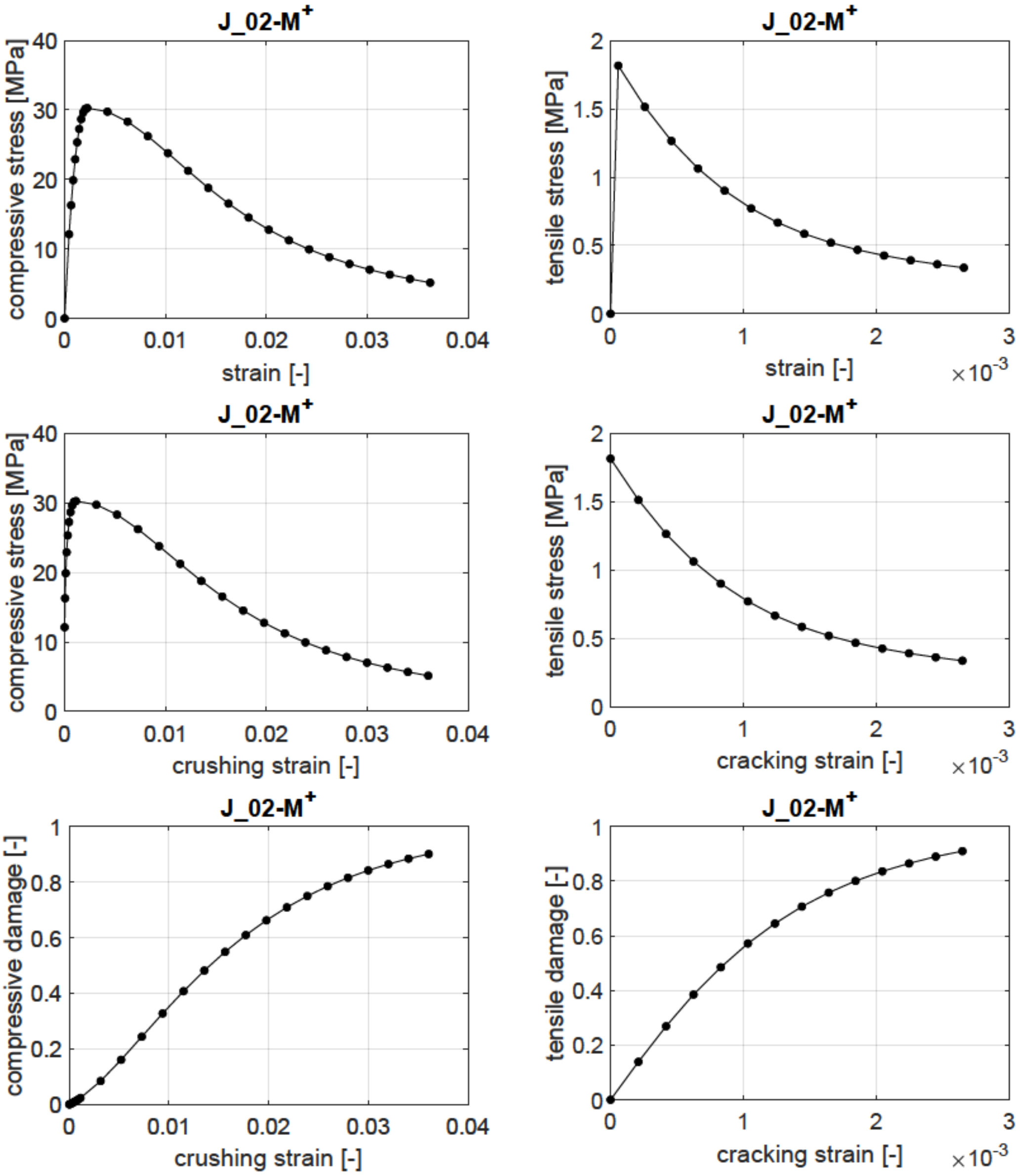

FIGURE 6.11: Stress, strain and damage for uni-axial tensile and compressive behaviour of concrete in $J\_02 - M^+$ specimen.

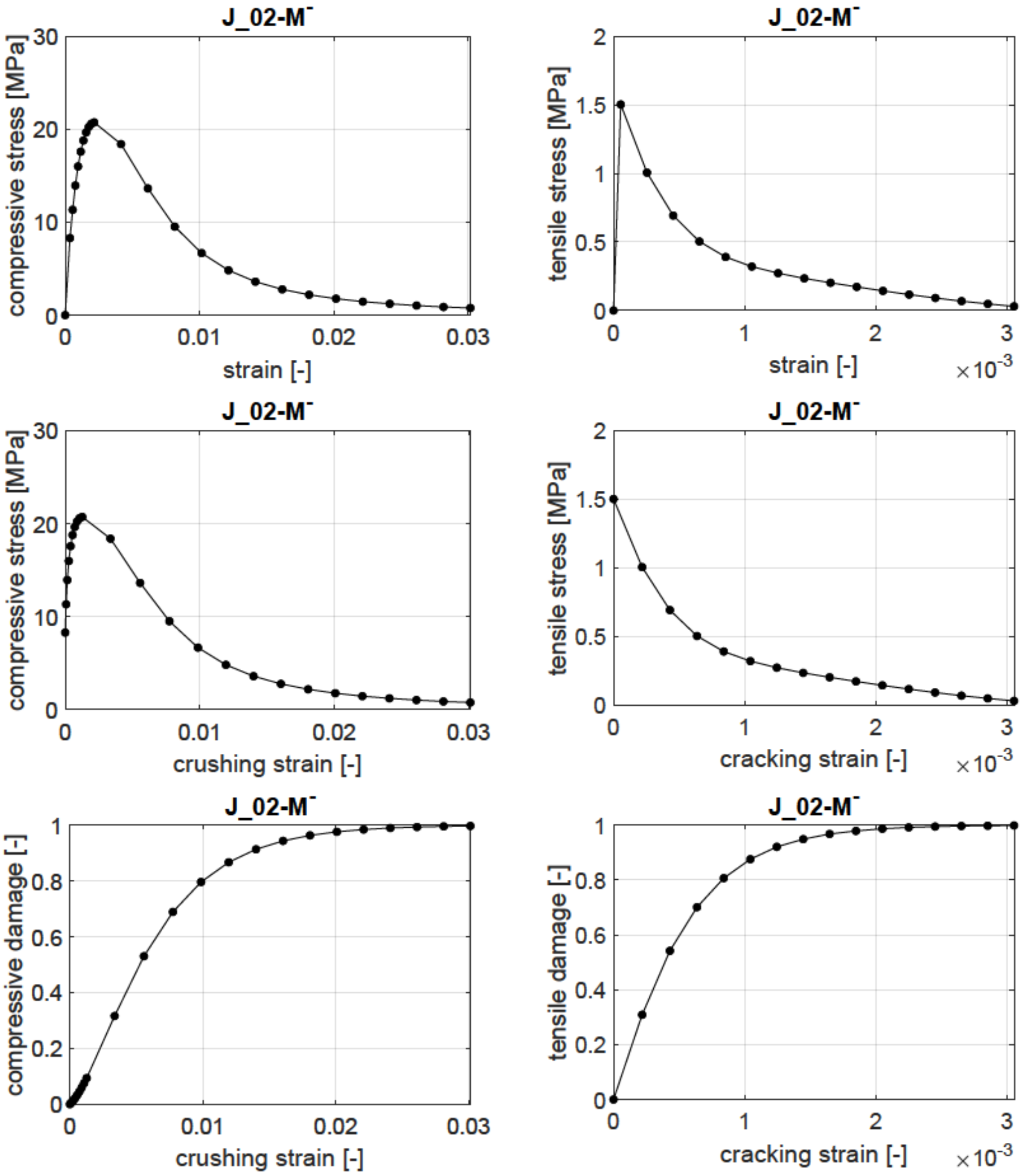

FIGURE 6.12: Stress, strain and damage for uni-axial tensile and compressive behaviour of concrete in $J\_02 - M^{-}$ specimen.

6.4.1.5 Concrete Plasticity

The constitutive parameters defining mechanical plasticity of the concrete in CDP model consist in four values, concerning the shape of the flow potential surface and the yield surface. The fundamental parameters are:

- K_c, the ratio of second stress invariants on tensile and compressive meridians;
- ψ, the dilatancy angle in deviatory plan at high confining pressure;
- f_{b0}/f_{c0}, the ratio between the bi-axial and uni-axial compressive yield strength;
- ϵ, the eccentricity of plastic potential surface.

The effective values can be identified by means of specific laboratory tests [58] or set to the default values or properly calibrated. In this work, some plasticity values were properly calibrated, others were assumed as default. Additionally, aiming at overcoming convergence problems of implicit analysis in Abaqus/Standard, viscosity parameter can be set to a small value, different from the default zero.

The effective stress, for the general three-dimensional multi-axial condition, is defined as:

$$\bar{\sigma} = (1-d)\boldsymbol{D}_0^{el} : (\boldsymbol{\varepsilon} - \boldsymbol{\varepsilon}^{pl}) \tag{6.4.22}$$

In Equation 6.4.22, $\boldsymbol{D}_0^{el}$ is the elastic stiffness tensor, σ and $\boldsymbol{\varepsilon}$ are respectively the stress and strain tensors, and d is the scalar damage parameter.

Two stress invariants of the effective stress tensor are useful to define both the plastic flow potential function and the yield surface, which are the hydrostatic pressure stress and the Mises equivalent effective stress:

$$\bar{p} = -\frac{1}{3}trace(\bar{\sigma}) \tag{6.4.23}$$

$$\bar{q} = \sqrt{\frac{3}{2}(\bar{\boldsymbol{S}} : \bar{\boldsymbol{S}})} \tag{6.4.24}$$

In Equation 6.4.24, $\bar{\boldsymbol{S}}$ is the effective stress deviator, equal to:

$$\bar{\boldsymbol{S}} = \bar{\sigma} + \bar{p}\boldsymbol{I} \tag{6.4.25}$$

The plastic flow in the CDP model is assumed to be non-associated potential plastic flow. The flow potential, G, serving this model is the Drucker-Prager hyperbolic function [73]:

$$G = \sqrt{(\varepsilon\sigma_{t0}tan\psi)^2 + \bar{q}^2} - \bar{p}tan\psi \tag{6.4.26}$$

in which:

- ϵ is the eccentricity parameter stating the rate at which the function approaches the asymptote. Indeed, the flow potential tends to a straight line as the eccentricity tends to zero;
- σ_{t0} is the uni-axial tensile stress at failure;
- ψ is the dilation angle measured in the p–q plane at high confining pressure.

The flow potential is always uniquely defined.

The eccentricity parameter modifies the curvature of the flow potential. In this work, the eccentricity has been set to the default value, $\epsilon = 0.1$, meaning the dilatation angle remain almost the same over a wide range of confining pressure.

The dilatancy angle, ψ, is a suitable parameter describing the phenomenon of the shear dilatancy, observed in all granular materials and in the cemented materials, like concrete, as well. Dilatancy represents the volume changes due to shear distortion of an element; hence ψ represents the ratio of plastic volume change over plastic shear strain. In other words, high dilatancy means a great increasing in volume and, in consequence, it corresponds to a high dilatancy angle. As clearly demonstrated in [54], the difference in the load-deformation behaviour between a strong dilatant and a non-dilatant material relies on the superior stiffness of the former as compared to the latter, while the resistances remain comparable. In [54], the values of the dilatancy angle have been investigated through test data then, in this work, ψ values have been calibrated, starting from the suggested ones.

The yield function of the model is by Lubliner et al.[55], with the modifications proposed by Lee and Fenves [56] including different evolution of strength under tension and compression. The evolution of the yield surface is controlled by the hardening variables, $\tilde{\varepsilon}^{pl}$ and $\tilde{\varepsilon}_c^{pl}$. In terms of effective stresses, the yield function can be expressed as:

$$F = \frac{1}{1-\alpha}\left(\bar{q} - 3\alpha\bar{p} + \beta(\tilde{\varepsilon}^{pl})\langle\hat{\bar{\sigma}}_{max}\rangle - \gamma\langle-\hat{\bar{\sigma}}_{max}\rangle\right) - \bar{\sigma}_c\tilde{\varepsilon}_c^{pl} = 0 \tag{6.4.27}$$

with:

$$\alpha = \frac{(\sigma_{b0}/\sigma_{c0}) - 1}{2(\sigma_{b0}/\sigma_{c0}) - 1}, \quad 0 \leq \alpha \leq 0.5 \tag{6.4.28}$$

$$\beta = \frac{\bar{\sigma}_c(\tilde{\varepsilon}_c^{pl})}{\bar{\sigma}_t(\tilde{\varepsilon}_t^{pl})}(1-\alpha) - (1+\alpha) \tag{6.4.29}$$

$$\gamma = \frac{3(1-K_c)}{2K_c - 1} \tag{6.4.30}$$

In Equation 6.4.27, $\hat{\bar{\sigma}}_{max}$ is the maximum principal effective stress.

In Equation 6.4.28, σ_{b0}/σ_{c0} is the ratio of initial bi-axial compressive yield stress and initial uni-axial compressive yield stress, as already referred. The exact value of this parameter can be evaluated by means of a laboratory bi-axial test [58]. In this work, the default value, $\sigma_{b0}/\sigma_{c0} = 1.16$, was assumed.

In Equation 6.4.29, $\bar{\sigma}_t(\tilde{\varepsilon}_t^{pl})$ is the effective tensile cohesion stress and $\bar{\sigma}_c(\tilde{\varepsilon}_c^{pl})$ is the effective compressive cohesion stress.

In Equation 6.4.30, K_c is the ratio of the second stress invariant on the tensile meridian, q_{TM}, to that on the compressive meridian, q_{CM}, at initial yield for any given value of the pressure invariant p such that the maximum principal stress is negative, $\hat{\sigma}_{max} \leq 0$ (see Figure 6.13). It must satisfy the condition $0.5 < K_c \leq 1$. In this work, the default value $K_c = 2/3$ has been assumed. However, the γ parameter could be exactly estimated by performing a full tri-axial test of concrete [58]. In conclusion, it is clearly seen that the shape of loading surface in the deviatoric plane depends on γ, Figure 6.13, whereas α is evaluated with reference to the yield surface for plane stress condition, i.e. the Kupfer's curve reported in Figure 6.14.

As revealed in advance, an additional parameter can be specified as part of the CDP model: the viscosity. Indeed, severe convergence difficulties can be frequent in implicit analysis programs, particularly when material models exhibit softening

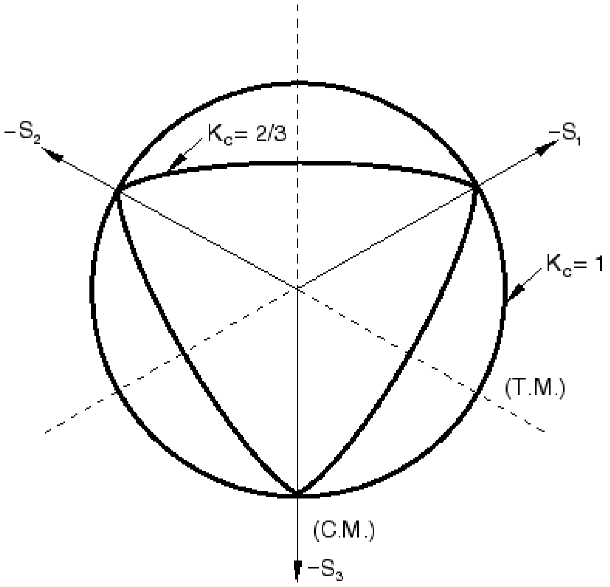

FIGURE 6.13: Yield surfaces in the deviatoric plane, corresponding to different values of K_c.

behaviour and stiffness degradation. The use of viscoplastic regularization of the constitutive equations is a common technique to overcome these kind of difficulties, making the consistent tangent stiffness of the softening material positive for sufficiently small time increments. In Abaqus/Standard the viscoplasticity lets the stresses exceeding the yield surface, by means of the Duvaut-Lions regularization. A small value, as compared to the characteristic time increment, of the viscosity parameter, μ, is often useful to reach convergence in the softening regime. It represents the relaxation time of the viscoplastic system and does not affect the analysis output. The default value of viscosity is zero, meaning no viscoplastic regularization is applied, but, in the performed analysis, it has been calibrated with the aim of completing the analysis.

The implemented parameters are summarised in Table 6.2.

Specimen	K_c	ψ	f_{b0}/f_{c0}	ϵ	μ
	-	(°)	-	-	-
$J\_01 - M^+$	0.67	20	1.16	0.1	0.0002
$J\_02 - M^+$	0.67	30	1.16	0.1	0.0001
$J\_02 - M^-$	0.67	20	1.16	0.1	0.0003

TABLE 6.2: CDP implemented constitutive parameters.

6.4.2 Steel

The steel reinforcement, rebars and stirrups, were modelled in Abaqus as beam elements embedded in the concrete host element. The metal plasticity model was used to describe the behaviour of the steel, by employing the effective material properties

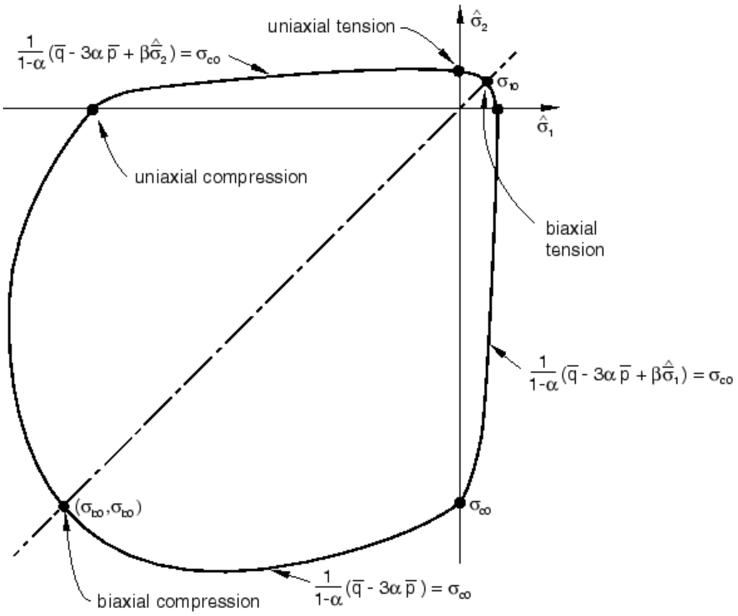

FIGURE 6.14: Yield surface in plane stress.

derived from characterization tests performed in the laboratory and listed in Chapter 3 for each specimen. The elastic perfectly plastic constitutive law was generally preferred to the elastic plastic hardening one.

6.5 Results

6.5.1 Conventional Specimens

6.5.1.1 Load-Displacement Curve

The comparison between the experimental and numerical results are illustrated in Figure 6.15, in terms of load versus displacement. In general, stiffness and strength are in good agreement. In particular, the FEM stiffness is slightly overrated at about $30kN$. The maximum load achieved in the experimental test was $86.06kN$, while it was $84.51kN$ in the FEM.

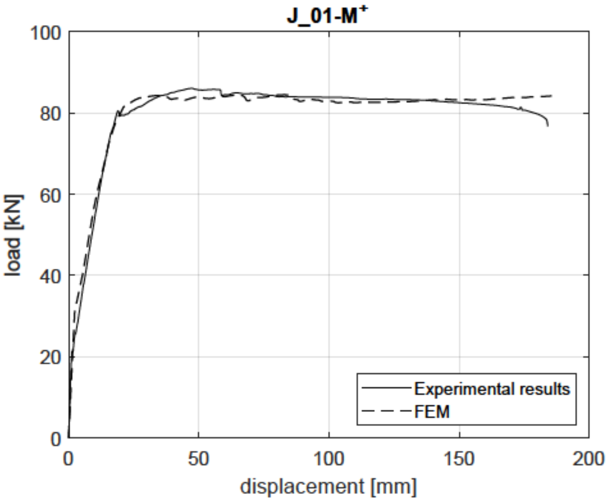

FIGURE 6.15: Comparison between experimental and simulated results of $J\_01 - M^+$ specimen.

6.5.1.2 Plasticity and Damage

The final plastic strain magnitude and concrete crushing damage affecting $J\_01 - M^+$ specimen are displayed, respectively, in Figure 6.16 and Figure 6.17. For the sake of comparison, photos of the experimental tests are reported on the left side. They show that the model is capable to exactly identify the areas affected by plasticity and crushing damage.

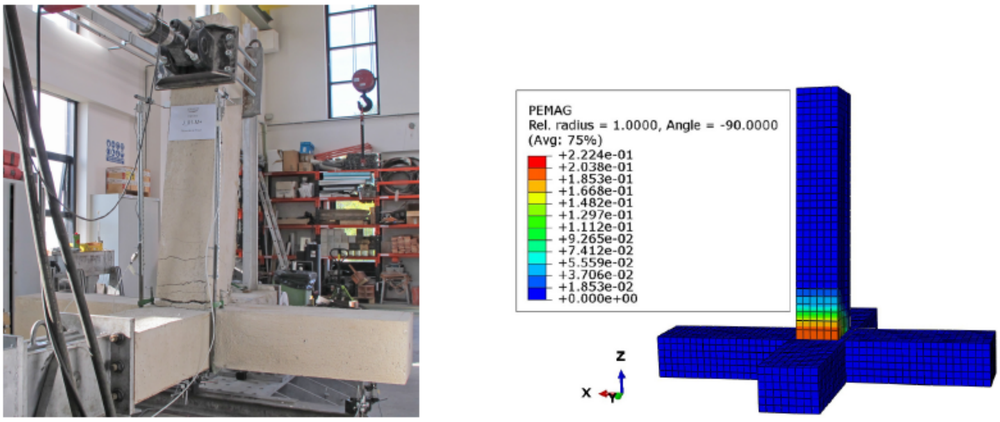

FIGURE 6.16: Plasticity at the final stage of the experimental and numerical analysis of $J\_01 - M^+$ specimen.

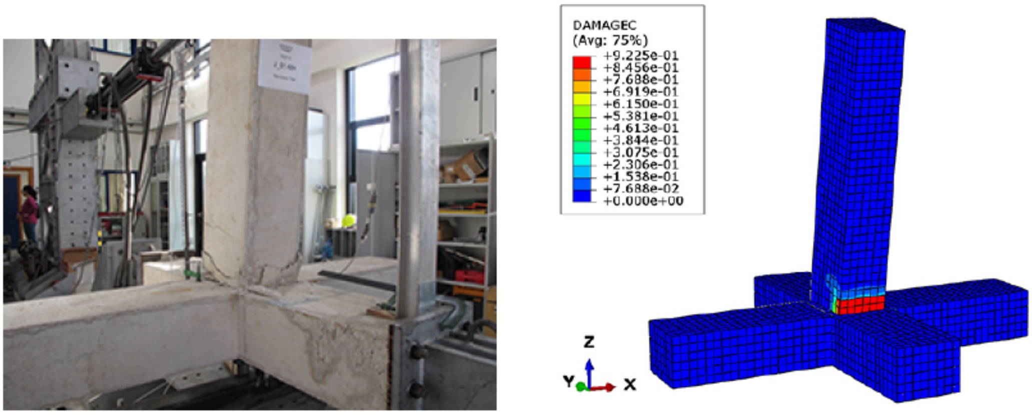

FIGURE 6.17: Crushing damage at the final stage of the experimental and numerical analysis of $J\_01 - M^{+}$ specimen.

6.5.2 Innovative Specimens

6.5.2.1 Load-Displacement Curve

The results of the FE analyses performed on innovative specimens are discussed in this Section in terms of load versus displacement. In Figure 6.18 and Figure 6.19, the response of, respectively, $J\_02 - M^{+}$ and $J\_02 - M^{-}$ numerical models was compared to that of the experimental tests. In this case, the experimental data of the monotonic and cyclic test were plotted, considering, for this latter, the skeleton curve. It should be recalled that the final objective is to calibrate the cyclic test. In Figure 6.18, the dotted line, $FEM - M$, follows the monotonic experimental curve, while the dashed line, $FEM - C$, follows the cyclic test envelope. Both the FEM curves provided excellent results in terms of stiffness, by catching also the transition from linear to non-linear behaviour. In terms of strength, the peak load in $FEM - M$ curve was equal to $44.79kN$, in accordance to the one achieved by the experimental monotonic curve, $44.50kN$. However, the displacements corresponding to the peak loads were not in agreement. The former was at $63.57mm$ and the latter at $41.00mm$. The peak loads observed in the skeleton and $FEM - C$ curves were, respectively, $38.88kN$ and $40.84kN$. Although the slight difference in the resistance, this latter model will be used for the future calibration of the cyclic test, accounting for the materials of the proper materials of $J\_02 - C$ specimen. Therefore, the further results shown below are related to this modeling. Since the $J\_02 - M^{-}$ monotonic test was unreliable, it becomes necessary to fit the FE curve with the skeleton curve of $J\_02 - C$ specimen, the dashed line in Figure 6.19. In the FEM, the stiffness is slightly overrated but perfectly parallel to the experimental curve. The FEM curve reached higher load values, due to the material properties of $J\_02 - M+$ specimen. Indeed, the peak load was $-58.18kN$ in the experimental monotonic curve, and $-56.11kN$ in the FEM curve.

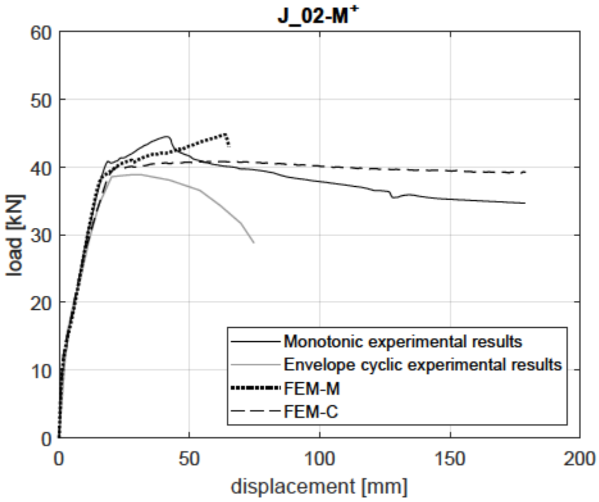

FIGURE 6.18: Comparison between experimental and simulated results of $J\_02 - M^{+}$ specimen.

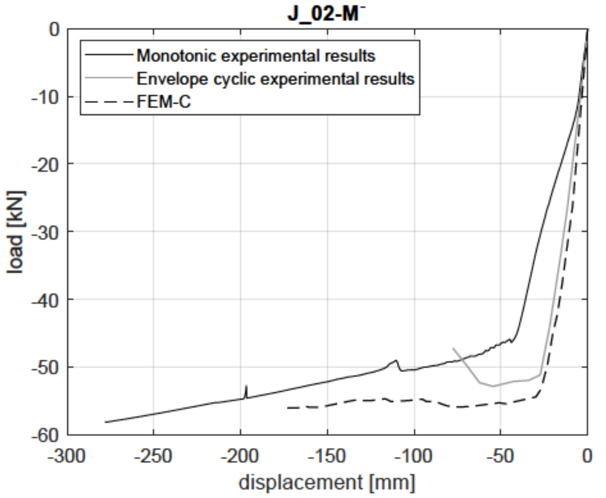

FIGURE 6.19: Comparison between experimental and simulated results of $J\_02 - M^{-}$ specimen.

6.5.2.2 Plasticity and Damage

From the results of the FE analyses performed on innovative specimens, the areas affected by plasticity and crushing damage were also pointed out. A comparison comparison between the final stage of the experimental test, on the left side of Figures, and the FE analysis, on the right side, are illustrated. In Figures 6.20 and 6.21, the plastic strain magnitude and the concrete crushing damage in $J\_02 - M+$ specimen are shown. In Figures 6.22 and 6.23, the plastic strain magnitude and the concrete crushing damage in $J\_02 - M-$ specimen are shown.

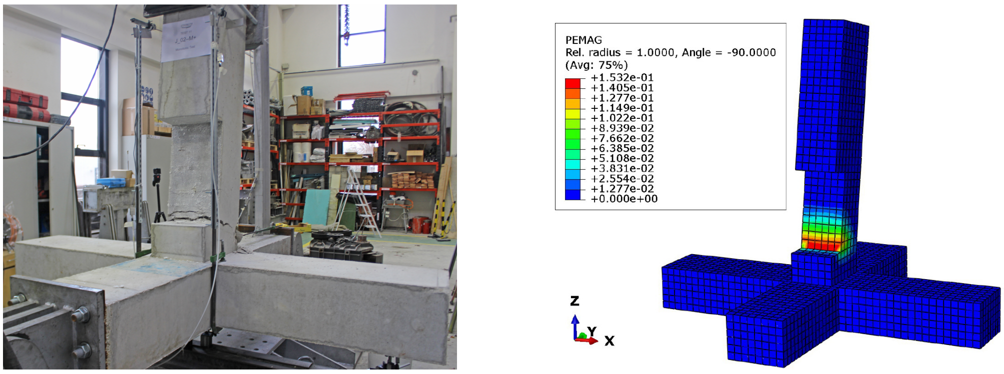

FIGURE 6.20: Plasticity at the final stage of the experimental and numerical analysis of $J\_02 - M^{+}$ specimen.

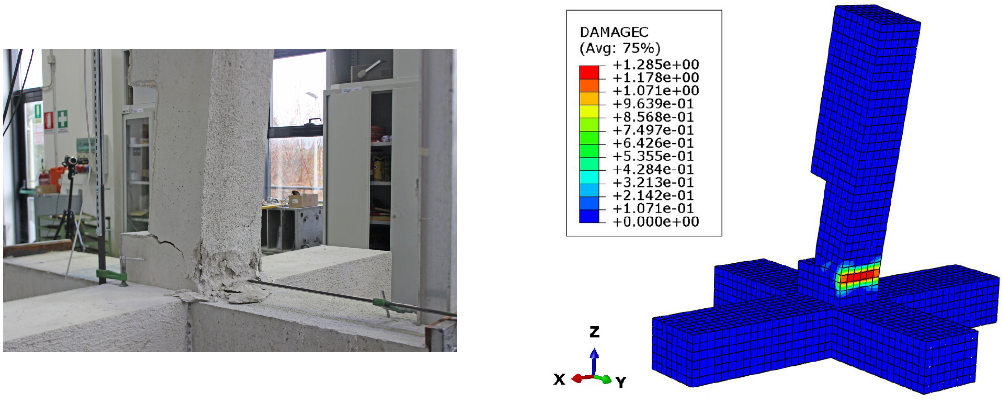

FIGURE 6.21: Crushing damage at the final stage of the experimental and numerical analysis of $J\_02 - M^{+}$ specimen.

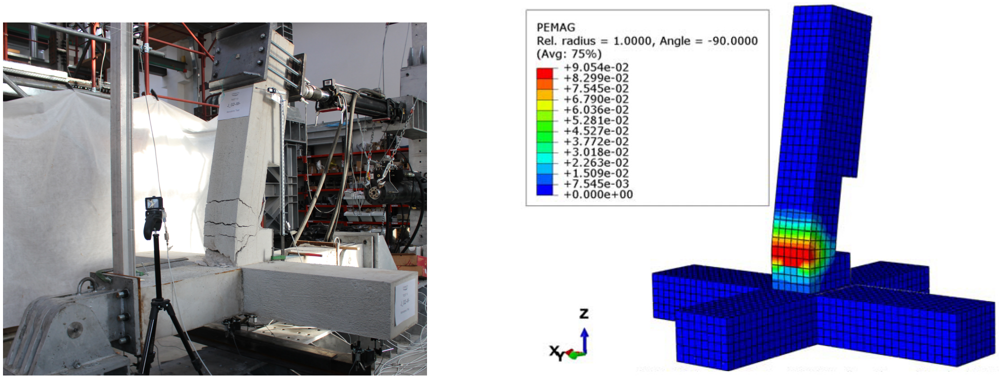

FIGURE 6.22: Plasticity at the final stage of the experimental and numerical analysis of $J\_02 - M^{-}$ specimen.

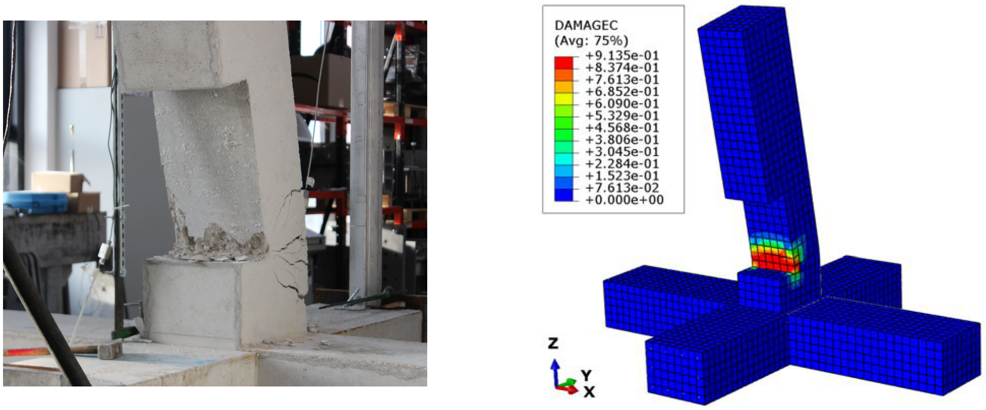

FIGURE 6.23: Crushing damage at the final stage of the experimental and numerical analysis of $J\_02 - M^{-}$ specimen.

Chapter 7

Conclusions and Future Developments

7.1 Main Conclusions

Since 1980, several experimental programs were devoted to investigating the influence of the RC slab in the beam-to-column connections. In the tested sub-assemblies and frames, the presence of the slab was found to mainly increase the flexural capacity of the beam, by acting as a beam flange. The slab action was referred to as "slab effect". The resistance and the stiffness of the structures were consequently increased. In seismic designed structures, the "slab effect" can be particularly detrimental since the flexural strength of the beam controls the capacity design rules. In particular, an enhanced flexural capacity of the beam reduces the column-to-beam moment ratio, thus shifting the plastic hinges in the adjacent columns and then altering the collapse mechanism of the structure. The experimental campaigns led to identifying different factors, of primary and secondary importance, determining the effective width of the slab acting as a flange for the beam. Based on the identified parameters, over the years, experimental formulas were derived and improved, with the aim to evaluate the exact width of the slab to account in the design stage. However, the wide experimental tests investigated a specific floor deck typology, made up of an integrated slab, monolithically cast with the beam.

Conversely, the present work evaluated, theoretically and experimentally, the contribution provided by a different RC floor deck to the resistance of connections designed according to the current Eurocodes. The most common and widely spread in the Mediterranean regions RC floor deck was considered, i.e. the one composed of RC joists and upper slab, with interlaid hollow tile blocks. With reference to the above-mentioned floor system, no experimental tests are available in the literature, but few numerical analyses[37] and studies on gravity load-designed buildings [38, 39]. Moreover, there is a gap in European rules [1, 44] in this area, since it is not specified how to account for the floor joists contribution in the resistance of RC connections. Indeed, in the case of a floor deck consisting of RC joists with the upper slab, it is preferable, since more rigorous, to use "joists effect" rather than "slab effect".

This thesis evolved from previous works of the same research team [40, 41], in which a theoretical model evaluating the joists contribution was developed. The model provides a formula computing the exact number of joists, within the influence area of a generic connection, which collaborate to the flexural strength of the beam (parallel to them). The joists and beam were assumed to act together, by constituting the so-called "equivalent beam".

The formula, properly modified, was applied in this work to design the 12 RC concrete beam-to-column joints experimentally tested at the STRENGTH (STRuctural ENGineering Test Hall) Laboratory of the University of Salerno. In particular, 6 conventional specimens and 6 innovative specimens were tested under quasi-static monotonic and cyclic loading. The tests were performed in displacement-control loading conditions. Each group of six conventional and innovative specimens was realised without and with the floor deck. Conventional modules without and with the floor deck were tagged, respectively, as J_01 and J_01_S. Innovative modules without and with the floor deck were tagged, respectively, as J_02 and J_02_S.

Conventional specimens, so-called since they were designed in compliance with the current European codes [1, 42], were tested for two main purposes. Firstly, the conventional specimens were tested to experimentally evaluate the over-resistance that the floor deck add to the connection. Secondly, they were tested in order to experimentally validate the accuracy of the employed "equivalent beam" theoretical model.

The results of the tests showed that the deck with joists, slab and tile blocks enhanced the resistance of the connection. Indeed, the specimens equipped with the floor deck, J_01_S, exhibited a greater flexural strength as compared to specimens without the deck, J_01. In accordance with the findings of the examined bibliography, the over-resistance was grater in hogging (+71%) rather than in sagging bending (+46%). When the slab underwent tensile stresses, indeed, a greater amount of reinforcement was involved in tension.

Experimental tests, moreover, proved that the "equivalent beam" theoretical model predicts the floor deck over-resistance fairly. The experimental results were compared to the expected values, computed by means of the "equivalent beam" model. The average difference between the experimental and expected values was 23% and 12%, respectively in positive and negative loading direction. Differences in the range $28 - 36\%$ were considered admissible since they were observed in the simple specimens J_01, considered as a benchmark. The reduced gap between the experimental and theoretical values, evaluated through the "equivalent beam" model, proved the accuracy of the model. In particular, the resistance of joints with the floor deck was quite accurately provided in positive loading direction; on the contrary, it was overrated in negative loading direction.

Also, the cracking evolution confirmed the actual involvement of the elements, which are at the base of the theoretical model. The diagonal cracks, spread over the beams supporting the joists, testified that the beam underwent torsional stress, due to the presence of the floor deck. Hence, the beam-joists interaction assumed in the model was proved. Besides, the joists were found to exhibit different displacement histories, once the slab underwent tensile stress. In particular, joists located at the same distance from the main beam showed the same trend. As a consequence, the joists along the bay span did not provide the same contribution to the beam resistance, rather it varied as the distance from the beam increased.

In addition to the above-mentioned conclusions about the response of conventional specimens, it should be noticed that the joint area was never affected by damage, neither in simple modules nor in modules with the floor deck. Hence, although the greater resistance due to the floor deck presence, the beam-to-column joints designed for the Medium Ductility Class (DCM) were sufficiently strong.

Innovative specimens were designed to reduce the resistance of the connection. Specifically, the main aim was to balance the over-resistance due to the floor deck and widely confirmed by the results of the experimental tests carried out on conventional specimens. In other words, it was expected that innovative connections, although the presence of the floor deck (*J*_02_*S*), exhibited a flexural strength close to that of simple conventional specimens (*J*_01).

Bearing in mind the basic concepts of the Reduced Beam Section (RBS) design, applied to steel structures, the flexural strength of the connection was reduced by modifying the beam section in a specific area. In particular, the effective height and the bottom reinforcement of the beam were reduced. These changes affected only a part of the beam, which was localised further away from the beam-column interface. Moreover, its extent was set equal to the plastic hinge length, evaluated according to EC8 [44]. In the innovative detail, indeed, the localised beam section reduction became the new plastic zone.

The results of the experimental campaign led up on innovative specimens, with and without the floor deck, demonstrated that the RBS effectively reduced the flexural strength of the connection. However, the reduction amount was different in positive and negative bending condition, due to the asymmetry of the RBS. By comparing innovative specimens with the same type of conventional specimens, i.e. *J*_02 versus *J*_01 and *J*_02_*S* versus *J*_01_*S*, the following conclusions were drawn. The flexural strength of simple innovative joints, *J*_02, decreased by 54% and 41%, respectively in positive and negative loading direction. The flexural strength of innovative specimens with the floor deck, *J*_02_*S*, reduced by 32% and 26% for, respectively, applied positive and negative displacements. Finally, with reference to simple conventional specimens, *J*_01, innovative specimens with the slab, *J*_02_*S*, showed the same resistance in positive bending conditions and 26% greater resistance in negative bending.

In summary, the resistance of innovative specimens with the floor deck was clearly much smaller than that of conventional specimens with the slab. Moreover, it was in perfect agreement with the resistance of simple conventional specimens, especially in positive loading direction. In conclusion, it can be stated that the design objective was achieved for positive bending moment, while it was not for negative bending moment. In this latter case, the floor deck still had a significant impact on the flexural strength of the connection. Since the response of innovative specimens is different in positive and negative loading direction, showing a greater increase of resistance once the slab underwent tensile stress, the innovative detail needs to be improved and consequently tested by means of Finite Element Analyses (FEA). The crucial point of the current detail is the continuity of the top beam steel reinforcement along the beam axis. Due to technological reasons, indeed, the same steel rebars equipped both the full-depth and reduced-depth part of the beam.

In order to understand the overall behaviour of innovative specimens, the beams supporting the joists were also analysed. As compared to conventional specimens, the beams of innovative specimens with the floor deck showed smaller rotations, in negative loading direction. The average peak rotation of longitudinal beams was $-0.0751 rad$, in conventional specimens, and $-0.0269 rad$, in innovative specimens. In this case, the crack pattern affecting the longitudinal beams was limited, due to the position of the rotational centre of the connection, which was shifted in the RBS.

The response of the joists displacements was also different under positive and negative uni-directional loading. Smaller joists displacements were found in the former case, as compared to the latter case.

According to the design purpose, the plastic hinge developed in the RBS. The results of the monotonic tests highlighted that the plasticity area was different in sagging and hogging bending, due to the asymmetry of the section. In the first case, plasticity developed in the RBS only. In the second case, it affected a larger area, centred at the beginning of the RBS, and extending toward the column and the beam end. However, it was far from the joint area, which is particularly vulnerable in RC structures. In this way, the plastic damage is surely moved away from the joint area to an area which is accessible in the case of retrofitting structural interventions.

Finally, a Finite Element Model (FEM) of the RC beam-to-column joints was investigated. The validation of the FEM was based on the experimental results. The FEM study was developed and analysed using Abaqus software. The analytical investigation was carried out through an extended comparative parametric study and was focused on the quantitative influence of certain simplified modelling assumptions and several critical modelling parameters on the response of the system. Great attention was given to define the material response, especially the reinforced concrete. The constitutive laws of concrete, both in compression and in tension, were modelled based on the results of laboratory tests and well-known literature references. In particular, the simple specimens, conventional and innovative, were calibrated according to a monotonic loading, as a preliminary stage before running cyclic analyses. The results of the calibrated numerical model were reported in terms of load-displacement curve, plasticity and concrete crushing damage. A good agreement between the experimental and numerical results was observed.

7.2 Future Developments

As a consequence of the above-referred conclusions, futures developments concerning the work herein discussed can be scheduled.

The main further development, which is currently ongoing, is the calibration of all the tested RC beam-to-column joints. Hence, the simple conventional and innovative specimens have to be calibrated according to the cyclic loading protocol. The specimens with the floor deck, instead, have to be calibrated according to the monotonic and cyclic loading protocol. The FEM, indeed, can provide additional information about the experimental tests. Moreover, further analyses can be carried out, accounting for different boundary and/or loading conditions, on the same specimens or different ones.

Further studies on the RBS detail of innovative specimens are necessary. For the reasons explained in Section 7.1, the RBS detail of innovative specimens have to be improved, by focusing on the design and the construction detail as well. Also in this case, numerical analyses are useful to investigate the response of the newly designed detail with the aim to find out the best solution.

Bibliography

[1] EN 1998-1 (Eurocode 8). *Design of Structures for Earthquake Resistance - Part 1: General Rules, Seismic Actions and Rules for Buildings*. European Committee for Standardization, Brussels, 2004.

[2] J.K. Editors: Wight, J.O. Jirsa, and W. Gene Corley. *SP-084: Earthquake Effects on Reinforced Concrete Structures - US Japan Research*. Vol. 84. ACI, 1985. DOI: `10.14359/14041`.

[3] U.S. Members of JTCC (Joint Technical Coordinating Committee) Group on Reinforced Concrete Building Structures. "U.S. Japan Research: Seismic Design Implications". In: *Journal of Structural Engineering* 114.9 (1988), pp. 2000–2016. DOI: `10.1061/(ASCE)0733-9445(1988)114:9(2000)`.

[4] N. Suzuki, S. Otani, and H. Aoyama. "The Effective Width of Slab in Reinforced Concrete Structures". In: *Transaction, Japan Concrete Institute* 5 (1983), pp. 309–316.

[5] M.R. Ehsani and J.K. Wight. "Effect of Transverse Beams and Slab on Behavior of Reinforced Concrete Beam-to-Column Connections". In: *Journal Proceedings*. Vol. 82. 2. 1985, pp. 188–195.

[6] A.J. Durrani and J.K. Wight. "Earthquake Resistance of Reinforced Concrete Interior Connections Including a Floor Slab". In: *ACI Structural Journal* 84.5 (1987), pp. 400–406. URL: `https://www.scopus.com/inward/record.uri?eid=2-s2.0-0023422002&partnerID=40&md5=20fcae9c4ae29d1d60d25900550027eb`.

[7] S.J. Pantazopoulou, J.P. Moehle, and B.M. Shahrooz. "Simple Analytical Model for T-beams in Flexure". In: *Journal of Structural Engineering (United States)* 114.7 (1988), pp. 1507–1523.

[8] C. W. French and J. P. Moehle. "Effect of Floor Slab on Behavior of Slab-Beam-Column Connections". In: *ACI SP-123, Design of Beam-Column Joints for Seismic Resistance, American Concrete Institute, Farmington Hills, Mich.* 21.15 (1991), pp. 225–258.

[9] C. W. French and A. Boroojerdi. "T-Beam Effect in Structures Subjected to Lateral Loading". In: *Proceedings of the Third U. S. National Conference on Earthquake Engineering.; Charleston, SC, USA;* Earthquake Engineering Research Inst, El Cerrito, CA, USA, 1986, pp. 1191–1202.

[10] M.R. Joglekar. "Behavior of Reinforced Concrete Floor Systems Under Lateral Load". PhD thesis. Austin: The University of Texas, 1986.

[11] H.E. Zerbe and A.J. Durrani. "Effect of a Slab on the Behavior of Exterior Beam to Column Connections". MA thesis. Houston, Texas: Rice University, 1985.

[12] O.V. Ammerman and C.W. French. "R /C Beam-Column-Slab Subassemblages Subjected to Lateral Loads". In: *Journal of Structural Engineering (United States)* 115.6 (1989), pp. 1289–1308.

[13] R. Leon and J.O. Jirsa. "Bidirectional Loading of R.C. Beam-Column Joints". In: *Earthquake Spectra* 2.3 (1986), pp. 537–564.

[14] A. Bas. "Behavior of Reinforced Concrete Beam-Column Connections with Floor Slabs under Bi-Directional Loads". MA thesis. Ontario, Canada: Department of Civil Engineering, University of Toronto, 1990.

[15] H. Aoyama. "Problems Associated with 'Weak-Beam' Design of Reinforced Concrete Frames". In: *Journal of the Faculty of Engineering, University of Tokyo, Series B* 38.2 (1985), pp. 75–105. URL: `https://www.scopus.com/inward/record.uri?eid=2-s2.0-0022122926&partnerID=40&md5=bc347e6fa82eb280f70c827eeed84899`.

[16] P.P.C. Cheung. "Seismic Design of Reinforced Concrete Beam-Column Joints With Floor Slab". PhD thesis. Christchurch, New Zealand: University of Canterbury, 1991.

[17] B.M. Shahrooz, S.J. Pantazopoulou, and S.P. Chern. "Modeling Slab Contribution in Frame Connections". In: *Journal of Structural Engineering (United States)* 118.9 (1992), pp. 2475–2494.

[18] N. Ning, W. Qu, and P. Zhu. "Role of Cast-in Situ Slabs in RC Frames under Low Frequency Cyclic Load". In: *Engineering Structures* 59 (2014), pp. 28–38. DOI: `10.1016/j.engstruct.2013.09.050`.

[19] X. Qi and S.J. Pantazopoulou. "Response of RC Frame under Lateral Loads". In: *Journal of Structural Engineering (United States)* 117.4 (1991), pp. 1167–1188.

[20] B.M. Shahrooz and Moehle J.P. *Experimental Study of Seismic Response of RC Setback Buildings*. Tech. rep. Berkeley: Earthquake Engineering Research Center, College of Engineering, University of California, 1987.

[21] Patrick Pak Chiu Cheung, T Paulay, and Robert Park. *A Reinforced Concrete Beam-Column Joint of a Prototype One-Way Frame with Floor Slab Designed for Earthquake Resistance*. Department of Civil Engineering, University of Canterbury, 1987.

[22] M. Shin and J.M. LaFave. "Reinforced Concrete Edge Beam-Column-Slab Connections Subjected to Earthquake Loading". In: *Magazine of Concrete Research* 56.5 (2004), pp. 273–291. DOI: `10.1680/macr.2004.56.5.273`. URL: `https://www.scopus.com/inward/record.uri?eid=2-s2.0-3142623092&doi=10.1680%2fmacr.2004.56.5.273&partnerID=40&md5=b37837e817878b9a086fc78bf37757d5`.

[23] S.J. Pantazopoulou and J.P. Moehle. "Identification of Effect of Slabs on Flexural Behavior of Beams". In: *Journal of Engineering Mechanics* 116.1 (1990), pp. 91–106. DOI: `10.1061/(ASCE)0733-9399(1990)116:1(91)`.

[24] S. Park and K.M. Mosalam. "Experimental Investigation of Non-Ductile RC Corner Beam-Column Joints with Floor Slabs". In: *Journal of Structural Engineering (United States)* 139.1 (2013), pp. 1–14. DOI: `10.1061/(ASCE)ST.1943-541X.0000591`.

[25] C.W. French and A. Boroojerdi. "Contribution of R/C Floor Slabs in Resisting Lateral Loads". In: *Journal of Structural Engineering (United States)* 115.1 (1989), pp. 1–18.

[26] H.E. Zerbe and A.J. Durrani. "Seismic Response of Connections in Two-Bay Reinforced Concrete frame subassemblies with a floor slab". In: *ACI Structural Journal* 87.4 (1990), pp. 406–415. URL: `https://www.scopus.com/inward/record.uri?eid=2-s2.0-0025462846&partnerID=40&md5=fbaaccf5a1533c718f4c6b0c29eddd8d`.

[27] M.A. Di Franco. "Effect of Spandrel Beam on Seismic Response of Concrete Frames". MA thesis. Montreal, Canada: Department of Civil Engineering and Applied Mechanics, McGill University, 1993.

[28] M.A. Di Franco, D. Mitchell, and P. Paultre. "Role of Spandrel Beams on Response of Slab-Beam-Column Connections". In: *Journal of Structural Engineering (United States)* 121.3 (1995), pp. 408–419. DOI: `10.1061/(ASCE)0733-9445(1995)121:3(408)`.

[29] P. Alaee, B. Li, and P.P.C. Cheung. "Parametric Investigation of 3D RC Beam-Column Joint Mechanics". In: *Magazine of Concrete Research* 67.19 (2015), pp. 1054–1069. DOI: `10.1680/macr.15.00005`.

[30] T. Rossetto et al. "The effect of slab and transverse beams on the behaviour of full-scale pre-1970's RC beam-column joints". In: *16th World Conference on Earthquake Engineering, 16WCEE 2017, Santiago Chile, 9th to 13th January*. 2017.

[31] H. Hitoshi, B. Satoshi, and M. Yasuhiro. "Reinforced Concrete Wide-Beam-to-Column Subassemblages Subjected to Lateral Load". In: *ACI Symposium Publication* 123 (1991), pp. 291–316.

[32] W.Y. Kam et al. "Influence of Slab on the Seismic Response of Sub-Standard Detailed Exterior Reinforced Concrete Beam Column Joints". In: *9th US National and 10th Canadian Conference on Earthquake Engineering 2010, Including Papers from the 4th International Tsunami Symposium*. Vol. 3. 2010, pp. 2188–2198.

[33] Ü. Yalçin and A.J. Durrani. "Effect of Slab on Inelastic Response of R/C building". In: *Journal of Structural Engineering (United States)* 119.5 (1993), pp. 1374–1387. DOI: `10.1061/(ASCE)0733-9445(1993)119:5(1374)`.

[34] S.J. Pantazopoulou and C.W. French. "Slab Participation in Practical Earthquake Design of Reinforced Concrete Frames". In: *ACI Structural Journal* 98.4 (2001), pp. 479–489. URL: `https://www.scopus.com/inward/record.uri?eid=2-s2.0-0035412967&partnerID=40&md5=0e39c96e8833026d1375c2abe06065f1`.

[35] R. Fenwick et al. "The Influence of Diaphragms on Strength of Beams". In: *New Zealand Society for Earthquake Engineering (NZSEE)*. 2006.

[36] S.M. Ahmed and U. Gunasekaran. "Effect of Floor Slabs on the Seismic Performance of RC Frames". In: *New Zealand Society for Earthquake Engineering (NZSEE)*. Mar. 2014.

[37] R. Nudo, G. Sarà, and S. Viti. "Influence of floor structures on seismic performance of RC frames". In: *13th World Conference on Earthquake Engineering : technical programme and handbook, August 1-6, 2004, Vancouver, British Columbia, Canada.* 2004.

[38] A. Masi. "Seismic Vulnerability Assessment of Gravity Load Designed R/C Frames". In: *Bulletin of Earthquake Engineering* 1.3 (2003), pp. 371–395. DOI: `10.1023/B:BEEE.0000021426.31223.60`.

[39] A. Masi and M. Vona. "Vulnerability Assessment of Gravity-Load Designed RC buildings: Evaluation of Seismic Capacity through Non-Linear Dynamic Analyses". In: *Engineering Structures* 45 (2012), pp. 257–269. DOI: `10.1016/j.engstruct.2012.06.043`. URL: `https://www.scopus.com/inward/record.uri?eid=2-s2.0-84866148491&doi=10.1016%2fj.engstruct.2012.06.043&partnerID=40&md5=8ec486c4614adc2d6e603ea5a57f05d6`.

[40] R. Montuori, E. Nastri, and V. Piluso. "Modelling of Floor Joists Contribution to the Lateral Stiffness of RC Buildings Designed for Gravity Loads". In: *Engineering Structures* 121 (2016), pp. 85–96. DOI: `10.1016/j.engstruct.2016.04.046`.

[41] R. Montuori et al. "The Effect of Floor Joists on the Elastic and Inelastic Behavior of R.C. Frames". In: *Engineering Structures* 196 (2019). DOI: `10.1016/j.engstruct.2019.06.003`.

[42] EN 1992-1-1 (Eurocode 2). *Design of concrete structures - Part 1-1: General Rules and Rules for Buildings*. European Committee for Standardization, Brussels, 2005.

[43] Ghersi, A. and Lenza, P. *Edifici antisismici in cemento armato. Nuove normative tecniche. Eurocodici e classi di rischio sismico (VII ed.).* D. Flaccovio, 2009.

[44] EN 1998-3 (Eurocode 8). *Design of structures for earthquake resistance - Part 3: Assessment and retrofitting of buildings*. European Committee for Standardization, Brussels, 2005.

[45] *UNI EN 12390-3:2009 - Testing hardened concrete - Part 3: Compressive strength of test specimens*. UNI EN 12390-3:2009. 2009.

[46] *UNI EN 12390-4:2009 - Testing hardened concrete - Part 4: Compressive strength - Specification for testing machines*. UNI EN 12390-4:2009. 2009.

[47] *UNI EN 6892-1:2016 - Metallic materials — Tensile testing — Part 1: Method of test at room temperature*. UNI EN 6892-1:2016. 2016.

[48] *UNI EN 15630-1:2019 - Steel for the reinforcement and prestressing of concrete - Test methods - Part 1: Reinforcing bars, rods and wire*. UNI EN 15630-1:2019. 2016.

[49] R. Park and T. Paulay. “Behaviour of Reinforced Concrete Beam-Column Joints Under Cyclic Loading”. In: *Proceedings Fifth World Conference on Earthquake Engineering, Rome*. 1973, p. 10.

[50] S. Hakuto, R. Park, and H. Tanaka. “Retrofitting of Reinforced Concrete Moment Resisting Frames.” In: (1995).

[51] American Concrete Institute (ACI). “Acceptance Criteria for Moment Frames Based on Structural Testing and Commentary (ACI 374.1-05)”. In: (2005).

[52] Dassault Systèmes. *Abaqus Software*. 2000.

[53] Dassault Systèmes. *Abaqus 6.13 Abaqus/CAE User's Guide*. 2013.

[54] P.A. Vermeer et al. *Non-associated Plasticity for Soils, Concrete and Rock*. Stevin-Laboratory of the Department of Civil Engineering of the Delft University of Technology; Rijswijk (ZH), 1984. URL: `https://books.google.it/books?id=WQrkGwAACAAJ`.

[55] J. Lubliner et al. “A Plastic-Damage Model for Concrete”. In: *International Journal of Solids and Structures* 25.3 (1989), pp. 229–326.

[56] J. Lee and G. L. Fenves. “Plastic-Damage Model for Cyclic Loading of Concrete Structures”. In: *Journal of Engineering Mechanics* 124.8 (1998), pp. 892–900. DOI: `doi:10.1061/(ASCE)0733-9399(1998)124:8(892)`.

[57] A. Earij et al. “Nonlinear three–dimensional finite–element modelling of reinforced–concrete beams: Computational challenges and experimental validation”. In: *Engineering Failure Analysis* 82 (Sept. 2017), pp. 92–115. DOI: `10.1016/j.engfailanal.2017.08.025`.

[58] T. Jankowiak and T. Łodygowski. “Identification of parameters of concrete damage plasticity constitutive model”. In: *Foundations of civil and environmental engineering* 6.1 (June 2005), pp. 53–69.

[59] B. Alfarah, F. López-Almansa, and S. Oller. "New methodology for calculating damage variables evolution in Plastic Damage Model for RC structures". In: *Engineering Structures* 132 (2017), pp. 70–86. DOI: `https://doi.org/10.1016/j.engstruct.2016.11.022`.

[60] L. Jason et al. "Damage and plasticity for concrete behavior". In: *European Congress on Com-putational Methods in Applied Sciences and Engineering, Jyväskylä* (2004).

[61] P.S. Wang and FJ. Vecchio. "VecTor2 and formworks user manual, University of Toronto, Canada." In: (2006).

[62] K. Genikomsou and M. Polak. "Finite element analysis of punching shear of concrete slabs using damaged plasticity model in ABAQUS". In: *Engineering Structures* 98 (Sept. 2015). DOI: `10.1016/j.engstruct.2015.04.016`.

[63] M.A. Najafgholipour et al. "Finite Element Analysis of Reinforced Concrete Beam-Column Connections with Governing Joint Shear Failure Mode". In: *Latin American Journal of Solids and Structures* 14 (Aug. 2017), pp. 1200–1225. ISSN: 1679-7825.

[64] J.G.M. Van Mier. *Strain-softening of concrete under multiaxial loading conditions*. Citeseer, 1984.

[65] Z. Bazant and B. Oh. "Crack Band Theory for Fracture of Concrete". In: *Matériaux et Constructions* 16 (May 1983), pp. 155–177. DOI: `10.1007/BF02486267`.

[66] W. B. Krätzig and R. Pölling. "An elasto-plastic damage model for reinforced concrete with minimum number of material parameters". In: *Computers & Structures* 82.15 (2004), pp. 1201–1215. ISSN: 0045-7949. DOI: `https://doi.org/10.1016/j.compstruc.2004.03.002"`. URL: `http://www.sciencedirect.com/science/article/pii/S0045794904000665`.

[67] A. Hillerborg. "The theoretical basis of a method to determine the fracture energy GF of concrete". In: *Materials and Structures/Materiaux et Constructions* 18.106 (1985), pp. 291–296. ISSN: 1359-5997.

[68] CEB-FIP. "Model code 2010". In: *Comité euro-international du béton* (2010).

[69] H. Cornelissen, D. A. Hordijk, and H. W. Reinhardt. "Experimental determination of crack softening characteristics of normalweight and lightweight concrete". In: vol. 31. 2. Delft University of Technology, 1986, pp. 291–296.

[70] "CEB-FIP Model Code 90". In: 213/214 (1993).

[71] V. Birtel and P. Mark. "Parameterised Finite Element Modelling of RC Beam Shear Failure". In: *2006 ABAQUS Users' Conference* (Jan. 2006).

[72] F. López-Almansa, B. Alfarah, and S. Oller. "Numerical simulation of RC frame testing with damaged plasticity model. Comparison with simplified models". In: *Second European conference on earthquake engineering and seismology (2ECEES), Istanbul*. Aug. 2014. DOI: `10.13140/2.1.3457.2169`.

[73] Daniel Charles Drucker and William Prager. “Soil mechanics and plastic analysis or limit design”. In: *Quarterly of applied mathematics* 10.2 (1952), pp. 157–165.